

# **Analysis of Confined Flows, Airfoils and Wings at Low Reynolds Numbers**

Araz Panahi

Department of Mechanical Engineering  
McGill University  
Montreal, Quebec, Canada

March 2019

A thesis submitted to McGill University in partial fulfilment of the requirements of  
the degree of Doctor of Philosophy

© Araz Panahi, 2019  
All Rights Reserved

## ABSTRACT

This thesis presents a deep analysis of the steady and unsteady viscous flows past airfoils and three-dimensional wings, and of three-dimensional confined flows at low Reynolds numbers. This research work was carried out in several cases studies: (i) steady and unsteady confined viscous flows; (ii) unsteady separations effects on the flow past stationary airfoils; (iii) effect of the ground proximity on the steady and unsteady viscous flows past oscillating and fixed airfoils; (iv) three-dimensional steady flows past wings at low Reynolds numbers.

The first part presents an efficient numerical method to solve three-dimensional steady and unsteady flows in a three-dimensional downstream-facing step channel at low Reynolds numbers. A finite-difference formulation and artificial compressibility were used on a stretched staggered grid for the solution of the Navier-Stokes equations, which is second-order accurate in space and time. The results were found to be in good agreement with the available experimental results. For the first time it was confirmed that the difference between the two-dimensional numerical solutions and the experimental results was due to the effect of the lateral walls in the experimental configuration.

The second part is the study of the unsteady effects on stationary airfoils due to unsteady flow separations at low Reynolds numbers. This study was performed with an efficient time-accurate numerical method using a pseudo-time relaxation procedure with artificial compressibility and a factored Alternate-Direction Implicit (ADI) scheme for the pseudo-time integration. The method is successfully validated by comparison with the experimental results obtained by Suwa *et al.* for triangular airfoils at low Reynolds numbers. It was found that the aerodynamic coefficients of lift and drag displayed periodic variations in time due to the unsteady flow separations occurring at low Reynolds numbers on stationary airfoils at relatively small angles of attack.

Analysis of the steady and unsteady flows over airfoils in the proximity of the ground was studied in the third part. Various flight evolutions of the micro-air-vehicles take place in the proximity of the ground or a ceiling, which require the aerodynamic solutions in these conditions at low Reynolds numbers. Solutions are presented for the unsteady lift and drag coefficients of several NACA airfoils in the proximity of the ground. A detailed study of the influence of

various geometric and flow parameters, such as the angle of attack, airfoil relative thickness, amplitude and frequency of oscillations and Reynolds number, on the flow separations in the proximity of the ground were carried out in this part. This study also presented the analysis of the unsteady flows past stationary airfoils in the proximity of the ground, aiming to determine the influence of the distance to the ground on these unsteady effects which are generated by the unsteady flow separations on the stationary airfoils at low Reynolds numbers. It was found that these unsteady effects appear at lower angles of attack for the airfoils in the proximity of the ground than in free flight.

The fourth and final case study is the three-dimensional analysis of the steady viscous flows past rectangular wings with various NACA airfoil sections at low Reynolds numbers. The solutions are obtained using an efficient numerical method to solve the Navier-Stokes equations for incompressible flows. The numerical solutions of the aerodynamic lift and drag coefficients obtained by this method are validated with the experimental results obtained by Sunada *et al.* for rectangular wings. A parametric study of the influence of various geometric and flow parameters, such as wing thickness, wing airfoil camber, angle of attack and Reynolds number is also presented.

The solutions obtained in all these studies are completely original and are validated by experimental results. They have also shown very interesting results, such as the effect of lateral walls in the experimental configurations, and the time variation of the aerodynamic lift and drag coefficients of the stationary airfoils due to the formation of the unsteady flow separations at low Reynolds numbers.

## RÉSUMÉ

Cette thèse présente une analyse approfondie des écoulements visqueux permanents et oscillatoires autour des profils aérodynamiques et des ailes tridimensionnelles, ainsi que des écoulements confinés tridimensionnels à faible nombre de Reynolds. Ces travaux de recherche ont été réalisés dans plusieurs études: i) les écoulements visqueux confinés permanents et oscillatoires; (ii) les effets de séparation nonstationnaires sur les profils aérodynamiques stationnaires; (iii) l'effet de la proximité du sol sur les écoulements visqueux stationnaires et oscillatoires autour des profils aérodynamiques fixes et oscillants; (iv) les écoulements en trois dimensions autour des ailes à faibles nombres de Reynolds.

La première partie présente une méthode numérique efficace pour résoudre les écoulements permanents et oscillatoires en trois dimensions dans un canal à faibles nombres de Reynolds. Une formulation à différences finies et une compressibilité artificielle ont été utilisées pour la solution des équations de Navier-Stokes, qui est précise au second ordre dans l'espace et dans le temps. Les résultats se sont avérés en bon accord avec les résultats expérimentaux disponibles. Pour la première fois, il a été confirmé que la différence entre les solutions numériques en deux dimensions et les résultats expérimentaux était due à l'effet des parois latérales dans la configuration expérimentale.

La seconde partie est l'étude des effets nonstationnaires sur les profils aérodynamiques stationnaires générés par les séparations d'écoulement oscillatoires à faibles nombres de Reynolds. Cette étude a été réalisée avec une méthode numérique efficace dans le temps, utilisant une procédure de relaxation pseudo-temporelle avec compressibilité artificielle et un schéma implicite de la direction alternative (ADI) factorisé pour l'intégration pseudo-temporelle. La méthode est validée avec succès par comparaison avec les résultats expérimentaux obtenus par Suwa et al. pour les profils aérodynamiques triangulaires à faibles nombres de Reynolds. On a constaté que les coefficients aérodynamiques de portance et de traînée présentaient des variations périodiques dans le temps en raison des séparations d'écoulement nonstationnaires se produisant à des nombres de Reynolds faibles sur des profils aérodynamiques fixes à des angles d'attaque relativement faibles.

L'analyse des écoulements permanents et oscillatoires sur les profils aérodynamiques à proximité du sol a été étudiée dans la troisième partie. Diverses évolutions de vol des micro-véhicules aériens se produisent à proximité du sol ou d'un plafond, ce qui nécessite des solutions aérodynamiques dans ces conditions à des faibles nombres de Reynolds. Des solutions sont présentées pour les coefficients de portance et de traînée oscillatoires de plusieurs profils aérodynamiques NACA à proximité du sol. Une étude détaillée de l'influence de divers paramètres géométriques et d'écoulement, tels que l'angle d'attaque, l'épaisseur relative du profil, l'amplitude et la fréquence des oscillations et le nombre de Reynolds, a été réalisée dans cette partie. Cette étude a également présenté l'analyse des écoulements oscillatoires autour des profils aérodynamiques stationnaires à proximité du sol, visant à déterminer l'influence de la distance au sol sur ces effets oscillatoires générés par les séparations d'écoulement oscillatoire sur les profils aérodynamiques stationnaires à des faibles nombres de Reynolds. Il a été constaté que ces effets oscillatoires apparaissent à des angles d'attaque plus faibles pour les profils aérodynamiques à proximité du sol qu'en vol libre.

La quatrième et dernière étude de cas est l'analyse tridimensionnelle des écoulements visqueux autour des ailes rectangulaires avec diverses sections de profil aérodynamique à faibles nombres de Reynolds. Les solutions sont obtenues en utilisant une méthode numérique efficace pour résoudre les équations de Navier-Stokes pour les écoulements incompressibles. Les solutions numériques des coefficients de portance et de traînée aérodynamiques obtenus par cette méthode sont validées avec les résultats expérimentaux obtenus par Sunada et al. pour les ailes rectangulaires. Une étude paramétrique de l'influence de divers paramètres géométriques et d'écoulement, tels que l'épaisseur de l'aile, la cambrure du profil de l'aile, l'angle d'attaque et le nombre de Reynolds est également présentée.

Les solutions obtenues dans toutes ces études sont originales et validées par des résultats expérimentaux. Ils ont également montré des résultats très intéressants, tels que l'effet des parois latérales dans les configurations expérimentales et la variation oscillatoire des coefficients de portance et de traînée aérodynamiques des profils aérodynamiques stationnaires dus à la formation des séparations d'écoulement oscillatoires à faibles nombres de Reynolds.

## **DEDICATION**

I would like to dedicate my thesis to my dear wife Sara, my beloved parents Hossein and Farah, my sister Aysan, and my brother Yashar for their constant encouragement and support during my doctoral studies.

## **ACKNOWLEDGMENT**

I would like to thank my supervisor, Professor Dan Mateescu, for his constant guidance, knowledge, encouragement, support, availability, patience, kindness, and outstanding mentorship throughout this research. He was abundantly helpful and offered invaluable assistance and his contributions in the field of applied aerodynamics have given novel methods and approaches to the evaluation and understanding of very complex aerodynamics problems, and this thesis is a good example thereof.

Many thanks to all my friends and colleagues at McGill University CFD lab, especially Abdurrazag Khaled, Manuel Munoz, Chao Wang, Valentine Roy, and Olivier Scholz for their never ending supports and continuous feedbacks.

This research would not have been possible without the financial assistance of McGill University Faculty of Engineering MIDA program, and Professor Dan Mateescu research fund.

## MAIN CONTRIBUTIONS

The main contributions of this thesis consist of the development of numerical methods and computational codes for the analysis of the steady and unsteady viscous flows past fixed or oscillating airfoils and wings in free flight or in the proximity of the ground, and of the three-dimensional confined flows at low Reynolds numbers. The obtained computational solutions are of topical interest for Micro-Aerial Vehicles (MAVs), Unmanned-Aerial Vehicles (UAVs), and for the steady and unsteady confined laminar flows in various industrial applications.

The main research contributions are summarized below.

### **Confined three-dimensional flows**

- 1) A novel three-dimensional method has been developed for the time-accurate solutions of the Navier-Stokes equations in the incompressible confined flows at low Reynolds numbers. This very efficient method is second-order accurate in space and time, uses artificial compressibility and a factored Alternate-Direction Implicit (ADI) scheme, and is based on a finite difference formulation on a stretched staggered grid. This method solves for the first time the three-dimensional steady and unsteady incompressible flows at low Reynolds numbers.
- 2) Original solutions have been obtained for the steady and unsteady confined viscous flows for the benchmark case of the downstream-facing step channel at low Reynolds numbers, which are generated by the time variable inflow velocities and by the oscillating walls.
- 3) The study of these confined steady flows at low Reynolds numbers, explains and confirms that the disagreement between the two-dimensional solutions and the experimental results is due to the three-dimensional effect of the lateral walls. The obtained three-dimensional computational solutions were in good agreement with the experimental results.
- 4) The multiple flow separations generated on the upper and lower walls have been thoroughly studied in function of the Reynolds number, span-to-height ratio, and the amplitude and frequency of the inflow velocity and the wall oscillations.

### **Unsteady separations effects on the flow past stationary airfoils**

- 1) The unsteady separations effects on the flow past stationary airfoils at low Reynolds numbers have been studied using an efficient time-accurate numerical method for the integration of the Navier-Stokes equations. This numerical method is based on a second-order three-point-backward implicit scheme for the real time discretization and a pseudo-time relaxation procedure using artificial compressibility and a factored alternate-direction implicit scheme for the pseudo-time integration. A special decoupling procedure using the continuity equation reduces the problem to the solution of scalar-tridiagonal systems of equations, which enhances substantially the computational efficiency of the method.
- 2) The solutions obtained for the triangular airfoil were found in good agreement with the experimental results, before the effects of unsteady flow separations become important, since the experimental results were obtained only for steady flows.
- 3) This study indicated for the first time that the lift and drag coefficients of the stationary airfoil have oscillations in time generated by the unsteady flow separations on the upper surface of airfoil at low Reynolds numbers, which appear at relatively low angles of attack (about 8 degrees).
- 4) These flow separations effects on the unsteady aerodynamic coefficients have been studied for various geometric and flow parameters, such as the angle of attack, relative thickness and camber, and Reynolds number.

### **Effect of the ground proximity on the steady and unsteady viscous flows past oscillating and fixed airfoils**

- 1) The effect of the ground proximity on the steady and unsteady flows past airfoils has been thoroughly studied to solve the problems encountered by the micro-air-vehicles flying in the proximity of the ground or ceiling. The method developed in the previous case study has been extended to solve this problem.
- 2) This study revealed the flow separations appear on the upper surface of the airfoil at lower angles of attack are due to the proximity of the ground. It was also found that the flow separation regions developed on the upper surface of the airfoil increase with the

getting closer to the ground, and for larger Reynolds numbers, thinner airfoils, and higher angles of attack.

- 3) The solutions for the lift and drag coefficients of the steady and unsteady flows for several symmetric and cambered NACA airfoils in the proximity of the ground are thoroughly analyzed in function of the distance to the ground. The unsteady flow separations on the airfoils are studied with the aid of flow visualizations illustrating the changes in the flow pattern at various moments in time.

### **Three-dimensional steady flows past rectangular wings at low Reynolds numbers**

- 1) An efficient numerical method has been developed to solve the Navier-Stokes equations for incompressible flows past rectangular wings at low Reynolds numbers. The problem is solved in a computational domain obtained from the physical flow domain by a coordinate transformation, and using a pseudo-time relaxation procedure with artificial compressibility, a factored alternate-direction implicit scheme, and a special decoupling procedure to reduce the problem to the solutions of scalar-tridiagonal systems of equations, which improves significantly the computational efficiency of the method. It is interesting to note that for the micro-air vehicles applications, the chord length is between 5 and 20 cm, Reynolds number is between 600 and 4000 and the Mach number is less than 0.03, which justifies the numerical method used in this thesis based on incompressible flows in comparison with the few solutions obtained with compressible flow solvers. This is especially important for the case of unsteady flows which occur due to the unsteady flow separation at relatively low angles of attack (about 8 degrees), as it was shown for the case of airfoils in this thesis.
- 2) The numerical solutions of the aerodynamic lift and drag coefficients obtained by this method are validated with the experimental results for rectangular wings.
- 3) The influence of various geometric and flow parameters on the aerodynamic coefficients, such as the wing thickness, wing airfoil camber, angle of attack and Reynolds number is thoroughly studied.

# TABLE OF CONTENTS

ABSTRACT .....	i
RÉSUMÉ .....	iii
DEDICATION .....	v
ACKNOWLEDGMENT .....	vi
MAIN CONTRIBUTIONS .....	vii
TABLE OF CONTENTS .....	x
LIST OF FIGURES .....	xv
LIST OF TABLES .....	xxvi
<b>1 Introduction .....</b>	<b>1</b>
1.1 Background and motivations of the study .....	1
1.2 Three-dimensional confined viscous flows at low Reynolds numbers .....	2
1.3 Study of unsteady flow separations on stationary airfoils at low Reynolds numbers .....	5
1.4 Steady and unsteady viscous flows over airfoils in the proximity of the ground .....	6
1.5 Steady viscous flows over wings at low Reynolds numbers .....	7
1.6 Thesis organization .....	10
<b>2 Steady and Unsteady Solutions for Three-Dimensional Confined Flows with Oscillating Walls and Variable Inflow Velocity .....</b>	<b>12</b>
2.1 Problem formulation and governing equations .....	13
2.1.1 Navier-Stokes equations for unsteady confined viscous flows .....	15
2.1.2 Boundary conditions .....	17
2.2 Method of solution for the unsteady three-dimensional confined viscous flows .....	18
2.2.1 Time-dependent coordinate transformation .....	18
2.2.2 Real-time discretization .....	20
2.2.3 Pseudo-time iterative relaxation technique .....	20
2.2.4 The linearization and alternating-direction implicit scheme .....	22
2.2.5 Special decoupling procedure .....	24
2.2.6 Spatial discretization on stretched staggered grids .....	25
2.3 Method validation .....	27
2.3.1 Validation for uniform rectangular channels .....	28

2.3.2 Comparison with the experimental data and effect of lateral walls .....	29
2.3.3 Grid sensitivity analysis for steady and unsteady internal flow solutions.....	30
2.3.4 Time-step convergence study .....	33
2.4 Steady solutions for the confined flows with backward-facing step channel .....	34
2.5 Solutions for three-dimensional unsteady confined flows with variable inflow velocity...	39
2.5.1 Influence of the amplitude of the inflow velocity fluctuations on the unsteady flow separations .....	41
2.5.2 Influence of the Reynolds number on the unsteady flow separations .....	41
2.6 Solutions for three-dimensional unsteady confined flows with oscillating walls and time-variable inflow velocity.....	43
2.6.1 Influence of the aspect ratio of the channel on the unsteady flow separations .....	45
2.6.2 Influence of the wall oscillation amplitude on the unsteady flow separations.....	46
2.6.3 Influence of the Reynolds number on the unsteady flow separations .....	47
2.6.4 Variation of the unsteady flow separations along the span of the channel.....	48
2.7 Summary of findings.....	50
<b>3 Unsteady Effects on Stationary Airfoils Due to Unsteady Flow Separations at Low Reynolds Numbers .....</b>	<b>52</b>
3.1 Problem formulation and numerical method.....	52
3.1.1 Navier-Stokes equations for unsteady viscous flows .....	53
3.1.2 Boundary conditions.....	54
3.2 Method of solution for unsteady viscous flows past stationary airfoils .....	55
3.2.1 Time-dependent coordinate transformation.....	55
3.2.2 Real-time discretization.....	58
3.2.3 Pseudo-time iterative relaxation technique.....	58
3.2.4 Alternating-direction implicit scheme .....	59
3.2.5 Lift and drag coefficients at low Reynolds numbers .....	61
3.3 Method validation .....	64
3.3.1 Comparison with experimental results .....	64
3.3.2 Grid sensitivity analysis.....	66
3.3.3 Time-step convergence study .....	67
3.4 Unsteady effects in the flow past the triangular airfoil .....	68
3.5 Unsteady solutions for several symmetric and cambered airfoils.....	77

3.5.1 Influence of Reynolds number for symmetric airfoils.....	85
3.5.2 Influence of the airfoil thickness for symmetric airfoils .....	86
3.5.3 Influence of the airfoil thickness for cambered airfoils.....	90
3.5.4 Influence of the airfoil relative camber .....	93
3.6 Summary of findings.....	94
<b>4 Analysis of Steady and Unsteady Viscous Flows past Airfoils in the Proximity of the Ground.....</b>	<b>96</b>
4.1 Problem formulation .....	97
4.2 Method of solution .....	99
4.3 Method validation for steady flows past airfoils far from the ground.....	102
4.4 Ground effect on the steady flows past airfoils at low Reynolds numbers .....	104
4.5 Unsteady flow solutions for oscillating airfoils in the proximity of the ground at low Reynolds numbers .....	108
4.5.1 Influence of the Reynolds number.....	108
4.5.2 Influence of the airfoil relative thickness .....	108
4.5.3 Influence of the oscillation frequency .....	111
4.5.4 Typical variations of the unsteady pressure coefficient .....	114
4.6 Solutions for unsteady flows past stationary airfoils in the proximity of the ground at low Reynolds numbers .....	115
4.6.1 Influence of the distance to the ground .....	116
4.6.2 Influence of the Reynolds number.....	123
4.6.3 Influence of the airfoil thickness .....	125
4.6.4 Influence of the distance to the ground for cambered airfoils.....	126
4.6.5 Influence of the relative camber .....	132
4.6.6 Influence of the relative thickness for cambered airfoils .....	133
4.6.7 Influence of the maximum camber position .....	134
4.7 Summary of findings.....	135
<b>5 Analysis of Steady Viscous Flows Past Wings at Low Reynolds Numbers .....</b>	<b>136</b>
5.1 Problem formulation and numerical method.....	137
5.2 Method of solution .....	142
5.3 Lift and drag coefficients of the rectangular wings.....	145
5.4 Method validation .....	146

5.5 Grid sensitivity analysis .....	147
5.6 Solutions of the steady viscous flows past rectangular wings .....	148
5.6.1 Influence of the Reynolds number.....	149
5.6.2 Influence of the wing thickness .....	150
5.6.3 Influence of Reynolds number and wing thickness on the variations of the local lift and drag coefficients along the semi-span of the wing .....	151
5.6.4 Influence of the wing camber .....	154
5.6.5 Streamline and flow pattern for steady viscous flows past wings .....	154
5.7 Summary of findings.....	157
<b>6 Conclusions.....</b>	<b>158</b>
6.1 Three-dimensional confined viscous flows at low Reynolds numbers .....	158
6.2 Unsteady flow separations on stationary airfoils at low Reynolds numbers.....	159
6.3 Steady and unsteady viscous flows past airfoils in the proximity of the ground .....	159
6.4 Steady viscous flows past wings at low Reynolds numbers .....	161
6.5 Future work .....	161
<b>LIST OF REFERENCES.....</b>	<b>162</b>
<b>APPENDICES.....</b>	<b>168</b>
<b>Appendix A.....</b>	<b>169</b>
Three-Dimensional backward-facing step channel .....	169
Alternating-direction implicit scheme .....	169
Spatial discretization for momentums .....	170
Spatial discretization of three successive sweeps.....	174
<b>Appendix B.....</b>	<b>184</b>
Steady and unsteady flows past airfoils .....	184
Time-dependent coordinate transformation coefficients.....	184
Alternating-direction implicit scheme .....	186
Spatial discretization for momentums .....	187
Spatial discretization of two successive sweeps.....	190
<b>Appendix C.....</b>	<b>192</b>
Steady viscous flows past wings .....	192
Geometrical coordinate transformation coefficients .....	192
Alternating-direction implicit scheme .....	194

Spatial discretization for momentums .....	196
Spatial discretization of three successive sweeps.....	201

## LIST OF FIGURES

Figure 2.1 Geometry of the rectangular channel with a downstream-facing step and an oscillating wall.....	14
Figure 2.2 Geometry of the three-dimensional staggered grid. ....	26
Figure 2.3 Three-dimensional stretched staggered grid with an oscillating wall configuration... ..	27
Figure 2.4 Typical flow pattern for the confined flow past a down-stream-facing step in a rectangular duct illustrating the flow separation regions by using the streamlines and the velocity profiles along the duct in the plane of symmetry ( $y = 0$ ). ....	27
Figure 2.5 Location of the separation and reattachment points on the upper and lower walls into the downstream-facing step ( $H/h = 2$ ) channel. ....	28
Figure 2.6 Velocity profiles at $y = 0$ (symmetry plane of the channel): (a) at several axial locations (for $2b/h = 1$ ), and (b) for several aspect ratios ( $2b/h$ ) at the axial location $x = 15$ .....	29
Figure 2.7 Steady flow over a downstream-facing step ( $h = 0.5$ ): Variation with the Reynolds number of the flow separation and reattachment locations on the upper wall ( $x_s$ and $x_r$ ) and the separation length on the lower wall ( $L_l$ ) in the symmetry plane of the channel ( $y = 0$ ). ....	30
Figure 2.8 Order of accuracy calculated from the grid sensitivity test data. ....	32
Figure 2.9 Several number of time steps per oscillation cycle describing the upper and lower wall separation length of unsteady confined flow past downstream-facing steps at $Re=400$ and inflow velocity amplitude $a=0.05$ and frequency $\omega=0.05$ .....	33
Figure 2.10 Influence of the Reynolds number on the variation of the flow separation and reattachment locations on the lower and upper walls ( $L_l$ , $x_s$ and $x_r$ ) along the span of the channel ( $y$ -direction) for $2b = 26.6$ and step height of $h = 0.5$ at various Reynolds numbers for $Re = 450, 600, 800$ and $1000$ . For the plane of symmetry ( $y = 0$ ): Comparison with the experimental results obtained by Armaly <i>et al.</i> [31] and Lee and Mateescu [13]......	35
Figure 2.11 Influence of the step height, $h_s = 1 - h$ , on the variations of the flow separation and reattachment locations on the upper and lower walls ( $x_s$ , $x_r$ and $L_l$ ) along the span of the channel ( $y$ -direction) for $2b = 26.6$ and for several step heights at $Re = 600$ . ....	36

Figure 2.12 Front views ( $x$ - $z$ plane) of the 3-D flow in the duct with a downstream-facing step ( $h = 0.5$ ), for $2b = 26.6$ at $Re = 600$ , illustrating the streamlines and the velocity contours at several distances from the plane of symmetry ( $y = 0$ ) towards the lateral wall ( $y = 13.3$ ). .....	37
Figure 2.13 Top view ( $x$ - $y$ plane) of the streamlines in the three-dimensional flow past a downstream-facing step ( $h = 0.5$ ), illustrating the flow separation regions on the lower and upper walls for $2b = 26.6$ at $Re = 600$ .....	37
Figure 2.14 Isometric view of the streamlines and velocity contours in a three-dimensional confined flow past a downstream-facing step ( $h = 0.5$ ), for $2b = 26.6$ at $Re = 600$ . .....	38
Figure 2.15 A detailed view of the streamlines and velocity contours in a three-dimensional confined flow past a downstream-facing step ( $h = 0.5$ ), for $2b = 26.6$ at $Re = 600$ . .....	38
Figure 2.16 Streamline patterns and velocity fields of the unsteady confined flow at various moments during the oscillatory cycle, $t/T = 3.0, 3.25, 3.5$ and $3.75$ , for $Re = 400, 600$ and $800$ , $\omega = 0.05$ and for three values of the amplitude of the inflow velocity variation, $a = 0.05, 0.2$ and $0.4$ ( $A = 0$ ). The color shades indicate the nondimensional values (with respect to $U_0$ ) of the local fluid velocity .....	40
Figure 2.17. Influence of the inflow velocity amplitude, $a$ , for fixed walls: Variation during the oscillatory cycle, $t/T$ , of the upper wall separation and reattachment locations and of the lower wall reattachment locations, for $Re = 400, 600$ and $800$ , $\omega = 0.05$ ( $2b = 26.6, A = 0$ ). .....	42
Figure 2.18. Influence of the Reynolds number, $Re$ : Variation during the oscillatory cycle, $t/T$ , of the upper and lower wall separation and reattachment locations, for $\omega = 0.05$ , $a = 0.05$ and $0.4$ ( $2b = 26.6, A = 0$ ).....	43
Figure 2.19 Streamline patterns and velocity fields of the unsteady confined flow at various moments during the oscillatory cycle, $t/T = 5.0, 5.25, 5.5$ and $5.75$ , for $Re = 600$ and $800$ , $\omega = 0.05$ and for two values of the amplitude of the inflow velocity variation, $a = 0$ and $0.05$ , and for the wall oscillation amplitude.....	44
Figure 2.20 Influence of the aspect ratio, $2b$ : Variation during the oscillatory cycle, $t/T$ , of the upper and lower wall separation and reattachment locations, for $Re = 600$ , $\omega = 0.05$ , $a = 0.05$ and for $A = 0.05, 0.1$ and $0.2$ . .....	45
Figure 2.21 Influence of the wall oscillation amplitude, $A$ : Variation during the oscillatory cycle, $t/T$ , of the upper and lower wall separation and reattachment locations, for $Re = 600$ , $\omega = 0.05$ , $a = 0.05$ and $A = 0.05, 0.1$ and $0.2$ . .....	46

Figure 2.22 Influence of the Reynolds number: Variation during the oscillatory cycle, $t/T$ , of the upper and lower wall separation and reattachment locations, for $\omega = 0.05$ , $A = 0.05$ , and $\alpha = 0$ and $0.05$ , and for $Re = 400, 600, 800$ and $1000$ ( $2b = 10$ , $y = 0$ ).	48
Figure 2.23 Spanwise variation of the unsteady flow separations: Variation during the oscillatory cycle, $t/T$ , of the upper and lower wall separation and reattachment locations, for wall amplitude oscillation $A = 0.05$ , inflow velocity amplitude, $\alpha = 0.05$ , and two Reynolds numbers $Re = 600$ and $800$ , at several locations along the span of the channel: $y = 0, 0.25b, 0.5b$ , and $0.75b$ .	49
Figure 2.24 Spanwise variation of the unsteady flow separations: Variation during the oscillatory cycle, $t/T$ , of the upper and lower wall separation and reattachment locations, for fixed walls ( $A = 0$ ), inflow velocity amplitude $\alpha = 0.1$ , and two Reynolds numbers $Re = 600$ and $800$ , at several locations along the span of the channel: $y = 0, 0.25b, 0.5b$ , and $0.75b$ .	50
Figure 3.1 Geometry of an airfoil placed in a uniform flow at the angle of attack $\alpha$ .	53
Figure 3.2 Geometry of the physical domain (top), and computational domain (bottom) ( $X, Y$ ) defined by coordinate transformations (3.6) to (3.7).	56
Figure 3.3 Staggered grid two-dimensional geometry.	61
Figure 3.4 Components of the resultant aerodynamics forces over the airfoil surface.	62
Figure 3.5 Integration of the pressure and shear stress distributions over an airfoil.	62
Figure 3.6 The variation with the angle of attack $\alpha$ of the time-averaged values of the lift and drag coefficients, $C_L$ and $C_D$ , of the triangular airfoil for $Re = 3000$ .	65
Figure 3.7 Influence of time steps per oscillation cycle: Comparison of lift and drag coefficients of NACA 0002 airfoil for $Re = 1000$ , at angle of attack, $\alpha = 14^\circ$ .and frequency $\omega = 0.05$ for several time steps, $N = 40, 60, 80$ and $100$ between the oscillatory cycle from $t/T = 5$ to $6$ .	67
Figure 3.8 Influence of time steps per oscillation cycle: showing the lift and drag coefficient variation of NACA 0002 airfoils for $Re = 1000$ , at angle of attack, $\alpha = 14^\circ$ .and frequency $\omega = 0.05$ for several time steps, $N = 40, 60, 80$ and $100$ between the oscillatory cycle from $t/T = 5.28$ to $5.34$ .	68
Figure 3.9 The variations with the nondimensional time, $t = t^*U_\infty/c$ , of the lift and drag coefficients, $C_L$ and $C_D$ , of the triangular airfoil for Reynolds number, $Re = 3000$ , at various angles of attack, $\alpha$ .	69

Figure 3.10 Illustration of the steady flow separations for the triangular airfoil for $Re = 3000$ at $\alpha = 2^\circ$ and $\alpha = 4^\circ$ .	70
Figure 3.11 Illustration of the unsteady flow separations for the triangular airfoil at various moments in time using the streamlines and the color shades indicating the nondimensional velocity field: For $Re = 3000$ at the angles of attack $\alpha = 6^\circ$ and $\alpha = 8^\circ$ .	71
Figure 3.12 Illustration of the unsteady flow separations for the triangular airfoil at various moments in time using the streamlines and the color shades indicating the nondimensional velocity field: For $Re = 3000$ at the angles of attack $\alpha = 10^\circ$ and $\alpha = 12^\circ$ .	72
Figure 3.13 Illustration of the unsteady flow separations for the triangular airfoil at various moments in time using the streamlines and the color shades indicating the nondimensional velocity field: For $Re = 3000$ at the angles of attack $\alpha = 14^\circ$ and $\alpha = 16^\circ$ .	73
Figure 3.14 The variations with the nondimensional time, $t = t*U_\infty/c$ , of the lift and drag coefficients, $C_L$ and $C_D$ , of the triangular airfoil for Reynolds number, $Re = 600$ , at various angles of attack, $\alpha$ .	74
Figure 3.15 The variations with the nondimensional time, $t = t*U_\infty/c$ , of the lift and drag coefficients, $C_L$ and $C_D$ , of the triangular airfoil for Reynolds number, $Re = 1000$ , at various angles of attack, $\alpha$ .	75
Figure 3.16 The variations with the nondimensional time, $t = t*U_\infty/c$ , of the lift and drag coefficients, $C_L$ and $C_D$ , of the triangular airfoil for Reynolds number, $Re = 1500$ , at various angles of attack, $\alpha$ .	76
Figure 3.17 The variations with the nondimensional time, $t = t*U_\infty/c$ , of the lift and drag coefficients, $C_L$ and $C_D$ , of the NACA 0004 airfoil for Reynolds number, $Re = 600$ , at various angles of attack, $\alpha$ .	77
Figure 3.18 The variations with the nondimensional time, $t = t*U_\infty/c$ , of the lift and drag coefficients, $C_L$ and $C_D$ , of the NACA 0004 airfoil for Reynolds number, $Re = 1000$ , at various angles of attack, $\alpha$ .	78
Figure 3.19 The variations with the nondimensional time, $t = t*U_\infty/c$ , of the lift and drag coefficients, $C_L$ and $C_D$ , of the NACA 0004 airfoil for Reynolds number, $Re = 1500$ , at various angles of attack, $\alpha$ .	79

Figure 3.20. Illustration of the steady flow separations for the NACA 0004 airfoil for two Reynolds numbers, $Re = 600$ and $1000$ , and at two angles of attack, $\alpha$ .....	80
Figure 3.21 Illustration of the unsteady flow separations for the NACA 0004 airfoil at various moments in time using the streamlines and the color shades indicating the nondimensional velocity field: For $Re = 600$ at the angles of attack $\alpha = 12^\circ$ and $\alpha = 14^\circ$ .....	81
Figure 3.22 Illustration of the unsteady flow separations for the NACA 0004 airfoil at various moments in time using the streamlines and the color shades indicating the nondimensional velocity field: For $Re = 600$ at the angles of attack $\alpha = 16^\circ$ and $\alpha = 18^\circ$ .....	82
Figure 3.23 Illustration of the unsteady flow separations for the NACA 0004 airfoil at various moments in time using the streamlines and the color shades indicating the nondimensional velocity field: For $Re = 1000$ at the angles of attack $\alpha = 10^\circ$ and $\alpha = 12^\circ$ .....	83
Figure 3.24 Illustration of the unsteady flow separations for the NACA 0004 airfoil at various moments in time using the streamlines and the color shades indicating the nondimensional velocity field: For $Re = 1000$ at the angles of attack $\alpha = 14^\circ$ and $\alpha = 16^\circ$ .....	84
Figure 3.25 Influence of Reynolds number for symmetric airfoils. Comparison of the variations with the nondimensional time, $t = t*U_\infty/c$ , of the lift coefficients, $C_L$ , of NACA 0004 airfoils for $Re = 600$ and $1000$ , at various angles of attack, $\alpha$ .....	85
Figure 3.26 Influence of Reynolds number for symmetric airfoils. Comparison of the variations with the nondimensional time, $t = t*U_\infty/c$ , of the drag coefficients, $C_D$ , of NACA 0004 airfoils for $Re = 600$ and $1000$ , at various angles of attack, $\alpha$ .....	86
Figure 3.27 Influence of the airfoil thickness for symmetric airfoils. Comparison of the variations with the nondimensional time, $t = t*U_\infty/c$ , of the lift coefficients, $C_L$ , of NACA 0002 and 0008 airfoils for Reynolds number $Re = 600$ , at various angles of attack, $\alpha$ .....	87
Figure 3.28 Influence of the airfoil thickness for symmetric airfoils. Comparison of the variations with the nondimensional time, $t = t*U_\infty/c$ , of the drag coefficients, $C_D$ , of NACA 0002 and 0008 airfoils for Reynolds number $Re = 600$ , at various angles of attack, $\alpha$ .....	88
Figure 3.29 Influence of the airfoil thickness for symmetric airfoils. Comparison of the variations with the nondimensional time, $t = t*U_\infty/c$ , of the lift coefficients, $C_L$ , of NACA 0002 and 0008 airfoils for Reynolds number $Re = 1000$ , at various angles of attack, $\alpha$ .....	89

Figure 3.30 Influence of the airfoil thickness for symmetric airfoils. Comparison of the variations with the nondimensional time, $t = t * U_{\infty} / c$ , of the drag coefficients, $C_D$ , of NACA 0002 and 0008 airfoils for Reynolds number $Re = 1000$ , at various angles of attack, $\alpha$ .	90
Figure 3.31 Influence of the airfoil thickness for cambered airfoils. Comparison of the variations with the nondimensional time, $t = t * U_{\infty} / c$ , of the lift coefficients, $C_L$ , of NACA 2402 and 2404 airfoils for Reynolds number $Re = 600$ , at various angles of attack, $\alpha$ .	91
Figure 3.32 Influence of the airfoil thickness for cambered airfoils. Comparison of the variations with the nondimensional time, $t = t * U_{\infty} / c$ , of the drag coefficients, $C_D$ , of NACA 2402 and 2404 airfoils at Reynolds number $Re = 600$ , for various angles of attack, $\alpha$ .	92
Figure 3.33 Influence of the airfoil relative camber. Comparison of the variations with the nondimensional time, $t = t * U_{\infty} / c$ , of the lift coefficients, $C_L$ , of NACA 2404 and 4404 airfoils for Reynolds number $Re = 600$ , at various angles of attack, $\alpha$ .	93
Figure 3.34 Influence of the airfoil relative camber. Comparison of the variations with the nondimensional time, $t = t * U_{\infty} / c$ , of the lift coefficients, $C_D$ , of NACA 2404 and 4404 airfoils for Reynolds number $Re = 600$ , at various angles of attack, $\alpha$ .	94
Figure 4.1 Geometry of an oscillating airfoil placed in a uniform flow at the variable incidence, $\alpha(t) = \alpha_0 + \alpha_A \cos(\omega t)$ , in the proximity of the ground.	97
Figure 4.2 Geometry of the physical $(\eta, \xi)$ and fixed computational domain $(X, Y)$ defined by the time-dependent coordinate transformations from equations (4.8) to (4.14).	100
Figure 4.3 Present solutions for $H = 12$ (no ground effect) for the lift coefficient of the isolated NACA 0002 and for the drag polar diagram for the isolated NACA 4402 airfoil for $Re = 1000$ and 2000, compared with the results obtained by Kunz and Kroo [28].	102
Figure 4.4 Present solutions obtained for $H = 12$ (no ground effect) for the pressure coefficient distribution on the NACA 0002 and NACA 0008 airfoils at zero incidence for Reynolds numbers $Re = 1000, 2000$ and $6000$ , compared with results obtained by Kunz and Kroo [28] and by Mateescu and Abdo [9, 10] for inviscid flows.	103
Figure 4.5 Influence of the Reynolds number. Typical variations of the lift and drag coefficients, $C_L$ and $C_D$ , with the angle of attack $\alpha$ for NACA 0004 airfoil at $Re = 600, 1000$ and $1500$ , for three nondimensional distances to the ground: $H = 0.3, H = 0.5$ and $H = 12$ (no ground effect).	104

Figure 4.6 Lift and drag coefficients,  $C_L$ ,  $C_D$ , and the lift-to-drag ratio,  $C_L/C_D$ , versus the angle of attack  $\alpha$  for  $Re = 1000$  for the nondimensional distances to the ground  $H = 0.3$ ,  $H = 0.5$  and  $H = 12$  (no ground effect)..... 105

Figure 4.7 Illustration of the flow separation on the upper surface of three NACA airfoils at angle of attack  $\alpha = 6^\circ$  and Reynolds number  $Re = 1000$  for the several distances to the ground  $H = 0.3$ ,  $H = 0.5$  and  $H = 12$  (no ground effect). The lines show the streamline patterns of the flow around the airfoil and the color shades indicate the nondimensional velocity fields (with respect to the uniform stream velocity  $U_\infty$ ) ..... 106

Figure 4.8 Illustration of the flow separation for NACA 0004 airfoil at angle of attack  $\alpha = 6^\circ$  for three Reynolds numbers,  $Re = 600$ ,  $1000$  and  $1500$  and for two distances to the ground:  $H = 0.5$  and  $H = 12$  (no ground effect)..... 107

Figure 4.9 Influence of Reynolds number: Solutions for the unsteady lift and drag coefficients for a NACA 0002 airfoil executing pitching oscillations with  $\alpha_0 = 0^\circ$ ,  $\alpha_A = 4^\circ$ ,  $\omega = 0.05$ , at  $Re = 600$  and  $1000$  for three distances to the ground:  $H = 0.3$ ,  $H = 0.5$ ,  $H = 12$  (no ground effect)... 109

Figure 4.10 Influence of Reynolds number: Solutions for the unsteady lift and drag coefficients for a NACA 0004 airfoil executing pitching oscillations with  $\alpha_0 = 0^\circ$ ,  $\alpha_A = 4^\circ$ ,  $\omega = 0.05$ , at  $Re = 600$  and  $1000$  for three distances to the ground:  $H = 0.3$ ,  $H = 0.5$ ,  $H = 12$  (no ground effect)... 110

Figure 4.11 Influence of Reynolds number: Solutions for the unsteady pitching moment coefficient,  $C_m$ , for a NACA 0002 and NACA 0004 airfoils executing pitching oscillations, with  $\alpha_0 = 0^\circ$ ,  $\alpha_A = 4^\circ$ ,  $\omega = 0.05$ , at  $Re = 600$  and  $1000$  for three distances to the ground:  $H = 0.3$ ,  $H = 0.5$ ,  $H = 12$  (no ground effect). ..... 111

Figure 4.12 Influence of the airfoil thickness: The unsteady aerodynamic coefficients for NACA 0002, NACA 0004 and NACA 0008 airfoils executing pitching oscillations with  $\alpha_0 = 0^\circ$ ,  $\alpha_A = 4^\circ$ ,  $\omega = 0.05$ , at  $Re = 1000$  for three distances to the ground:  $H = 0.3$ ,  $H = 0.5$ ,  $H = 12$  ..... 112

Figure 4.13 Influence of the oscillation frequency for NACA 0002 at two frequencies,  $\omega = 0.05$  and  $0.10$ , and for two values of the mean incidence  $\alpha_0 = 0^\circ$  and  $\alpha_0 = 2^\circ$ , at  $Re = 1000$  and for two distances to the ground:  $H = 0.3$  and  $H = 12$  (no ground effect)..... 113

Figure 4.14 Variations of pressure coefficient along the chord during the oscillatory cycle,  $t/T$ : For NACA 0004 and NACA 0002 airfoils oscillating with  $\alpha_A = 4^\circ$ ,  $\omega = 0.05$ , and with  $\alpha_0 = 0^\circ$  and  $\alpha_0 = 2^\circ$ , respectively, at  $Re = 1000$  and for  $H = 0.3$ ,  $H = 0.5$ ,  $H = 12$  (no ground effect)... 114

Figure 4.15 Influence of the distance to the ground,  $H$ : The variations with the nondimensional time,  $t = t^*U_\infty/c$ , of the lift coefficient,  $C_L$ , of the NACA 0004 airfoil for several nondimensional distances to the ground,  $H = 0.3, 0.5, 1.0$  and  $12$  (no ground effect), for  $Re = 1000$  and at various angles of attack,  $\alpha$  ..... 115

Figure 4.16 Influence of the distance to the ground,  $H$ : The variations with the nondimensional time,  $t = t^*U_\infty/c$ , of the drag coefficient,  $C_D$ , of the NACA 0004 airfoil for several distances to the ground,  $H = 0.3, 0.5, 1.0$  and  $12$  (no ground effect), for Reynolds number,  $Re = 1000$ , and at various angles of attack,  $\alpha$  ..... 116

Figure 4.17 Illustrations of the steady flow separations for the NACA 0004 airfoil for two Reynolds numbers,  $Re = 600$  and  $1000$  and at three angles of attack,  $\alpha = 4^\circ$ ,  $\alpha = 6^\circ$  and  $\alpha = 8^\circ$  at the nondimensional distance to the ground  $H = 0.5$  ..... 117

Figure 4.18 Illustration of the flow separations for the NACA 0004 airfoil at various moments in time,  $t = t^*U_\infty/c$ , comparison between two nondimensional distances to the ground,  $H = 0.5$  and  $H = 12$  (no ground effect), for  $Re = 1000$  and at  $\alpha = 10^\circ$  ..... 119

Figure 4.19 Illustration of the flow separations for the NACA 0004 airfoil at various moments in time,  $t = t^*U_\infty/c$ , comparison between two nondimensional distances to the ground,  $H = 0.3$  and  $H = 1$  (no ground effect), for  $Re = 1000$  and at  $\alpha = 10^\circ$  ..... 120

Figure 4.20 Illustration of the flow separations for the NACA 0004 airfoil at various moments in time,  $t = t^*U_\infty/c$ , comparison between two nondimensional distances to the ground,  $H = 0.5$  and  $H = 12$  (no ground effect), for  $Re = 1000$  and at  $\alpha = 12^\circ$  ..... 121

Figure 4.21 Illustration of the flow separations for the NACA 0004 airfoil at various moments in time,  $t = t^*U_\infty/c$ , comparison between two nondimensional distances to the ground,  $H = 0.3$  and  $H = 1$  (no ground effect), for  $Re = 1000$  and at  $\alpha = 12^\circ$  ..... 122

Figure 4.22 Influence of Reynolds number: Comparison of the variations with the nondimensional time,  $t = t^*U_\infty/c$ , of the lift and drag coefficients,  $C_L$  and  $C_D$ , for NACA 0002 airfoil for two Reynolds numbers,  $Re = 600$  and  $1500$ , at the distance to the ground  $H = 0.5$ , for various angles of attack,  $\alpha$  ..... 123

Figure 4.23 Influence of Reynolds number: Comparison of the variations with the nondimensional time,  $t = t^*U_\infty/c$ , of the lift and drag coefficients,  $C_L$  and  $C_D$ , for NACA 0004 airfoil for two Reynolds numbers,  $Re = 600$  and  $1000$ , at the distance to the ground  $H = 0.5$ , for various angles of attack,  $\alpha$  ..... 124

Figure 4.24 Influence of the airfoil thickness: Comparison of the variations with the nondimensional time,  $t = t^*U_\infty/c$ , of the lift coefficients,  $C_L$  and  $C_D$ , for two symmetric airfoils, NACA 0002 and NACA 0008 for Reynolds number,  $Re = 600$ , and the distance to the ground  $H = 0.5$ , for various angles of attack,  $\alpha$  ..... 125

Figure 4.25 Influence of the airfoil thickness: Comparison of the variations with the nondimensional time,  $t = t^*U_\infty/c$ , of the lift coefficients,  $C_L$  and  $C_D$ , for two symmetric airfoils, NACA 0002 and NACA 0008 for Reynolds number,  $Re = 1000$ , and the distance to the ground  $H = 0.5$ , for various angles of attack,  $\alpha$  ..... 126

Figure 4.26 Influence of the distance to the ground,  $H$ , for a cambered airfoil: The variations with the nondimensional time,  $t = t^*U_\infty/c$ , of the lift coefficient,  $C_L$ , of the NACA 2404 airfoil for several nondimensional distances to the ground,  $H = 0.3, 0.5, 1.0$  and  $12$  (no ground effect), for Reynolds number,  $Re = 1000$ , and at various angles of attack,  $\alpha$  ..... 127

Figure 4.27 Influence of the distance to the ground,  $H$ , for a cambered airfoil: The variations with the nondimensional time,  $t = t^*U_\infty/c$ , of the drag coefficient,  $C_D$ , of the NACA 2404 airfoil for several nondimensional distances to the ground,  $H = 0.3, 0.5, 1.0$  and  $12$  (no ground effect), for Reynolds number,  $Re = 1000$ , and at various angles of attack,  $\alpha$  ..... 128

Figure 4.28 Illustration of the flow separations for NACA 2404 airfoil at various moments in time using the streamlines and the color shades indicating the nondimensional velocity field for  $H = 0.5$  and  $H = 12$ , for  $Re = 1000$  and at  $\alpha = 10^\circ$  ..... 129

Figure 4.29 Illustration of the flow separations for NACA 2404 airfoil at various moments in time using the streamlines and the color shades indicating the nondimensional velocity field for  $H = 0.3$  and  $H = 1$ , for  $Re = 1000$  and at  $\alpha = 10^\circ$  ..... 130

Figure 4.30 Illustration of the flow separations for NACA 4404 airfoil at various moments in time using the streamlines and the color shades indicating the nondimensional velocity field for  $H = 0.3$  and  $H = 0.5$ , for  $Re = 1000$  and at  $\alpha = 10^\circ$  ..... 131

Figure 4.31 Influence of the relative camber for two cambered airfoil NACA 4404 and NACA 2404: The variations with the nondimensional time,  $t = t^*U_\infty/c$ , of the lift and drag coefficients,  $C_L$  and  $C_D$ , for Reynolds number,  $Re = 1000$ , and distance to the ground,  $H = 0.5$  at various angles of attack,  $\alpha$  ..... 132

Figure 4.32 Influence of the airfoil thickness of cambered airfoils. Comparison of the variations with the nondimensional time,  $t = t^*U_\infty/c$ , of the lift and drag coefficients,  $C_L$  and  $C_D$ , for

two cambered airfoils, NACA 2402 and 2404 for Reynolds number, $Re = 1000$ , and distance to the ground $H = 0.5$ at various angles of attack, $\alpha$ .....	133
Figure 4.33 Influence of the maximum camber position. Comparison of the variations with the nondimensional time, $t = t^*U_\infty/c$ , of the lift and drag coefficients, $C_L$ and $C_D$ , for two cambered airfoils, NACA 4404 and 4304 for Reynolds number, $Re = 1000$ , and distance to the ground $H = 0.5$ at various angles of attack, $\alpha$ .....	134
Figure 5.1. Geometry of a half rectangular wing placed in a uniform flow at the angle of attack $\alpha$ .....	138
Figure 5.2. Geometry of the half wing in the physical domain $(\xi, \eta, \zeta)$ and of the flat plate in the computational domain $(X, Y, Z)$ obtained by the coordinate transformations (5.7) to (5.8). ....	140
Figure 5.3. Geometry of the staggered grid. ....	144
Figure 5.4. The variation with the angle of attack, $\alpha$ , for the lift and drag coefficients, $C_L$ and $C_D$ , of the rectangular wing with NACA0006 airfoil and aspect ratio 7.25 at Reynolds number $Re = 4000$ . ....	147
Figure 5.5. Influence of the Reynolds number on the aerodynamic coefficients: Comparison of the lift and drag coefficients, $C_L$ and $C_D$ , for a rectangular wing with NACA0002 airfoil section of aspect ratio 8 for two Reynolds numbers, $Re = 600$ and $1000$ , at several angles of attack, $\alpha$ .....	149
Figure 5.6. Influence of the Reynolds number on the aerodynamic coefficients: Comparison of the lift and drag coefficients, $C_L$ and $C_D$ , for a rectangular wing with NACA 0004 airfoil section and aspect ratio 8 for two Reynolds numbers, $Re = 600$ and $1500$ , at several angles of attack, $\alpha$ .....	150
Figure 5.7. Influence of the wing thickness on the aerodynamic coefficients: Comparison of the lift and drag coefficients, $C_L$ and $C_D$ , for a rectangular wing with NACA0002 and NACA0008 airfoil sections and aspect ratio 8 for Reynolds number $Re = 600$ at several angles of attack, $\alpha$ . .....	150
Figure 5.8. Influence of the wing thickness on the aerodynamic coefficients: Comparison of the lift and drag coefficients, $C_L$ and $C_D$ , for a rectangular wing with NACA0002 and NACA0008 airfoil sections and aspect ratio 8 for Reynolds number $Re = 1000$ at several angles of attack, $\alpha$ . .....	151

Figure 5.9. Influence of the Reynolds number on the variation of the local aerodynamic coefficients along the wing semi-span: Comparison of  $C_l$  and  $C_d$  for a rectangular wing with NACA 0004 airfoil section of aspect ratio 8 for two Reynolds numbers,  $Re = 600$  and  $1500$ , at angles of attack  $\alpha = 6^\circ$  and  $8^\circ$  ..... 152

Figure 5.10. Influence of the wing thickness on the variation of the aerodynamic coefficients along the semi-span of the wing: Comparison of  $C_l$  and  $C_d$ , for two rectangular wings with NACA 0002 and NACA 0008 airfoil sections, aspect ratio 8 for  $Re = 600$  at the angles of attack  $\alpha = 2^\circ$  and  $4^\circ$  ..... 153

Figure 5.11. Influence of the wing camber on the aerodynamic coefficients: Comparison of the wing lift and drag coefficients,  $C_L$  and  $C_D$ , for two rectangular wings with NACA 2404 and NACA 4404 airfoil section, aspect ratio 8 for  $Re = 1000$  at several incidences. .... 154

Figure 5.12. Illustration of the velocity contours and streamlines indicating the nondimensional velocity for the wing with NACA 0008 airfoil section for  $Re = 1000$  and angle of attack  $\alpha = 8^\circ$  at various spanwise locations  $y = 0$ ,  $y = 0.25(b/2)$ ,  $y = 0.5(b/2)$ , and  $y = 0.75(b/2)$ ..... 155

Figure 5.13. Isometric view of the velocity contours in a flow past a half-wing with NACA 0008 airfoil section for  $Re = 1000$  at angle of attack  $\alpha = 8^\circ$  illustrated in the physical domain  $(\xi, \eta, \zeta)$ . .... 156

Figure 5.14. Velocity contours and streamlines in the  $(\eta, \zeta)$  plane (side view) of a flow past a wing with NACA 0008 airfoil section for  $Re = 1000$  at angle of attack  $\alpha = 8^\circ$  ..... 156

## LIST OF TABLES

Table 2.1 Analysis of downstream length ( $L_l$ ) for $Re = 600$ : comparison of separation length on the lower wall ( $L_l$ ) and flow separation and reattachment locations on the upper wall ( $x_s$ and $x_r$ ), for $L_0 = 25$ .....	31
Table 2.2 Analysis of upstream length ( $L_0$ ) for $Re = 600$ : comparison of separation length on the lower wall ( $L_l$ ) and flow separation and reattachment locations on the upper wall ( $x_s$ and $x_r$ ), for $L_l = 75$ .....	31
Table 2.3 Grid sensitivity of the numerical solution for $h = 0.5$ , $Re = 600$ , $2b = 26.6$ , $L_0 = 25$ , and $L_l = 75$ based on the computed non-dimensional lengths of separation and reattachment. ....	32
Table 2.4 Sensitivity of the time steps per oscillation cycle of the numerical solution for $N=40$ , 60, 80 and 100 with $Re = 400$ at $t/T=3.95$ based on the computed nondimensional lengths of separation and reattachment.....	34
Table 3.1 Grid sensitivity of the numerical solution for NACA 0002 airfoil in steady flow for Reynolds number $Re = 1000$ and incidence $\alpha_0 = 4^\circ$ .....	66
Table 3.2 Sensitivity of the time steps per oscillation cycle of the numerical solution for $N=40$ , 60, 80 and 100 of the unsteady flow past NACA 0004 airfoil for $Re = 1000$ , at angle of attack, $\alpha = 14^\circ$ .and frequency $\omega=0.05$ at $t/T=5.34$ based on the computed lift and drag coefficients. The grid size used is 310 x 131 grid points for each variable.....	67
Table 5.1 Grid sensitivity of the numerical solution for steady flow past rectangular wing with NACA 0004 airfoil section for $Re = 1500$ at angle of attack, $\alpha = 4^\circ$ based on the computed aerodynamic coefficients, $C_L$ and $C_D$ .....	148

# Chapter 1

## Introduction

The unsteady flow problems are present in numerous engineering fields such as in thermo-fluid systems, pumps, nuclear reactors, gas and hydraulic turbines, aeronautics, and Micro-Electro-Mechanical Systems (MEMS). These unsteady flow problems can be studied experimentally or computationally. However, experimental studies are sometimes difficult and challenging to be handled. The analysis of the unsteady flows using numerical methods requires excellent computational efficiency and accuracy. These requirements are made even more difficult by the complexity of the fluid flow problems, involving usually flow separation regions and oscillating boundaries, especially at very low Reynolds numbers. In this case, the solutions of the Navier-Stokes equations are required to compute these flow separation regions accurately. In this thesis, a new numerical method has been developed and applied in order to study the steady and unsteady two-dimensional and three-dimensional flow problems at very low Reynolds numbers. This method has been applied to two different study cases, internal flows such as the confined flows in a backward-facing step channel, and external flows such as the unsteady flows over two-dimensional airfoils and three-dimensional aircraft wings. Each case study will be analyzed and discussed separately in several chapters throughout of this thesis.

### 1.1 Background and motivations of the study

A particular interest has recently been devoted to the analysis of steady and unsteady flows at low Reynolds numbers ( $Re < 6000$ ) [10, 11] where the viscous effect is very considerable throughout the flows. These fluid flows are usually present in confined flows, such as fluid-structure interaction problems, and in external flow problems, such as the steady and unsteady aerodynamics of airfoils and wings. This study is becoming increasingly important from both fundamental and engineering applications points of view, due to recent advances in small Unmanned-Aerial Vehicles (UAVs) [17], Micro-Air Vehicles (MAVs) [18], special military aircraft, as well as researches on bird/insect flying aerodynamics [19]. More recently, research interest has been increased for steady and unsteady confined fluid flows at very low Reynolds numbers for various engineering applications related to the cooling flows in miniature electronic devices [20] or to the aluminum continuous casting operation to a near-net shape [21]. These

engineering applications demonstrate why the analysis of the steady and unsteady laminar flows received a topical interest worldwide [1-16, 22, 23, 24, 25].

The fluid flows are dominated by viscosity at low Reynolds numbers, between 400 and 6000. As a result, the analysis of these flows is very challenging and different from those of higher Reynolds number flows. One important physical phenomenon that occurs in this case is the flow separation which is more significant at very low Reynolds numbers. The separation of the flow and its subsequent reattachment to a solid surface exists in many industrial and aeronautical systems. In external flows, the flow separations increases the drag and decreases the lift force, and for internal flows, it reduces efficiency. The importance and complexity of such flows to engineering equipment have been stressed in many publications (e.g., see Abbott and Kline [26] and Eaton and Johnston [27]).

Aerodynamics of airfoils and wings at very low Reynolds numbers are extensively studied in the past years. As an example, micro-aerial vehicles fly at Reynolds numbers of 1000 or even lower. These small aircrafts can operate in various indoor or outdoor environments including tunnels, desert, and jungles [18, 19]. Several authors (such as Kunz and Kroo [28]) found that many successful aerodynamic codes developed for the normal range of Reynolds numbers are not well suited for very low Reynolds number flow. The aerodynamics of airfoils at low Reynolds numbers have also been studied by Mateescu *et al.* [1-16] with a numerical method based on a finite-difference formulation with artificial compressibility introduced by Chorin [30], using domain decomposition.

The literature review shows the majority of the studies have been carried out in the range of  $Re > 10^5$ , and there are few publications for the study of laminar flows either experimentally or computationally at very low Reynolds numbers. For this reason, the present research has focused on the study of laminar viscous flows at very low Reynolds numbers in several case studies.

## **1.2 Three-dimensional confined viscous flows at low Reynolds numbers**

Flow separations and reattachments as one of the important fundamental subjects in fluid mechanics, have been the focus of intensive studies for many decades. To understand this phenomenon better, the flow in a channel with a sudden expansion, such as backward-facing step has been studied experimentally and computationally. The backward-facing step flow became a very popular benchmark problem for validating different Computational Fluid Dynamics (CFD)

methods in comparison with the available experimental data (e.g. Armaly *et al.* [31], Goldstein *et al.* [32], Eaton *et al.* [33], Kim and Moin [34], Grant *et al.* [35], and Lee and Mateescu [13]) and/or numerical fluid dynamics simulation codes (e.g. Gartling [36] and Mateescu and Venditti [12]).

For instance, Gartling [36] found an accurate solution of the incompressible viscous steady flow past a two-dimensional downstream-facing step channel, applying the Galerkin-based finite method. This solution shows a strong separation on the lower wall channel and a weaker one on the upper wall channel. Mateescu and Venditti [12] made further research on the steady flows in a similar geometry to obtain more precise and efficient numerical results for steady confined flows using a method based on a finite-difference formulation and the artificial compressibility concept. This numerical method is capable of predicting and analyzing the steady and unsteady laminar viscous flows past the two-dimensional backward-facing step channel. It is characterized by excellent accuracy and computational efficiency. For example, the finally converged solution for two-dimensional flow over a backward-facing step has been obtained for 500 x 50 grid points in one hour of computing time on a PC (Intel dual-core i7 CPU) using FORTRAN 90. However, using a finite element method required a longer computing time: 0.2 hours per iteration (including matrix assembly, triangularization, and back-substitution) on a CRAY XMP/416 using FORTRAN 77 for 400 x 20 elements with nine nodes [36].

Lee and Mateescu [13] performed experimental investigations of flows in a two-dimensional downstream-facing step channel. The obtained experimental data showed good agreement with the previous numerical and experimental results. The separation and reattachment lengths of the upper and lower walls and the streamwise velocity were measured non-intrusively using multi-element hot-film sensor arrays and a bank of constant temperature anemometers. The reattachment and separation location points produced by the fully developed laminar and transitional flows were analyzed.

Mateescu *et al.* [16] presented a thorough analysis of the unsteady confined viscous flows generated by the variations in time of the inflow velocities and by oscillating walls (which can occur in the practical industrial applications). The time-accurate solutions of the Navier–Stokes equations for these unsteady flows were obtained with a finite-difference method using artificial compressibility on a stretched staggered grid. This method was then applied to obtain solutions

for the benchmark unsteady confined flows past a two-dimensional downstream-facing step with oscillating walls, which displays multiple flow separation regions on the upper and lower walls.

In the last three decades, there have been many studies on two-dimensional flows past backward-facing step channel. In the recent years, there has been significant progress in these analyses based on different CFD techniques in which three-dimensional calculations have become affordable for many research centers.

Williams and Baker [37] analyzed laminar flow in a three-dimensional backward-facing step geometry. The solution correctly predicts the reattachment lengths for  $100 < Re < 800$  and confirms the effect of three-dimensionality. They also found that the sidewalls result in the creation of a wall jet, located at the lower channel wall and pointing from the side wall towards the channel mid-plane.

Chiang and Sheu [38] carried out three-dimensional simulations of laminar flow in a step geometry with a similar expansion ratio to the Armaly *et al.* study case [31] for various Reynolds numbers and aspect ratios. They observed that the flow develops into a two-dimensional profile at the plane of symmetry when the aspect ratios are increased up to 50 and higher.

Nie and Armaly [39] obtained the results of laminar forced convection flow in a backward-facing step geometry. They presented that the size of the primary recirculation gets larger with increasing the step height. They also have shown that the jet-like flow near the side wall lies on the stepped wall which causes a shorter reattachment length near the side wall.

In addition to the obvious engineering interests, this study is also motivated by an academic interest related to the steady laminar flows past downstream-facing step channel. The two-dimensional numerical solutions for the flow separation and reattachment locations in this confined flow problem, such as those obtained by Gartling [36] and by Mateescu and Venditti [12], were found to be not in good agreement with the experimental results obtained by Armaly *et al.* [31] and by Lee and Mateescu [13], especially for larger Reynolds numbers (between 700 and 1200). In the studies performed by Mateescu and Panahi [4, 5, 7, 8] it was shown that this disagreement between the two-dimensional numerical solutions and experimental results is due to the three-dimensional effect of the lateral walls in the experimental configuration, as opposed to the rigorous two-dimensional numerical solution. However, up to now, this explanation has not been scientifically confirmed by theoretical or numerical three-dimensional solutions for this

problem. Therefore, this study represents a novel contribution, which has not been previously reported.

The primary objectives of this section when considering the unsteady internal laminar flows is to obtain time-accurate solutions of the Navier-Stokes equations for three-dimensional unsteady confined flows with harmonic variations in time of the inflow velocities coupled with the oscillations of the channel walls. This study is carried out with an efficient time-accurate method, which is capable of solving the multiple flow separation regions developed on the lower and upper walls of the channel. It is also interesting to estimate the effect of the amplitudes and the frequencies of the inflow velocity and of the oscillating walls to obtain solutions for the three-dimensional flows with multiple separation regions in a channel with a downstream-facing step.

### **1.3 Study of unsteady flow separations on stationary airfoils at low Reynolds numbers**

The dream to design an aircraft that can fly at low Reynolds numbers is not new. There are many publications related to the design of low-speed airfoils that are still relevant today [40-45]. At the time these studies were first published, low Reynolds number flows were considered in the order of fifty to hundred thousand. However, for the micro-aerial vehicles the Reynolds number varies from several hundreds to several thousands. Recently, a new experimental facility has been built with the specific goal of studying the flows in this range of Reynolds numbers [46]. The goal of these experimental works and the corresponding numerical studies is the analysis of micro-aerial vehicles.

The airfoil aerodynamics at these low Reynolds number flows is dominated by viscous effects and flow separation phenomena is very different from those of conventional aircraft. Several studies have been published on the airfoil analysis in steady flow at very low Reynolds numbers. Kunz and Kroo [28] used in their computational study of low Reynolds number flows the INS2D code developed at NASA Ames based on an upwind finite differencing scheme developed by Rogers and Kwak [29]. Mateescu and Abdo [10] also studied the steady flows past airfoils at low Reynolds numbers with a method using artificial compressibility and a central finite-difference formulation on stretched staggered grids. A previous study analyzing the unsteady flows past oscillating airfoils at low Reynolds numbers has been published by Mateescu *et al.* [14].

The focus of the present study is to analyze the unsteady flows past stationary airfoils at low Reynolds numbers. This work is performed by an efficient time-accurate numerical method developed for the solution of the unsteady Navier-Stokes equations, which is second-order-accurate in time and space. A second-order three point-backward implicit scheme is used first for the real-time discretization, followed by a pseudo-time relaxation procedure using artificial compressibility and a factored alternate-direction implicit scheme for the pseudo-time integration. A second-order central finite-difference formulation is used on a stretched staggered grid, which avoids the odd-and-even points decoupling. A special decoupling procedure using the continuity equation reduces the problem to the solution of scalar-tridiagonal systems of equations, which enhances substantially the computational efficiency of the method.

The numerical method is first validated by comparison with the experimental results obtained by Suwa *et al.* [47, 48] for a flat plate and a triangular airfoil in the various angles of attack at Reynolds number of 3000. These experimental results are presented in the form of lift and drag coefficients for several angles of attack.

This work aims to analyze the unsteady effects in the flows past stationary airfoils generated by the unsteady flow separations developed on the airfoil upper surface at low Reynolds numbers. This leads to the study of the unsteady effects on the aerodynamic coefficients generated by the unsteadiness of the flow separations, occurring at relatively small angles of attack. It is also important to obtain the numerical results for the lift and drag coefficients and the lift-to-drag ratio for several symmetric and cambered NACA airfoils at different Reynolds numbers.

## **1.4 Steady and unsteady viscous flows over airfoils in the proximity of the ground**

Ground effect is one of the aerodynamic phenomena that can be seen on an aircraft during take-off and landing when the wings are in the proximity of the ground. This close vicinity of the ground changes the flow of air around the wing leading to an increase in the lift and a reduction in the induced drag of the wing [49].

Various flight evolutions of the micro-aerial vehicles take place in the proximity of the ground, a ceiling or a wall, which require the aerodynamic solutions in these conditions at low

Reynolds numbers. To date, there are no published studies for steady or unsteady flows past airfoils in the proximity of the ground at low Reynolds numbers.

This unsteady flow problem is solved in a rectangular computational domain, obtained from the physical domain by time-dependent coordinate transformations for various sub-domains, in which the boundary conditions are efficiently and rigorously implemented. Solutions for the airfoils in the proximity of the ground at low Reynolds number flows are obtained with an efficient numerical method developed by the author for the time-accurate solution of the Navier-Stokes equations, which is second-order accurate in both time and space.

This study devoted to the analysis of the steady and unsteady flows past fixed and oscillating airfoils at low Reynolds numbers (from 400 to 6000) in the proximity of the ground. This work presents a detailed study of the influence of various parameters, such as Reynolds number, angle of attack, airfoil relative thickness, and amplitude and frequency of oscillations on the flow separations occurring on the airfoil and aerodynamic coefficients (lift, drag and lift-to-drag ratio) in the proximity of the ground.

The unsteady flows past the stationary airfoils in the proximity of the ground at low Reynolds numbers are also studied in this research. The goal is to analyze the effect of the ground proximity on the stationary airfoils considering these unsteady effects generated by the unsteady flows separations, which are shown to appear at even lower angles of attack near the ground. This study presents solutions for the oscillations in time of the lift and drag coefficients of several symmetric and cambered stationary airfoils in the proximity of the ground, which are generated by the unsteady flow separations developed on the airfoil upper surface at low Reynolds numbers. The influence of various geometric and flow parameters, such as the distance to the ground, the angle of attack, relative thickness and camber, and Reynolds number on the unsteady aerodynamic coefficients and on the unsteady flow separations is also studied in this research.

## **1.5 Steady viscous flows over wings at low Reynolds numbers**

The steady flows around wing sections and airfoils have been significantly studied during the past decades for their aeronautical and engineering applications. At the early studies, the method of conformal transformations has been applied to obtain inviscid steady flow solutions for various airfoil shapes including Joukowski, Karman-Trefftz, and Carafoli airfoils [50-54].

Glauert and Birnbaum [55] developed classical thin airfoil theory and established the foundation of the aerodynamics of thin airfoils of arbitrary shapes in incompressible flows, by using a modified Fourier series for the distributed vortex intensity on the chord.

More recently, computational solutions have been obtained using various numerical methods for solving the Euler or Navier–Stokes equations, such as those based on finite-difference or finite-volume formulations (for examples see Anderson [50, 56], Drela and Giles [57, 58], Jameson *et al.* [59], Elrefaie *et al.* [60], Nelson *et al.* [61] and Mateescu and Stanescu [62]). Several authors solved the viscous flows past airfoils and wings numerically by combining inviscid Euler solvers, or panel methods, with the analysis of the boundary layer, developed along the airfoil contour (see Cebeci [63] and Drela and Giles [57, 58]).

The literature review shows that the external flows past airfoils have been substantially studied both experimentally and numerically at higher Reynolds number regimes. For example, Peterson [64] published experimental results of pressure distribution, induced forces and boundary layer measurements for NACA 64A010 airfoil at Reynolds number of  $Re = 4.1 \times 10^6$  with different angles of attack. Similarly, Derkesen *et al.* [65] published several experimental results for NACA 0012 airfoil in steady flows at different Reynolds numbers ranging from 5,000 to 60,000, with angles of attack varying from 8 to 12 degrees. They have noticed the fluctuation in the velocity and vorticity due to the increase of Reynolds number and angle of attack.

However, there is a lack of experimental and numerical studies for steady and unsteady flows past airfoils and wings at very low Reynolds numbers ( $Re < 6000$ ). As it is discussed earlier, the study of laminar flows at this range of Reynolds numbers is somewhat challenging and difficult to perform due to viscous effects. Commercial and open source CFD software also show limitations for studies at very low Reynolds numbers. Maughmer and Coder [66] conducted a benchmark investigation of commercial and open source software like PROFIL 07, XFOIL 6.94, and ANSYS FLUENT 12.1.2. They published a comparison between experimental results and the theoretical methods computations used to predict the aerodynamics characteristics of static airfoils concluding that for most of the programs when the Reynolds number decreases below 70,000 the predictions of the aerodynamic characteristics deteriorate.

As a result, there is a need to analyze the steady and unsteady flows past airfoils and wings at low Reynolds numbers. The viscous effect and flow separation phenomenon in this type of flows are dominant and very challenging and different from those aircraft flying at Reynolds numbers

between  $Re = 10 \times 10^6$  and  $100 \times 10^6$  in the compressible flow regime. At these low Reynolds numbers, the fluid flow past the airfoil is incompressible, and many authors use the concept of artificial compressibility introduced by Chorin [30, 67, 68]. In incompressible flows at low Reynolds numbers, the occurring separation phenomena create difficulties for the numerical methods related to their convergence, stability, and accuracy.

Mateescu and Abdo [10] presented a numerical method for the flows past airfoils at very low Reynolds numbers based on a pseudo-time integration method using artificial compressibility for solving the Navier–Stokes equations accurately. The method was first successfully validated for the flows with multiple separation regions past a downstream-facing step by comparison with previous experimental and computational results at very low Reynolds numbers between 400 and 1200 [13]. The airfoil solutions were validated by comparison with the results obtained by Kunz and Kroo [28] for Reynolds numbers between 1000 and 6000, and excellent agreement was found between the two sets of results.

Broering and Lian [69] reported a numerical study of tandem flapping wing aerodynamics in both two- and three-dimensions. The simulations were based on the incompressible Navier-Stokes equations, discretized on overlapping grids. They found that vortex interactions highly depend on the phase lag angle and spacing between the forewing and hindwing, and three-dimensional cases exhibited a spanwise variation in the Leading Edge-Vortex (LEV) structure and a weaker LEV formation at mid-span compared to the two-dimensional cases with the same kinematics.

Recently, Mateescu and Munoz [14] developed a numerical method to solve steady and unsteady flows past airfoils at very low Reynolds numbers. The solutions are obtained with an efficient numerical method and presented for the unsteady aerodynamic coefficients (unsteady lift and drag coefficients, and lift-to-drag ratio) of the airfoils executing pitching oscillations at low Reynolds numbers.

In this thesis, a new efficient numerical method is used to solve the steady Navier-Stokes equations for three-dimensional viscous flows in the incompressible regime at very low Reynolds numbers, between 600 and 6000. There are few experimental data by several authors. Sunada *et al.* [70] investigated the aerodynamic characteristics of various rectangular wings at Reynolds number 4000. Their study presented the experimental aerodynamic lift and drag coefficients obtained for these wings. The influence of camber ratio, thickness ratio, and

streamline shape has also been presented in their research. The results were shown in the form of a comparison of the lift and drag coefficients, which is used to validate this new numerical method.

This analysis is performed with an efficient numerical method to solve the Navier-Stokes equations in a fixed computational domain, obtained from the physical domain by a geometrical coordinate transformation. This novel approach has the advantage of solving the problem in a fixed rectangular computational domain in which the boundary conditions are implemented efficiently and rigorously. The numerical method is second-order accurate in space, and a pseudo-time relaxation procedure is used with artificial compressibility. A factored Alternate-Direction Implicit (ADI) scheme is used for the pseudo-time integration. It is important to mention here that while the ADI scheme reduces the problem to the solution of block tri-diagonal systems of equations, the special decoupling procedure mentioned earlier reduces further the problem to the solution of several sets of scalar-tridiagonal systems of equations, which are much more efficient to solve computationally.

The main objective of this research is to analyze and obtain accurate and efficient steady solutions for three-dimensional flows past wings. Furthermore, various aerodynamic coefficients such as lift and drag coefficients along the chord and span of the wing are calculated for various low Reynolds numbers between 400 and 4000.

## **1.6 Thesis organization**

After the introduction, in Chapter 2, the analysis of the steady and unsteady three-dimensional internal flows with oscillating walls and variable inflow velocity is presented. The geometry and the boundary conditions of the problem are formulated, and the Navier-Stokes equations for incompressible flows are introduced in non-dimensional form, for computational convenience. The method of solution is then discussed through the presentation of a synthesis of its various features, such as the time-dependent transformation, the real-time discretization approach, the pseudo-time iterative technique, the ADI scheme and the special decoupling procedure leading to the reduction of the problem to the solution of a set of scalar-tridiagonal systems of equations.

Chapter 3 is devoted to studying of unsteady effects on stationary airfoils generated by the unsteady flow separations at low Reynolds numbers. This study presents solutions for the oscillations in time of the lift and drag coefficients of several symmetric and cambered airfoils.

The influence of various geometric and flow parameters, such as the angle of attack, relative thickness and camber, and Reynolds number on the unsteady aerodynamic coefficients and the flow separation is also studied.

Chapter 4 presents the analysis of the steady and unsteady viscous flows over airfoils in the proximity of ground. After the problem formulation, the novel time-dependent coordinate transformation defining the fixed computational domain with six sub-domains is presented. The time-accurate numerical method to solve the modified Navier-Stokes equations in the fixed computational domain is also presented. Unsteady effects on the stationary airfoils in the vicinity of the ground, which are due to the unsteady flow separations, are also studied thoroughly in this chapter.

Chapter 5 is focused on the presentation and discussion of the solutions obtained for steady viscous flows over rectangular wings with NACA airfoil sections at low Reynolds numbers. After introducing the problem formulation, a novel geometrical coordinate transformation defining the fixed computational domain with six sub-domains is presented. The numerical method is used to solve the modified Navier-Stokes equations in the fixed computational domain.

Chapter 6 is devoted to the conclusions of the present study and suggestions for future works. The main contributions of this thesis are summarized after the Acknowledgment.

## Chapter 2

### Steady and Unsteady Solutions for Three-Dimensional Confined Flows with Oscillating Walls and Variable Inflow Velocity

This Chapter is devoted to the analysis of the steady and unsteady confined viscous flows that are present in many engineering systems. A three-dimensional backward-facing step channel has been chosen as a benchmark problem for this study. Unsteady flows are usually generated by an oscillating wall and by the variations in time of the inflow velocities. These flows have to be taken into account in the study of flow-induced vibration and instability of these systems.

In this chapter, a numerical method is presented for three-dimensional laminar steady and unsteady confined flows which can be used to obtain accurate and efficient solutions for the flows with multiple separation regions. Time-accurate solutions of the Navier-Stokes equations for steady and unsteady flows are obtained with a numerical method developed by the author. The method is second-order accurate in space and time, and is based on a finite difference formulation on a stretched staggered grid which uses artificial compressibility. A factored Alternate-Direction Implicit (ADI) scheme and a special decoupling procedure, based on the utilization of the continuity equation, are used to substantially enhance the computational efficiency of the method by reducing the problem to the solution of scalar-tridiagonal systems of equations.

This method was successfully validated by comparison with the theoretical results obtained by White [71] for a fully developed velocity profile in the uniform rectangular channels at several axial locations. The current three-dimensional results are also compared with experimental results conducted by Lee and Mateescu [13], Armaly *et al.* [31] and with the two-dimensional solution obtained by Mateescu *et al.* [16] for confined flows past backward-facing step channel.

The formation of the flow separation regions is thoroughly analyzed in this chapter. A special interest is to study the effect of the inflow velocity variations, Reynolds numbers, reduced frequency of oscillations, and amplitude of oscillating wall on the flow separations appearing in confined viscous flows. The author found no previous solutions for three-dimensional unsteady confined flows generated by time variable inflow velocities and by oscillating walls.

## 2.1 Problem formulation and governing equations

As an example of steady and unsteady confined laminar flows, consider a flow in a rectangular channel of downstream height  $H$  and downstream width  $2bH$ . The upstream portion of the channel of length  $Hl_0$  has the same width,  $2bH$ , and an upstream height  $hH$  which is suddenly enlarged to the downstream height through a downstream-facing step of height  $(1-h)H$ , as shown in Figure 2.1. The downstream length of the channel is denoted by  $Hl_1$ . The numerical solutions presented further were obtained for  $h = 0.5$ .

This flow is referred to the Cartesian coordinates  $Hx$ ,  $Hy$  and  $Hx$  centered at the step corner in the plane of symmetry of the channel, where  $x$ ,  $y$  and  $z$  are nondimensional coordinates (with respect to  $H$ ).

At the channel inlet ( $Hx = -Hl_0$ ) there is a fully developed laminar unsteady flow defined by the axial fluid velocity  $u(y, z)$  expressed in White [71]

$$u(l_0, y, z) = \frac{16h^2}{\pi^3} C \sum_{k=0}^{\infty} \frac{(-1)^k}{(2k+1)} \left[ 1 - \frac{\cosh(2k+1) \frac{\pi y}{h}}{\cosh(2k+1) \frac{\pi b}{h}} \right] \cos \left[ (2k+1) \frac{\pi}{2} \frac{2z-h}{h} \right], \quad (2.1)$$

where  $C$  is related to the time-variable mean flow velocity in the form

$$C = U(t) \left( 3/h^2 \right) \left[ 1 - \frac{192}{\pi^5} \frac{h}{b} \sum_{k=0}^{\infty} \frac{1}{(2k+1)^5} \tanh(2k+1) \frac{\pi b}{h} \right]^{-1}, \quad (2.2)$$

and  $U(t)$  is the mean inflow velocity at time  $t$  in the form of

$$U(t) = U_0 (1 - a \sin(\omega t)), \quad (2.3a)$$

and in the steady case where ( $t = 0$ ) the mean inflow velocity becomes

$$U(t) = U_0, \quad (2.3b)$$

where  $U_0$  is the time-average mean velocity,  $t = U_0 t^* / H$  and  $\omega = \omega^* H / U_0$  are the nondimensional time and the reduced frequency of oscillation ( $\omega^* = 2\pi f$  is the radian frequency of the oscillation), and  $a$  is the nondimensional amplitude of the inflow velocity oscillation.



hyperbolic cosine becomes very close to unity and the numerical evaluations with a finite number of digits is affected by large truncation errors. In this case, this ratio can be successively expressed as

$$\frac{\cosh(Ky)}{\cosh(Kb)} = \frac{\exp(Ky) - \exp(-Ky)}{\exp(Kb) - \exp(-Kb)} \approx e^{K(y-b)}, \quad (2.7)$$

and the general series term for large values of  $K$  becomes

$$T_k = \frac{(-1)^k}{(2k+1)} \left[ 1 - e^{K(y-b)} \right] \cos \left( K \left( z - \frac{h}{2} \right) \right) \quad \text{for } K \gg 1 \text{ and } b/h \gg 1, \quad (2.8)$$

where the exponential can be expanded in Taylor series as

$$1 - e^{K(y-b)} = - \sum_{n=1}^m \frac{1}{(2n)!} K^{2n} (y-b)^{2n} \quad (2.9)$$

Thus, the velocity profile of the fully-developed laminar flow can be numerically calculated in the form

$$u(-l_0, y, z) = \frac{16h^2}{\pi^3} C \sum_{k=0}^{N_1} \frac{(-1)^k}{(2k+1)} \left[ 1 - \frac{\cosh(2k+1) \frac{\pi y}{h}}{\cosh(2k+1) \frac{\pi b}{h}} \right] \cos \left[ (2k+1) \frac{\pi}{2} \frac{2z-h}{h} \right] - \frac{16h^2}{\pi^3} C \sum_{k=N_1}^N \frac{(-1)^k}{(2k+1)} \left\{ \sum_{n=1}^m \frac{1}{(2n)!} \left[ (2k+1) \frac{\pi}{2} (y-b) \right]^{2n} \right\} \cos \left[ (2k+1) \frac{\pi}{2} \frac{2z-h}{h} \right], \quad (2.10)$$

where  $N_1$  has the following indicated values in function of the downstream aspect ratio,  $2b$ , of the channel and for step height  $h = 0.5$ :

$2b$	1	2	4	8	12	16	26.6
$N_1$	112	55	27	13	8	6	3

### 2.1.1 Navier-Stokes equations for unsteady confined viscous flows

Applying the conservation of mass and Newton's second laws to an infinitesimal, fixed control volume yield the continuity and momentum equations as follows:

In vector form

$$\nabla \bullet \mathbf{V}^* = 0, \quad (2.11)$$

$$\frac{\partial \mathbf{V}^*}{\partial t^*} + \nabla \bullet (\mathbf{V}^* \mathbf{V}^*) + \frac{\nabla p^*}{\rho} = \nu \nabla^2 \mathbf{V}^* \quad \text{where } \mathbf{V}^* = \{u^*, v^*, w^*\}^T \quad (2.12)$$

In three-dimensional Cartesian coordinate form:

$$\frac{\partial u^*}{\partial x^*} + \frac{\partial v^*}{\partial y^*} + \frac{\partial w^*}{\partial z^*} = 0, \quad (2.13)$$

$$\frac{\partial u^*}{\partial t^*} + \frac{\partial}{\partial x^*} \left( u^{*2} + \frac{p^*}{\rho} \right) + \frac{\partial}{\partial y^*} (v^* u^*) + \frac{\partial}{\partial z^*} (w^* u^*) = \nu \left( \frac{\partial^2 u^*}{\partial x^{*2}} + \frac{\partial^2 u^*}{\partial y^{*2}} + \frac{\partial^2 u^*}{\partial z^{*2}} \right), \quad (2.14)$$

$$\frac{\partial v^*}{\partial t^*} + \frac{\partial}{\partial x^*} (u^* v^*) + \frac{\partial}{\partial y^*} \left( v^{*2} + \frac{p^*}{\rho} \right) + \frac{\partial}{\partial z^*} (w^* v^*) = \nu \left( \frac{\partial^2 v^*}{\partial x^{*2}} + \frac{\partial^2 v^*}{\partial y^{*2}} + \frac{\partial^2 v^*}{\partial z^{*2}} \right), \quad (2.15)$$

$$\frac{\partial w^*}{\partial t^*} + \frac{\partial}{\partial x^*} (u^* w^*) + \frac{\partial}{\partial y^*} (v^* w^*) + \frac{\partial}{\partial z^*} \left( w^{*2} + \frac{p^*}{\rho} \right) = \nu \left( \frac{\partial^2 w^*}{\partial x^{*2}} + \frac{\partial^2 w^*}{\partial y^{*2}} + \frac{\partial^2 w^*}{\partial z^{*2}} \right), \quad (2.16)$$

where,  $u^*$ ,  $v^*$ ,  $w^*$ , and  $p^*$  are dimensional velocity components and pressure which can be defined as  $u^* = uU_0$ ,  $v^* = vU_0$ ,  $w^* = wU_0$ , and  $p^* = \rho U_0^2 p$ . The dimensional coordinates can be expressed as  $x^* = xH$ ,  $y^* = yH$ , and  $z^* = zH$ , where the dimensional time is  $t^* = tH/U_0$  (where  $\rho$  is the fluid density).

The nondimensionalization is implemented in the incompressible continuity and Navier-Stokes equations in which the fluid velocity vectors are nondimensionalized with respect to  $U_0$ , time-average mean velocity and the Cartesian coordinates  $x$ ,  $y$  and  $z$  are nondimensionalized with respect to  $H$ , downstream channel height. Thus, the nondimensional form of the equations can be written as follows:

$$\frac{\partial u}{\partial x} + \frac{\partial v}{\partial y} + \frac{\partial w}{\partial z} = 0, \quad (2.17)$$

$$\frac{\partial u}{\partial t} + \frac{\partial}{\partial x} (u^2 + p) + \frac{\partial}{\partial y} (vu) + \frac{\partial}{\partial z} (wu) = \frac{1}{\text{Re}} \left( \frac{\partial^2 u}{\partial x^2} + \frac{\partial^2 u}{\partial y^2} + \frac{\partial^2 u}{\partial z^2} \right), \quad (2.18)$$

$$\frac{\partial v}{\partial t} + \frac{\partial}{\partial x} (uv) + \frac{\partial}{\partial y} (v^2 + p) + \frac{\partial}{\partial z} (wv) = \frac{1}{\text{Re}} \left( \frac{\partial^2 v}{\partial x^2} + \frac{\partial^2 v}{\partial y^2} + \frac{\partial^2 v}{\partial z^2} \right), \quad (2.19)$$

$$\frac{\partial w}{\partial t} + \frac{\partial}{\partial x}(uw) + \frac{\partial}{\partial y}(vw) + \frac{\partial}{\partial z}(w^2 + p) = \frac{1}{\text{Re}} \left( \frac{\partial^2 w}{\partial x^2} + \frac{\partial^2 w}{\partial y^2} + \frac{\partial^2 w}{\partial z^2} \right) \quad (2.20)$$

where,  $\text{Re} = U_0 H / \nu$  represents the time-average mean Reynolds number based on the downstream channel height, which is related to the Reynolds number, which is related to the Reynolds number based on the hydraulic diameter as  $\text{Re}_D = \text{Re} 4b / (2b + 1)$  (where  $\nu$  is the kinematic viscosity).

The time-dependent Navier-Stokes equations for the incompressible flow past a backward-facing step channel can be expressed in nondimensional conservation form as

$$\frac{\partial \mathbf{V}}{\partial t} + \mathbf{Q}(\mathbf{V}, p) = 0, \quad \nabla \cdot \mathbf{V} = \frac{\partial u}{\partial x} + \frac{\partial v}{\partial y} + \frac{\partial w}{\partial z} = 0, \quad (2.21)$$

where  $\mathbf{V} = \{u, v, w\}^T$ , which represents the dimensionless fluid velocity vector, and  $\mathbf{Q}(\mathbf{V}, p)$ , which includes the convective derivative, pressure and viscous terms, are expressed in three-dimensional Cartesian coordinates as

$$\mathbf{V} = \{u, v, w\}^T, \quad (2.22)$$

$$\mathbf{Q}(\mathbf{V}, p) = \mathcal{Q} \{ Q_u(u, v, w, p), Q_v(u, v, w, p), Q_w(u, v, w, p) \}^T, \quad (2.23)$$

$$Q_u(u, v, w, p) = \frac{\partial(uu)}{\partial x} + \frac{\partial(vu)}{\partial y} + \frac{\partial(wu)}{\partial z} + \frac{\partial p}{\partial x} - \frac{1}{\text{Re}} \left( \frac{\partial^2 u}{\partial x^2} + \frac{\partial^2 u}{\partial y^2} + \frac{\partial^2 u}{\partial z^2} \right), \quad (2.24)$$

$$Q_v(u, v, w, p) = \frac{\partial(uv)}{\partial x} + \frac{\partial(vv)}{\partial y} + \frac{\partial(wv)}{\partial z} + \frac{\partial p}{\partial y} - \frac{1}{\text{Re}} \left( \frac{\partial^2 v}{\partial x^2} + \frac{\partial^2 v}{\partial y^2} + \frac{\partial^2 v}{\partial z^2} \right), \quad (2.25)$$

$$Q_w(u, v, w, p) = \frac{\partial(uw)}{\partial x} + \frac{\partial(vw)}{\partial y} + \frac{\partial(ww)}{\partial z} + \frac{\partial p}{\partial z} - \frac{1}{\text{Re}} \left( \frac{\partial^2 w}{\partial x^2} + \frac{\partial^2 w}{\partial y^2} + \frac{\partial^2 w}{\partial z^2} \right), \quad (2.26)$$

$$\nabla \cdot \mathbf{V} = \frac{\partial u}{\partial x} + \frac{\partial v}{\partial y} + \frac{\partial w}{\partial z}, \quad (2.27)$$

in which  $u$ ,  $v$ ,  $w$  and  $p$  represent the dimensionless velocity components and pressure, nondimensionalized with respect to  $U_0$  and  $\rho U_0^2$ , respectively.

## 2.1.2 Boundary conditions

No-slip boundary conditions are considered at the solid walls. The inflow and outflow boundaries of the computational domain are situated at a distance  $Hl_0$  and  $Hl_1$  upstream and

downstream from the step, respectively. The inflow boundary condition is defined by equation (2.1), and the outflow boundary conditions for the velocity components are based on an extrapolation to second-order accuracy from inside the computational domain. The outlet pressure is obtained by integrating the momentum equation from the bottom wall (Mateescu and Venditti [12]). The implementation of the boundary conditions is shown in Appendix A.

## 2.2 Method of solution for the unsteady three-dimensional confined viscous flows

The development of a time-accurate method is shown in this section, which starts with the time-dependent transformation from the physical domain to the fixed computational domain, and applied to Navier-Stokes equations. It is followed by the real-time discretization of the Navier-Stokes equations. A detailed description of the pseudo-time relaxation technique applied to Navier-Stokes equations is also shown. The alternate-direction implicit scheme and the implementation of the special decoupling procedure are performed, and finally, the spatial discretization on stretched staggered grids is carried out.

### 2.2.1 Time-dependent coordinate transformation

For a rigorous implementation of the boundary conditions on the oscillating walls, the real fluid flow domain with moving boundaries is transformed into a fixed computational domain by the time-dependent coordinate transformation

$$X = x, \quad Y = y, \quad Z = f(x, z, t), \quad t = t \quad (2.28)$$

where  $f(x, z, t)$  is defined in terms of oscillation mode,  $g(x, t)$  defined by equation (2.5), in the form

$$f(x, z, t) = \begin{cases} z/h & \text{for } x < 0 \\ 1 - \frac{h-z}{1-g(x,t)} & \text{for } 0 < x < l \\ 1-h+z & \text{for } x > l \end{cases} \quad (2.29)$$

Thus in the fixed computational domain  $(X, Y, Z)$ , the lower and upper boundaries of the channel before and after the step are defined by the equations  $Z = 0$  and  $Z = 1$ .

In the fixed computational domain, the Navier-Stokes and the continuity equations can be expressed as:

$$\frac{\partial \mathbf{V}}{\partial t} + \mathbf{G}(\mathbf{V}, p) = 0, \quad \nabla \cdot \mathbf{V} = 0, \quad (2.30)$$

$$\mathbf{V} = \{u, v, w\}^T, \quad \mathbf{G}(\mathbf{V}, p) = \{G_u(u, v, w, p), G_v(u, v, w, p), G_w(u, v, w, p)\}^T, \quad (2.31)$$

$$\begin{aligned} G_u(u, v, w, p) = & \frac{\partial(uu)}{\partial X} + C_1 \frac{\partial^2 u}{\partial X^2} + C_2 \frac{\partial(uu)}{\partial Z} + \frac{\partial(vu)}{\partial Y} + C_3 \frac{\partial(wu)}{\partial Z} + C_4 \frac{\partial u}{\partial Z} + \frac{\partial p}{\partial X} \\ & + C_2 \frac{\partial p}{\partial Z} + C_5 \frac{\partial^2 u}{\partial Z^2} + C_6 \frac{\partial^2 u}{\partial Z \partial X} + C_1 \frac{\partial^2 u}{\partial Y^2}, \end{aligned} \quad (2.32)$$

$$\begin{aligned} G_v(u, v, w, p) = & \frac{\partial(uv)}{\partial X} + C_1 \frac{\partial^2 v}{\partial X^2} + C_2 \frac{\partial(uv)}{\partial Z} + \frac{\partial(vv)}{\partial Y} + C_3 \frac{\partial(wv)}{\partial Z} + C_4 \frac{\partial v}{\partial Z} + \frac{\partial p}{\partial Y} \\ & + C_5 \frac{\partial^2 v}{\partial Z^2} + C_6 \frac{\partial^2 v}{\partial Z \partial X} + C_1 \frac{\partial^2 v}{\partial Y^2}, \end{aligned} \quad (2.33)$$

$$\begin{aligned} G_w(u, v, w, p) = & \frac{\partial(uw)}{\partial X} + C_1 \frac{\partial^2 w}{\partial X^2} + C_2 \frac{\partial(uw)}{\partial Z} + \frac{\partial(vw)}{\partial Y} + C_3 \frac{\partial(ww)}{\partial Z} + C_4 \frac{\partial w}{\partial Z} + C_3 \frac{\partial p}{\partial Z} \\ & + C_5 \frac{\partial^2 w}{\partial Z^2} + C_6 \frac{\partial^2 w}{\partial Z \partial X} + C_1 \frac{\partial^2 w}{\partial Y^2}, \end{aligned} \quad (2.34)$$

$$\nabla \cdot \mathbf{V} = \frac{\partial u}{\partial X} + \frac{\partial v}{\partial Y} + C_2 \frac{\partial u}{\partial Z} + C_3 \frac{\partial w}{\partial Z}, \quad (2.35)$$

in which the coefficients  $C_1, C_2, C_3, \dots, C_6$  are defined as:

$$\begin{aligned} C_1 = -\frac{1}{\text{Re}}, \quad C_2 = -\frac{\partial f}{\partial x}, \quad C_3 = -\frac{\partial f}{\partial z}, \quad C_4 = \frac{\partial f}{\partial t} - \frac{1}{\text{Re}} \left( \frac{\partial^2 f}{\partial x^2} + \frac{\partial^2 f}{\partial z^2} \right) \\ C_5 = -\frac{1}{\text{Re}} \left[ \left( \frac{\partial f}{\partial x} \right)^2 + \left( \frac{\partial f}{\partial z} \right)^2 \right], \quad C_6 = -\frac{2\partial f}{\text{Re} \partial x}, \end{aligned}$$

and in the steady case these coefficients are as following

$$\begin{aligned} C_1 = -\frac{1}{\text{Re}}, \quad C_2 = 0, \quad C_3 = 0, \quad C_4 = 0 \\ C_5 = -\frac{1}{\text{Re}}, \quad C_6 = 0 \end{aligned}$$

The derivation of these coefficients is presented in Appendix A.

## 2.2.2 Real-time discretization

A second-order three-point backward implicit scheme is used to perform the discretization of the momentum equation in real-time:

$$\left(\frac{\partial \mathbf{V}}{\partial t}\right)^{n+1} = \frac{3\mathbf{V}^{n+1} - 4\mathbf{V}^n + \mathbf{V}^{n-1}}{2\Delta t}, \quad (2.36)$$

where the three consecutive time levels and the time step are represented by the superscripts  $n-1$ ,  $n$  and  $n+1$ , and  $\Delta t = t^{n+1} - t^n = t^n - t^{n-1}$  respectively. Hence, equations (2.30) can be expressed at the time level  $t^{n+1}$  in the form

$$\mathbf{V}^{n+1} + \alpha \mathbf{G}^{n+1} = \mathbf{F}^n, \quad \nabla \cdot \mathbf{V}^{n+1} = 0, \quad (2.37)$$

where  $\alpha = \frac{2\Delta t}{3}$ ,  $\mathbf{G}^{n+1} = \mathbf{G}(\mathbf{V}^{n+1}, p^{n+1})$  and  $\mathbf{F}^n = \frac{4\mathbf{V}^n - \mathbf{V}^{n-1}}{3}$ .

The initial conditions are specified for  $\mathbf{V}^1$  and  $p^1$ , throughout the fluid domain for the computational initialization of the previous momentum equation. It means that the solution should be known at previous time level  $t^1$ . A simple implicit Euler scheme is used instead of the second-order three-point-backward implicit scheme to start the advance to the next time level  $t^2$ . Then, only at the first time iteration  $\alpha = \Delta t$  and  $\mathbf{F}^n = \mathbf{V}^n$ . The solution of the flow quantities  $\mathbf{V}^{n+1}$  and  $p^{n+1}$  is done by imposing boundary conditions at the inlet, outlet, and on the moving surfaces of the airfoil, which are analyzed in following sections of this chapter.

## 2.2.3 Pseudo-time iterative relaxation technique

To advance the solution of the semi-discretized equations from real-time level  $t^n$  to  $t^{n+1}$ , an iterative pseudo-time relaxation procedure with artificial compressibility is used in the following form

$$\frac{\partial \tilde{\mathbf{V}}}{\partial \tau} + \tilde{\mathbf{V}} + \alpha \tilde{\mathbf{G}}(\tilde{\mathbf{V}}, p) = \mathbf{F}^n, \quad \delta \left( \frac{\partial \tilde{p}}{\partial \tau} \right) + D\tilde{\mathbf{V}} = 0, \quad (2.38)$$

where  $\tilde{\mathbf{V}}(\tau)$  and  $\tilde{p}(\tau)$  denote the pseudo-functions corresponding to the variable velocity and pressure at pseudo time  $\tau$ , between the real time levels  $t^n$  and  $t^{n+1}$ , and  $\delta$  represents an artificially-added compressibility. Pseudo-continuity and Navier-Stokes equations (2.38) are

solved in pseudo-time. An implicit Euler scheme is used in this respect to discretize these equations between the pseudo-time levels  $\tau^\nu$  and  $\tau^{\nu+1} = \tau^\nu + \Delta\tau$ , and the resulting equations are expressed as

$$\frac{\tilde{\mathbf{V}}^{\nu+1} - \tilde{\mathbf{V}}^\nu}{\Delta\tau} + \tilde{\mathbf{V}}^{\nu+1} + \alpha \tilde{\mathbf{G}}^{\nu+1} = \mathbf{F}^n, \quad \frac{\tilde{p}^{\nu+1} - \tilde{p}^\nu}{\Delta\tau} + \frac{1}{\delta} \nabla \cdot \tilde{\mathbf{V}}^{\nu+1} = 0, \quad (2.39)$$

where  $\Delta\tau$  is the pseudo-time step and the superscript  $\nu$  indicates the solution at pseudo-time level  $\tau^\nu = \nu\Delta\tau$  and  $\tilde{\mathbf{G}}^{\nu+1} = \mathbf{G}(\tilde{\mathbf{V}}^{\nu+1}, \tilde{p}^{\nu+1})$ . To start the pseudo-time integration initial conditions are required, then  $\mathbf{V}^n$  and  $p^n$  take the following values:

$$\tilde{\mathbf{V}}^\nu \Big|_{\nu=1} = \mathbf{V}^n, \quad \tilde{p}^\nu \Big|_{\nu=1} = p^n \quad (2.40)$$

Once the steady state is reached at  $\nu = k$ , the pseudo-time derivatives become zero

$$\tilde{\mathbf{V}}^{k+1} = \tilde{\mathbf{V}}^k, \quad \tilde{p}^{k+1} = \tilde{p}^k \quad (2.41)$$

and then (at that point)

$$\tilde{\mathbf{V}}^{k+1} \equiv \mathbf{V}^{n+1}, \quad \tilde{p}^{k+1} \equiv p^{n+1} \quad (2.42)$$

Introducing the pseudo-time variations,

$$\Delta\tilde{\mathbf{V}}^\nu = \tilde{\mathbf{V}}^{\nu+1} - \tilde{\mathbf{V}}^\nu, \quad \Delta\tilde{p}^\nu = \tilde{p}^{\nu+1} - \tilde{p}^\nu, \quad \Delta\tilde{\mathbf{G}}^\nu = \tilde{\mathbf{G}}^{\nu+1} - \tilde{\mathbf{G}}^\nu \quad (2.43)$$

Then equations (2.38) can be written in delta form as

$$(1 + \Delta\tau)\Delta\tilde{\mathbf{V}}^\nu + \delta\Delta\tilde{\mathbf{G}}^\nu(\tilde{\mathbf{V}}^\nu, \tilde{p}^\nu) = \Delta\tau(\mathbf{F}^n - \tilde{\mathbf{V}}^\nu - \alpha\tilde{\mathbf{G}}^\nu(\tilde{\mathbf{V}}^\nu, \tilde{p}^\nu)), \quad (2.44)$$

$$\Delta\tilde{p}^\nu + \frac{\Delta\tau}{\delta} \nabla \cdot (\Delta\tilde{\mathbf{V}}^\nu) = -\frac{\Delta\tau}{\delta} \nabla \cdot \tilde{\mathbf{V}}^\nu \quad (2.45)$$

The last two equations are iterated in pseudo-time until variations are equal to zero ( $\Delta\tilde{\mathbf{V}}^\nu = 0$  and  $\Delta\tilde{p}^\nu = 0$ ). Although there are many different methods to calculate the value of the artificial relaxation parameter  $\delta$  and  $\Delta\tau$ , (for example, see Soh [72, 73] and Mateescu *et al.* [23, 24]) in this research these values are optimized by numerical experimentation.

## 2.2.4 The linearization and alternating-direction implicit scheme

In previous sections the implementation of a time integration method for the solution of the Navier-Stokes equations was shown. The introduction of spatial differential operators is required to go on further obtaining numerical solution of the system of equations. In addition, to facilitate the pseudo-time iterative process, the implicit nonlinear system of equations (2.44) and (2.45) are linearized.

The linearization of the  $\Delta\check{\mathbf{V}}^\nu$  and  $\Delta\check{\mathbf{G}}^\nu$  terms is done by lagging the velocity components in the pseudo-time variation. This method of linearization is simple, efficient and fits well in this implicit scheme. It is expressed as

$$\Delta\check{\mathbf{V}}^\nu = \begin{bmatrix} \Delta u \\ \Delta v \\ \Delta w \end{bmatrix} = \begin{bmatrix} \check{u}^{\nu+1} - \check{u}^\nu \\ \check{v}^{\nu+1} - \check{v}^\nu \\ \check{w}^{\nu+1} - \check{w}^\nu \end{bmatrix}, \quad (2.46)$$

$$\Delta\check{\mathbf{G}}^\nu = \begin{bmatrix} \Delta G_u \\ \Delta G_v \\ \Delta G_w \end{bmatrix} = \begin{bmatrix} \check{G}_u^{\nu+1} - \check{G}_u^\nu \\ \check{G}_v^{\nu+1} - \check{G}_v^\nu \\ \check{G}_w^{\nu+1} - \check{G}_w^\nu \end{bmatrix}, \quad (2.47)$$

where,

$$\begin{aligned} \Delta G_u(u, v, w, p) = & \frac{\partial(\check{u}^\nu \Delta u)}{\partial X} + C_1 \frac{\partial^2 \Delta u}{\partial X^2} + C_2 \frac{\partial(\check{u}^\nu \Delta u)}{\partial Z} + \frac{\partial(\check{v}^\nu \Delta u)}{\partial Y} + C_3 \frac{\partial(\check{w}^\nu \Delta u)}{\partial Z} \\ & + C_4 \frac{\partial \Delta u}{\partial Z} + \frac{\partial \Delta p}{\partial X} + C_2 \frac{\partial \Delta p}{\partial Z} + C_5 \frac{\partial^2 \Delta u}{\partial Z^2} + C_6 \frac{\partial^2 \Delta u}{\partial Z \partial X} + C_1 \frac{\partial^2 \Delta u}{\partial Y^2}, \end{aligned} \quad (2.48)$$

$$\begin{aligned} \Delta G_v(u, v, w, p) = & \frac{\partial(\check{u}^\nu \Delta v)}{\partial X} + C_1 \frac{\partial^2 \Delta v}{\partial X^2} + C_2 \frac{\partial(\check{u}^\nu \Delta v)}{\partial Z} + \frac{\partial(\check{v}^\nu \Delta v)}{\partial Y} + C_3 \frac{\partial(\check{w}^\nu \Delta v)}{\partial Z} \\ & + C_4 \frac{\partial \Delta v}{\partial Z} + \frac{\partial \Delta p}{\partial Y} + C_5 \frac{\partial^2 \Delta v}{\partial Z^2} + C_6 \frac{\partial^2 \Delta v}{\partial Z \partial X} + C_1 \frac{\partial^2 \Delta v}{\partial Y^2}, \end{aligned} \quad (2.49)$$

$$\begin{aligned} \Delta G_w(u, v, w, p) = & \frac{\partial(\check{u}^\nu \Delta w)}{\partial X} + C_1 \frac{\partial^2 \Delta w}{\partial X^2} + C_2 \frac{\partial(\check{u}^\nu \Delta w)}{\partial Z} + \frac{\partial(\check{v}^\nu \Delta w)}{\partial Y} + C_3 \frac{\partial(\check{w}^\nu \Delta w)}{\partial Z} \\ & + C_4 \frac{\partial \Delta w}{\partial Z} + C_3 \frac{\partial \Delta p}{\partial Z} + C_5 \frac{\partial^2 \Delta w}{\partial Z^2} + C_6 \frac{\partial^2 \Delta w}{\partial Z \partial X} + C_1 \frac{\partial^2 \Delta w}{\partial Y^2}, \end{aligned} \quad (2.50)$$

$$\nabla \bullet (\Delta \mathbf{V}) = \frac{\partial \Delta u}{\partial X} + \frac{\partial \Delta v}{\partial Y} + C_2 \frac{\partial \Delta u}{\partial Z} + C_3 \frac{\partial \Delta w}{\partial Z} \quad (2.51)$$

Equations can be written (2.44) and (2.45) in a global matrix form as

$$[\mathbf{I} + \alpha \Delta \tau (\mathbf{D}_X + \mathbf{D}_Y + \mathbf{D}_Z)] \Delta \Phi = \Delta \tau \mathbf{S} \quad (2.52)$$

where  $\Delta \Phi = [\Delta u, \Delta v, \Delta w, \Delta p]^T$ ,  $\alpha = 2\Delta t/3$ , and  $\mathbf{I}$  is the identity matrix, and where

$$\mathbf{D}_X = \begin{bmatrix} M + \frac{1}{\alpha} & 0 & 0 & \frac{\partial}{\partial x} \\ 0 & M & 0 & 0 \\ 0 & 0 & M & 0 \\ \frac{1}{\delta} \frac{\partial}{\partial x} & 0 & 0 & 0 \end{bmatrix}, \quad \mathbf{D}_Y = \begin{bmatrix} N & 0 & 0 & 0 \\ 0 & N + \frac{1}{\alpha} & 0 & \frac{\partial}{\partial y} \\ 0 & 0 & N & 0 \\ 0 & \frac{1}{\delta} \frac{\partial}{\partial y} & 0 & 0 \end{bmatrix}, \quad (2.53a)$$

$$\mathbf{D}_Z = \begin{bmatrix} R & 0 & 0 & C_2 \frac{\partial}{\partial z} \\ 0 & R & 0 & 0 \\ 0 & 0 & R + \frac{1}{\alpha} & C_3 \frac{\partial}{\partial z} \\ C_2 \frac{1}{\delta} \frac{\partial}{\partial z} & 0 & C_3 \frac{1}{\delta} \frac{\partial}{\partial z} & 0 \end{bmatrix}, \quad \mathbf{S} = \begin{bmatrix} F_u^n - \tilde{u}^v - \alpha G_u \\ F_v^n - \tilde{v}^v - \alpha G_v \\ F_w^n - \tilde{w}^v - \alpha G_w \\ -(1/\delta) \mathbf{D} \tilde{\mathbf{V}}^v \end{bmatrix}, \quad (2.53b)$$

in which the differential operators  $M$ ,  $N$  and  $R$  are defined as

$$M = \frac{\partial(\tilde{u}^v \Phi)}{\partial X} + C_1 \frac{\partial^2 \Phi}{\partial X^2}, \quad N = \frac{\partial(\tilde{v}^v \Phi)}{\partial Y} + C_1 \frac{\partial^2 \Phi}{\partial Y^2}, \quad (2.54)$$

$$R = C_2 \frac{\partial(\tilde{u}^v \Phi)}{\partial Z} + C_3 \frac{\partial(\tilde{w}^v \Phi)}{\partial Z} + C_4 \frac{\partial \Phi}{\partial Z} + C_5 \frac{\partial^2 \Phi}{\partial Z^2} + C_6 \frac{\partial^2 \Phi}{\partial X \partial Z}, \quad (2.55)$$

where  $\Phi$  can be  $\Delta u$ ,  $\Delta v$ ,  $\Delta w$  or  $\Delta p$ .

A factored Alternate-Direction Implicit (ADI) scheme is then applied to the left hand side of equation (2.52)

$$[\mathbf{I} + \alpha \Delta \tau (\mathbf{D}_X + \mathbf{D}_Y + \mathbf{D}_Z)] \Delta \Phi = (\mathbf{I} + \alpha \Delta \tau \mathbf{D}_X)(\mathbf{I} + \alpha \Delta \tau \mathbf{D}_Y)(\mathbf{I} + \alpha \Delta \tau \mathbf{D}_Z) \Delta \Phi \quad (2.56)$$

It should be mentioned that the approximate factorization eliminates the quadratic terms  $\alpha^2 \Delta \tau^2 \mathbf{D}_X \mathbf{D}_Y$ ,  $\alpha^2 \Delta \tau^2 \mathbf{D}_Y \mathbf{D}_Z$ ,  $\alpha^2 \Delta \tau^2 \mathbf{D}_X \mathbf{D}_Z$ , and cubic term  $\alpha^3 \Delta \tau^3 \mathbf{D}_X \mathbf{D}_Y \mathbf{D}_Z$  from left hand side of equation (2.52). Therefore, it is important to keep  $\Delta \tau$  sufficiently small. This ADI scheme can produce some convergence issues if  $\Delta \tau$  takes large values.

The ADI scheme reduces the solution to the sets of several scalar-tridiagonal systems of equations. Thus, equation (2.52) changes to

$$(I + \alpha \Delta \tau \mathbf{D}_X)(I + \alpha \Delta \tau \mathbf{D}_Y)(I + \alpha \Delta \tau \mathbf{D}_Z) \Delta \Phi = \Delta \tau S \quad (2.57)$$

The ADI scheme requires the introduction of intermediate variables  $\Delta \bar{\Phi}$  and  $\Delta \Phi^*$  to solve the linear implicit system of equations. The variable  $\Delta \bar{\Phi}$  has the components  $\Delta \bar{u}$ ,  $\Delta \bar{v}$ ,  $\Delta \bar{w}$  and  $\Delta \bar{p}$  which are calculated in the Z-sweep

$$[I + \alpha \Delta \tau \mathbf{D}_Z] \Delta \bar{\Phi} = \Delta \tau S \quad (2.58)$$

Next, in the X-sweep the values of  $\Delta \Phi^* = [\Delta u^*, \Delta v^*, \Delta w^*, \Delta p^*]^T$  are computed

$$[I + \alpha \Delta \tau \mathbf{D}_X] \Delta \Phi^* = \Delta \bar{\Phi} \quad (2.59)$$

and finally, in the Y-sweep the values of  $\Delta \Phi = [\Delta u, \Delta v, \Delta w, \Delta p]^T$  are obtained

$$[I + \alpha \Delta \tau \mathbf{D}_Y] \Delta \Phi = \Delta \Phi^* \quad (2.60)$$

Hence, after the ADI method application, by replacing the equations (2.53a) and (2.53b) into (2.58), (2.59) and (2.60), the scalar form of Z-sweep, X-sweep and Y-sweep can be obtained. The details are presented in Appendix A.

## 2.2.5 Special decoupling procedure

A special decoupling procedure [9, 10, 11], based on the utilization of the continuity equation, is used for each sweep to eliminate the pressure term from momentum equations. In this manner, the problem is reduced to the solution of several sets of decoupled scalar-tridiagonal systems of equations. As a result, this method is characterized by excellent computational efficiency and accuracy. For example, for Z-sweep the corresponding relation from continuity equation can be used:

$$\Delta \bar{p} = -\frac{\Delta \tau}{\delta} \left( \nabla \cdot \check{\mathbf{V}}^v + C_2 \frac{\partial \Delta \bar{u}}{\partial Z} + C_3 \frac{\partial \Delta \bar{w}}{\partial Z} \right), \quad \Delta p = \Delta \bar{p} - \frac{\Delta \tau}{\delta} \left( \frac{\partial \Delta \bar{u}}{\partial X} \right) \quad (2.61)$$

## 2.2.6 Spatial discretization on stretched staggered grids

These equations are further spatially discretized by central differencing on a stretched staggered grid, in which the flow variables  $u$ ,  $v$ ,  $w$  and  $p$  are defined at different positions, as shown in Figure 2.2.

By using a staggered grid, this method avoids the odd-and-even point decoupling while preserving the second-order accuracy in space of the method. To obtain a good spatial resolution the grid is stretched by increasing the number of points in regions where higher velocity gradients are present such as near the solid walls. The stretched-staggered grid can be seen in Figure 2.3. The grid is stretched along one direction independently of the other coordinate direction and is defined by hyperbolic sine and tangent functions in the  $x$ ,  $y$  and  $z$ -directions.

$$X_i = X_0 + (X_{Nx} - X_0) \frac{\sinh(\gamma i/Nx)}{\sinh(\gamma)}, \quad (2.62)$$

$$Y_j = Y_0 + (Y_{Ny} - Y_0) \frac{\sinh(\gamma j/Ny)}{\sinh(\gamma)}, \quad (2.63)$$

$$Z_k = Z_0 + (Z_{Nz} - Z_0) \left[ \frac{1}{2} + \frac{\tanh(\gamma(2k - Nz)/2Nz)}{2 \tanh(\gamma/2)} \right], \quad (2.64)$$

where,  $X_0$ ,  $Y_0$ ,  $Z_0$  are the start coordinates points of the grid,  $X_{Nx}$ ,  $Y_{Ny}$ ,  $Z_{Nz}$  are the end coordinate points of the grid,  $Nx$ ,  $Ny$ ,  $Nz$  are the number of grid points in  $X$ ,  $Y$ , and  $Z$  directions, and  $\gamma$  is the stretching parameter.

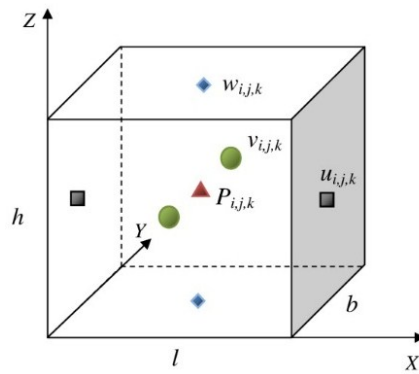
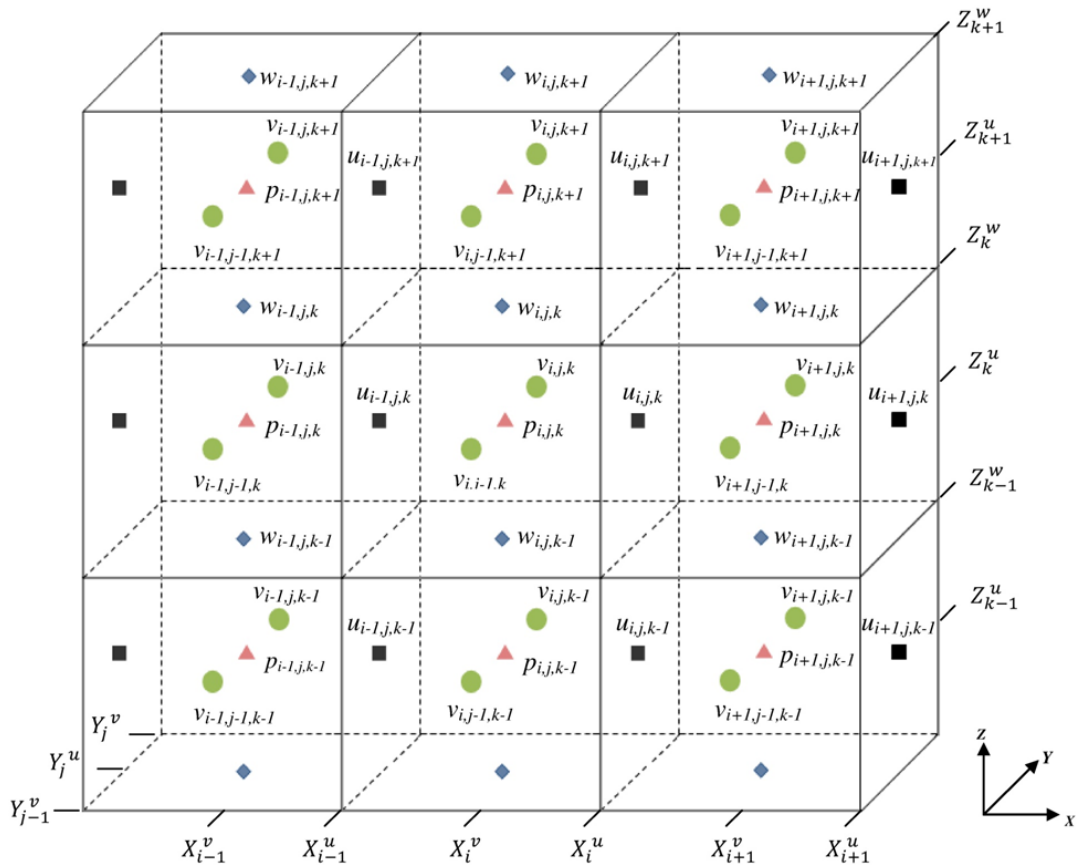


Figure 2.2 Geometry of the three-dimensional staggered grid.

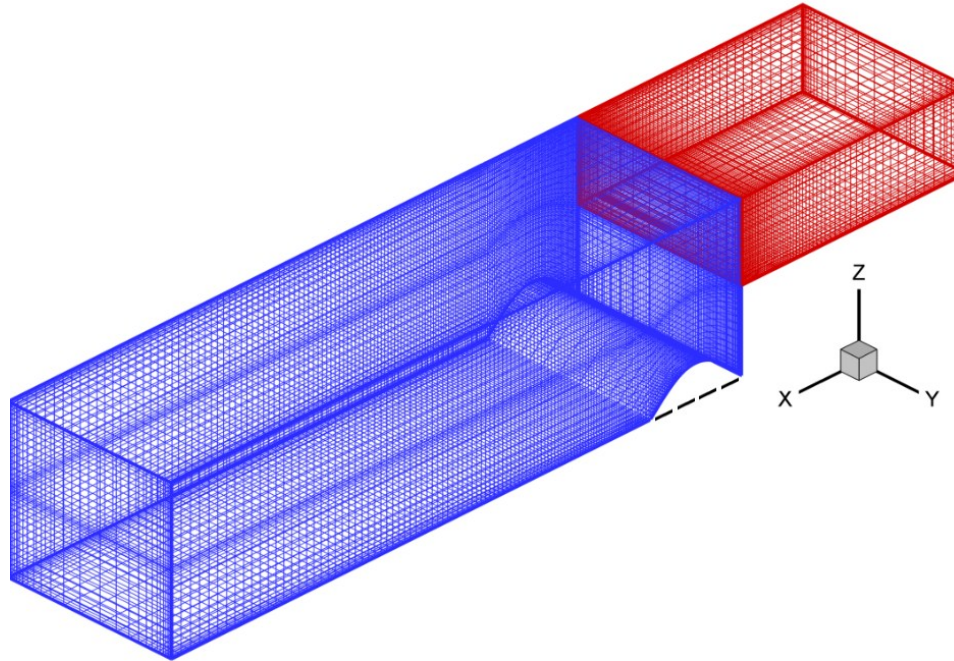


Figure 2.3 Three-dimensional stretched staggered grid with an oscillating wall configuration

### 2.3 Method validation

The numerical method has been successfully validated by comparison with experimental results available for three-dimensional steady flows past a downstream-facing step and with previous two-dimensional computational solutions.

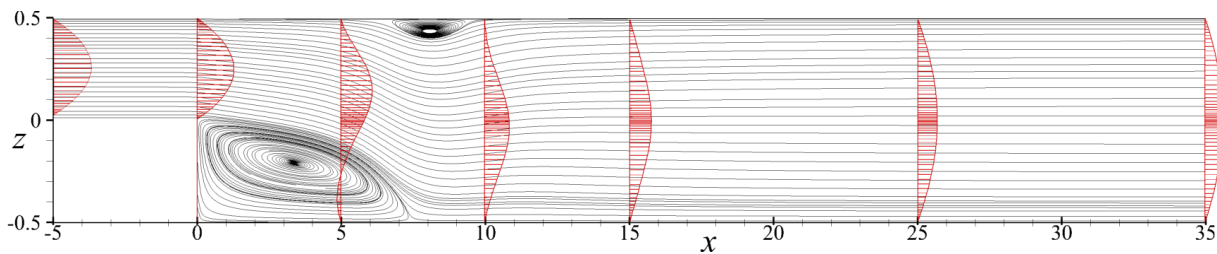


Figure 2.4 Typical flow pattern for the confined flow past a down-stream-facing step in a rectangular duct illustrating the flow separation regions by using the streamlines and the velocity profiles along the duct in the plane of symmetry ( $y = 0$ ).

The main feature of this confined flow past a downstream-facing step is the presence of two flow separation regions, one on the lower wall and the other one on the upper wall. This typical flow pattern is illustrated in Figure 2.4 by using the streamlines and the velocity profiles in the

plane of symmetry ( $y = 0$ ) along the channel at various axial locations. The axial locations of the flow separation  $x_s$  and reattachment  $x_r$  on the upper wall (with upper separation length  $L_u = x_r - x_s$ ) and the lower wall separation length  $L_l$  are used to validate the solutions by comparison with previous numerical and experimental results. These points represent the characteristic features of this flow as shown in Figure 2.5.

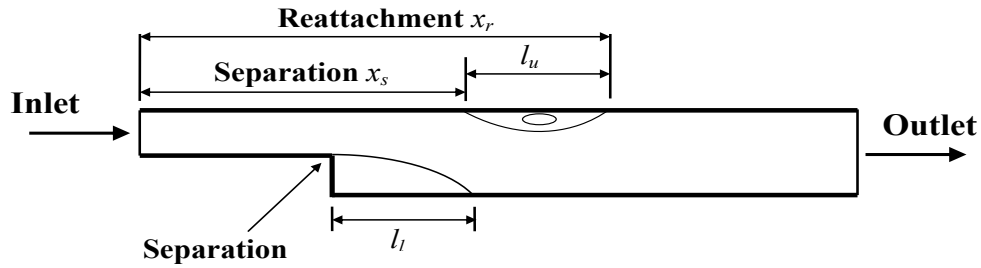


Figure 2.5 Location of the separation and reattachment points on the upper and lower walls into the downstream-facing step ( $H/h = 2$ ) channel.

### 2.3.1 Validation for uniform rectangular channels

This method is first validated for the flows in a uniform rectangular channel of width  $2b$  and height  $h$  (similar to the upstream portion of the channel in Figure 2.1, which has the aspect ratio  $2b/h$ ) with the axial length of 25, by considering a fully-developed laminar flow or a uniform flow at the inlet.

The velocity profiles obtained in the symmetry plane of the channel ( $y = 0$ ), are starting from the fully-developed laminar profile as shown in Figures 2.6 (a) and 2.6 (b) for various aspect ratios ( $2b/h = 1, 2, 4, 8$ ) and at various axial locations ( $x = 0, 5, 10, 15, 25$ ).

Very good agreement was found between the present numerical results and the theoretical solutions [71]. The present numerical method maintaining very good accuracy with the fully-developed laminar velocity profile along the channel, as expected.

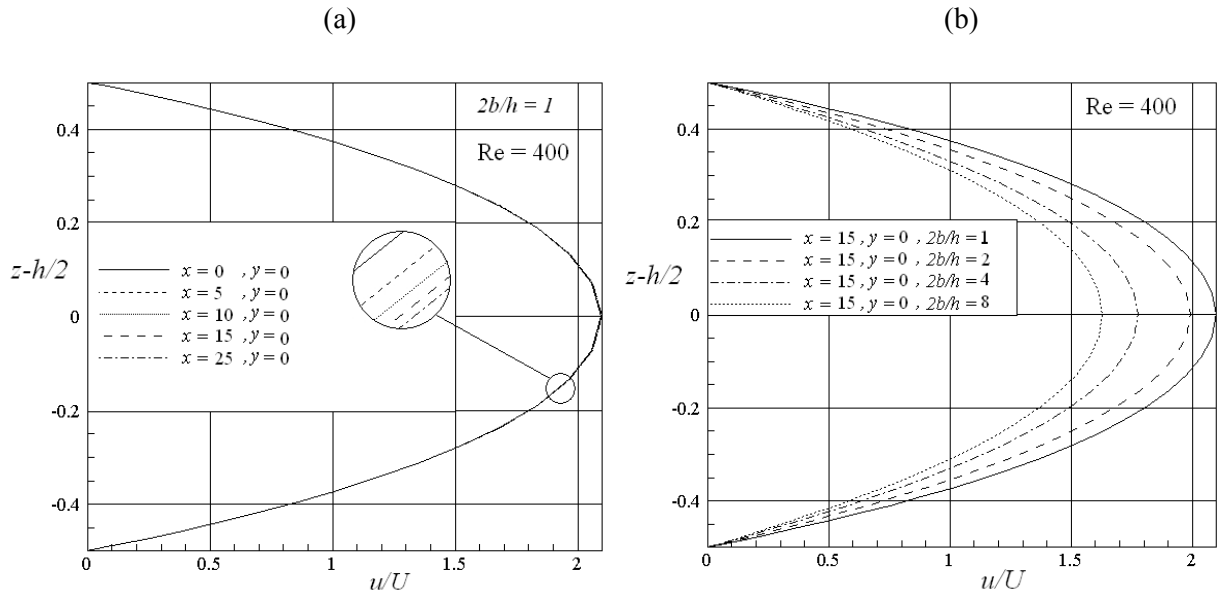


Figure 2.6 Velocity profiles at  $y = 0$  (symmetry plane of the channel): (a) at several axial locations (for  $2b/h = 1$ ), and (b) for several aspect ratios ( $2b/h$ ) at the axial location  $x = 15$ .

### 2.3.2 Comparison with the experimental data and effect of lateral walls

The computed locations of the flow separation and reattachment on the upper and lower walls in the plane of symmetry ( $y = 0$ ) are shown in Figure 2.7 in comparison with the experimental results obtained by Armaly *et al.* [31] and by Lee and Mateescu [13], and two-dimensional numerical results by Mateescu and Venditti [12].

One can notice good agreement between the present solutions and the experimental results, while the two-dimensional solutions obtained by Mateescu and Venditti are not in good agreement with the experimental results especially for larger Reynolds numbers.

This confirms the explanation advanced in [31, 36] that the disagreement between the two-dimensional solutions and the experimental results is due to the three-dimensional effects due to the lateral walls in the experimental configuration. This explains why three-dimensional study of confined laminar flows is important in this research.

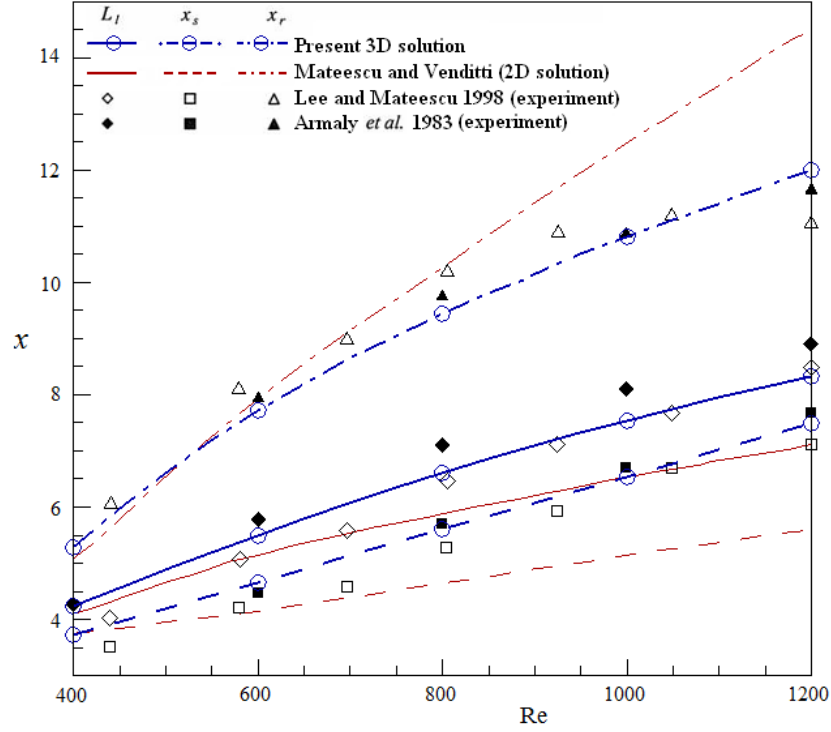


Figure 2.7 Steady flow over a downstream-facing step ( $h=0.5$ ): Variation with the Reynolds number of the flow separation and reattachment locations on the upper wall ( $x_s$  and  $x_r$ ) and the separation length on the lower wall ( $L_l$ ) in the symmetry plane of the channel ( $y=0$ ).

Comparison between:

- |         |                             |   |
|---------|-----------------------------|---|
| ---○--- | Present solution:           | 3D solutions for the aspect ratio $2b = 26.6$ ; |
| -----   | Mateescu and Venditti [12]: | 2D solutions (for $2b \rightarrow \infty$ );    |
| □, ◇, △ | Lee and Mateescu [13]:      | Experimental results (for $2b = 26.6$ );        |
| ■, ◆, ▲ | Armaly <i>et al.</i> [31]:  | Experimental results.                           |

### 2.3.3 Grid sensitivity analysis for steady and unsteady internal flow solutions

The grid sensitivity has been investigated for the presented numerical solution through the mesh refinement applied to the steady and unsteady flow cases. Through the geometry analysis, it is found the length of upstream and downstream should be at least  $L_0=25$ , and  $L_l=75$ . Beyond these two channel lengths the numerical results are not affected. These results are obtained by using  $240 \times 68 \times 68$  grid points, and shown in Tables 2.1 and 2.2.

Present 3D Results	$L_l$	$x_s$	$x_r$
$L_l = 45$	4.96	4.21	7.75
$L_l = 55$	5.01	4.20	7.82
$L_l = 65$	5.04	4.24	7.87
$L_l = 75$	5.06	4.27	7.91
$L_l = 85$	5.06	4.27	7.91

Table 2.1 Analysis of downstream length ( $L_l$ ) for  $Re = 600$ : comparison of separation length on the lower wall ( $L_l$ ) and flow separation and reattachment locations on the upper wall ( $x_s$  and  $x_r$ ), for  $L_0 = 25$ .

Present 3D Results	$L_l$	$x_s$	$x_r$
$L_0 = 5$	5.01	4.21	7.85
$L_0 = 10$	5.03	4.24	7.88
$L_0 = 15$	5.04	4.25	7.89
$L_0 = 25$	5.06	4.27	7.91
$L_0 = 35$	5.06	4.27	7.91

Table 2.2 Analysis of upstream length ( $L_0$ ) for  $Re = 600$ : comparison of separation length on the lower wall ( $L_l$ ) and flow separation and reattachment locations on the upper wall ( $x_s$  and  $x_r$ ), for  $L_l = 75$ .

To find the ideal grid points, the solution is solved for a confined steady flow at  $Re = 600$  in a backward-facing step with total span of  $2b = 26.6$ , step height  $h = 0.5$ , upstream channel length  $L_0 = 25$ , and downstream channel length  $L_l = 75$ .

The criteria of comparison are based on the lower wall separation length  $L_l$ , and the upper wall separation and reattachment locations  $x_s$  and  $x_r$  (with upper separation length  $L_u = x_r - x_s$ ).

The results of the grid sensitivity test are shown in Table 2.3. It can be seen there is no discrepancy between the solution obtained by using  $240 \times 68 \times 68$  grid points and the fully converged solution obtained with  $300 \times 88 \times 88$  grid points and beyond this grid density ( $240 \times 68 \times 68$ ), the numerical solution is not influenced by increasing the number of grid points.

Number of grid points	Lower wall	Upper wall		
	$L_l$	$L_u = x_r - x_s$	$x_s$	$x_r$
160 x 28 x 28	4.932	3.621	4.143	7.765
180 x 38 x 38	5.025	3.638	4.226	7.854
200 x 48 x 48	5.068	3.643	4.274	7.913
220 x 58 x 58	5.073	3.654	4.285	7.932
240 x 68 x 68	5.081	3.667	4.293	7.957
260 x 78 x 78	5.081	3.667	4.293	7.957
300 x 88 x 88	5.081	3.667	4.293	7.957

Table 2.3 Grid sensitivity of the numerical solution for  $h = 0.5$ ,  $Re = 600$ ,  $2b = 26.6$ ,  $L_0 = 25$ , and  $L_1 = 75$  based on the computed non-dimensional lengths of separation and reattachment.

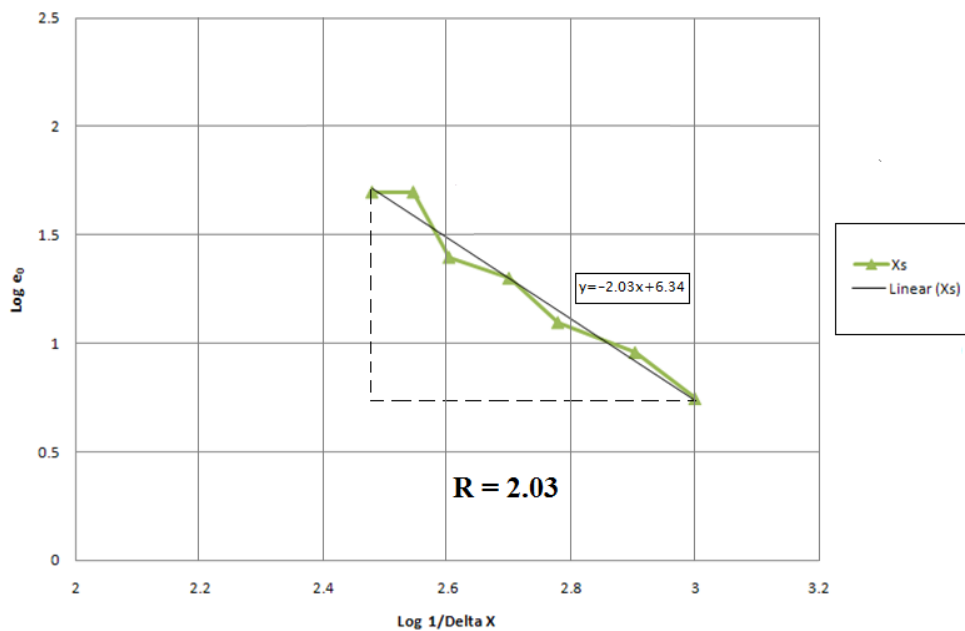


Figure 2.8 Order of accuracy calculated from the grid sensitivity test data.

The order of accuracy is validated and as shown in Figure 2.8. To check the order of accuracy the mean absolute error ( $\text{Log } e_0$ ) for the upper separation point is plotted with respect to grid spacing. The slope of the dashed curve, which is the linear regression of the upper separation point is 2.03 and as a result the method is second-order accurate.

### 2.3.4 Time-step convergence study

Considering the unsteady confined flow case, the size of the nondimensional real-time step is  $\Delta t = 2\pi/(\omega N)$  with a number of steps during an oscillation period of  $N=80$ . The number of steps is taken from the analysis of the upper and lower wall separations. Figure 2.9 shows a portion of the oscillation cycle from  $3.9 t/T$  to  $4 t/T$  of the wall separation length. One can see from Table 2.4 that the separation lengths keep constants after  $N=80$ .

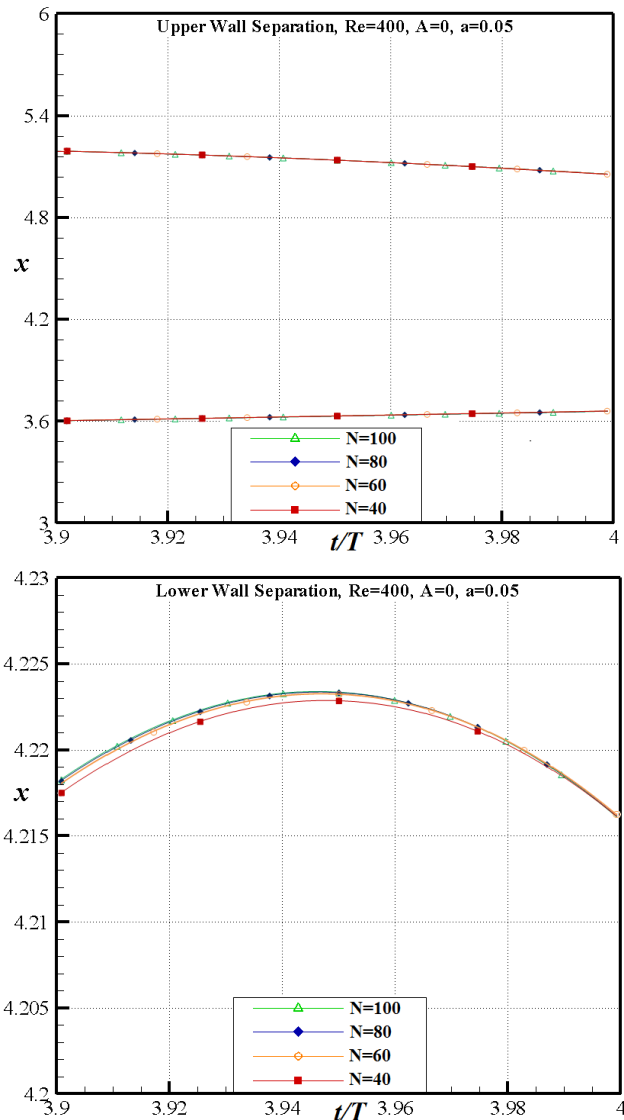


Figure 2.9 Several number of time steps per oscillation cycle describing the upper and lower wall separation length of unsteady confined flow past downstream-facing steps at  $Re=400$  and inflow velocity amplitude  $a=0.05$  and frequency  $\omega=0.05$ .

The real-time integration started from the steady flow solution for fixed walls and inflow velocity variation, and it was performed until all variables in the computational domain were executing repeatable and exact harmonic oscillations from one period to the next, usually after 3 oscillation cycles or less, as shown in Figure 2.9.

Time steps per cycle	$t/T$	$L_l$	$L_u$
40	3.95	4.2217	1.8578
60	3.95	4.2220	1.8566
80	3.95	4.2220	1.8567
100	3.95	4.2220	1.8567

Table 2.4 Sensitivity of the time steps per oscillation cycle of the numerical solution for  $N=40$ , 60, 80 and 100 with  $Re = 400$  at  $t/T=3.95$  based on the computed nondimensional lengths of separation and reattachment (see Figure 2.9).

## 2.4 Steady solutions for the confined flows with backward-facing step channel

After validation the method has been used to obtain steady solutions for the flows in a channel with a backward-facing step (shown in Figure 2.1). The variations of the flow separation and reattachment locations ( $x_s$  and  $x_r$ ) on the upper wall and the separation length ( $L_l$ ) on the lower wall along the span of the channel, from the plane of symmetry ( $y = 0$ ) towards the lateral wall at  $y = 13.3$  are shown in comparison with experimental results conducted by Lee and Mateescu [13] and Armaly et al. [31] only in the plane of symmetry ( $y = 0$ ) in Figure 2.10. These results are computed for total span  $2b = 26.6$ , step height  $h = 0.5$  (expansion ratio,  $ER = 2$ ), and various Reynolds numbers,  $Re = 450, 600, 800$  and  $1000$ .

The typical variations of the flow separation and reattachment locations on the upper and lower walls ( $x_s$ ,  $x_r$  and  $L_l$ ) along the span of the channel ( $y$ -direction) with the non-dimensional step height  $h_s = 1 - h$  are shown in Figure 2.11. The results are obtained for total span  $2b = 26.6$ , and for several step heights  $h = 0.4, 0.5$  and  $0.6$  at  $Re = 600$ .

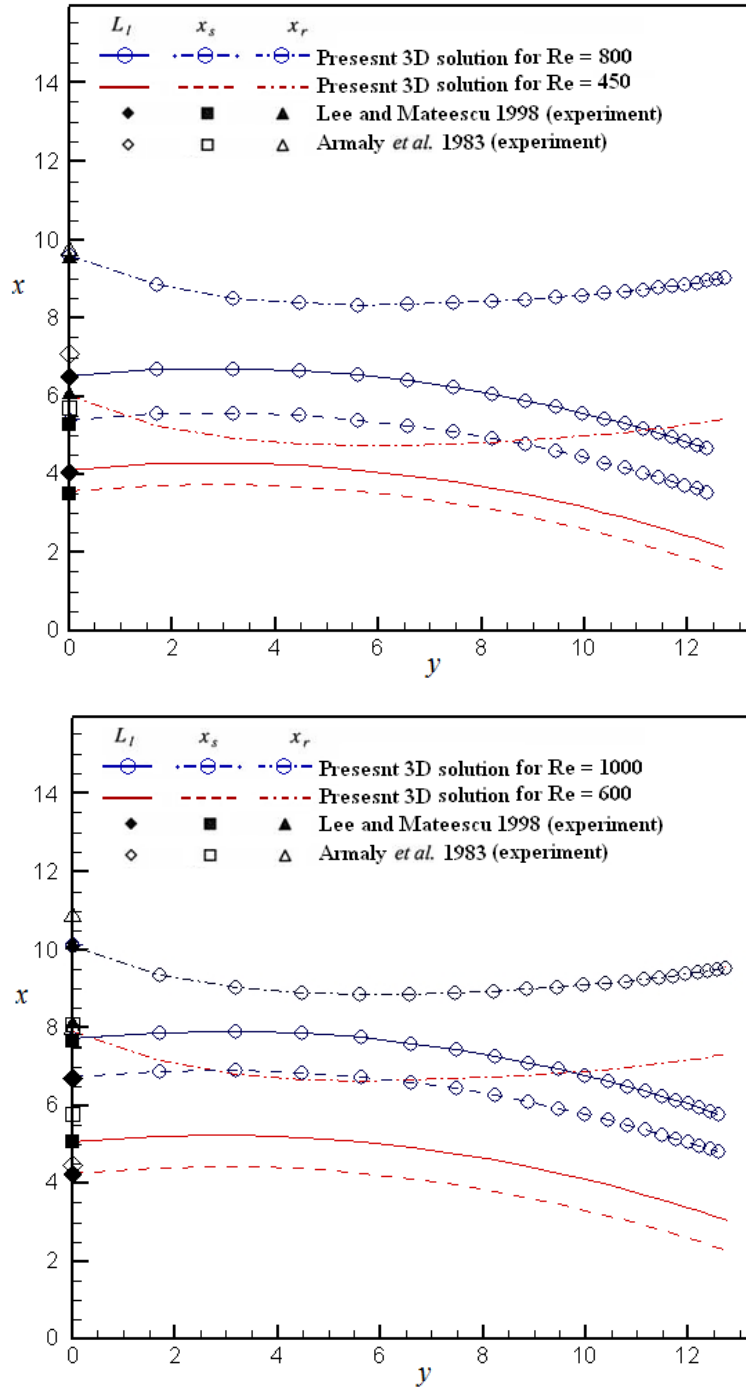


Figure 2.10 Influence of the Reynolds number on the variation of the flow separation and reattachment locations on the lower and upper walls ( $L_l$ ,  $x_s$  and  $x_r$ ) along the span of the channel ( $y$ -direction) for  $2b = 26.6$  and step height of  $h = 0.5$  at various Reynolds numbers for  $Re = 450, 600, 800$  and  $1000$ . For the plane of symmetry ( $y = 0$ ): Comparison with the experimental results obtained by Armaly *et al.* [31] and Lee and Mateescu [13].

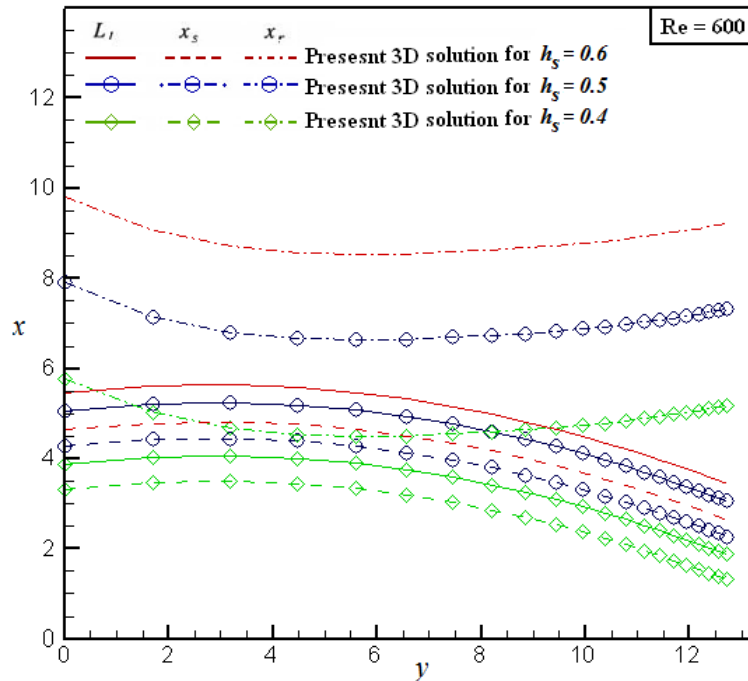


Figure 2.11 Influence of the step height,  $h_s = 1 - h$ , on the variations of the flow separation and reattachment locations on the upper and lower walls ( $x_s$ ,  $x_r$  and  $L_l$ ) along the span of the channel ( $y$ -direction) for  $2b = 26.6$  and for several step heights at  $Re = 600$ .

The typical front views ( $x-z$  planes) of the flow as viewed from the longitudinal planes  $y = 0$ ,  $y = 4$ ,  $y = 8$  and  $y = 13$  towards the lateral wall ( $y = 13.3$ ) are illustrated in Figure 2.12 for  $2b = 26.6$  and  $h = 0.5$  at  $Re = 600$ , by using streamlines (represented by continuous lines) and velocity contours. The color shades indicate the magnitude of the nondimensional flow velocity with respect to the mean flow velocity,  $U_0$ , according to the scale included in the figure.

A top view of the channel ( $x-y$  plane) illustrating the flow separation regions on the lower and upper walls is also shown in Figure 2.13 for  $2b = 26.6$  at  $Re = 600$ . For a better illustration of the flow separation regions in this complex three-dimensional flow, the isometric view of the streamlines and the velocity contours is indicated in Figure 2.14, and a more detailed isometric view is shown in Figure 2.15.

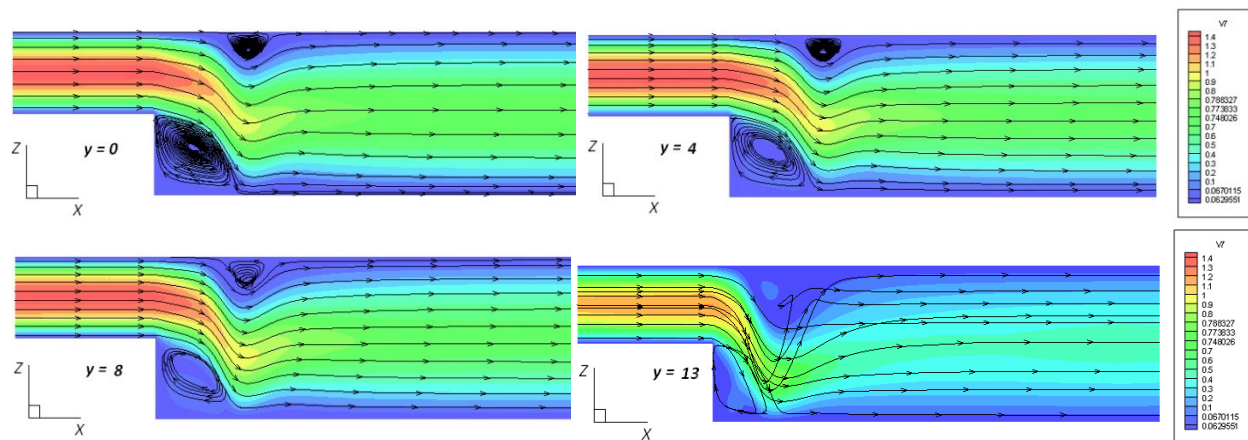


Figure 2.12 Front views ( $x$ - $z$  plane) of the 3-D flow in the duct with a downstream-facing step ( $h = 0.5$ ), for  $2b = 26.6$  at  $Re = 600$ , illustrating the streamlines and the velocity contours at several distances from the plane of symmetry ( $y = 0$ ) towards the lateral wall ( $y = 13.3$ ).

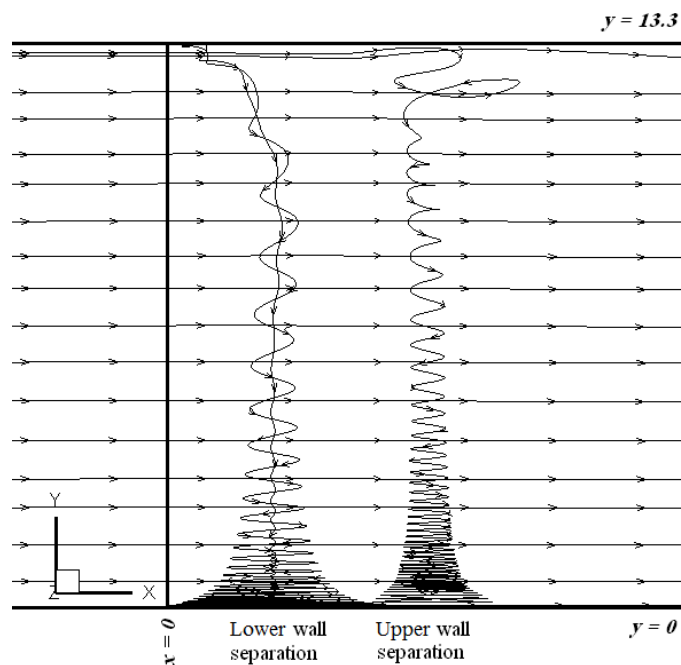


Figure 2.13 Top view ( $x$ - $y$  plane) of the streamlines in the three-dimensional flow past a downstream-facing step ( $h = 0.5$ ), illustrating the flow separation regions on the lower and upper walls for  $2b = 26.6$  at  $Re = 600$ .

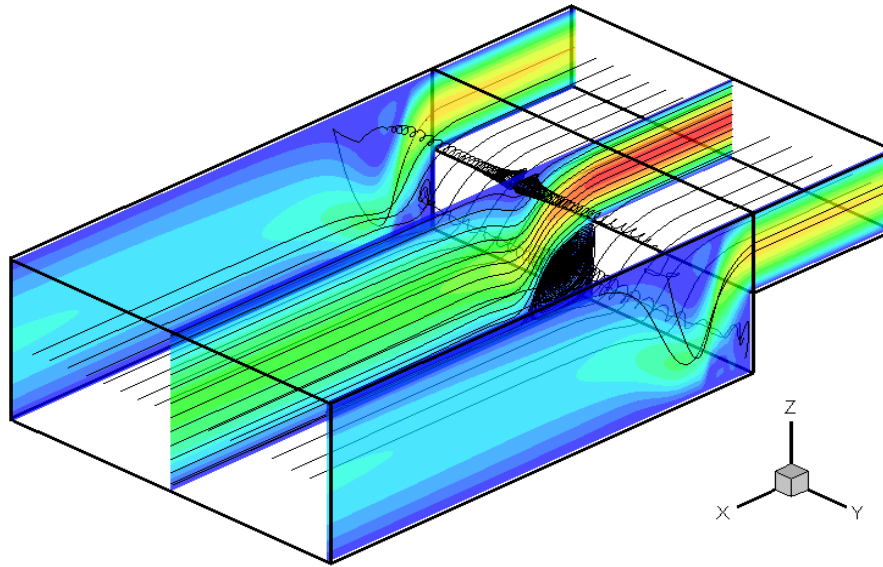


Figure 2.14 Isometric view of the streamlines and velocity contours in a three-dimensional confined flow past a downstream-facing step ( $h = 0.5$ ), for  $2b = 26.6$  at  $Re = 600$ .

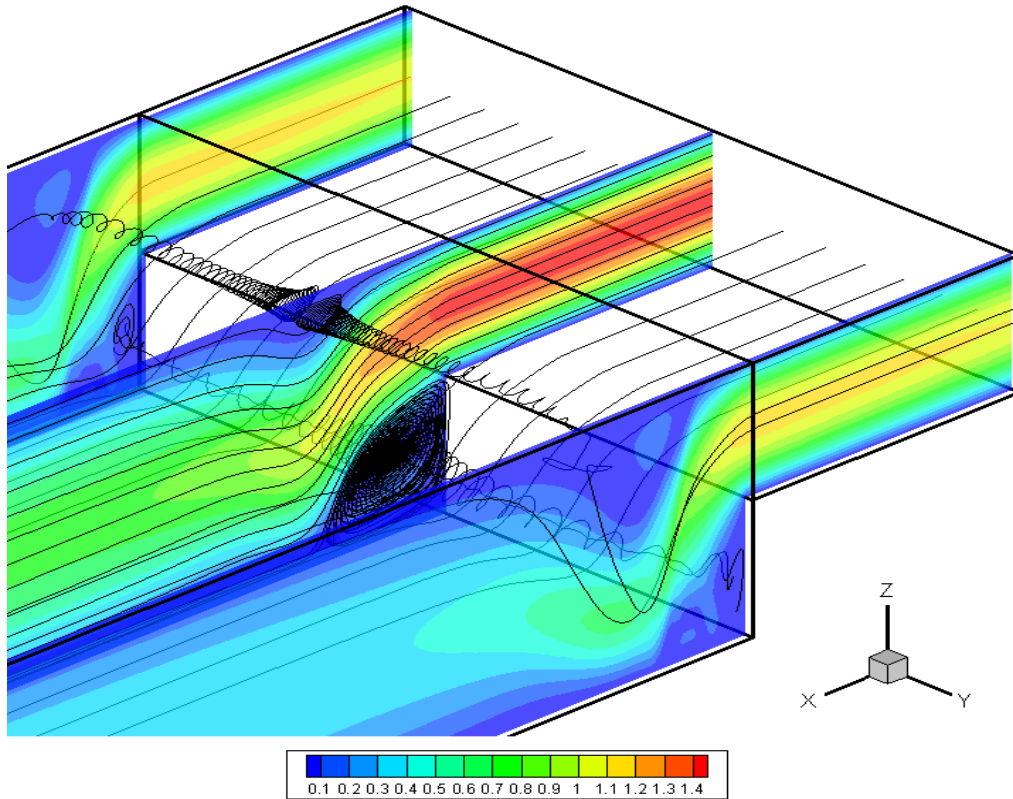


Figure 2.15 A detailed view of the streamlines and velocity contours in a three-dimensional confined flow past a downstream-facing step ( $h = 0.5$ ), for  $2b = 26.6$  at  $Re = 600$ .

## 2.5 Solutions for three-dimensional unsteady confined flows with variable inflow velocity

The numerical method presented in Section 2.2 is applied to obtain solutions for the unsteady confined flows past downstream-facing step generated by harmonic variations in time of the inflow velocities defined by equations (2.1) to (2.3), when the channel walls are fixed ( $A = 0$ , where  $A$  is the amplitude of wall oscillation). Computations have been performed for the step height  $(1-h)H = 0.5H$  (where  $h = 0.5$ , and expansion ratio  $ER = 2$ ), and for the aspect ratio of the channel 26.6 in respect to downstream height  $H$ . Numerical solutions have been obtained for various values of the Reynolds number,  $Re = HU_0/\nu$ , and for various values of the amplitude of the inflow velocity,  $a$ , and of the reduced frequency of oscillations,  $\omega$ . In the computations, the size of the nondimensional real time step is defined as  $\Delta t = T/N$ , where the number of real time steps during an oscillation period ( $T = 2\pi/\omega$ ) was taken  $N = 80$  as it was shown in section 2.3.4.

The pseudo-time computations have been performed using  $\delta = 0.8$  and  $\Delta \tau = 0.01$ , and convergence was assumed to be reached when the RMS residuals were less than  $10^{-5}$ . The real time integration was started from the steady flow solution for fixed walls and constant inflow velocity (obtained by Mateescu, Panahi and Roy [8]), and was performed until all variables in the computational domain were executing repeatable harmonic oscillations from one period to the next (usually after 3 oscillation cycles). The number of sub-iterations in pseudo-time are less than 100 for each time step depending on the case. This leads to have a fast converging numerical method.

The streamline patterns and the velocity contours in the plane of symmetry ( $y = 0$ ) of the unsteady confined flow at various moments during the oscillatory cycle,  $t/T = 3.0, 3.25, 3.5$  and  $3.75$ , for the Reynolds numbers  $Re = 400, 600, \text{ and } 800$ , for the reduced frequency  $\omega = 0.05$ , and for three values of the amplitude of the inflow velocity variation,  $a = 0.05, 0.2$  and  $0.4$  are shown in Figure 2.16 for the case of fixed walls ( $A = 0$ ).

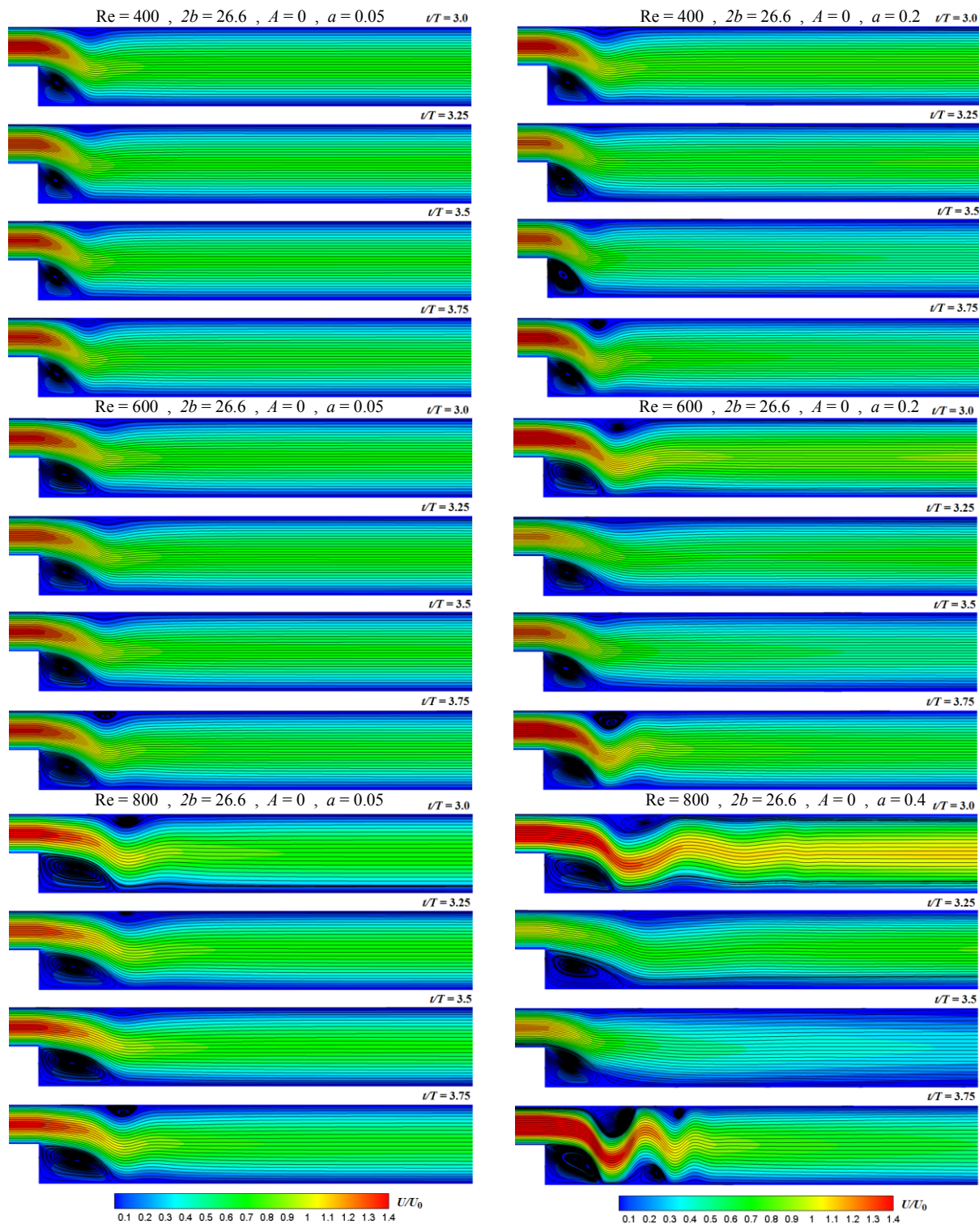


Figure 2.16 Streamline patterns and velocity fields of the unsteady confined flow at various moments during the oscillatory cycle,  $t/T = 3.0, 3.25, 3.5$  and  $3.75$ , for  $Re = 400, 600$  and  $800$ ,  $\omega = 0.05$  and for three values of the amplitude of the inflow velocity variation,  $a = 0.05, 0.2$  and  $0.4$  ( $A = 0$ ). The color shades indicate the nondimensional values (with respect to  $U_0$ ) of the local fluid velocity

### **2.5.1 Influence of the amplitude of the inflow velocity fluctuations on the unsteady flow separations**

The typical influence of the inflow velocity oscillation amplitude,  $a$ , on the lower wall separation length ( $L_l$ ) and on the upper wall separation and reattachment locations ( $x_s$  and  $x_r$ ) is illustrated in Figure 2.17 for the case of fixed walls ( $A = 0$ ). These solutions were obtained in the plane of symmetry of the channel ( $y = 0$ ) for several values of the amplitudes of the inflow velocity variation,  $a$ , and of the Reynolds number,  $Re$ , and for the reduced frequency  $\omega = 0.05$ , and the non-dimensional period of oscillations denoted by  $T = 2\pi/\omega$ .

It is interesting to note that the upper wall flow separation is present only during a portion of the oscillatory cycle (being absent for the rest of the cycle) when the inflow velocity amplitude is larger, such as  $a > 0.05$  for  $Re \leq 600$ , and  $a \geq 0.2$  for  $Re = 800$ . At  $Re = 800$ , one can notice the formation of secondary flow separation regions on the lower and upper walls for  $a = 0.4$ , which appear only during a small portion (about one quarter) of the oscillatory cycle. The formation of these secondary flow separation regions on the lower and upper walls can also be seen in the flow visualizations for  $Re = 800$  shown in Figure 2.17.

### **2.5.2 Influence of the Reynolds number on the unsteady flow separations**

The typical influence of the inflow velocity oscillation amplitude,  $a$ , on the lower wall separation length ( $L_l$ ) and on the upper wall separation and reattachment locations ( $x_s$  and  $x_r$ ) is illustrated in Figure 2.18 for the case of fixed walls ( $A = 0$ ) with variable inflow velocity. These solutions are obtained for several values of the amplitudes of the inflow velocity variation,  $a$  and of the Reynolds number,  $Re$ , and for the reduced frequency  $\omega = 0.05$ .

Again one can observe the formation of the secondary flow separation region on the lower and upper walls for  $Re = 800$  and  $a = 0.4$ .

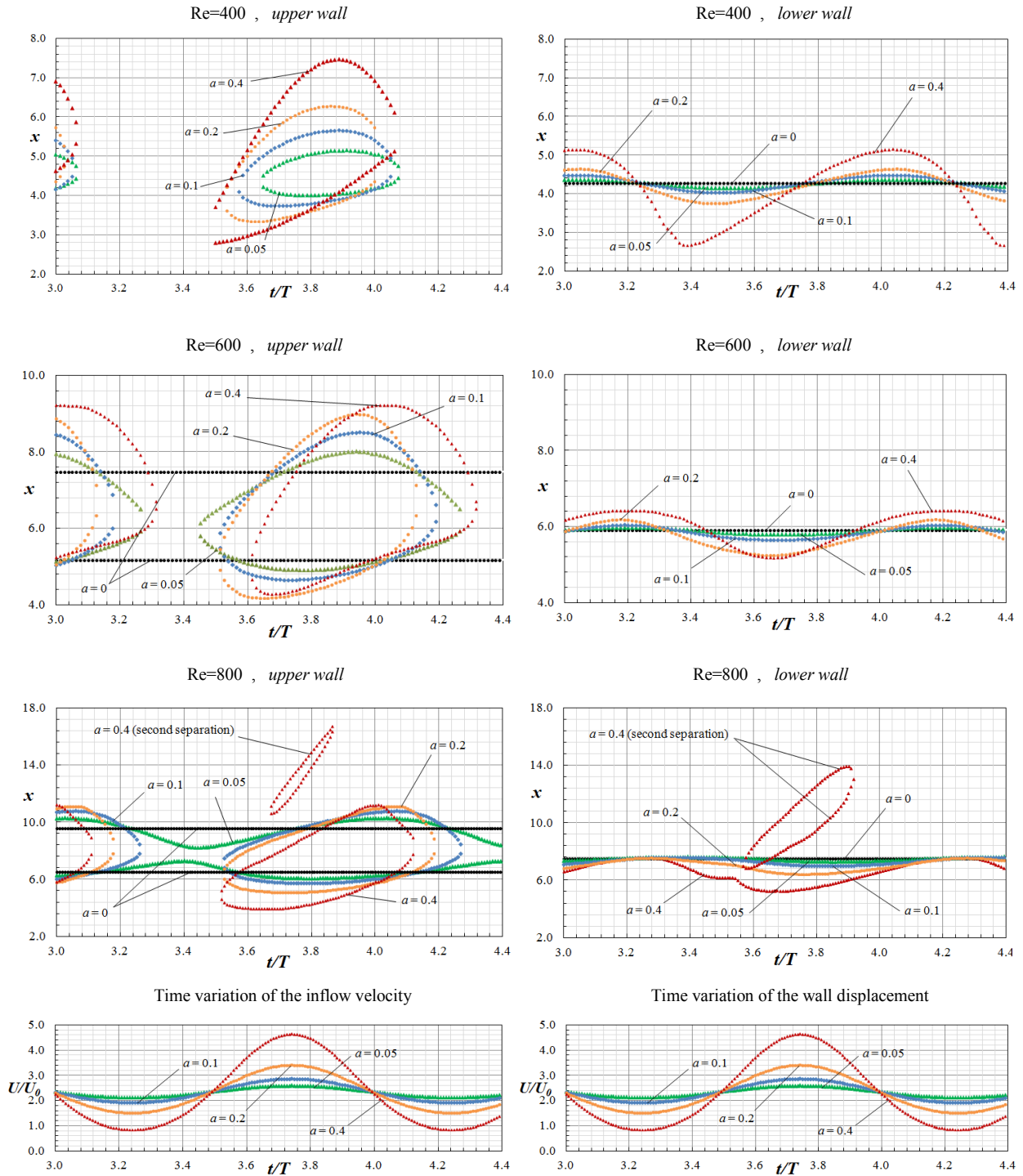


Figure 2.17. Influence of the inflow velocity amplitude,  $a$ , for fixed walls: Variation during the oscillatory cycle,  $t/T$ , of the upper wall separation and reattachment locations and of the lower wall reattachment locations, for  $Re = 400, 600$  and  $800$ ,  $\omega = 0.05$  ( $2b = 26.6$ ,  $A = 0$ ).

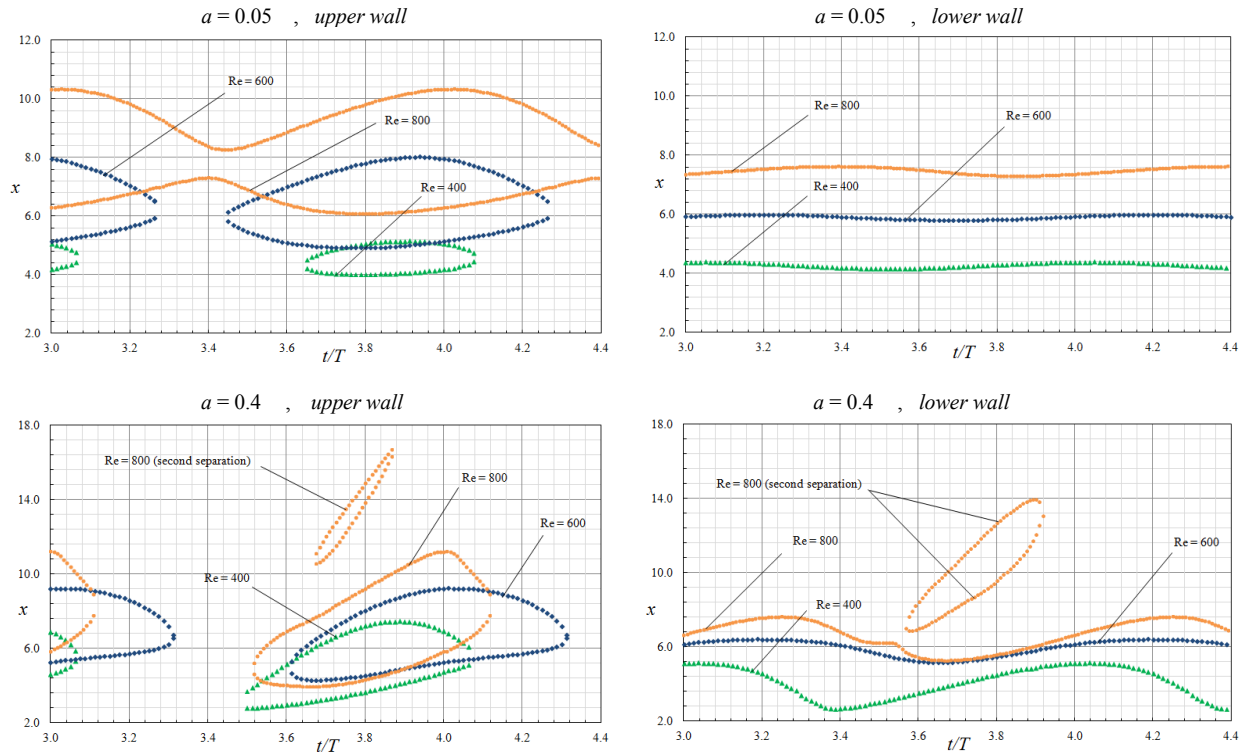


Figure 2.18. Influence of the Reynolds number,  $Re$ : Variation during the oscillatory cycle,  $t/T$ , of the upper and lower wall separation and reattachment locations, for  $\omega = 0.05$ ,  $a = 0.05$  and  $0.4$  ( $2b = 26.6$ ,  $A = 0$ ).

## 2.6 Solutions for three-dimensional unsteady confined flows with oscillating walls and time-variable inflow velocity

Numerical solutions are also obtained for the unsteady confined flows past downstream-facing steps generated by oscillating wall ( $A \neq 0$ ), defined by equations (2.4), and (2.5), and by harmonic variations in time of the inflow velocities defined by equations (2.1) to (2.3).

Computations have been performed for the step height  $(1-h)H = 0.5H$  (where  $h = 0.5$ ) and for the nondimensional length of the oscillating wall  $l = 10$ .

The streamline patterns and the velocity contours in the plane of symmetry ( $y = 0$ ) of the unsteady confined flow at various moments during the oscillatory cycle,  $t/T = 3.0, 3.25, 3.5$  and  $3.75$ , for the Reynolds numbers  $Re = 600$  and  $800$ , with the reduced frequency  $\omega = 0.05$ , and for two values of the amplitude of the inflow velocity variation,  $a = 0$  and  $0.05$ , are shown in Figure 2.19 for the case of the wall oscillation amplitude  $A = 0.05$ . In this figure, the color shades indicate the nondimensional values (with respect to  $U_0$ ) of the local fluid velocity.

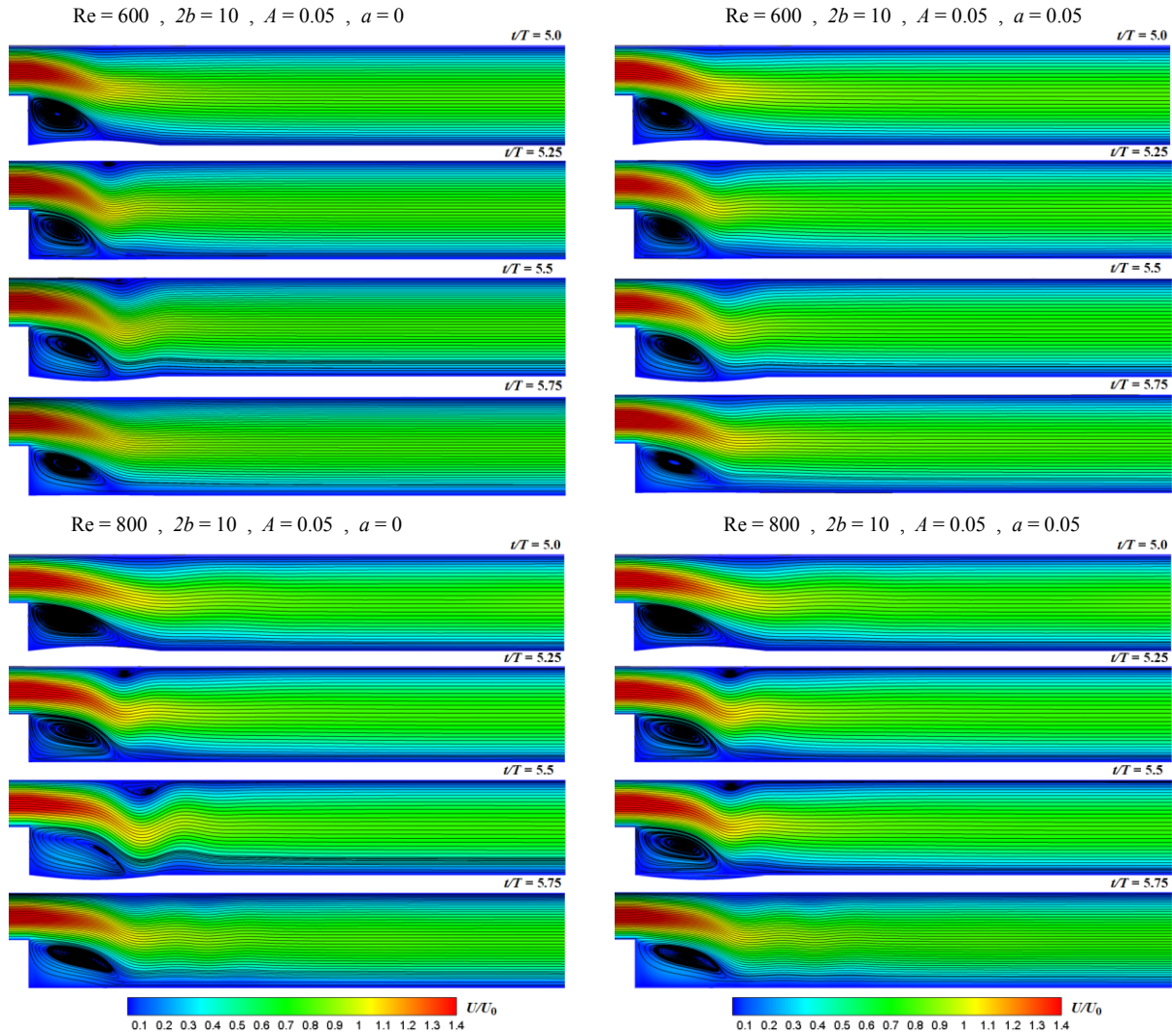


Figure 2.19 Streamline patterns and velocity fields of the unsteady confined flow at various moments during the oscillatory cycle,  $t/T = 5.0, 5.25, 5.5$  and  $5.75$ , for  $Re = 600$  and  $800$ ,  $\omega = 0.05$  and for two values of the amplitude of the inflow velocity variation,  $a = 0$  and  $0.05$ , and for the wall oscillation amplitude  $A = 0.05$ . The color shades indicate the nondimensional values (with respect to  $U_0$ ) of the local fluid velocity.

## 2.6.1 Influence of the aspect ratio of the channel on the unsteady flow separations

The typical influence of the aspect ratio of the downstream portion of the channel,  $2b$ , on the lower wall separation length ( $L_l$ ) and on the upper wall separation and reattachment locations ( $x_s$  and  $x_r$ ) is illustrated in Figure 2.20 for Reynolds number  $Re=600$  and the reduced frequency  $\omega=0.05$ . These solutions are obtained in the plane of symmetry of the channel ( $y=0$ ) for the inflow velocity amplitude,  $a=0.05$ , and for several values of the amplitude of the wall oscillation,  $A=0.05, 0.1$  and  $0.2$ , for two values of the channel aspect ratio,  $2b=26.6$  and  $10$ .

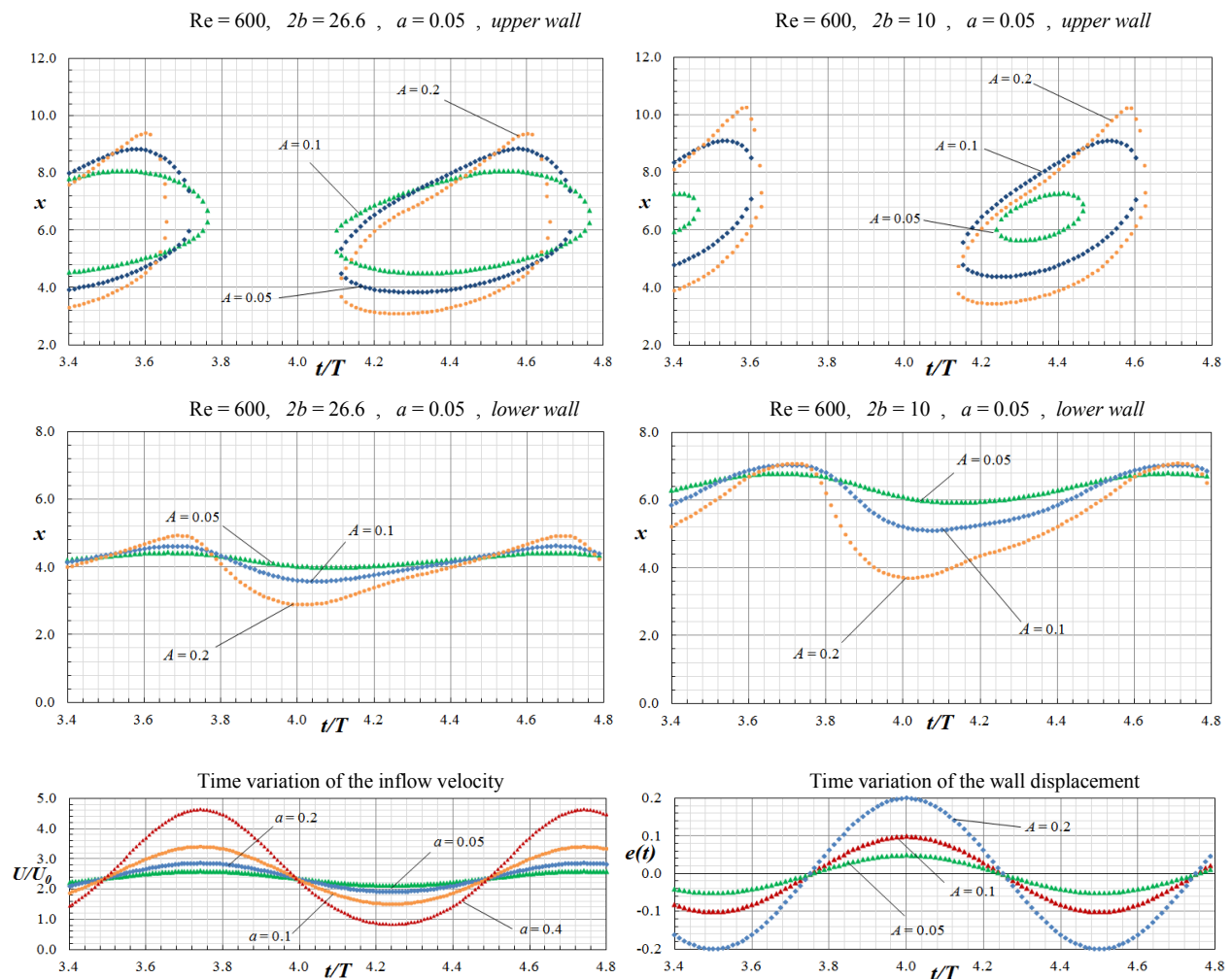


Figure 2.20 Influence of the aspect ratio,  $2b$ : Variation during the oscillatory cycle,  $t/T$ , of the upper and lower wall separation and reattachment locations, for  $Re=600$ ,  $\omega=0.05$ ,  $a=0.05$  and for  $A=0.05, 0.1$  and  $0.2$ .

It can be noticed that the presence of the upper wall separation during the oscillatory cycle is reduced for the lower aspect ratio of the channel, while the length of the lower wall separation increases and has larger oscillation amplitudes at the lower aspect ratio,  $2b = 10$ .

### 2.6.2 Influence of the wall oscillation amplitude on the unsteady flow separations

The typical influence of the wall oscillation amplitude,  $A$ , on the lower wall separation length ( $L_l$ ) and on the upper wall separation and reattachment locations ( $x_s$  and  $x_r$ ) is illustrated in Figure 2.21 for the oscillation frequency  $\omega = 0.05$  and Reynolds number  $Re = 600$ .

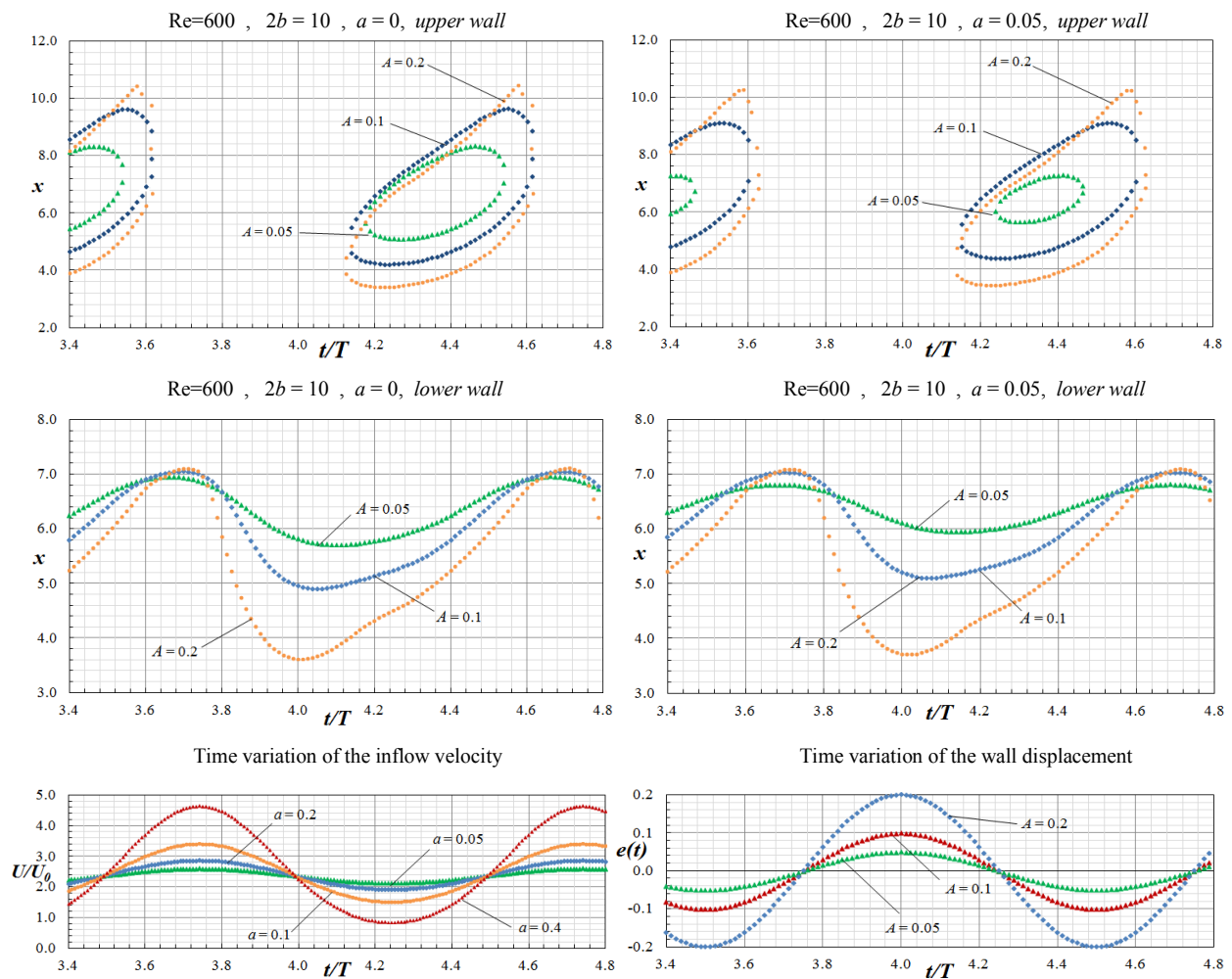


Figure 2.21 Influence of the wall oscillation amplitude,  $A$ : Variation during the oscillatory cycle,  $t/T$ , of the upper and lower wall separation and reattachment locations, for  $Re = 600$ ,  $\omega = 0.05$ ,  $a = 0.05$  and  $A = 0.05, 0.1$  and  $0.2$ .

These solutions are obtained in the plane of symmetry of the channel ( $y = 0$ ) for the aspect ratio,  $2b = 10$ , two values of the inflow velocity amplitude,  $a = 0$  (that is steady inlet flow velocity) and  $a = 0.05$ , and for several values of the amplitude of the wall oscillation,  $A = 0.05, 0.1$  and  $0.2$ .

It can be seen that the length and the time duration of the upper wall separation gets larger by increasing the wall oscillation amplitude,  $A$ , and the length of the lower wall separation has larger oscillation amplitudes at the larger wall amplitude oscillations.

### **2.6.3 Influence of the Reynolds number on the unsteady flow separations**

The typical influence of the Reynolds number on the lower wall separation length ( $L_l$ ) and on the upper wall separation and reattachment locations ( $x_s$  and  $x_r$ ) is illustrated in Figure 2.22 for the oscillation frequency  $\omega = 0.05$ , wall oscillation amplitude  $A = 0.05$  and for two values of the inflow velocity amplitude,  $a = 0$  and  $a = 0.05$ . These solutions are obtained in the plane of symmetry of the channel ( $y = 0$ ) for the aspect ratio,  $2b = 10$ , two values of the inflow velocity amplitude,  $a = 0$  (that is steady inflow velocity) and  $a = 0.05$ , and for several values of the Reynolds number,  $Re = 400, 600, 800$  and  $1000$ .

One can notice that the length and the time duration of the upper wall separation increase with the Reynolds number for both values of the inflow velocity amplitudes, and the length of the lower wall separation also increases with the Reynolds number.

It is interesting to note the formation of a secondary flow separation at the lower wall at,  $Re = 1000$  (the largest Reynolds number included in Figure 2.22), which has a duration of about one quarter of the oscillatory cycle, slightly shorter for  $a = 0.05$ .

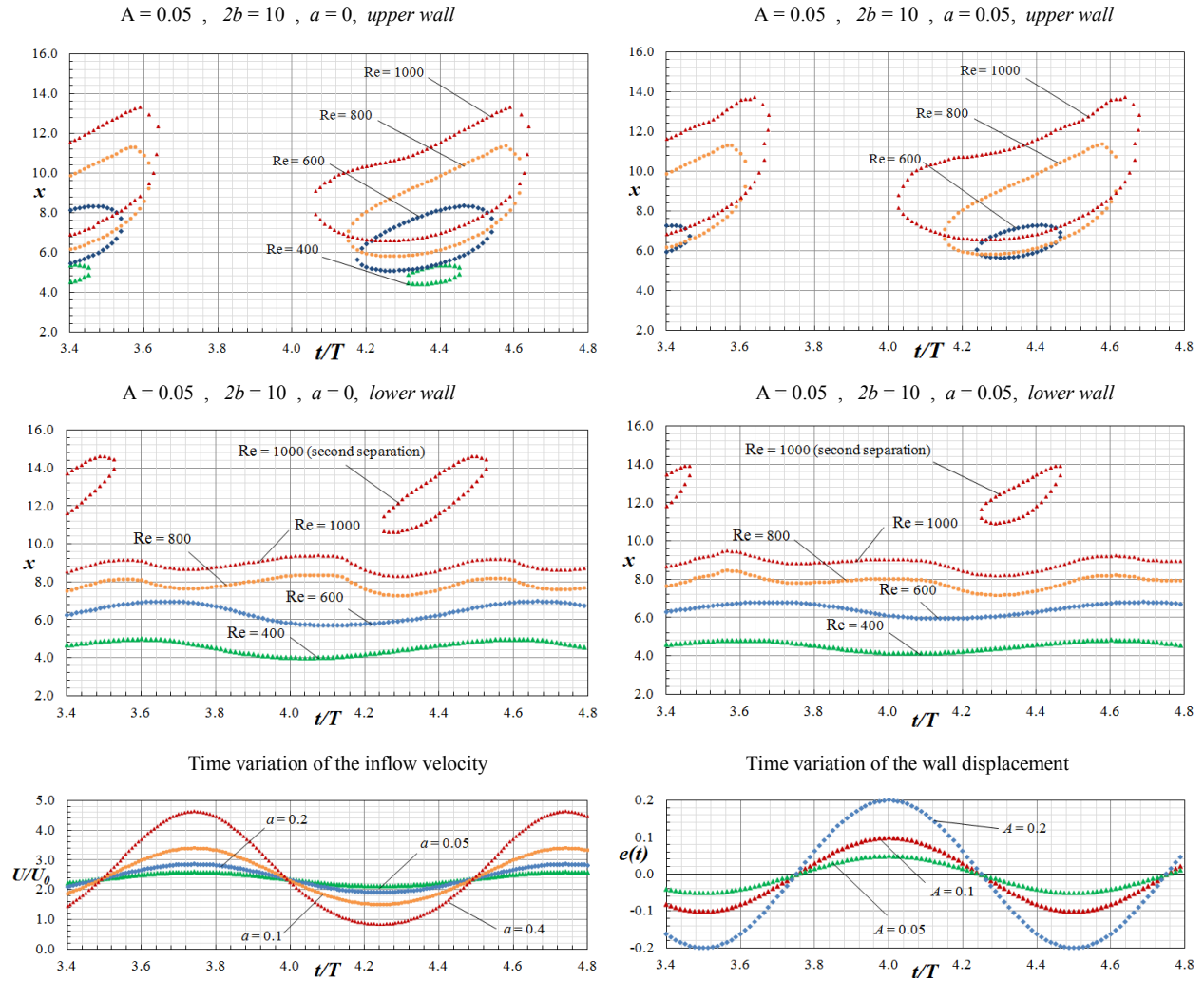


Figure 2.22 Influence of the Reynolds number: Variation during the oscillatory cycle,  $t/T$ , of the upper and lower wall separation and reattachment locations, for  $\omega = 0.05$ ,  $A = 0.05$ , and  $a = 0$  and  $0.05$ , and for  $Re = 400, 600, 800$  and  $1000$  ( $2b = 10$ ,  $y = 0$ ).

### 2.6.4 Variation of the unsteady flow separations along the span of the channel

The typical variations along the span (with  $y$ ) of the unsteady lower wall separation length ( $L_l$ ) and of the upper wall separation and reattachment locations ( $x_s$  and  $x_r$ ) is illustrated in Figures 2.23 and 2.24 for the channel aspect ratio,  $2b = 10$ , at two Reynolds numbers  $Re = 600$  and  $800$ , and for several locations along the span of the channel:  $y = 0, 0.25b, 0.5b$ , and  $0.75b$ .

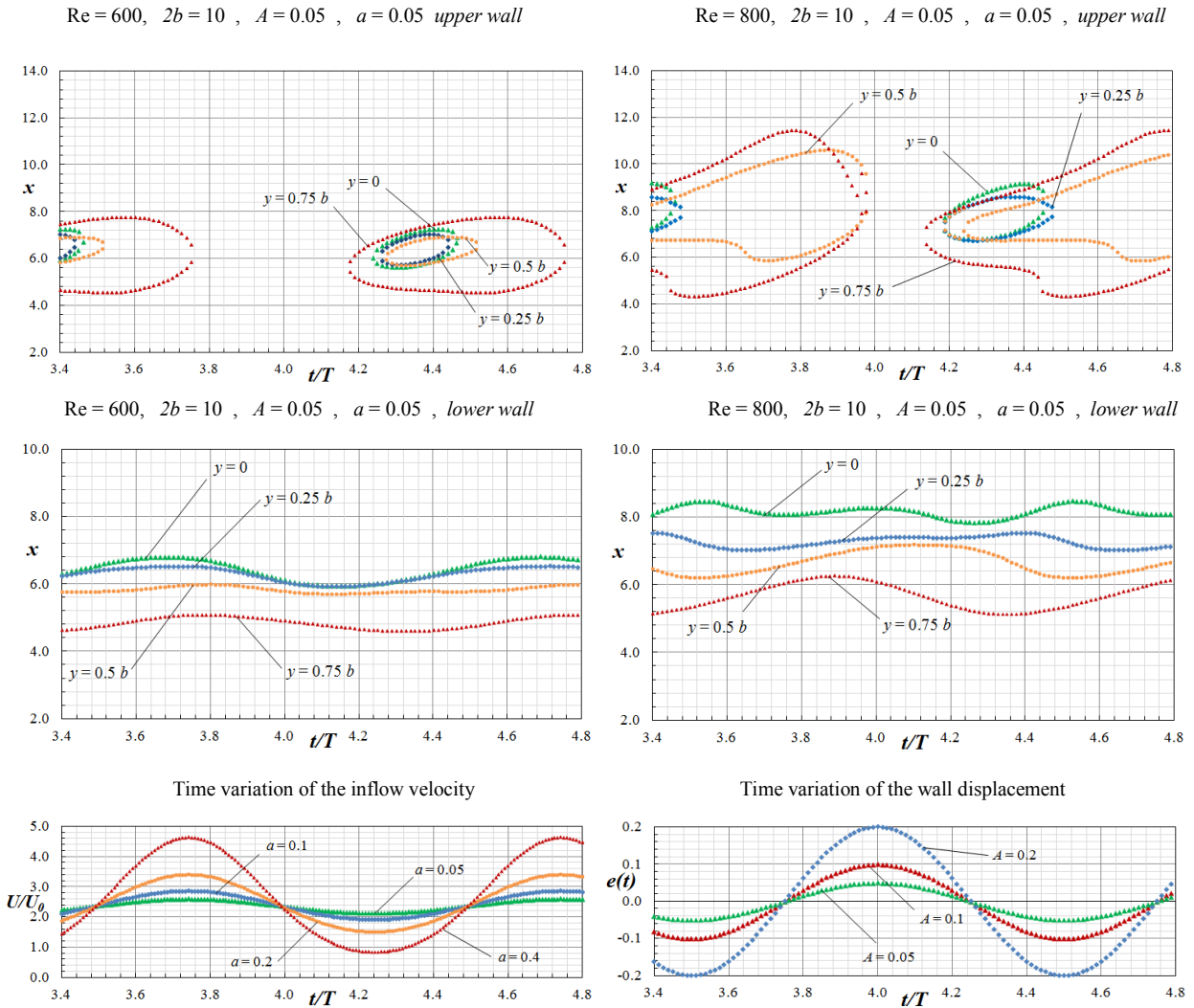


Figure 2.23 Spanwise variation of the unsteady flow separations: Variation during the oscillatory cycle,  $t/T$ , of the upper and lower wall separation and reattachment locations, for wall amplitude oscillation  $A = 0.05$ , inflow velocity amplitude,  $a = 0.05$ , and two Reynolds numbers  $Re = 600$  and  $800$ , at several locations along the span of the channel:  $y = 0$ ,  $0.25b$ ,  $0.5b$ , and  $0.75b$ . (aspect ratio  $2b = 10$  and reduced frequency of oscillations  $\omega = 0.05$ )

The spanwise variations of the unsteady flow separations is shown in Figure 2.23 for the oscillation frequency  $\omega = 0.05$ , wall amplitude oscillation  $A = 0.05$ , inflow velocity amplitude  $a = 0.05$ , and two Reynolds numbers  $Re = 600$  and  $800$ , in four longitudinal planes along the span of the channel:  $y = 0$ ,  $0.25b$ ,  $0.5b$ , and  $0.75b$ .

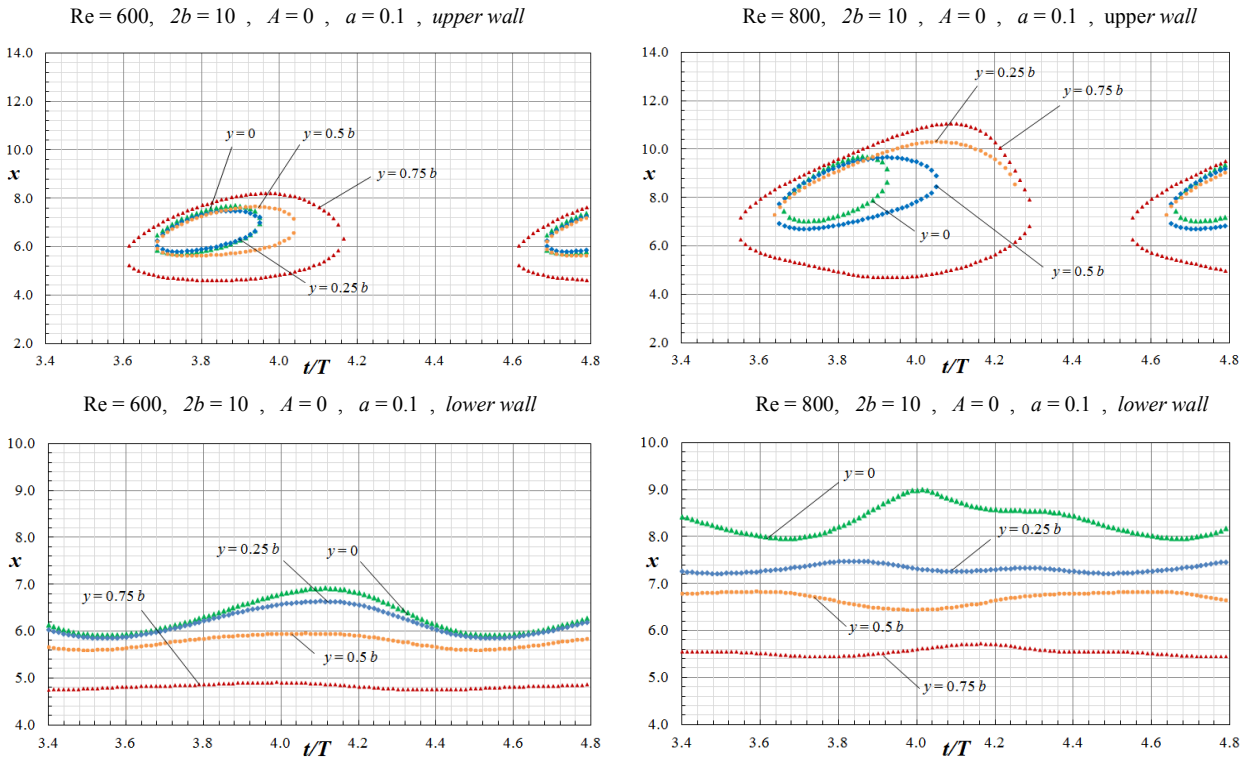


Figure 2.24 Spanwise variation of the unsteady flow separations: Variation during the oscillatory cycle,  $t/T$ , of the upper and lower wall separation and reattachment locations, for fixed walls ( $A=0$ ), inflow velocity amplitude  $a=0.1$ , and two Reynolds numbers  $Re=600$  and  $800$ , at several locations along the span of the channel:  $y=0, 0.25b, 0.5b$ , and  $0.75b$ . (aspect ratio  $2b=10$  and reduced frequency of oscillations  $\omega=0.1$ )

The spanwise variations of the unsteady flow separations is illustrated in Figure 2.24 for fixed walls ( $A=0$ ), inflow velocity amplitude  $a=0.1$ , oscillation frequency  $\omega=0.05$ , and two values of Reynolds numbers  $Re=600$  and  $800$ , at several locations along the span of the channel  $y=0, 0.25b, 0.5b$ , and  $0.75b$ .

## 2.7 Summary of findings

A novel three-dimensional method has been developed for the time-accurate solutions of the Navier-Stokes equations in the incompressible confined flows at low Reynolds numbers (between 400 and 6000). This very efficient method is second-order accurate in space and time, uses artificial compressibility and a factored Alternate-Direction Implicit scheme, and is based

on a finite difference formulation on a stretched staggered grid. This method solves for the first time the three-dimensional steady and unsteady incompressible flows at low Reynolds numbers.

Original solutions have been obtained for the steady and unsteady confined viscous flows for the benchmark case of the downstream-facing step channel at low Reynolds numbers, which are generated by the time variable inflow velocities and by the oscillating walls.

The study of these confined steady flows at low Reynolds numbers, explains and confirms that the disagreement between the two-dimensional solutions and the experimental results is due to the three-dimensional effect of the lateral walls. The obtained three-dimensional computational solutions were in good agreement with the experimental results. The multiple flow separations generated on the upper and lower walls have been thoroughly studied in function of the Reynolds number, span-to-height ratio, and the amplitude and frequency of the inflow velocity and the wall oscillations.

## Chapter 3

# Unsteady Effects on Stationary Airfoils Due to Unsteady Flow Separations at Low Reynolds Numbers

This chapter presents the unsteady flow analysis of the stationary airfoils at low Reynolds numbers, which is performed to study the unsteady effects on the aerodynamic coefficients generated by the unsteadiness of the flow separations appearing at angles of attack above 8 degrees.

The unsteady flow analysis of the stationary airfoils at low Reynolds numbers is performed with an efficient time-accurate numerical method developed by the author for the solution of the Navier-Stokes equations at low Reynolds numbers, which is second-order accurate in time and space. A second-order three-point-backward implicit scheme is used first for the real-time discretization, followed by a pseudo-time relaxation procedure using artificial compressibility and a factored Alternate-Direction Implicit (ADI) scheme for the pseudo-time integration. Then, a second-order central finite difference formulation is used on a stretched staggered grid to avoid the odd-and-even points decoupling in this numerical method. A special decoupling procedure using the continuity equation reduces the problem to the solution of scalar-tridiagonal systems of equations, which enhances substantially the computational efficiency of the method.

The numerical method is validated by comparison with experimental results obtained by Suwa *et al.* [47, 48]. Solutions are obtained for the unsteady lift and drag coefficients of a triangular airfoil and several symmetric and cambered airfoils. The flow separation is also studied with the aid of flow visualizations illustrating the changes in the flow pattern at various moments in time. The influence of various geometric and flow parameters, such as the angle of attack, relative thickness and camber, and Reynolds number on the unsteady aerodynamic coefficients and the flow separation is also studied in this chapter.

### 3.1 Problem formulation and numerical method

Consider a cambered airfoil of chord  $c$  placed at an incidence  $\alpha$  in a uniform stream of velocity  $U_\infty$ , as shown in Figure 3.1. The airfoil is referred to a Cartesian reference system of coordinates  $cx$  and  $cy$ , where  $x$  and  $y$  are nondimensional coordinates (with respect to the

chord  $c$ ), with the  $x$ -axis along the airfoil chord and its origin at the airfoil leading edge. The airfoil upper and lower surfaces are defined by the equations

$$y = e_1(x) = h(x) + e(x), \quad \text{and} \quad y = -e_2(x) = h(x) - e(x), \quad (3.1)$$

where the subscripts 1 and 2 refer to the upper and lower surfaces, and where  $h(x)$  and  $e(x)$  define, respectively, the camberline and the airfoil thickness variation along the airfoil chord. The special case of symmetric airfoils is characterized by  $e_1(x) = e_2(x) = e(x)$  and  $h(x) = 0$ .

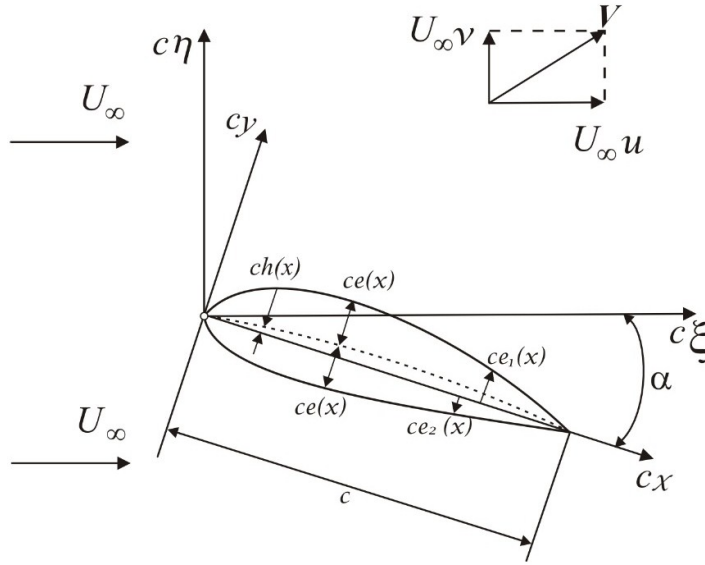


Figure 3.1 Geometry of an airfoil placed in a uniform flow at the angle of attack  $\alpha$ .

The viscous fluid flow past the oscillating airfoil is referred to a fixed Cartesian reference system of coordinates  $c\xi$  and  $c\eta$  defined by the equations

$$\xi = x \cos \alpha + y \sin \alpha, \quad \eta = -\sin \alpha + y \cos \alpha, \quad (3.2)$$

where  $\xi$  and  $\eta$  are nondimensional coordinates with respect to the airfoil chord  $c$ , with the  $\xi$ -axis parallel to the uniform stream velocity  $U_\infty$ , which is inclined with the angle  $\alpha$  with respect to the airfoil chord as shown in Figure 3.1.

Velocity components along the fixed  $\xi$ - and  $\eta$ -axes are defined as  $U_\infty u$  and  $U_\infty v$ , where  $u$  and  $v$  are the nondimensional velocity components with respect to  $U_\infty$ .

### 3.1.1 Navier-Stokes equations for unsteady viscous flows

The time-dependent Navier-Stokes and continuity equations for the incompressible flow past the airfoil can be expressed in nondimensional conservation form as

$$\frac{\partial \mathbf{V}}{\partial t} + \mathbf{Q}(\mathbf{V}, p) = \mathbf{0} \ , \quad \nabla \cdot \mathbf{V} = \frac{\partial u}{\partial \xi} + \frac{\partial v}{\partial \eta} = 0 \ , \quad (3.3)$$

where  $t = t^* U_\infty / c$  is the nondimensional time ( $t^*$  is the dimensional time),  $\mathbf{V} = \{u, v\}^T$  represents the vector of the dimensionless velocity components and  $\mathbf{Q}(\mathbf{V}, p)$ , which includes the convective derivative, pressure and viscous terms, can be expressed in two-dimensional Cartesian coordinates in the form

$$\mathbf{Q}(\mathbf{V}, p) = \{Q_u(u, v, p), Q_v(u, v, p)\}^T \ , \quad (3.4)$$

$$Q_u(u, v, p) = \frac{\partial(uu)}{\partial \xi} + \frac{\partial(vu)}{\partial \eta} + \frac{\partial p}{\partial \xi} - \frac{1}{\text{Re}} \left( \frac{\partial^2 u}{\partial \xi^2} + \frac{\partial^2 u}{\partial \eta^2} \right) \ , \quad (3.5a)$$

$$Q_v(u, v, p) = \frac{\partial(uv)}{\partial \xi} + \frac{\partial(vv)}{\partial \eta} + \frac{\partial p}{\partial \eta} - \frac{1}{\text{Re}} \left( \frac{\partial^2 v}{\partial \xi^2} + \frac{\partial^2 v}{\partial \eta^2} \right) \ , \quad (3.5b)$$

where  $p$  is the dimensionless pressure, nondimensionalized with respect to  $\rho U_\infty^2$ , and  $\text{Re} = c U_\infty / \nu$  is the Reynolds number based on the chord length ( $\rho$  and  $\nu$  are the fluid density and kinematic viscosity). In the present computational analysis we focus our attention on flows at low Reynolds numbers, in which the viscous effects play very important role.

### 3.1.2 Boundary conditions

No-slip boundary conditions are implemented on the airfoil contour and non-penetration condition (normal velocity component equals to zero,  $v = 0$ ) are applied on the upper and lower boundaries of the computational domain.

Also, the viscous boundary conditions are imposed on the airfoil upper and lower surfaces which are transformed in the computational domain to a solid wall, in which  $u = 0$  and  $v = 0$ . The upper and lower far-field boundaries can be imposed as those of the uniform stream ( $u = 1$ ).

## 3.2 Method of solution for unsteady viscous flows past stationary airfoils

The time-accurate method that is devolved in this section starts with the time-dependent transformation of the physical domain to the fixed computational domain. This transformation is applied to Navier-Stokes equations, and it is followed by the real-time discretization of the Navier-Stokes equations. A detailed description of the pseudo-time relaxation technique applied to Navier-Stokes equations is also presented. After that, the ADI scheme and the special decoupling procedure are implemented and finally the spatial discretization on stretched staggered grids is carried out.

### 3.2.1 Time-dependent coordinate transformation

The problem is solved in a fixed rectangular computational domain with six sub-domains, which is obtained from a rectangular physical domain indicated in Figure 3.2 by a geometrical transformation defined as

$$X = g(\xi, \eta), \quad Y = f(\xi, \eta) \quad , \quad (3.6)$$

where  $g(\xi, \eta)$  and  $f(\xi, \eta)$  are defined for each domain in the following forms:

**Domain 1** (for  $x < 0$  and  $0 < \eta < H_1$ ):

$$g(\xi, \eta) = \frac{\xi \cos \alpha - \eta \sin \alpha}{L_0 \cos \alpha + \eta \sin \alpha} L_0, \quad f(\xi, \eta) = \eta \quad (3.7a)$$

**Domain 2** (for  $x < 0$  and  $-H_2 < \eta < 0$ ):

$$g(\xi, \eta) = \frac{\xi \cos \alpha - \eta \sin \alpha}{L_0 \cos \alpha + \eta \sin \alpha} L_0, \quad f(\xi, \eta) = \eta \quad (3.7b)$$

**Domain 3** (for  $0 < x < 1$  and  $e_1(x) < y < H_1$ ):

$$g(\xi, \eta) = \xi \cos \alpha - \eta \sin \alpha, \quad f(\xi, \eta) = \frac{y - e_1(x)}{H_1 - e_1(x) \cos \alpha + x \sin \alpha} H_1 \cos \alpha \quad (3.7c)$$

**Domain 4** (for  $0 < x < 1$  and  $-H_2 < y < -e_2(x)$ ):

$$g(\xi, \eta) = \xi \cos \alpha - \eta \sin \alpha, \quad f(\xi, \eta) = \frac{y + e_2(x)}{H_2 - e_2(x) \cos \alpha - x \sin \alpha} H_2 \cos \alpha \quad (3.7d)$$

**Domain 5** (for  $x > 1$  and  $-\sin \alpha < \eta < H_1$ ):

$$g(\xi, \eta) = \frac{\xi \cos \alpha - \eta \sin \alpha - 1}{L_1 \cos \alpha - \eta \sin \alpha - 1} (L_1 - 1) + 1, \quad f(\xi, \eta) = \frac{\eta + \sin \alpha}{H_1 + \sin \alpha} H_1 \quad (3.7e)$$

**Domain 6** (for  $x > 1$  and  $-H_2 < \eta < -\sin \alpha$ ):

$$g(\xi, \eta) = \frac{\xi \cos \alpha - \eta \sin \alpha - 1}{L_1 \cos \alpha - \eta \sin \alpha - 1} (L_1 - 1) + 1, \quad f(\xi, \eta) = \frac{\eta + \sin \alpha}{H_2 - \sin \alpha} H_2 \quad (3.7f)$$

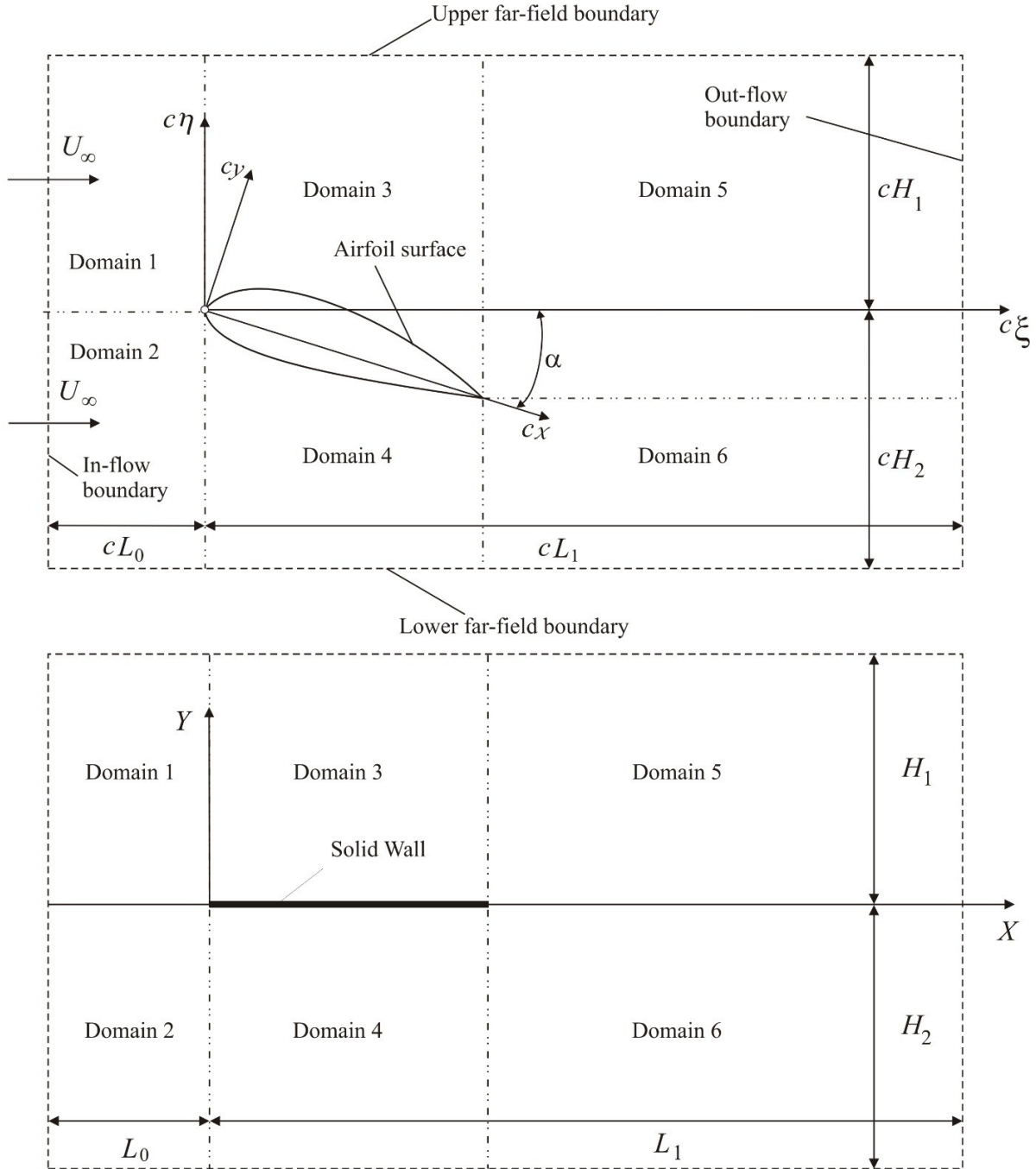


Figure 3.2 Geometry of the physical domain (top), and computational domain (bottom)  $(X, Y)$  defined by coordinate transformations (3.6) to (3.7).

In equations (3.7c) and (3.7d),  $x$  and  $y$  are defined in function of the coordinates  $\xi$  and  $\eta$  by the relations

$$x = \xi \cos \alpha - \eta \sin \alpha, \quad y = \xi \sin \alpha + \eta \cos \alpha \quad (3.8)$$

In equations (3.7a) to (3.7f),  $\eta = H_1$  and  $\eta = -H_2$  are the nondimensional physical coordinates of the upper and lower far-field boundaries of the computational domain (which are considered equal in the specific numerical applications presented further,  $H_1 = H_2 = H$ ), while  $\xi = -L_0$  and  $\xi = L_1$  are the nondimensional physical coordinates of the inflow and outflow boundaries, as shown in Figure 3.2.

In the computational domain  $(X, Y)$ , the upstream inflow and downstream outflow boundaries and the upper and lower boundaries are defined by the same nondimensional coordinates  $X = -L_0$ ,  $X = L_1$  and  $Y = H_1$ ,  $Y = -H_2$ , respectively. The Navier-Stokes and continuity equations can be expressed in the computational domain, as

$$\frac{\partial \mathbf{V}}{\partial t} + \mathbf{G}(\mathbf{V}, p) = 0, \quad D\mathbf{V} = 0, \quad (3.9)$$

where

$$\mathbf{V} = \{u, v\}^T, \quad \mathbf{G}(\mathbf{V}, p) = \{G_u(u, v, p), G_v(u, v, p)\}^T, \quad (3.10)$$

$$G_u(u, v, p) = C_7 \frac{\partial(uuu)}{\partial X} + C_2 \frac{\partial(uuu)}{\partial Y} + C_4 \frac{\partial(vuu)}{\partial X} + C_3 \frac{\partial(vuu)}{\partial Y} + C_7 \frac{\partial p}{\partial X} + C_2 \frac{\partial p}{\partial Y} + C_1 \frac{\partial^2 u}{\partial X^2} + C_6 \frac{\partial^2 u}{\partial X \partial Y} + C_5 \frac{\partial^2 u}{\partial Y^2}, \quad (3.11)$$

$$G_v(u, v, p) = C_7 \frac{\partial(vuu)}{\partial X} + C_2 \frac{\partial(vuu)}{\partial Y} + C_4 \frac{\partial(vv)}{\partial X} + C_3 \frac{\partial(vv)}{\partial Y} + C_4 \frac{\partial p}{\partial X} + C_3 \frac{\partial p}{\partial Y} + C_1 \frac{\partial^2 v}{\partial X^2} + C_6 \frac{\partial^2 v}{\partial X \partial Y} + C_5 \frac{\partial^2 v}{\partial Y^2}, \quad (3.12)$$

$$D\mathbf{V} = C_7 \frac{\partial u}{\partial X} + C_2 \frac{\partial u}{\partial Y} + C_4 \frac{\partial v}{\partial X} + C_3 \frac{\partial v}{\partial Y}, \quad (3.13)$$

in which the expressions of the coefficients  $C_1, C_2, C_3, \dots, C_7$  are obtained for each domain from the coordinate transformations (3.6) to (3.7), the details are explained in Appendix B.

### 3.2.2 Real-time discretization

In order to study the unsteady effects in the flow past stationary airfoils at low Reynolds numbers, the Navier-Stokes equations is first discretized in real time based on a second-order three-point-backward implicit scheme:

$$\left( \frac{\partial \mathbf{V}}{\partial t} \right)^{n+1} = \frac{3\mathbf{V}^{n+1} - 4\mathbf{V}^n + \mathbf{V}^{n-1}}{2\Delta t} \quad , \quad (3.14)$$

where the superscripts  $n-1$ ,  $n$  and  $n+1$  indicate three consecutive real time levels, and  $\Delta t = t^{n+1} - t^n = t^n - t^{n-1}$  represents the real time step. Thus, equations (3.14) can be expressed at the time level  $t^{n+1}$  in the form

$$\mathbf{V}^{n+1} + \alpha \mathbf{G}^{n+1} = \mathbf{F}^n \quad , \quad D\mathbf{V}^{n+1} = 0 \quad , \quad (3.15)$$

where  $\alpha = 2\Delta t/3$ ,  $\mathbf{G}^{n+1} = \mathbf{G}(\mathbf{V}^{n+1}, p^{n+1})$  and  $\mathbf{F}^n = (4\mathbf{V}^n - \mathbf{V}^{n-1})/3$ .

### 3.2.3 Pseudo-time iterative relaxation technique

An iterative pseudo-time relaxation procedure with artificial compressibility is then used in order to advance the solution of the semi-discretized equations from the real time level  $t^n$  to  $t^{n+1}$  in the form

$$\frac{\partial \check{\mathbf{V}}}{\partial \tau} + \check{\mathbf{V}} + \alpha \check{\mathbf{G}}(\check{\mathbf{V}}, \check{p}) = \mathbf{F}^n \quad , \quad \delta \frac{\partial \check{p}}{\partial \tau} + D\check{\mathbf{V}} = 0 \quad (3.16)$$

where  $\check{\mathbf{V}}(\tau)$  and  $\check{p}(\tau)$  denote the pseudo-functions corresponding to the variable velocity and pressure at pseudo-time  $\tau$ , between the real time levels  $t^n$  and  $t^{n+1}$ , and  $\delta$  represents an artificially-added compressibility.

Pseudo Navier-Stokes and continuity equations (3.16) are solved in pseudo-time. An implicit Euler scheme is used in this respect to discretize these equations in pseudo-time, and the resulting equations are expressed as

$$\frac{\check{\mathbf{V}}^{\nu+1} - \check{\mathbf{V}}^\nu}{\Delta \tau} + \check{\mathbf{V}}^{\nu+1} + \alpha \check{\mathbf{G}}^{\nu+1} = \mathbf{F}^n \quad , \quad (3.17)$$

$$\frac{\check{p}^{\nu+1} - \check{p}^\nu}{\Delta \tau} + \frac{1}{\delta} \nabla \bullet \check{\mathbf{V}}^{\nu+1} = 0 \quad , \quad (3.18)$$

where  $\Delta\tau$  is the pseudo-time step and the superscript  $\nu$  indicates the solution at pseudo-time level  $\tau^\nu = \nu\Delta\tau$  and  $\tilde{\mathbf{G}}^{\nu+1} = \mathbf{G}(\tilde{\mathbf{V}}^{\nu+1}, \tilde{p}^{\nu+1})$ . To facilitate the pseudo-time iterative process, the implicit nonlinear system of equations shown in (3.17) and (3.18) are linearized.

$$(1 + \Delta\tau)\Delta\tilde{\mathbf{V}}^\nu + \delta\Delta\tilde{\mathbf{G}}^\nu(\tilde{\mathbf{V}}^\nu, \tilde{p}^\nu) = \Delta\tau(\mathbf{F}^n - \tilde{\mathbf{V}}^\nu - \alpha\tilde{\mathbf{G}}^\nu(\tilde{\mathbf{V}}^\nu, \tilde{p}^\nu)), \quad (3.19)$$

$$\Delta\tilde{p}^\nu + \frac{\Delta\tau}{\delta}\nabla \cdot (\Delta\tilde{\mathbf{V}}^\nu) = -\frac{\Delta\tau}{\delta}\nabla \cdot \tilde{\mathbf{V}}^\nu \quad (3.20)$$

### 3.2.4 Alternating-direction implicit scheme

The ADI scheme is applied to reduce the effort to solve the linearized equations (3.19) and (3.20). Then, an implicit Euler scheme is used to discretize equations (3.16) between the pseudo-time levels  $\tau^\nu$  and  $\tau^{\nu+1} = \tau^\nu + \Delta\tau$ , and the resulting equations are expressed in terms of the pseudo-time variations  $\Delta\tilde{u} = \tilde{u}^{\nu+1} - \tilde{u}^\nu$ ,  $\Delta\tilde{v} = \tilde{v}^{\nu+1} - \tilde{v}^\nu$ ,  $\Delta\tilde{p} = \tilde{p}^{\nu+1} - \tilde{p}^\nu$ .

Writing equations (3.19) and (3.20) in a global matrix form

$$[\mathbf{I} + \alpha\Delta\tau(\mathbf{D}_X + \mathbf{D}_Y)]\Delta\mathbf{f} = \Delta\tau\mathbf{S}, \quad (3.21)$$

where  $\Delta\mathbf{f} = [\Delta u, \Delta v, \Delta p]^\top$ ,  $\alpha = 2\Delta t/3$ ,  $\mathbf{I}$  is the identity matrix, and

$$\mathbf{D}_X = \begin{bmatrix} M + \frac{1}{\alpha} & 0 & C_7 \frac{\partial}{\partial X} \\ 0 & M & C_4 \frac{\partial}{\partial X} \\ \frac{C_7}{\alpha\delta} \frac{\partial}{\partial X} & \frac{C_4}{\alpha\delta} \frac{\partial}{\partial X} & 0 \end{bmatrix}, \quad \mathbf{D}_Y = \begin{bmatrix} N & 0 & C_2 \frac{\partial}{\partial Y} \\ 0 & N + \frac{1}{\alpha} & C_3 \frac{\partial}{\partial Y} \\ \frac{C_2}{\alpha\delta} \frac{\partial}{\partial Y} & \frac{C_3}{\alpha\delta} \frac{\partial}{\partial Y} & 0 \end{bmatrix}, \quad (3.22)$$

$$\mathbf{S} = \begin{bmatrix} F_u^n - \tilde{u}^\nu - \alpha G_u^\nu \\ F_v^n - \tilde{v}^\nu - \alpha G_v^\nu \\ -(1/\delta) D\tilde{\mathbf{V}}^\nu \end{bmatrix},$$

in which the differential operators  $M$  and  $N$  are defined as

$$M = C_7 \frac{\partial(\tilde{u}^\nu \phi)}{\partial X} + C_4 \frac{\partial(\tilde{v}^\nu \phi)}{\partial X} + C_1 \frac{\partial^2 \phi}{\partial X^2}, \quad (3.23)$$

$$N = C_2 \frac{\partial(\tilde{u}^\nu \phi)}{\partial Y} + C_3 \frac{\partial(\tilde{v}^\nu \phi)}{\partial Y} + C_6 \frac{\partial^2 \phi}{\partial Y \partial X} + C_5 \frac{\partial^2 \phi}{\partial Y^2}, \quad (3.24)$$

where  $\phi$  can be  $\Delta u$ ,  $\Delta v$  or  $\Delta p$ .

The optimal value of the artificial compressibility,  $\delta$ , and the size of the pseudo-time step,  $\Delta\tau$ , are determined, as indicated in our previous studies by Mateescu *et al.* [11, 14, 16], the values for  $\delta$  and  $\Delta\tau$  are eventually optimized by numerical experimentation.

A factored ADI scheme is used to separate equation (3.21) into two successive sweeps in the  $Y$  and  $X$  directions, defined by the equations (3.25) and (3.26). It is important to mention that the approximate factorization, which implies the elimination of the quadratic term  $\alpha^2 \Delta\tau^2 \mathbf{D}_X \mathbf{D}_Y$ , produces some convergence issues for the ADI scheme. This situation can be noticed when  $\Delta\tau$  takes large values, however, the convergence issues can be neglected when  $\Delta\tau$  is sufficiently small.

The ADI method requires the introduction of an intermediate variable  $\Delta\mathbf{f}^*$  to solve the linear implicit system of equations. This variable has the components of  $\Delta u^*$ ,  $\Delta v^*$  and  $\Delta p^*$ , which are calculated in the  $Y$ -sweep

$$[\mathbf{I} + \alpha \Delta\tau \mathbf{D}_Y] \Delta\mathbf{f}^* = \Delta\tau \mathbf{S} \quad (3.25)$$

Next, in the  $X$ -sweep the values of  $\Delta\mathbf{f} = [\Delta u, \Delta v, \Delta p]^T$  are computed

$$[\mathbf{I} + \alpha \Delta\tau \mathbf{D}_X] \Delta\mathbf{f} = \Delta\mathbf{f}^* \quad (3.26)$$

These equations are further spatially discretized by central differencing on a stretched staggered grid, in which the flow variables  $u$ ,  $v$  and  $p$  are defined at different positions, as shown in Figure 3.3. By using a staggered grid, this method avoids the odd-and-even point decoupling while preserving the second-order accuracy in space of the method. The grid stretching is defined by hyperbolic sine functions in  $X$  and  $Y$  directions.

A special decoupling procedure [9, 10, 11], based on the utilization of the continuity equation, is used for each sweep to eliminate the pressure from the momentum equations. The following relations, which are derived from the continuity equation expressed for each sweep, are used to eliminate the pseudo-time variations of the pressure from the systems of equations for the pseudo-time variations of the velocity components in each sweep.

$$\Delta p^* = -\frac{\Delta\tau}{\delta} \left[ D\tilde{\mathbf{V}}^v + C_2 \frac{\partial(\Delta u^*)}{\partial Y} + C_3 \frac{\partial(\Delta v^*)}{\partial Y} \right], \quad \Delta p = \Delta p^* - \frac{\Delta\tau}{\delta} \frac{\partial(\Delta u)}{\partial X} \quad (3.27)$$

In this manner, the problem is reduced to the solution of two sets of decoupled scalar-tridiagonal systems of equations, for each sweep. As a result, this method is characterized by excellent computational efficiency and accuracy.

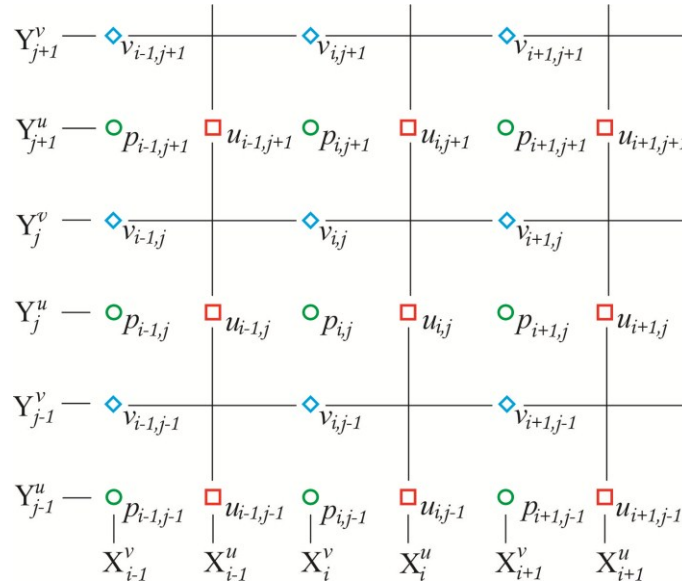


Figure 3.3 Staggered grid two-dimensional geometry.

### 3.2.5 Lift and drag coefficients at low Reynolds numbers

The aerodynamic lift and drag forces are entirely due to pressure and shear stress distribution over a body surface. The pressure  $p$  can be obtained by solving the Navier-Stokes equations, acts normal and the shear stress  $\tau$  acts tangential to the airfoil surface.

To calculate the lift and drag coefficients, consider an airfoil of chord  $c = 1$ , placed at incidence  $\alpha$  in a uniform flow of velocity  $U_\infty$  as depicted in Figure 3.4.

The resultant aerodynamic force  $R$ , is the net product of  $p$  and  $\tau$  distributions integrated over the complete airfoil. The aerodynamic lift  $L$  per units span is the component of  $R$  perpendicular to  $U_\infty$  and the drag force  $D$  is parallel to it. The normal force  $N$  is defined as the component of  $R$  perpendicular to the chord of the airfoil and the chordwise force  $A$  is parallel to it.

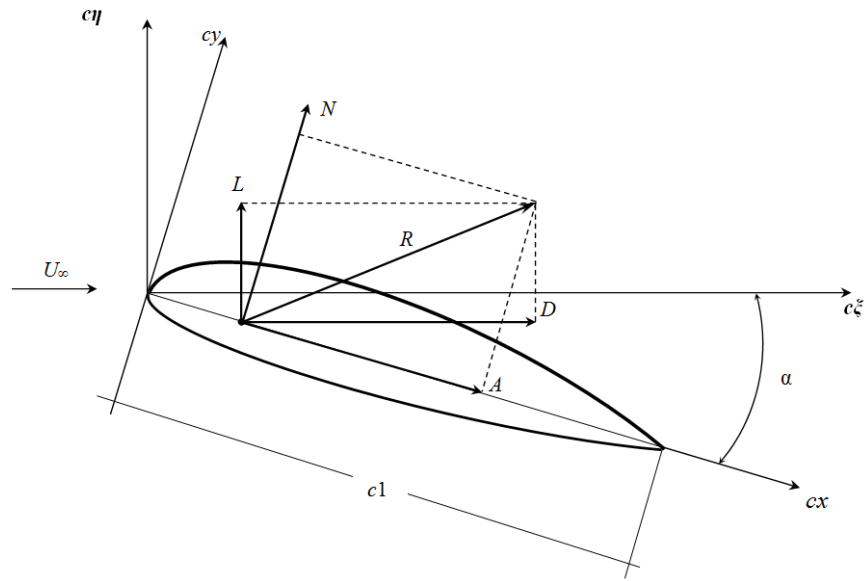


Figure 3.4 Components of the resultant aerodynamics forces over the airfoil surface.

From Figure 3.4, one obtains

$$L = N \cos \alpha - A \sin \alpha \quad (3.28)$$

$$D = N \sin \alpha + A \cos \alpha \quad (3.29)$$

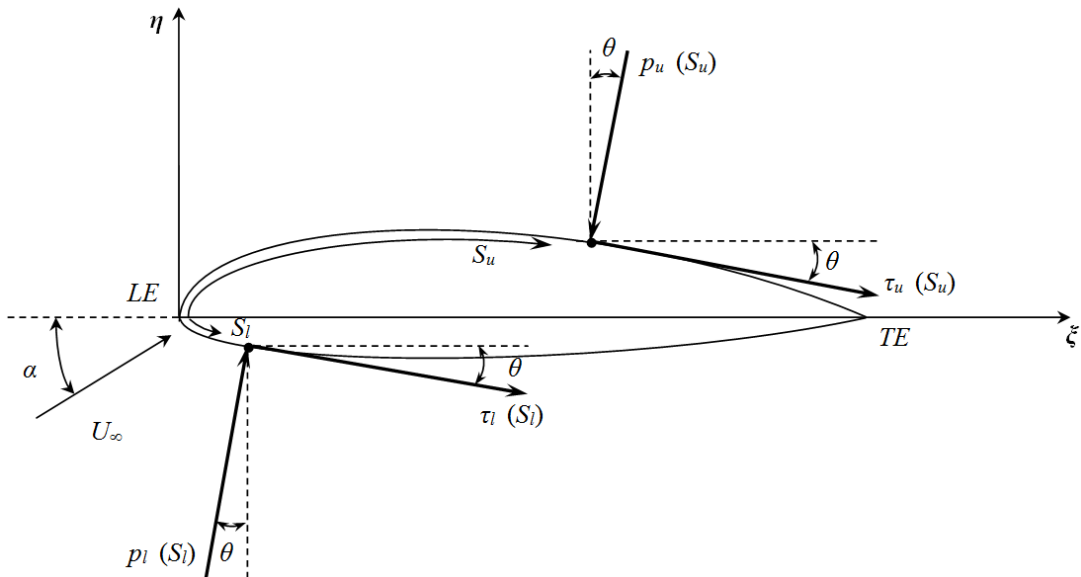


Figure 3.5 Integration of the pressure and shear stress distributions over an airfoil.

The pressure and shear stress on the upper surface of the airfoil are denoted by  $p_u$  and  $\tau_u$ , and for the lower surface by  $p_l$  and  $\tau_l$ , as shown in Figure 3.5. At a given point, the pressure is normal to the surface and is oriented at an angle  $\theta$  relative to the vertical axis; and shear stress is tangential to the surface and is oriented at the same angle relative to the horizontal axis. In Figure 3.5, the sign convention is positive when measured clockwise.

Consider an elemental surface unit area on the airfoil  $dS = ds \cdot 1$ , (from the leading edge (LE) to the trailing edge (TE)), one obtains the normal force  $N$ , and tangential force  $A$ , per unit span

$$N = -\int_{LE}^{TE} (p_u \cos \theta + \tau_u \sin \theta) ds_u + \int_{LE}^{TE} (p_l \cos \theta - \tau_l \sin \theta) ds_l \quad (3.30)$$

$$A = \int_{LE}^{TE} (-p_u \sin \theta + \tau_u \cos \theta) ds_u + \int_{LE}^{TE} (p_l \sin \theta - \tau_l \cos \theta) ds_l \quad (3.31)$$

The normal and tangential coefficients are then expressed in terms of pressure coefficient  $C_p$ , and skin friction coefficient  $C_f$ , by noting the following

$$dx = ds \cos \theta \quad (3.32)$$

$$dy = -(ds \sin \theta) \quad (3.33)$$

Replacing equations (3.32) and (3.33) into equations (3.30) and (3.31), the forces coefficients are obtained as follows

$$C_N = -\int_0^1 (C_{pl} - C_{pu}) dx + \int_0^1 \left( C_{fu} \frac{dy_u}{dx} + C_{fl} \frac{dy_l}{dx} \right) dx \quad (3.34)$$

$$C_A = \int_0^1 \left( C_{pu} \frac{dy_u}{dx} + C_{pl} \frac{dy_l}{dx} \right) dx + \int_0^1 (C_{fu} - C_{fl}) dx \quad (3.35)$$

with

$$C_N = \frac{N}{c \frac{1}{2} \rho_\infty U_\infty^2}, \quad C_A = \frac{A}{c \frac{1}{2} \rho_\infty U_\infty^2} \quad (3.36)$$

where  $C_p = 2(p - p_\infty)$  is the nondimensional pressure coefficient ( $p$  is nondimensionalized respect to  $\rho_\infty U_\infty^2$ ) and  $C_f = \tau / \left( \frac{1}{2} \rho_\infty U_\infty^2 \right)$  is the skin friction coefficient, while  $dy/dx$  is the slope of the surface.

The lift and drag coefficients in two-dimensional form can be expressed as

$$C_L = C_N \cos \alpha - C_A \sin \alpha , \quad (3.37)$$

$$C_D = C_N \sin \alpha + C_A \cos \alpha , \quad (3.38)$$

with  $C_L = L / \left( \frac{1}{2} \rho_\infty U_\infty^2 \right)$  and  $C_D = D / \left( \frac{1}{2} \rho_\infty U_\infty^2 \right)$ .

### 3.3 Method validation

The numerical method has been successfully validated by comparison with experimental results available for steady flows past a triangular airfoil at low Reynolds numbers (there are no published experimental results for unsteady flows).

#### 3.3.1 Comparison with experimental results

The numerical method presented in section 3.1 is validated for steady flows by comparison with the experimental results obtained by Suwa *et al.* [47, 48] for a triangular airfoil at low Reynolds numbers. The tested triangular airfoil, with a flat bottom, is defined by the following equations of the upper and lower surfaces

$$y = e_1(x) = \begin{cases} \varepsilon x/s & \text{for } 0 < x < s \\ \varepsilon(1-x)/(1-s) & \text{for } s < x < 1 \end{cases} , \quad \text{and} \quad y = -e_2(x) = 0 , \quad (3.39)$$

where  $\varepsilon = 0.05$  and  $s = 0.30$ .

The experimental results are obtained for the lift and drag coefficients of this triangular airfoil at Reynolds number  $Re = 3000$  and Mach number  $M = 0.15$ . These results are obtained by static measurements, and for this reason they can be compared with the time-averaged solutions obtained with the present numerical method.

The time-averaged values of the present solutions for the lift and drag coefficients,  $C_L$  and  $C_D$ , of the triangular airfoil at  $Re = 3000$  are compared in Figure 3.6 with the experimental results presented in [47, 48]. The maximum and minimum values of these coefficients are also shown in Figure 3.6.

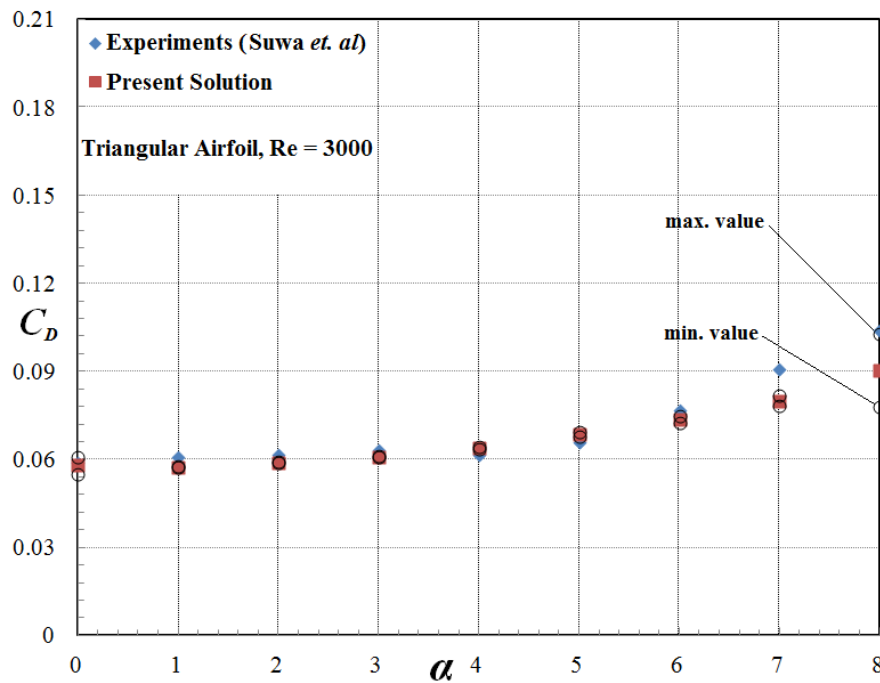
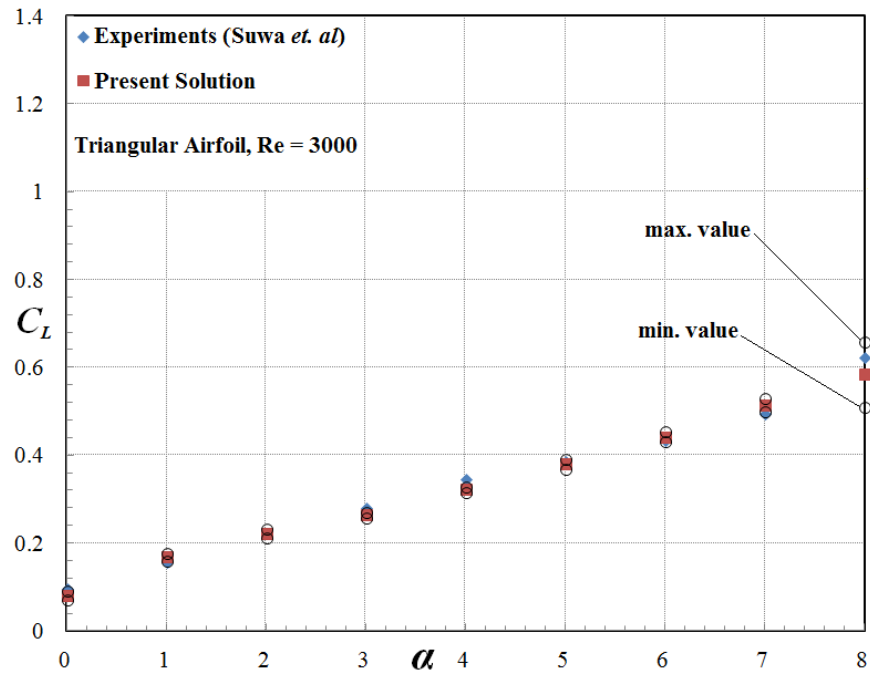


Figure 3.6 The variation with the angle of attack  $\alpha$  of the time-averaged values of the lift and drag coefficients,  $C_L$  and  $C_D$ , of the triangular airfoil for  $Re = 3000$ . Comparison between: ■ Present time-averaged solutions; ● Experimental steady results Suwa [47, 48]; ○ Maximum and minimum values of the current solution.

Good agreement can be noticed between the present time-averaged solutions of the lift and drag coefficients and the experimental results, with some differences at  $\alpha = 7^\circ$  and  $8^\circ$  for which the unsteady effects become stronger in the present numerical solution. In other words, when the angle of attack increases, the numerical solution becomes unsteady and cannot be compared with experimental steady results.

### 3.3.2 Grid sensitivity analysis

The sensitivity of the numerical solution with the mesh refinement procedure has been performed for the steady flow past a NACA 0002 airfoil for Reynolds number  $Re = 1000$  at incidence  $\alpha_0 = 4^\circ$ . It should be noticed the lift, and drag coefficients used as a criteria for this comparison. The results for the grid sensitivity test are gathered in Table 3.1. One can notice that the solution obtained by using  $260 \times 101$  grid points for each variable (or  $520 \times 202$  grid points for staggered grid in total) is very close to the fully converged solution, which is obtained by  $310 \times 131$  grid points for each variable, and beyond this the numerical solution is not influenced by grid refinement. All the solutions presented in this study were obtained using  $620 \times 262$  total grid points ( $310 \times 131$  grid points for each variable).

Grid points for each variable	$C_L$	$C_D$
130 x 41	0.3255	0.1001
180 x 61	0.3286	0.1016
220 x 81	0.3355	0.1021
260 x 101	0.3376	0.1031
310 x 131	0.3382	0.1033
420 x 151	0.3382	0.1033

Table 3.1 Grid sensitivity of the numerical solution for NACA 0002 airfoil in steady flow for Reynolds number  $Re = 1000$  and incidence  $\alpha_0 = 4^\circ$ .

### 3.3.3 Time-step convergence study

For the unsteady flow past an oscillatory airfoil case, the real-time step is defined as  $\Delta t = 2\pi/(\omega N)$ . The time step can be analyzed by giving different values to  $N$ , the number of points per period, for example  $N=40, 60, 80$  and  $100$ . Figure 3.7 and 3.8 shows the variation of the lift and drag coefficients during the oscillatory cycle. The Figure 3.7 shows the coefficients at the oscillatory cycle from  $t/T= 5$  to  $6$  and the Figure 3.8 illustrates the coefficients from  $t/T= 5.28$  to  $5.34$ . One can see that the major deviation is presented by the curve calculated with  $N=40$ . This situation matches with the data shown in Table 3.2 in which the lift and drag coefficients converge after  $N=80$  at oscillatory cycle point  $t/T=5.34$ . Therefore, the selected number of time steps per cycle was  $N=80$ .

Time steps per cycle	$t/T$	$C_L$	$C_D$
40	5.34	1.19795	0.326121
60	5.34	1.18598	0.326433
80	5.34	1.16601	0.326507
100	5.34	1.16601	0.326507

Table 3.2 Sensitivity of the time steps per oscillation cycle of the numerical solution for  $N=40, 60, 80$  and  $100$  of the unsteady flow past NACA 0002 airfoil for  $Re = 1000$ , at angle of attack,  $\alpha = 14^\circ$ . and frequency  $\omega=0.05$  at  $t/T=5.34$  based on the computed lift and drag coefficients. The grid size used is  $310 \times 131$  grid points for each variable.

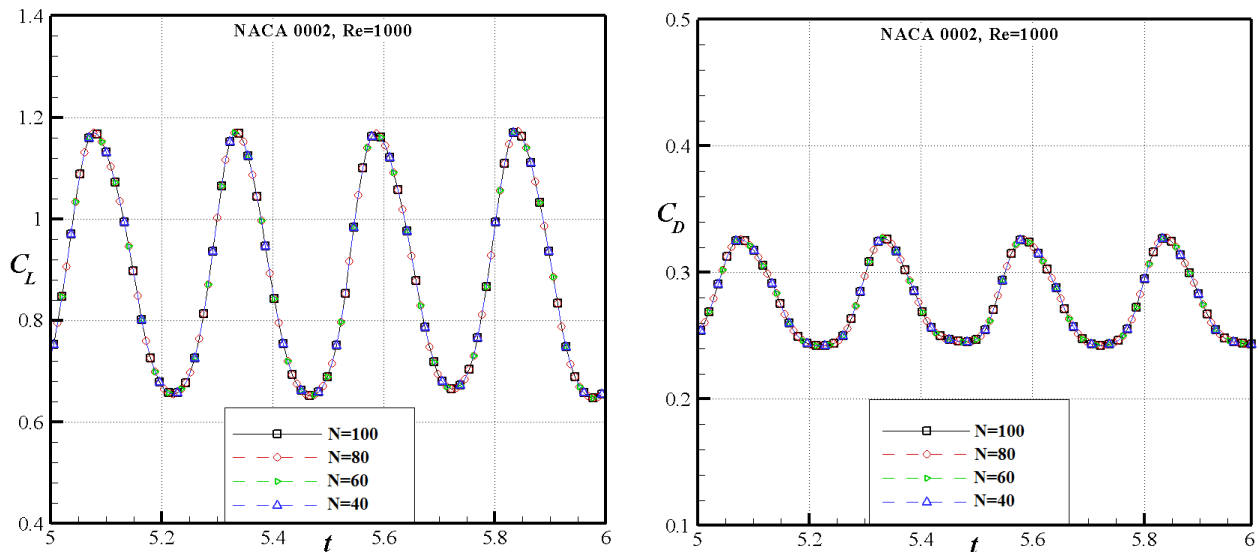


Figure 3.7 Influence of time steps per oscillation cycle: Comparison of the lift and drag coefficients of NACA 0002 airfoil for  $Re = 1000$ , at angle of attack,  $\alpha = 14^\circ$ . and frequency  $\omega=0.05$  for several time steps,  $N = 40, 60, 80$  and  $100$  between the oscillatory cycle from  $t/T=5$  to  $6$ .

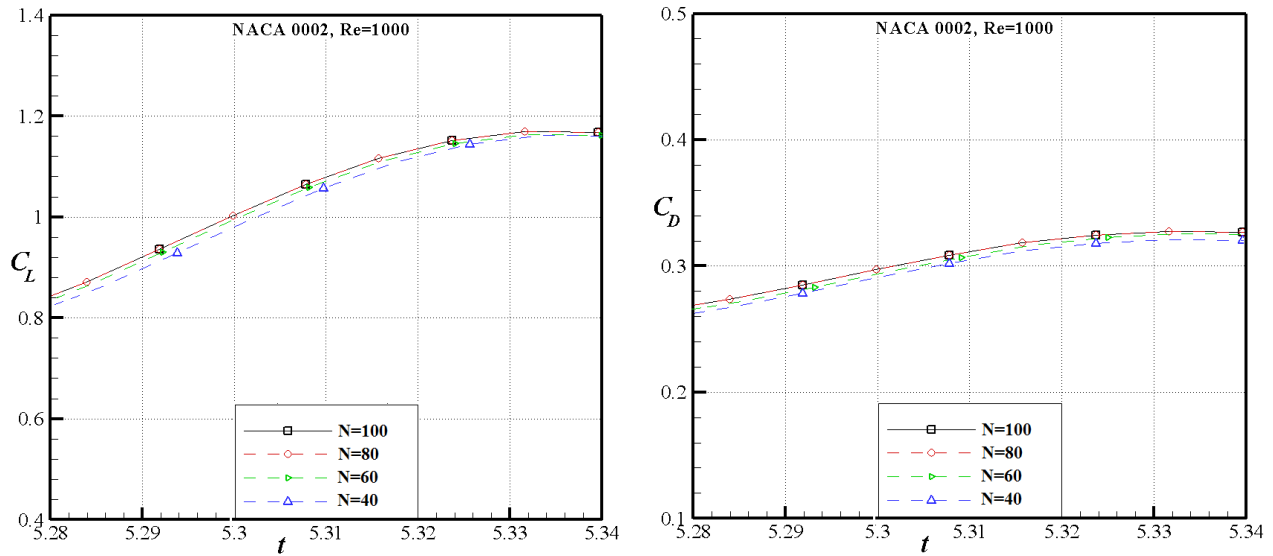


Figure 3.8 Influence of time steps per oscillation cycle: showing the lift and drag coefficient variation of NACA 0002 airfoils for  $Re = 1000$ , at angle of attack,  $\alpha = 14^\circ$  and frequency  $\omega=0.05$  for several time steps,  $N = 40, 60, 80$  and  $100$  between the oscillatory cycle from  $t/T=5.28$  to  $5.34$ .

### 3.4 Unsteady effects in the flow past the triangular airfoil

For angles of attack larger than  $\alpha = 6^\circ$ , the computed aerodynamic coefficients of lift and drag,  $C_L$  and  $C_D$ , of the triangular airfoil display periodic variations in time as shown in Figure 3.9 for  $Re = 3000$ .

One can observe that up to the aerodynamic coefficients are practically constant in time. With the increase in incidence, the lift and drag coefficients display periodic variations in time. The amplitude of these variations in time increases substantially with the angle of attack, for incidences larger than  $\alpha = 10^\circ$ . The oscillations of the aerodynamic coefficients become more complex, due to an increasing complexity of the unsteady flow separations.

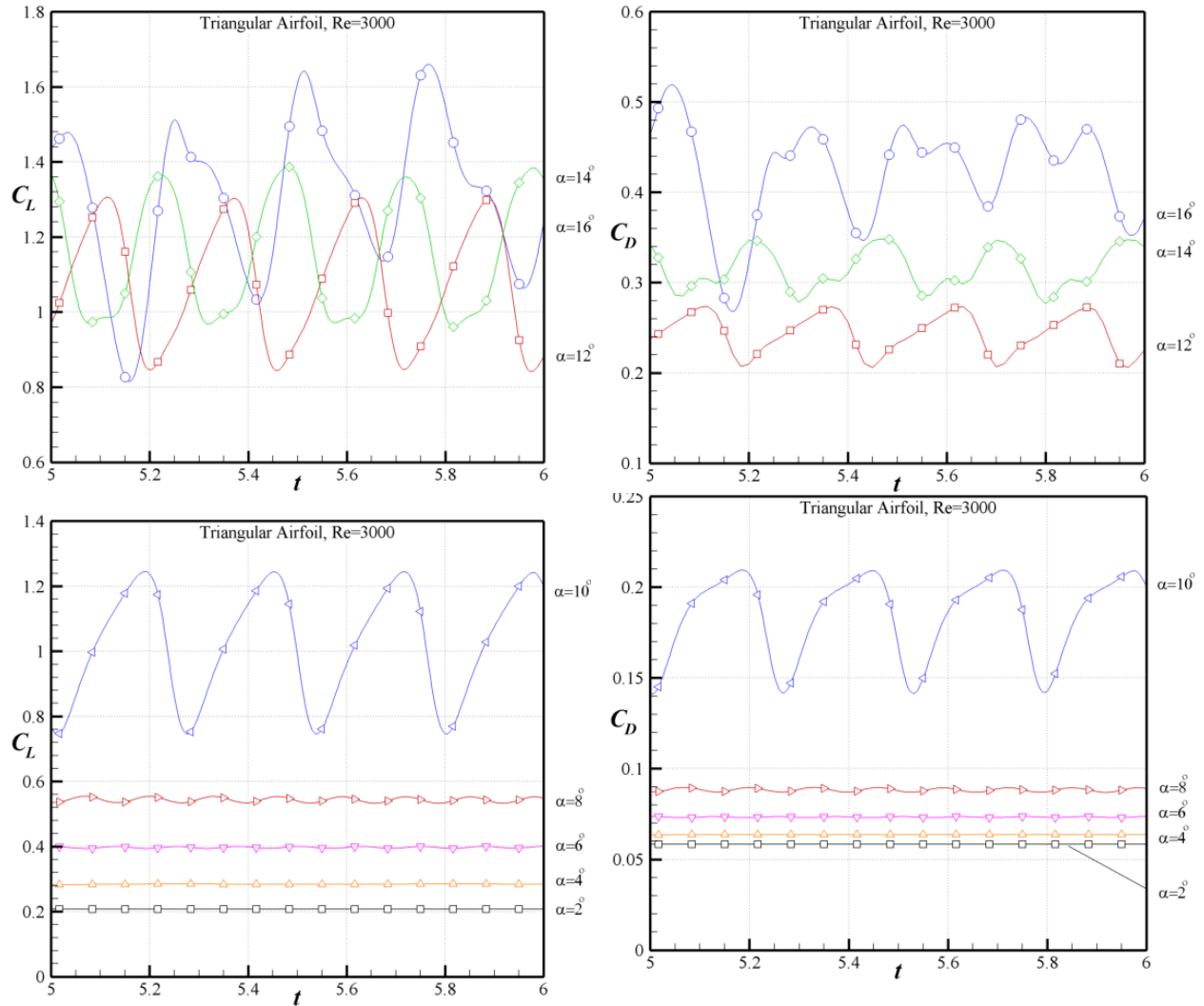


Figure 3.9 The variations with the nondimensional time,  $t = t^*U_\infty/c$ , of the lift and drag coefficients,  $C_L$  and  $C_D$ , of the triangular airfoil for Reynolds number,  $Re = 3000$ , at various angles of attack,  $\alpha$ .

The behavior is consistent with the results of the flow separation analysis, which revealed that for incidences smaller than  $\alpha = 6^\circ$  the flow separation behind the ridge (situated at  $x = s = 0.30$ ) is well organized and does not present oscillations in time, as it can be seen in the flow visualizations shown in Figure 3.10. In these flow visualizations, the streamlines are represented by continuous lines, and the flow velocity field is represented by color shades related to the non-dimensional velocity  $V/U_\infty$ .

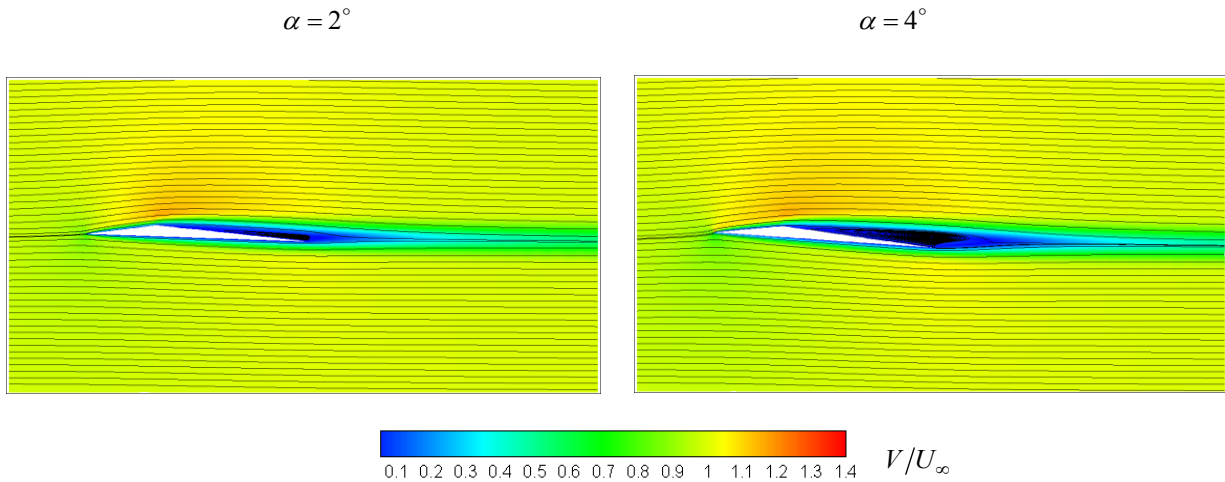


Figure 3.10 Illustration of the steady flow separations for the triangular airfoil for  $Re = 3000$  at  $\alpha = 2^\circ$  and  $\alpha = 4^\circ$ .

At incidences larger than  $\alpha = 6^\circ$ , the complexity of the flow separations and their variations in time increase when the angle of attack increases. The most complex pattern of the flow separations is displayed for incidences larger than  $\alpha = 12^\circ$ . This can be seen in Figures 3.11 to 3.13, which present illustrations of the flow separations at various moments in time for the triangular airfoil for Reynolds number,  $Re = 3000$ , at various incidences  $\alpha = 6^\circ, 8^\circ, 10^\circ, 12^\circ, 14^\circ$  and  $16^\circ$ . The lines in these figures show the streamline pattern of the flow around the airfoil, and the color shades indicate the nondimensional velocity field (with respect to the uniform stream velocity  $U_\infty$ ).

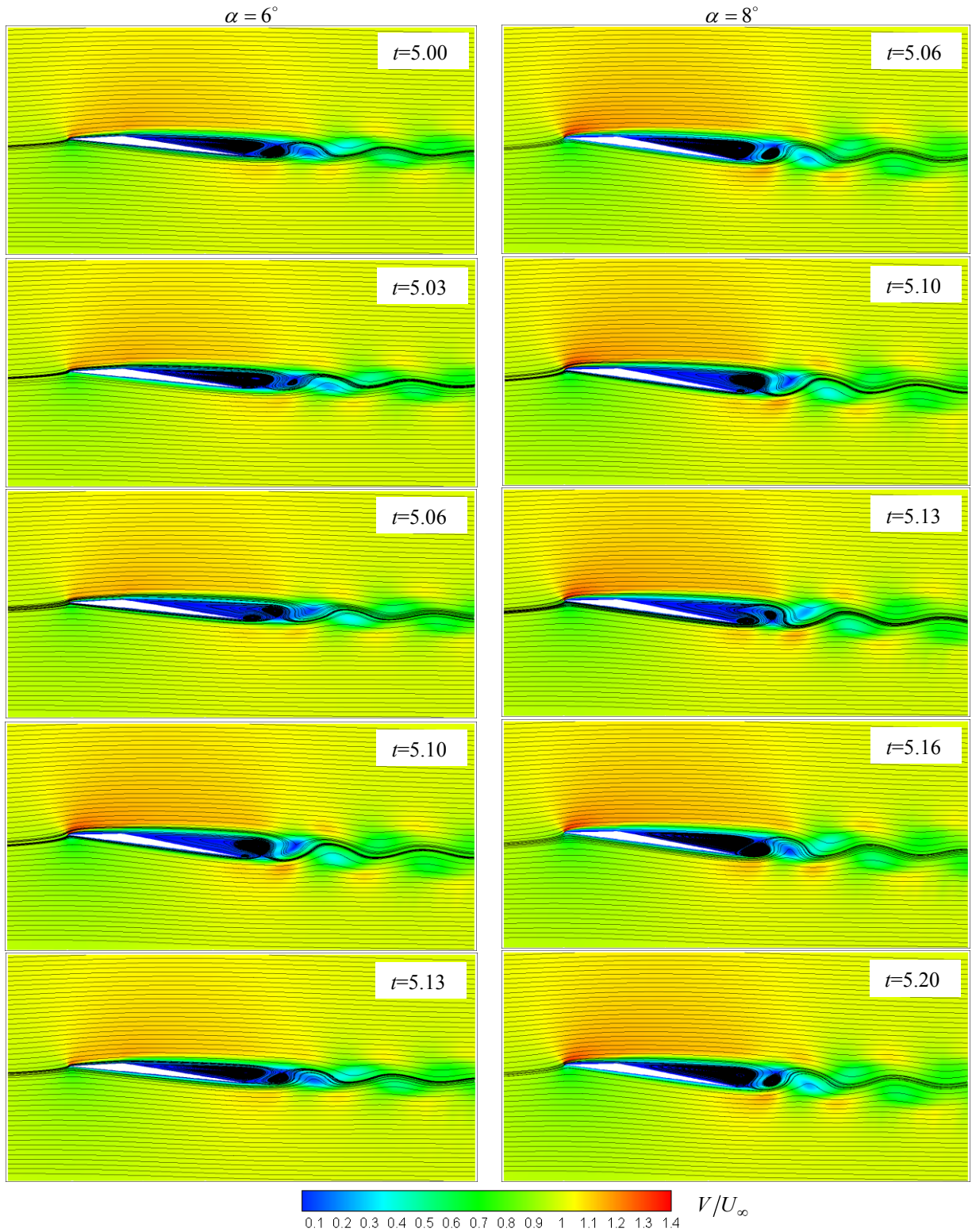


Figure 3.11 Illustration of the unsteady flow separations for the triangular airfoil at various moments in time using the streamlines and the color shades indicating the nondimensional velocity field: For  $Re = 3000$  at the angles of attack  $\alpha = 6^\circ$  and  $\alpha = 8^\circ$ .

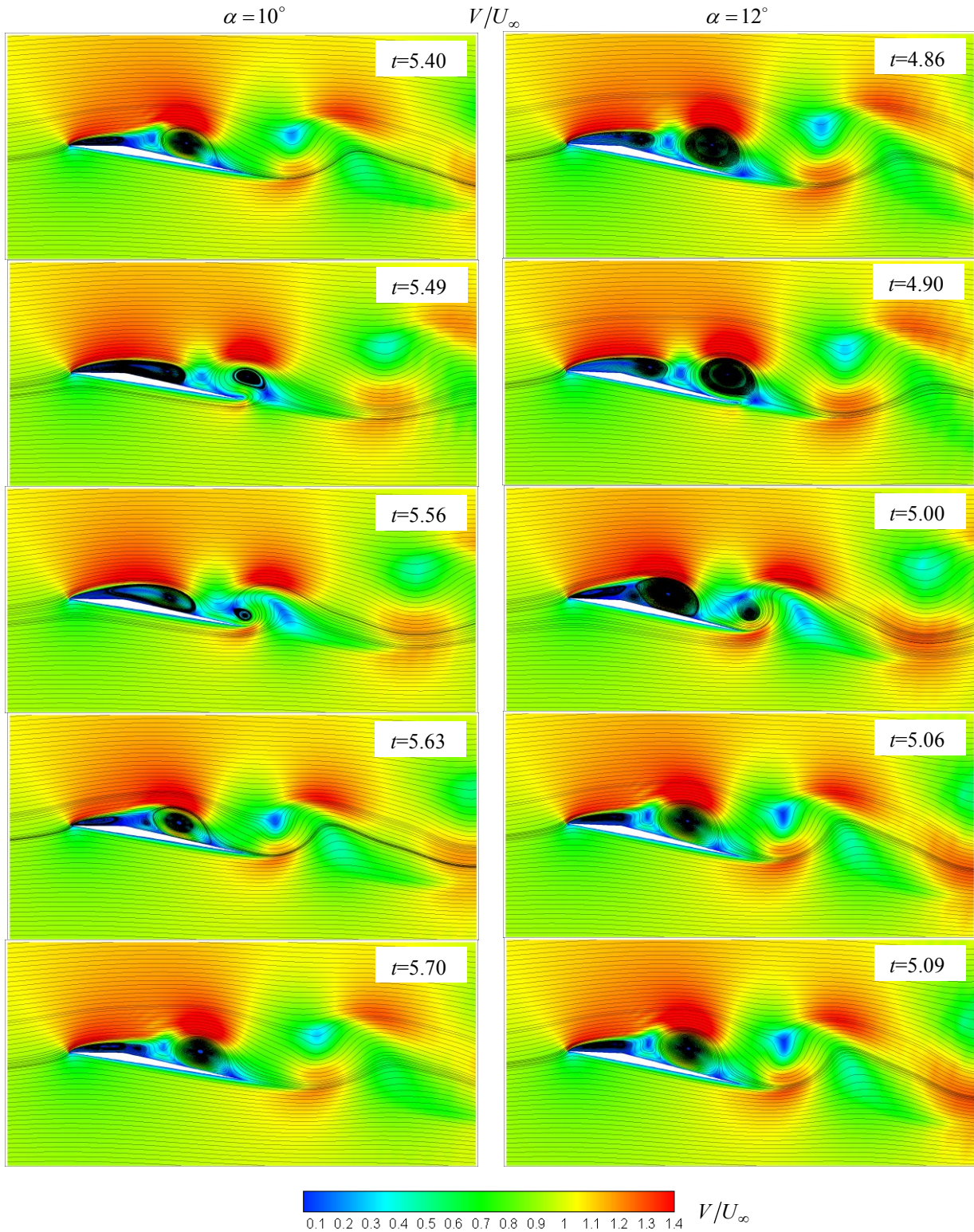


Figure 3.12 Illustration of the unsteady flow separations for the triangular airfoil at various moments in time using the streamlines and the color shades indicating the nondimensional velocity field: For  $Re = 3000$  at the angles of attack  $\alpha = 10^\circ$  and  $\alpha = 12^\circ$ .

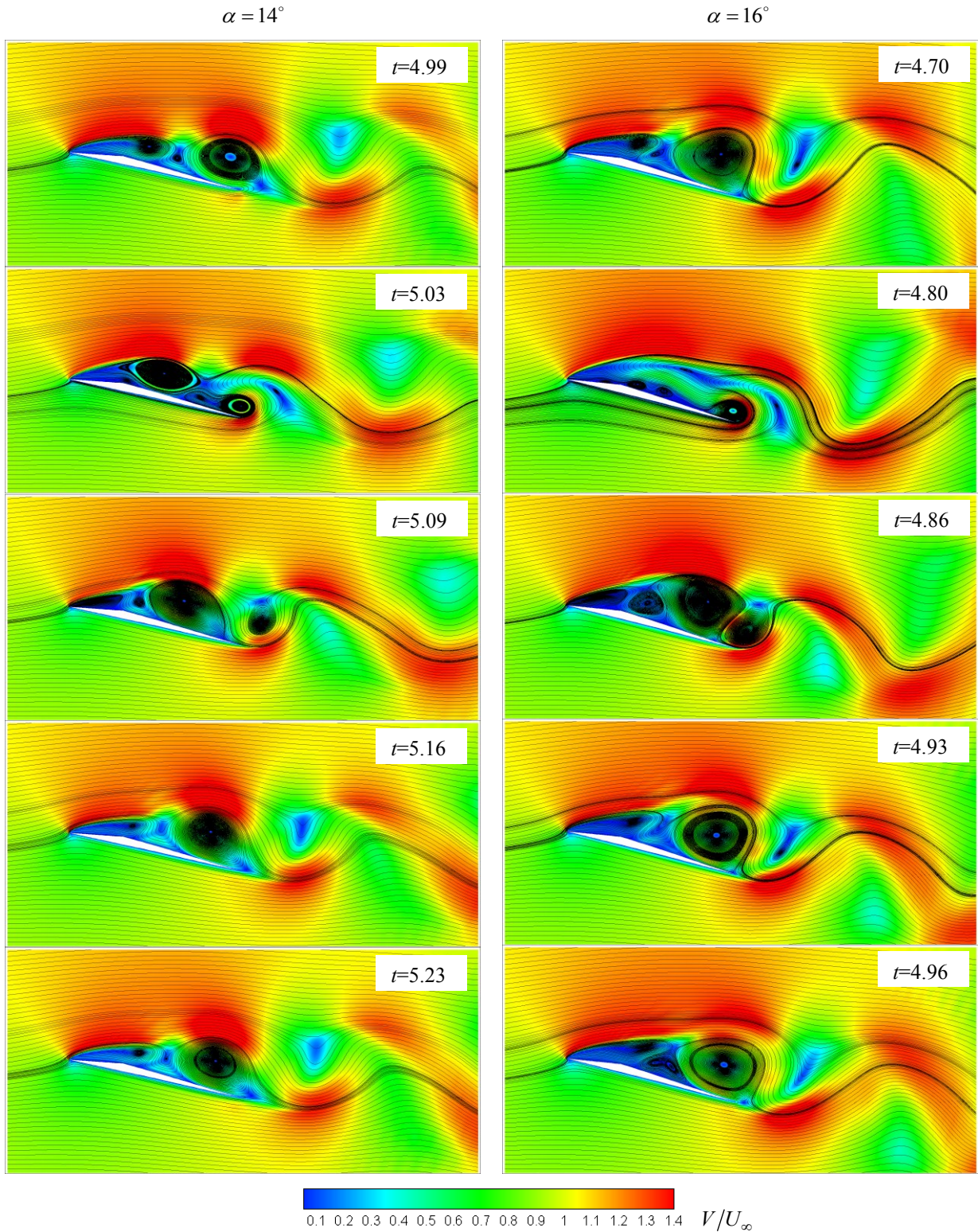


Figure 3.13 Illustration of the unsteady flow separations for the triangular airfoil at various moments in time using the streamlines and the color shades indicating the nondimensional velocity field: For  $Re = 3000$  at the angles of attack  $\alpha = 14^\circ$  and  $\alpha = 16^\circ$ .

These illustrations of the variation in time of the flow separation pattern shown in Figures 3.11 to 3.13 are consistent with the oscillatory variations in time of the aerodynamic coefficients shown in Figure 3.9. It can be seen these unsteady flow separation structures, appearing in the flow past stationary airfoils at low Reynolds numbers, generate the oscillatory variations in time of the lift and drag coefficients.

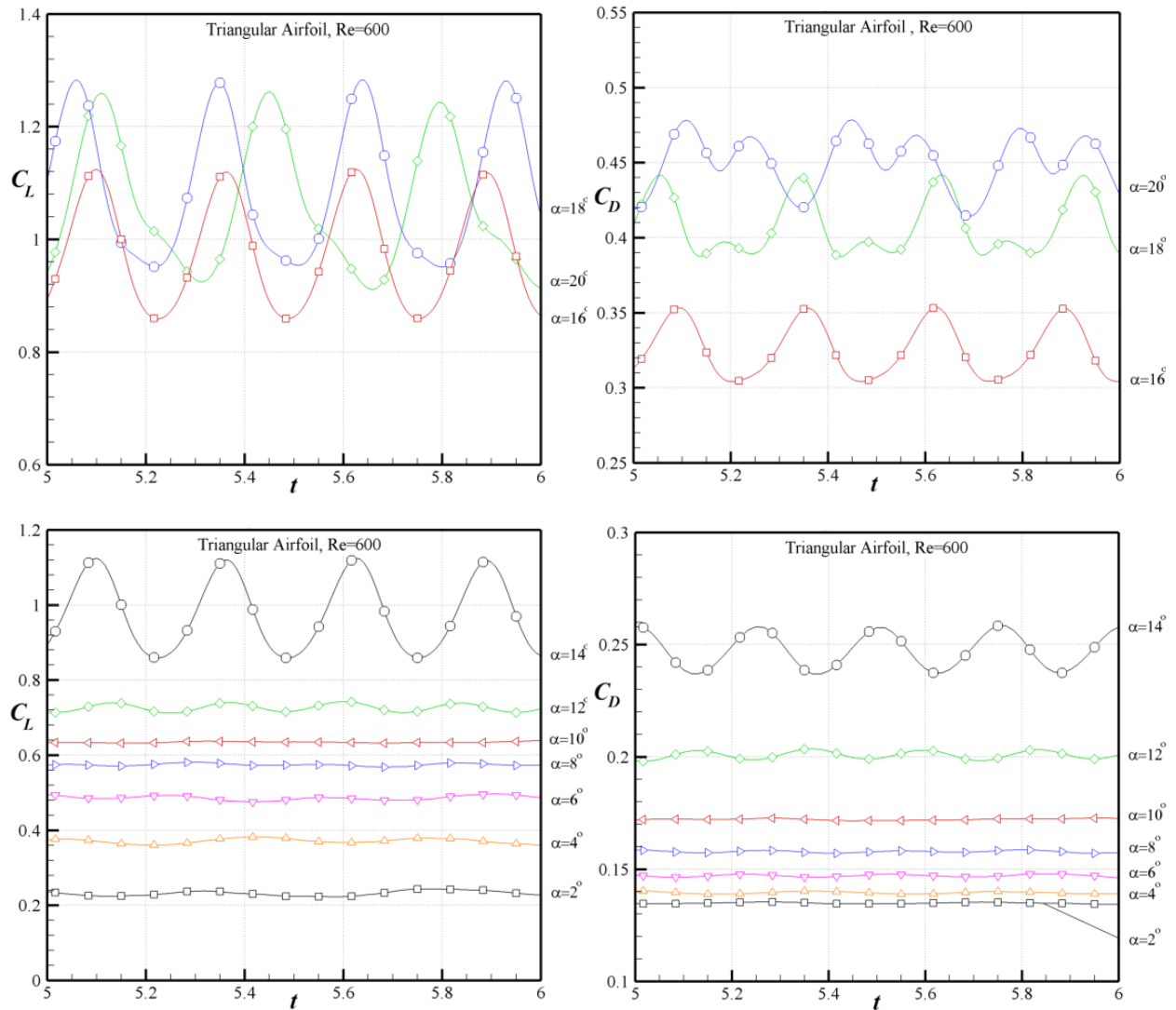


Figure 3.14 The variations with the nondimensional time,  $t = t*U_\infty/c$ , of the lift and drag coefficients,  $C_L$  and  $C_D$ , of the triangular airfoil for Reynolds number,  $Re = 600$ , at various angles of attack,  $\alpha$ .

After presenting the results for the triangular airfoil at  $Re = 3000$ , which was chosen because of available experimental results. The numerical results can be also obtained for the triangular airfoil at Reynolds numbers  $Re = 600, 1000$  and  $1500$  for the aerodynamic coefficients of lift and drag,  $C_L$  and  $C_D$ , as shown in Figures 3.14 to 3.16. These new set of results can help to study the influence of Reynolds number on the unsteady effects generated by the unsteady flow separations at low Reynolds numbers.

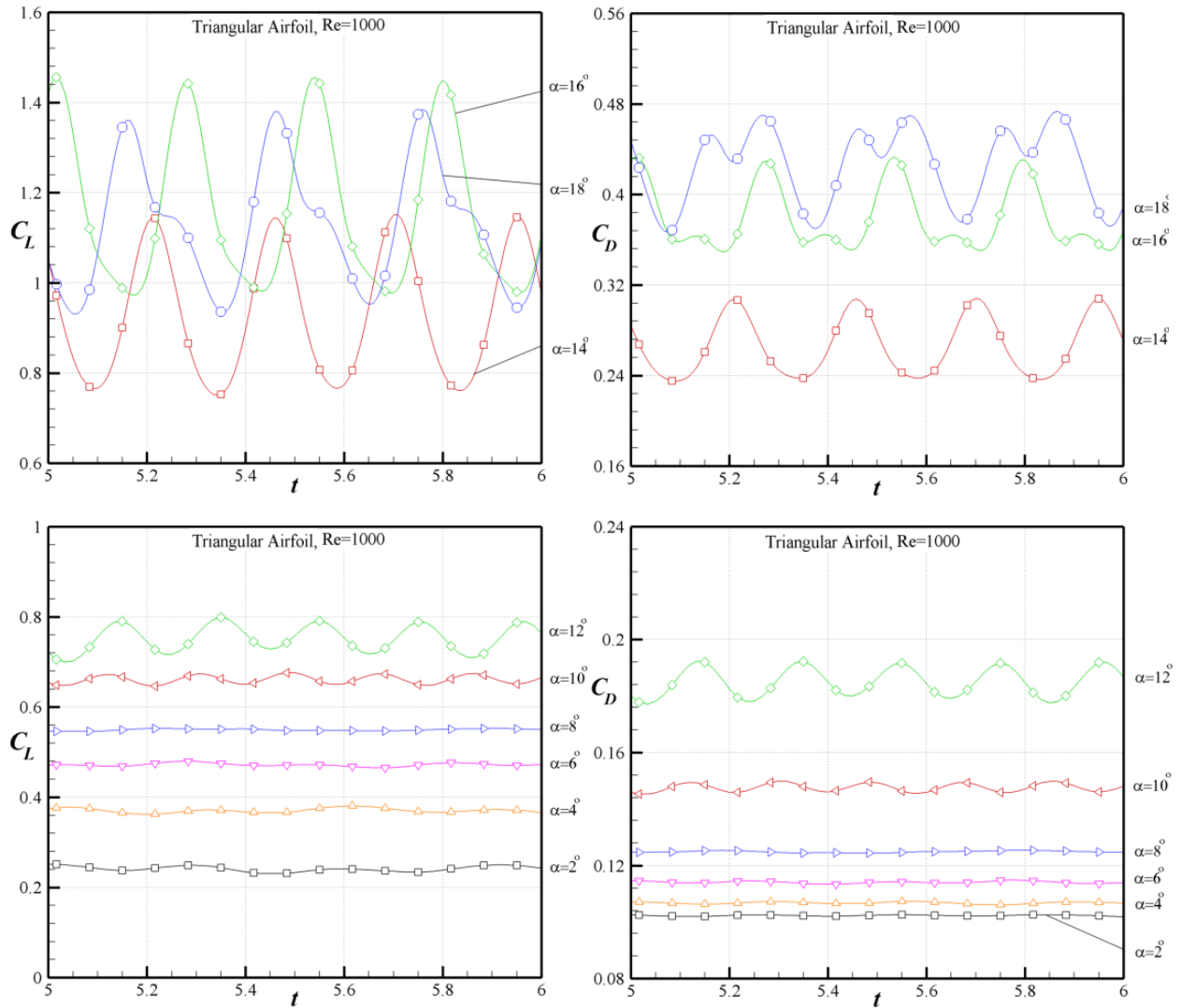


Figure 3.15 The variations with the nondimensional time,  $t = t * U_\infty / c$ , of the lift and drag coefficients,  $C_L$  and  $C_D$ , of the triangular airfoil for Reynolds number,  $Re = 1000$ , at various angles of attack,  $\alpha$ .

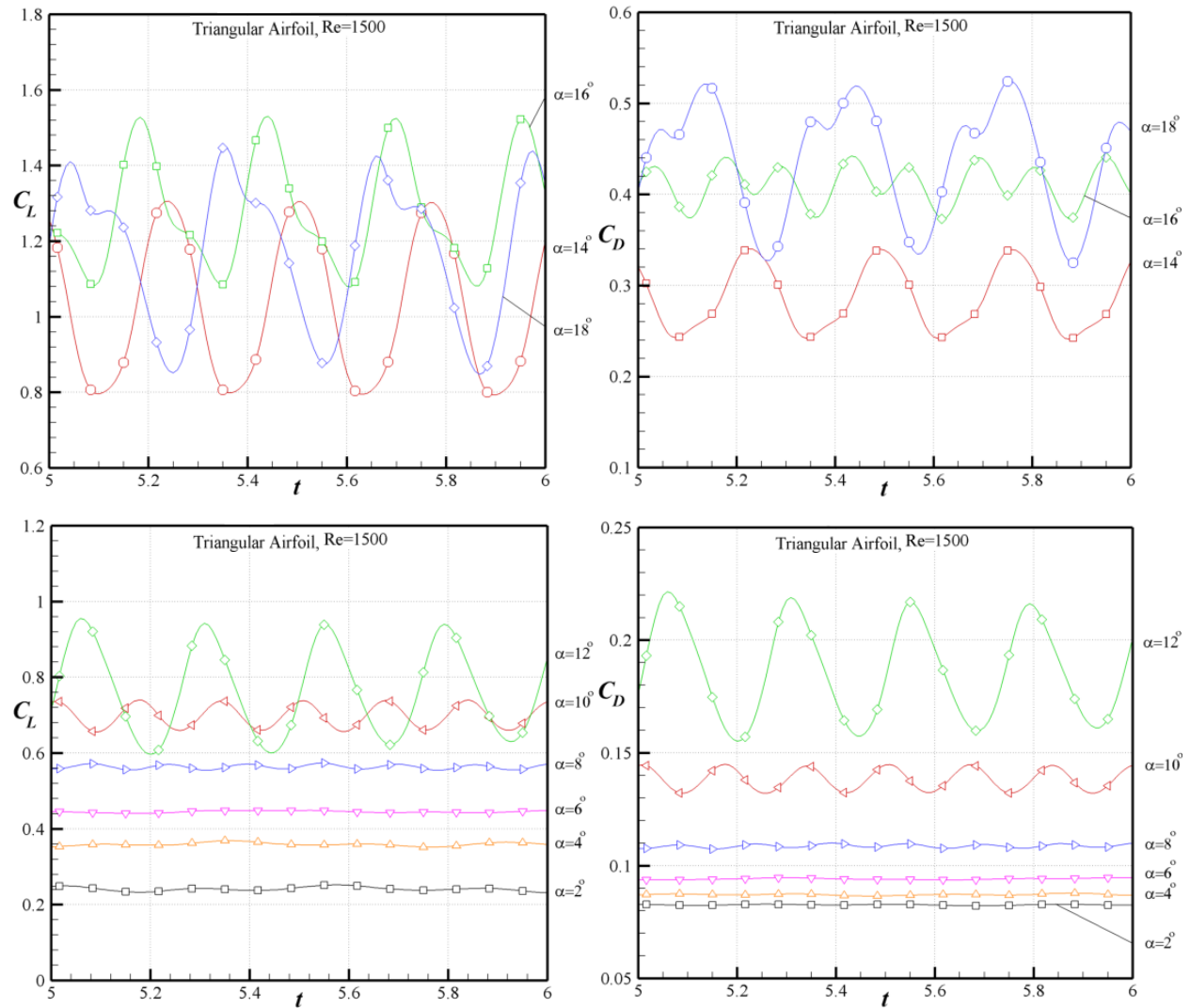


Figure 3.16 The variations with the nondimensional time,  $t = t * U_{\infty} / c$ , of the lift and drag coefficients,  $C_L$  and  $C_D$ , of the triangular airfoil for Reynolds number,  $Re = 1500$ , at various angles of attack,  $\alpha$ .

One can notice, at angles of attack larger than  $\alpha = 10^\circ$  in Figure 3.14, and larger than  $\alpha = 8^\circ$  in Figure 3.15 and 3.16, as the Reynolds number increases the amplitudes of the oscillations in time of the lift and drag coefficients become larger. This is where the numerical solution enters into unsteadiness region and the lift and drag coefficients are not constant in a real time. Therefore, in one oscillation cycle there are minimum and maximum values for these two coefficients at higher angles of attack as shown in Figures 3.14 to 3.16.

### 3.5 Unsteady solutions for several symmetric and cambered airfoils

The numerical method presented in section 3.1 is then used to obtain solutions for several symmetric and cambered airfoils at various angles of attack, in order to study the unsteady effects generated by the unsteady flow separations at low Reynolds numbers.

The aerodynamic coefficients of lift and drag  $C_L$  and  $C_D$  of the NACA 0004 airfoil are shown in Figure 3.17, 3.18 and 3.19 for the Reynolds numbers  $Re = 600$ , 1000 and 1500; respectively.

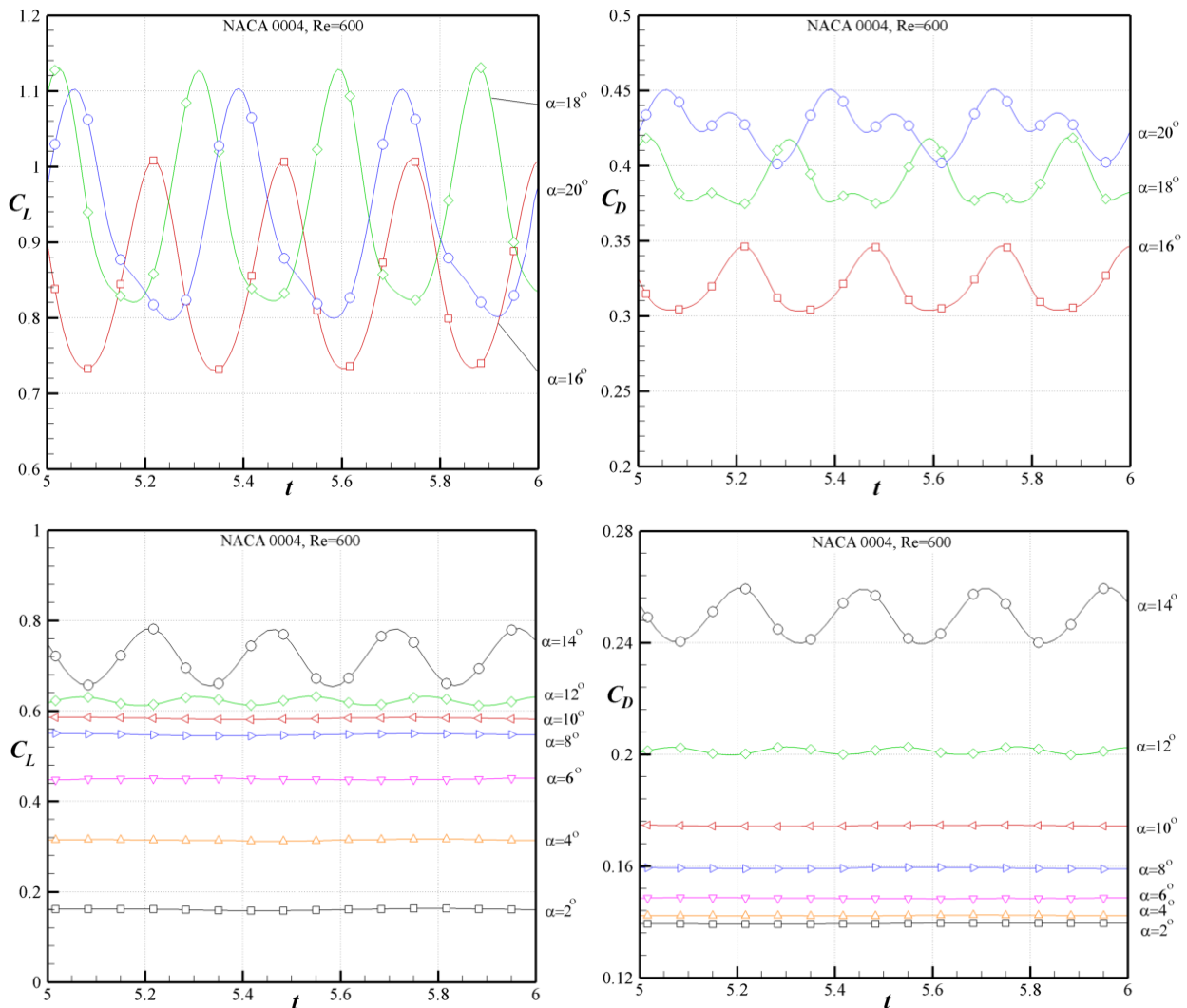


Figure 3.17 The variations with the nondimensional time,  $t = t*U_\infty/c$ , of the lift and drag coefficients,  $C_L$  and  $C_D$ , of the NACA 0004 airfoil for Reynolds number,  $Re = 600$ , at various angles of attack,  $\alpha$ .

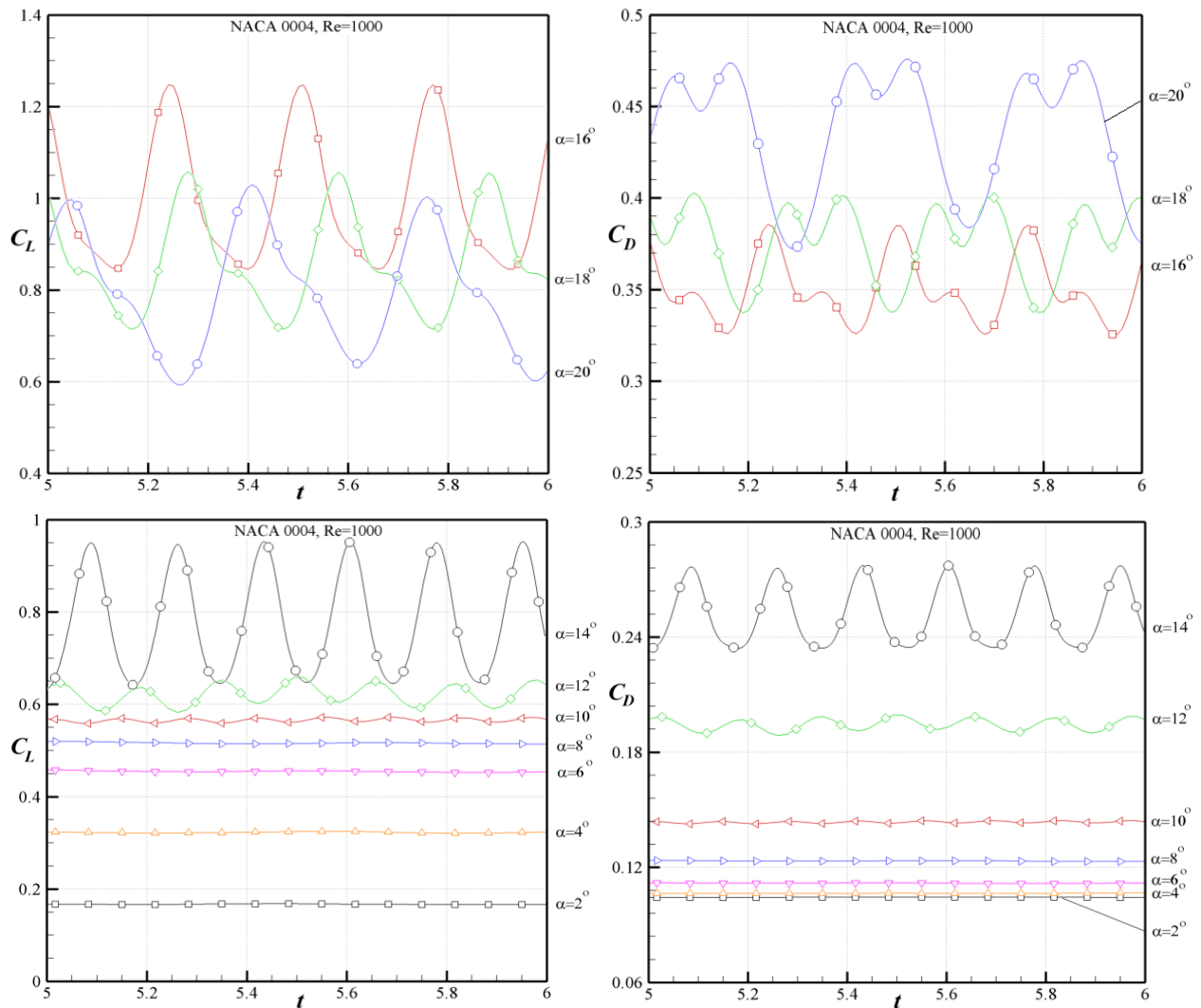


Figure 3.18 The variations with the nondimensional time,  $t = t^*U_\infty/c$ , of the lift and drag coefficients,  $C_L$  and  $C_D$ , of the NACA 0004 airfoil for Reynolds number,  $Re = 1000$ , at various angles of attack,  $\alpha$ .

One can be seen that the amplitudes of the oscillations in time of the lift and drag coefficients increase when the angle of attack,  $\alpha$  goes up, this is more significant at angles of attack larger than  $\alpha = 10^\circ$ . By comparing Figures 3.17 to 3.19, it is apparent that these oscillations grow with an increase in Reynolds number.

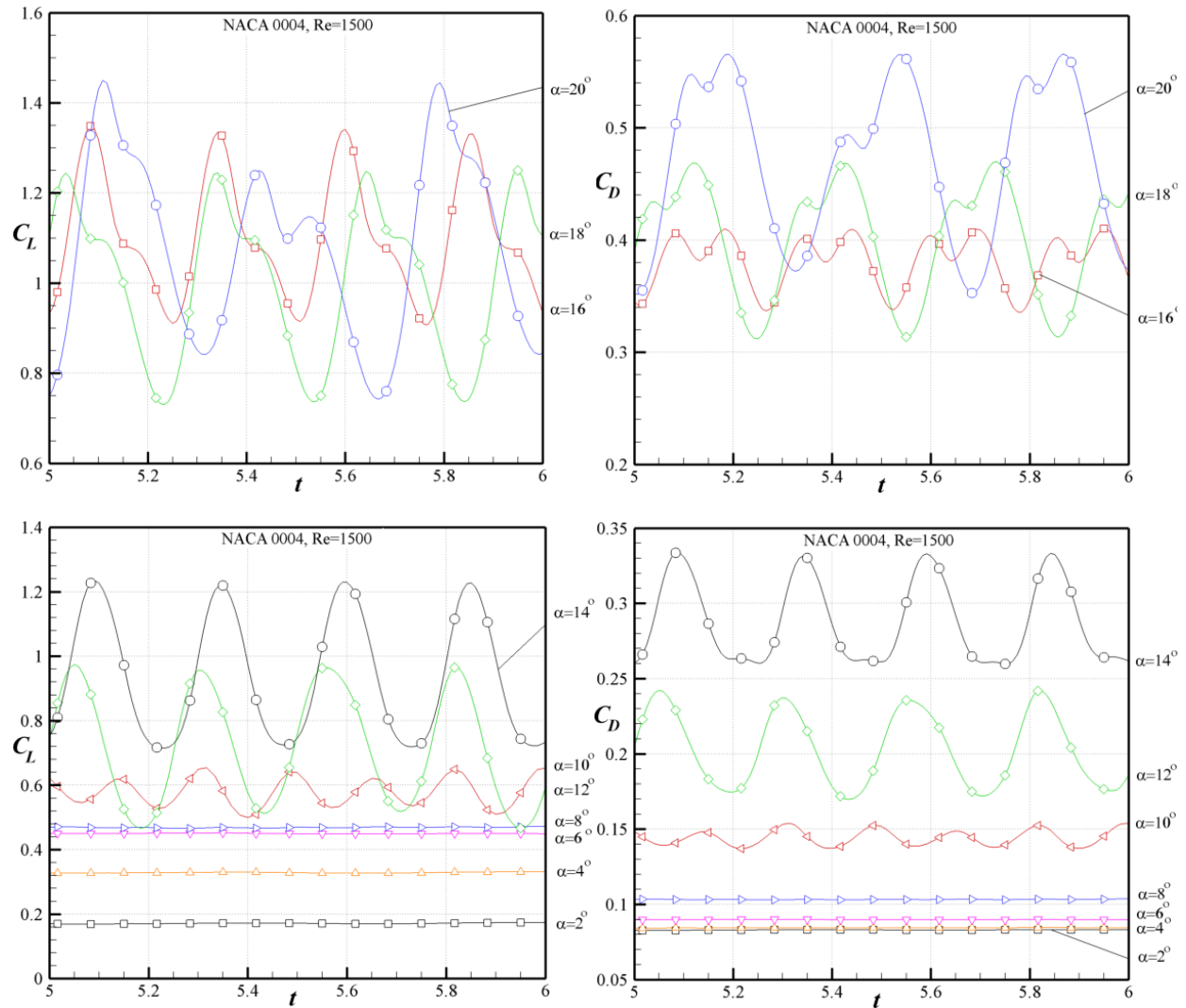


Figure 3.19 The variations with the nondimensional time,  $t = t * U_{\infty} / c$ , of the lift and drag coefficients,  $C_L$  and  $C_D$ , of the NACA 0004 airfoil for Reynolds number,  $Re = 1500$ , at various angles of attack,  $\alpha$ .

One can observe that up to  $\alpha = 8^\circ$  the aerodynamic coefficients are practically constant in time. With the increase in incidence, the lift and drag coefficients display periodic variations in time; as a result the solution becomes unsteady. The amplitude of these variations in time increases as the angle of attack goes up, and for incidences larger than  $\alpha = 10^\circ$  these oscillations of the aerodynamic coefficients become more complex, due to complexity of the unsteady flow separations at higher angle of attack.

As it can be seen in the flow visualizations shown in Figure 3.20, this behavior is consistent with the results of the flow separation analysis, which revealed that for incidences smaller than  $\alpha = 8^\circ$  for  $Re = 1000$ , and  $\alpha = 10^\circ$  for  $Re = 600$ , the flow separation is well organized and does not present oscillations in time.

In these flow visualizations, the streamlines are represented by continuous lines, and the flow velocity field is represented by color shades related to the non-dimensional velocity  $V/U_\infty$ .

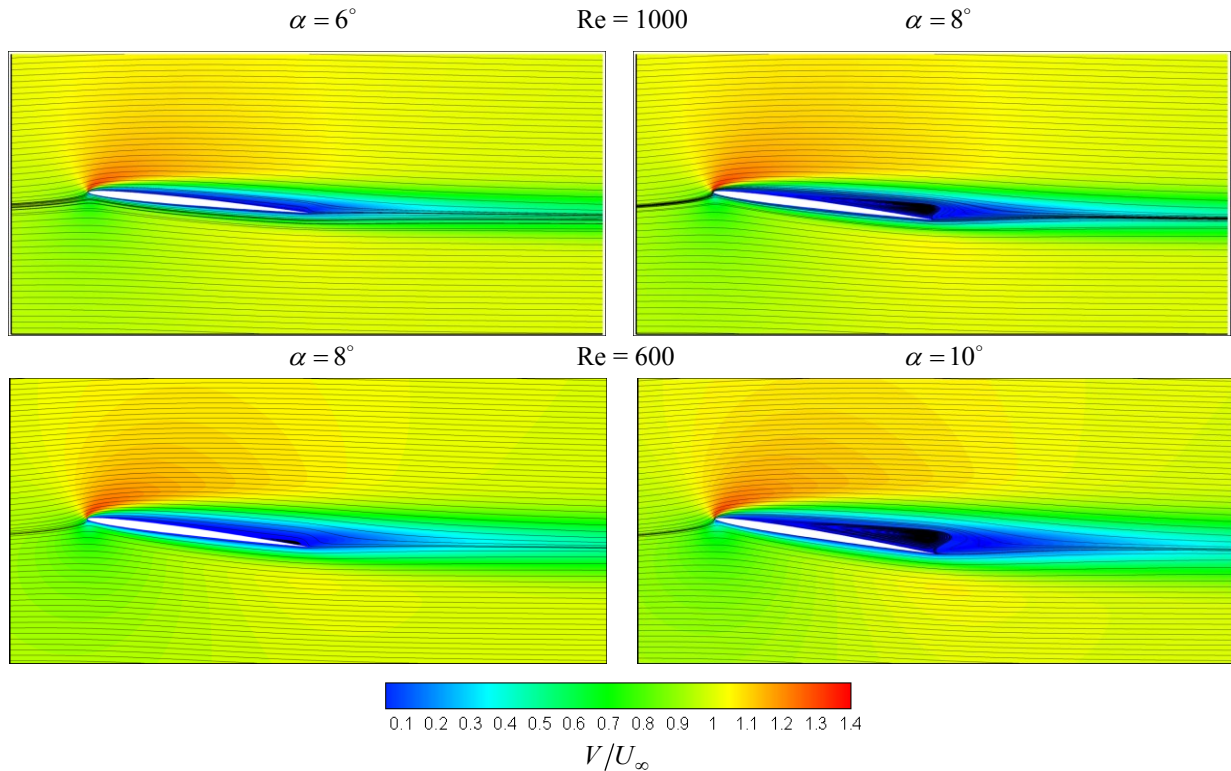


Figure 3.20. Illustration of the steady flow separations for the NACA 0004 airfoil for two Reynolds numbers,  $Re = 600$  and  $1000$ , and at two angles of attack,  $\alpha$ .

At incidences larger than  $\alpha = 8^\circ$ , the complexity of the flow separations and their variations in time increase as the incidence becomes larger. The most complex pattern of the flow separations is displayed for incidences larger than  $\alpha = 14^\circ$ . This can be seen in Figures 3.22 and 3.22 which present illustrations of the flow separations at various moments in time for the NACA 0004 airfoil at Reynolds number  $Re = 600$  and  $Re = 1000$  for various incidences  $\alpha = 14^\circ, 16^\circ$ , and  $18^\circ$ . The lines in these figures show the streamline pattern of the flow around the airfoil, and the color shades indicate the nondimensional velocity.

The following flow visualizations indicated in Figures 3.21 to 3.24 are consistent with the oscillatory variations in time of the aerodynamic coefficients shown in Figure 3.17 and 3.18, indicating that these unsteady flow separation structures, occurring in the flow past stationary airfoils at low Reynolds numbers, generate the oscillatory variations in time of the lift and drag coefficients

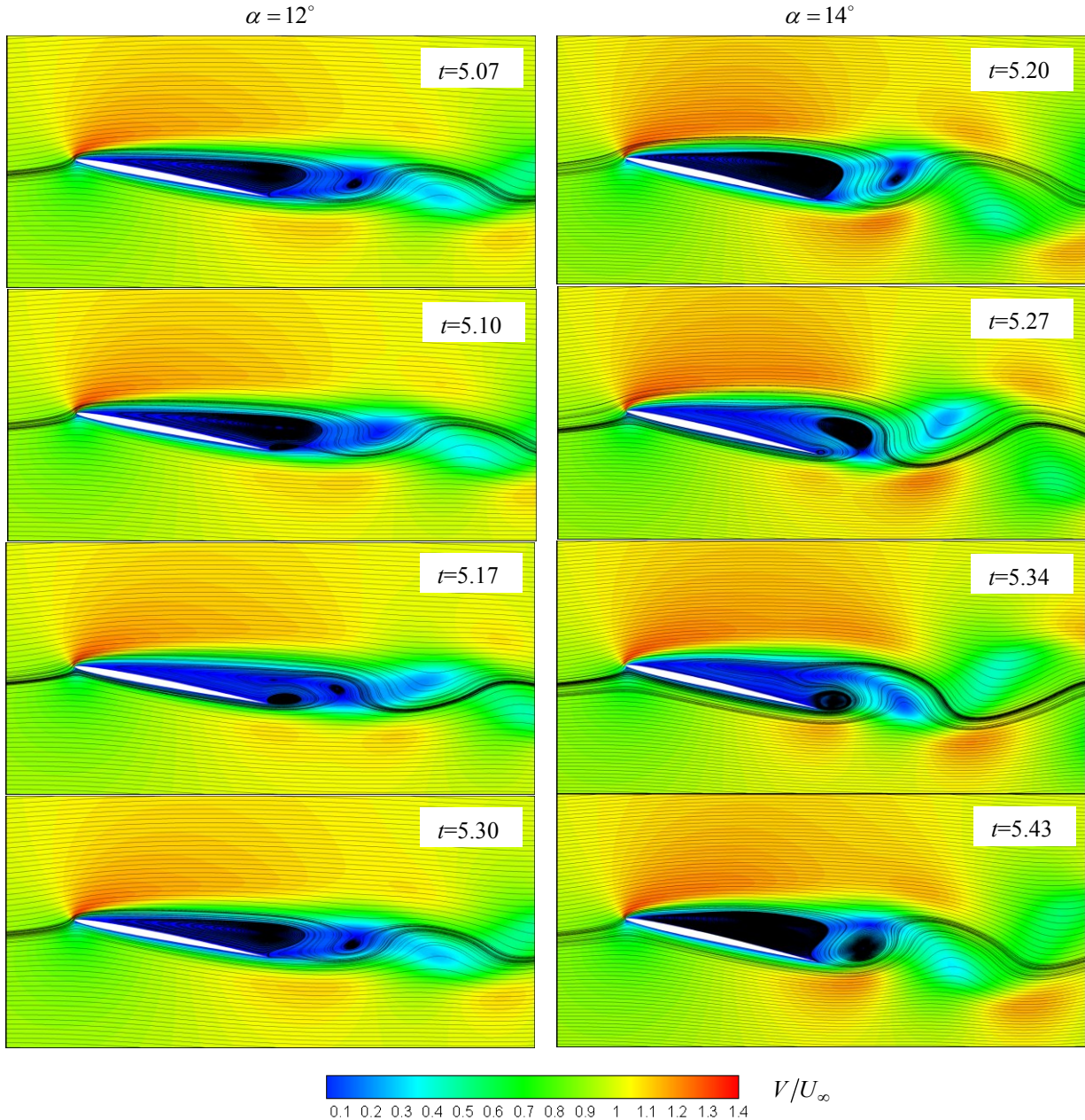


Figure 3.21 Illustration of the unsteady flow separations for the NACA 0004 airfoil at various moments in time using the streamlines and the color shades indicating the nondimensional velocity field: For  $Re = 600$  at the angles of attack  $\alpha = 12^\circ$  and  $\alpha = 14^\circ$ .

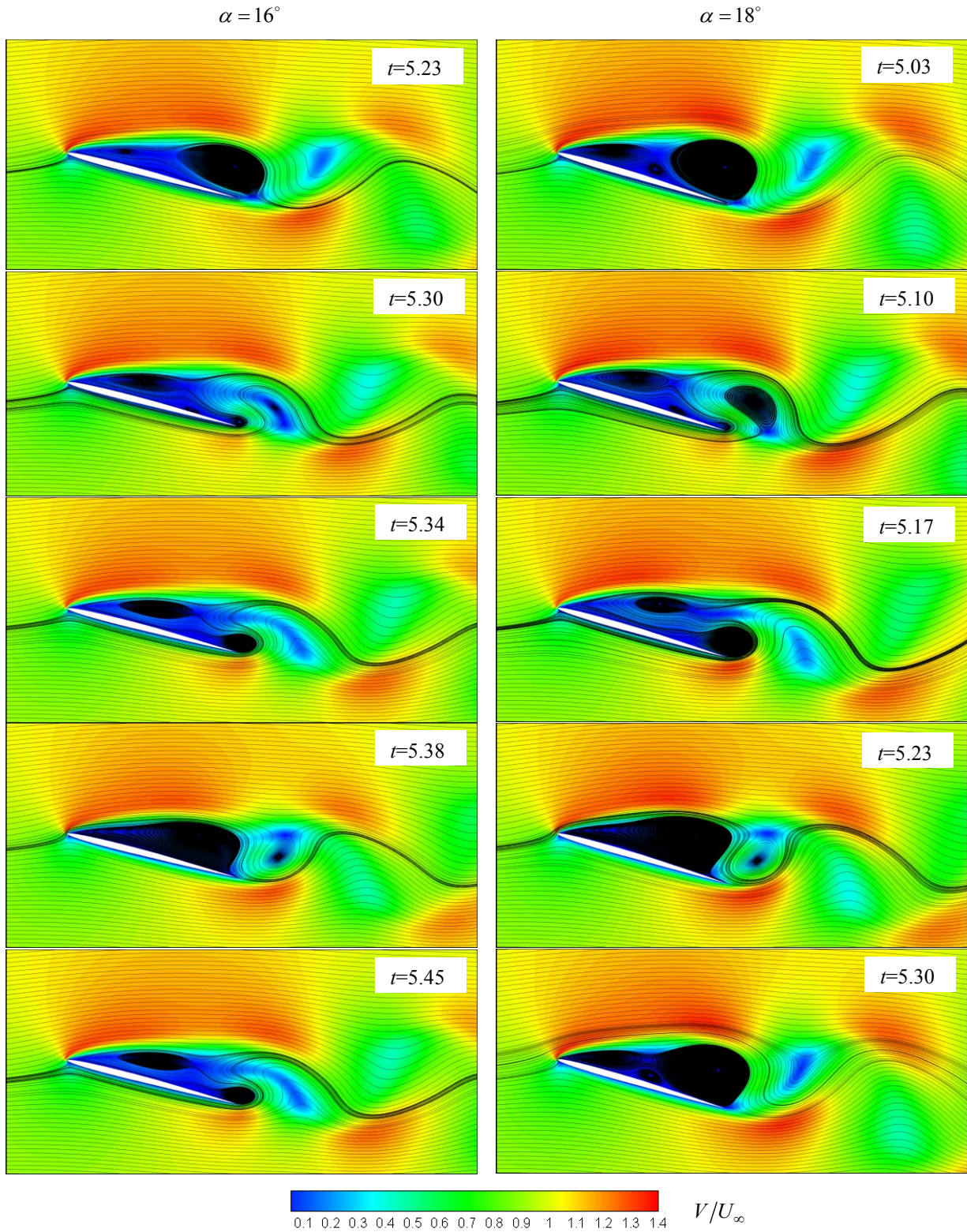


Figure 3.22 Illustration of the unsteady flow separations for the NACA 0004 airfoil at various moments in time using the streamlines and the color shades indicating the nondimensional velocity field: For  $Re = 600$  at the angles of attack  $\alpha = 16^\circ$  and  $\alpha = 18^\circ$ .

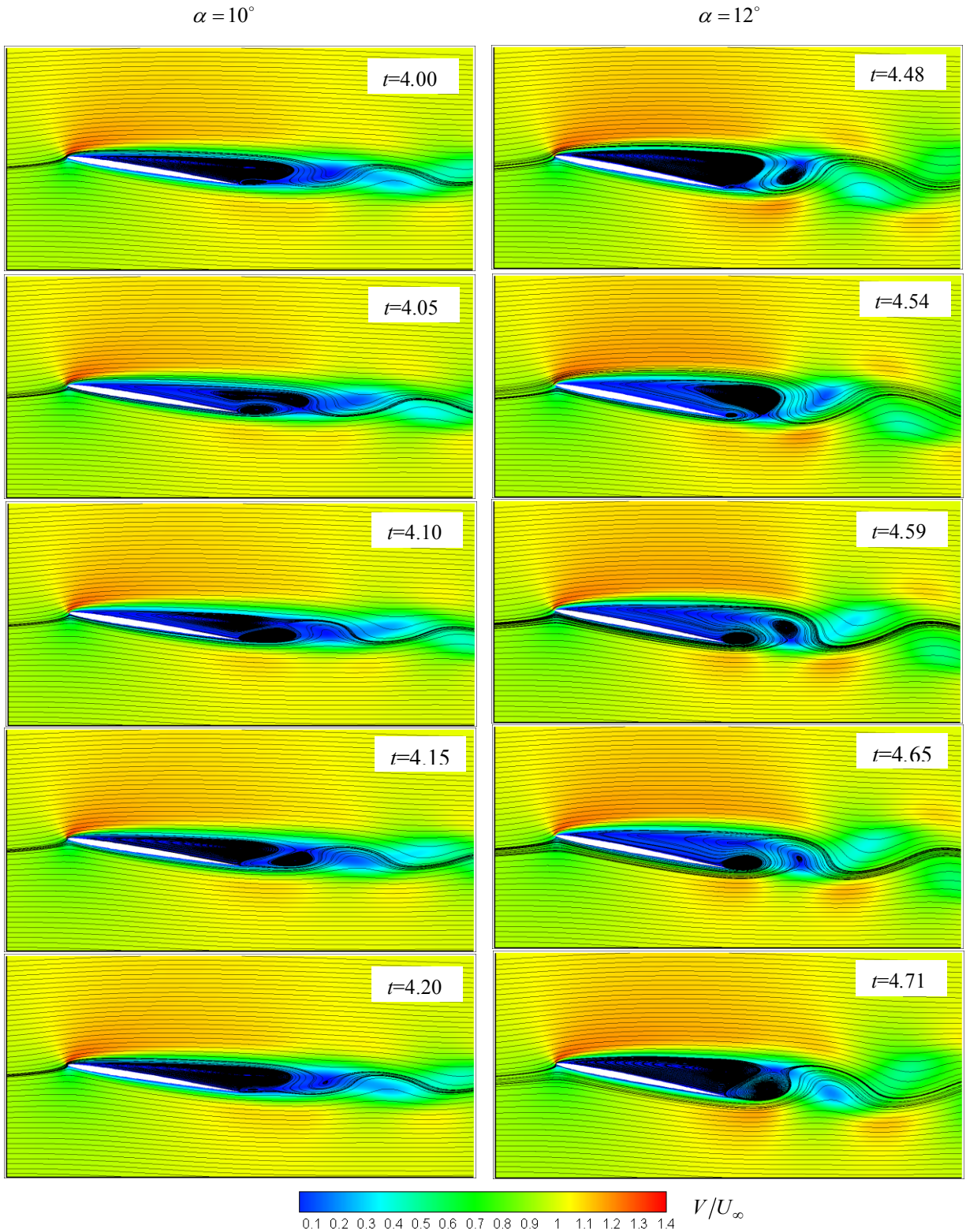


Figure 3.23 Illustration of the unsteady flow separations for the NACA 0004 airfoil at various moments in time using the streamlines and the color shades indicating the nondimensional velocity field: For  $Re = 1000$  at the angles of attack  $\alpha = 10^\circ$  and  $\alpha = 12^\circ$ .

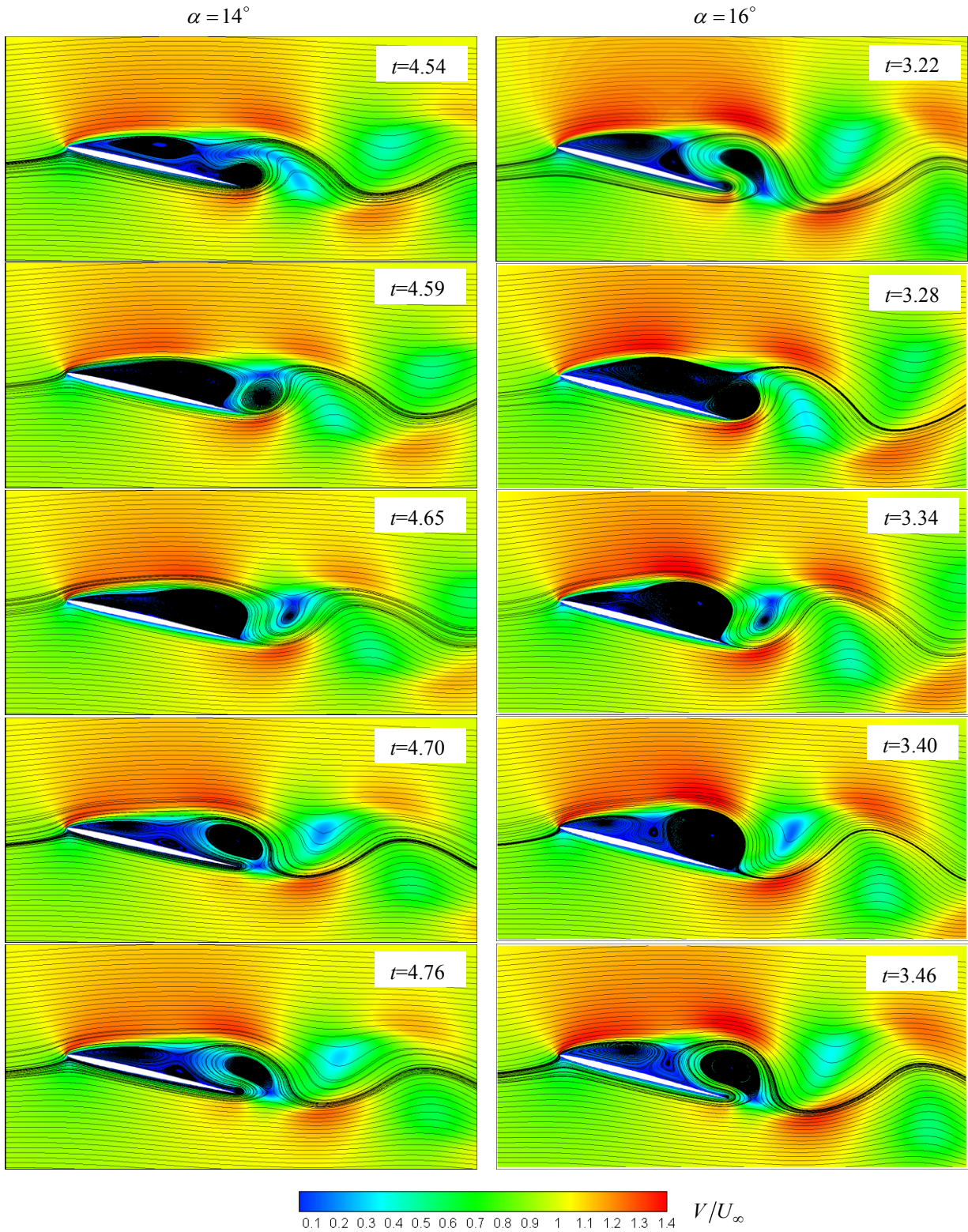


Figure 3.24 Illustration of the unsteady flow separations for the NACA 0004 airfoil at various moments in time using the streamlines and the color shades indicating the nondimensional velocity field: For  $Re = 1000$  at the angles of attack  $\alpha = 14^\circ$  and  $\alpha = 16^\circ$ .

### 3.5.1 Influence of Reynolds number for symmetric airfoils

The influence of the Reynolds number on the flow separations can be observed by comparing the flow visualizations shown in Figures 3.21 to 3.24. For instance, in Figure 3.22 the flow visualizations for NACA 0004 airfoil, and  $\alpha = 16^\circ$  at  $Re = 600$  can be compared with Figure 3.24 for the same airfoil and same angle of attack at  $Re = 1000$ . It is noticeable that for the same angle of attack,  $\alpha$ , the unsteadiness of the flow separations increases with the increment in Reynolds number.

The influence of the Reynolds number on the unsteady effects generated by the unsteady flow separations at low Reynolds numbers can be also observed by comparing the results shown in Figures 3.25 and 3.26 for  $Re = 600$  and  $Re = 1000$  over the symmetric airfoil NACA 0004.

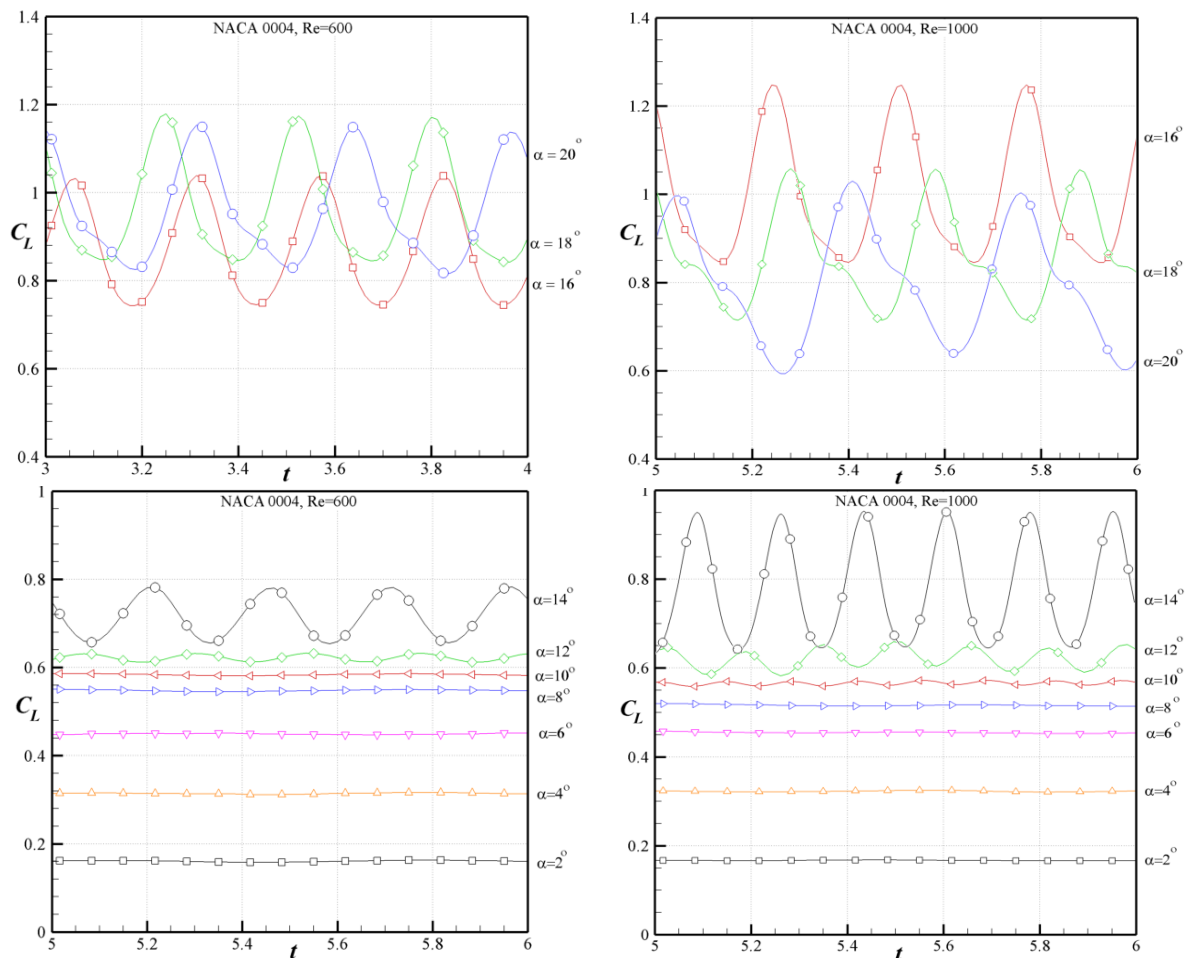


Figure 3.25 Influence of Reynolds number for symmetric airfoils. Comparison of the variations with the nondimensional time,  $t = t^*U_\infty/c$ , of the lift coefficients,  $C_L$ , of NACA 0004 airfoils for  $Re = 600$  and  $1000$ , at various angles of attack,  $\alpha$ .

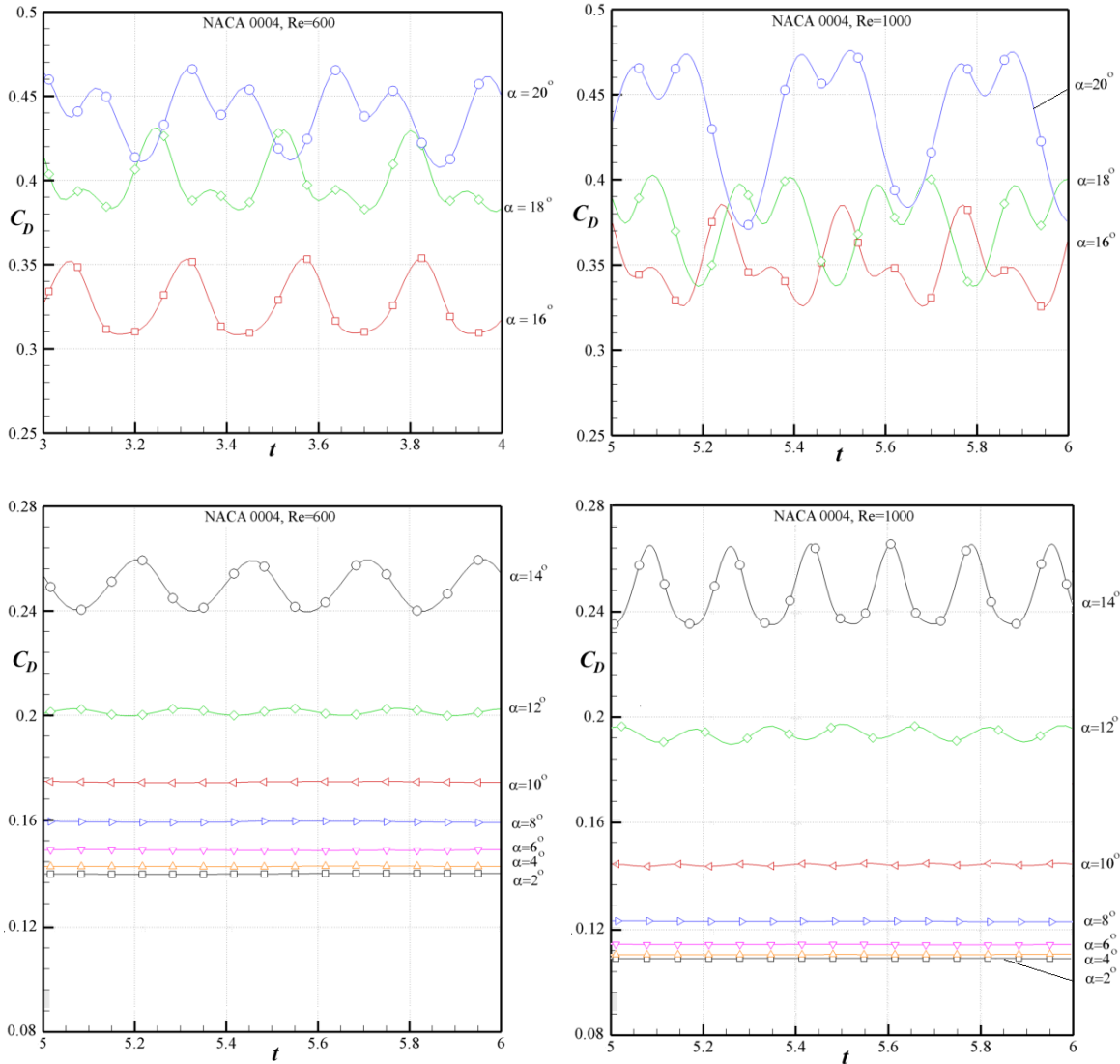


Figure 3.26 Influence of Reynolds number for symmetric airfoils. Comparison of the variations with the nondimensional time,  $t = t \cdot U_\infty / c$ , of the drag coefficients,  $C_D$ , of NACA 0004 airfoils for  $Re = 600$  and  $1000$ , at various angles of attack,  $\alpha$ .

From above figures it can be seen that the amplitude of oscillations goes higher as the Reynolds number increases, and the stall conditions happen in a smaller angle of attack ( $\alpha = 18^\circ$ ) when Reynolds number is larger.

### 3.5.2 Influence of the airfoil thickness for symmetric airfoils

The influence of the relative thickness of the symmetric airfoil on the unsteady effects generated by the unsteady flow separations at low Reynolds numbers can be studied by

comparing the results shown in Figures 3.27 and 3.28 for the symmetric NACA 0002 and 0008 airfoils at  $Re = 600$ , and the results shown in Figures 3.29 and 3.30 for the same NACA airfoils at  $Re = 1000$ .

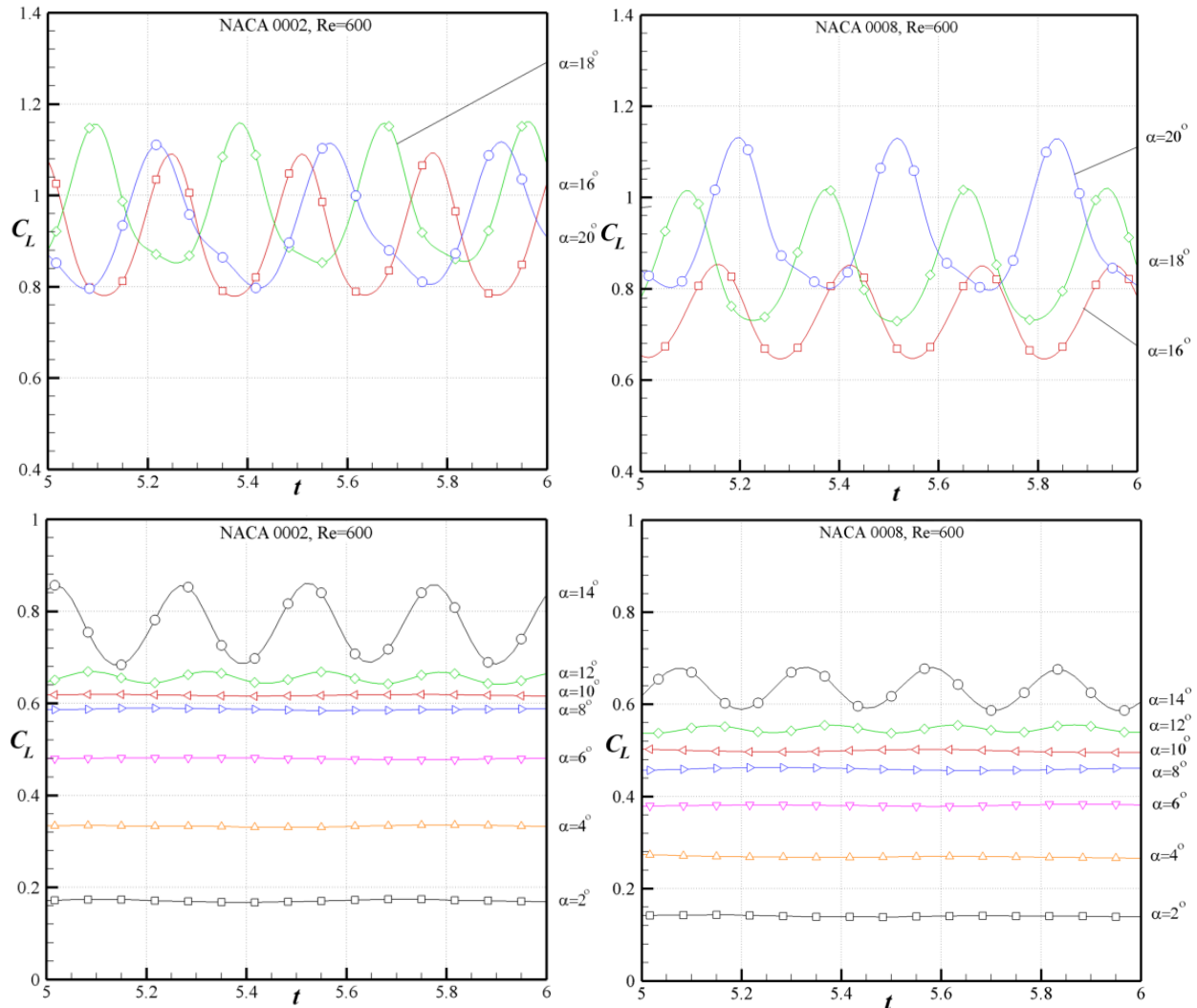


Figure 3.27 Influence of the airfoil thickness for symmetric airfoils. Comparison of the variations with the nondimensional time,  $t = t*U_\infty/c$ , of the lift coefficients,  $C_L$ , of NACA 0002 and 0008 airfoils for Reynolds number  $Re = 600$ , at various angles of attack,  $\alpha$ .

One can be seen that the amplitudes of the oscillations in time of the aerodynamic coefficients are larger for the thinner airfoil, NACA 0002, at the same angle of attack, and that the stall conditions appear at smaller incidence ( $\alpha = 20^\circ$ ) for the thinner airfoil.

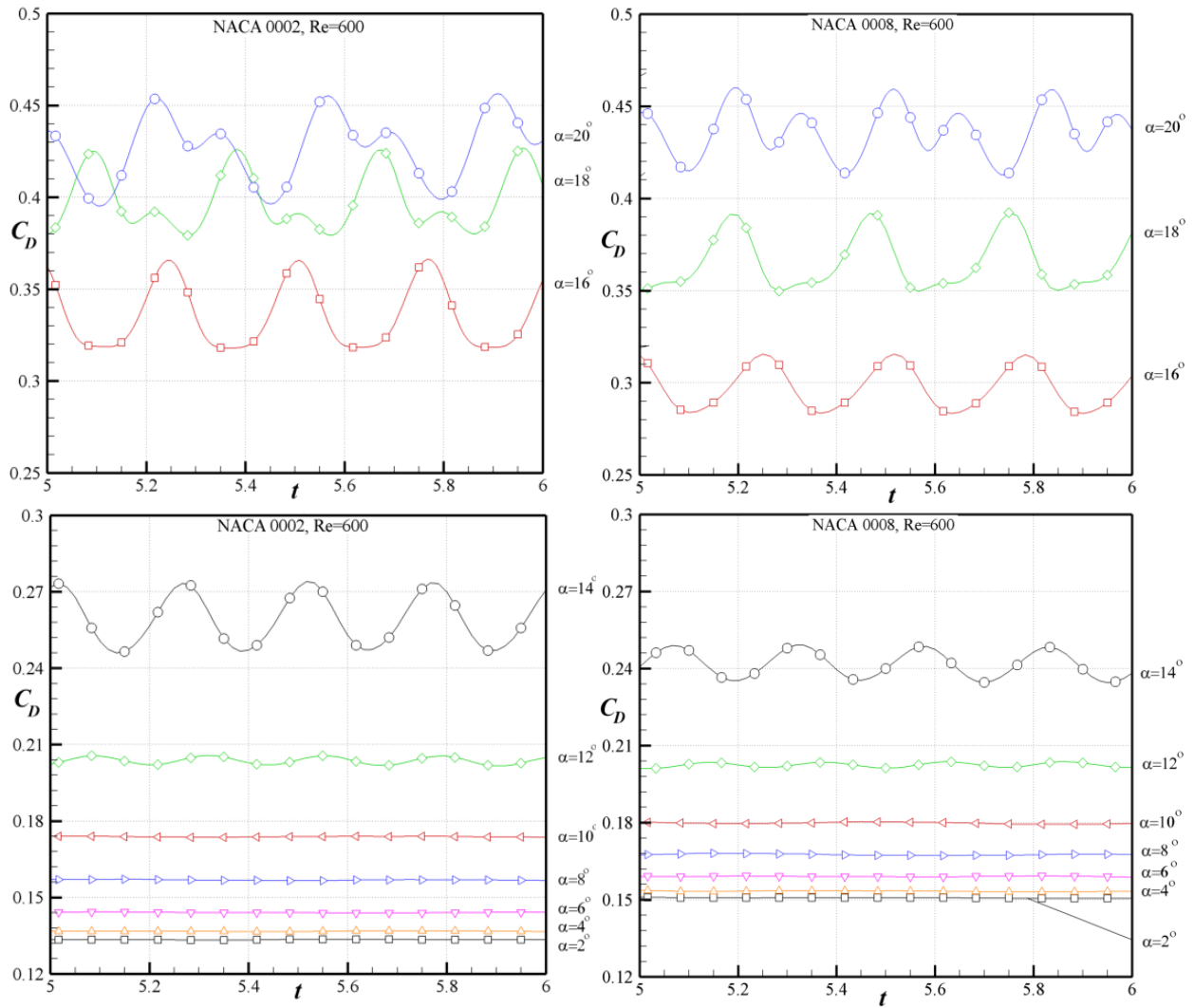


Figure 3.28 Influence of the airfoil thickness for symmetric airfoils. Comparison of the variations with the nondimensional time,  $t = t * U_\infty / c$ , of the drag coefficients,  $C_D$ , of NACA 0002 and 0008 airfoils for Reynolds number  $Re = 600$ , at various angles of attack,  $\alpha$ .

Similar comparisons are shown in Figures 3.29 and 3.30 for a different Reynolds number,  $Re = 1000$ , in order to evaluate influence of the Reynolds number as well as influence of the airfoil thickness for NACA 0004 symmetric airfoil.

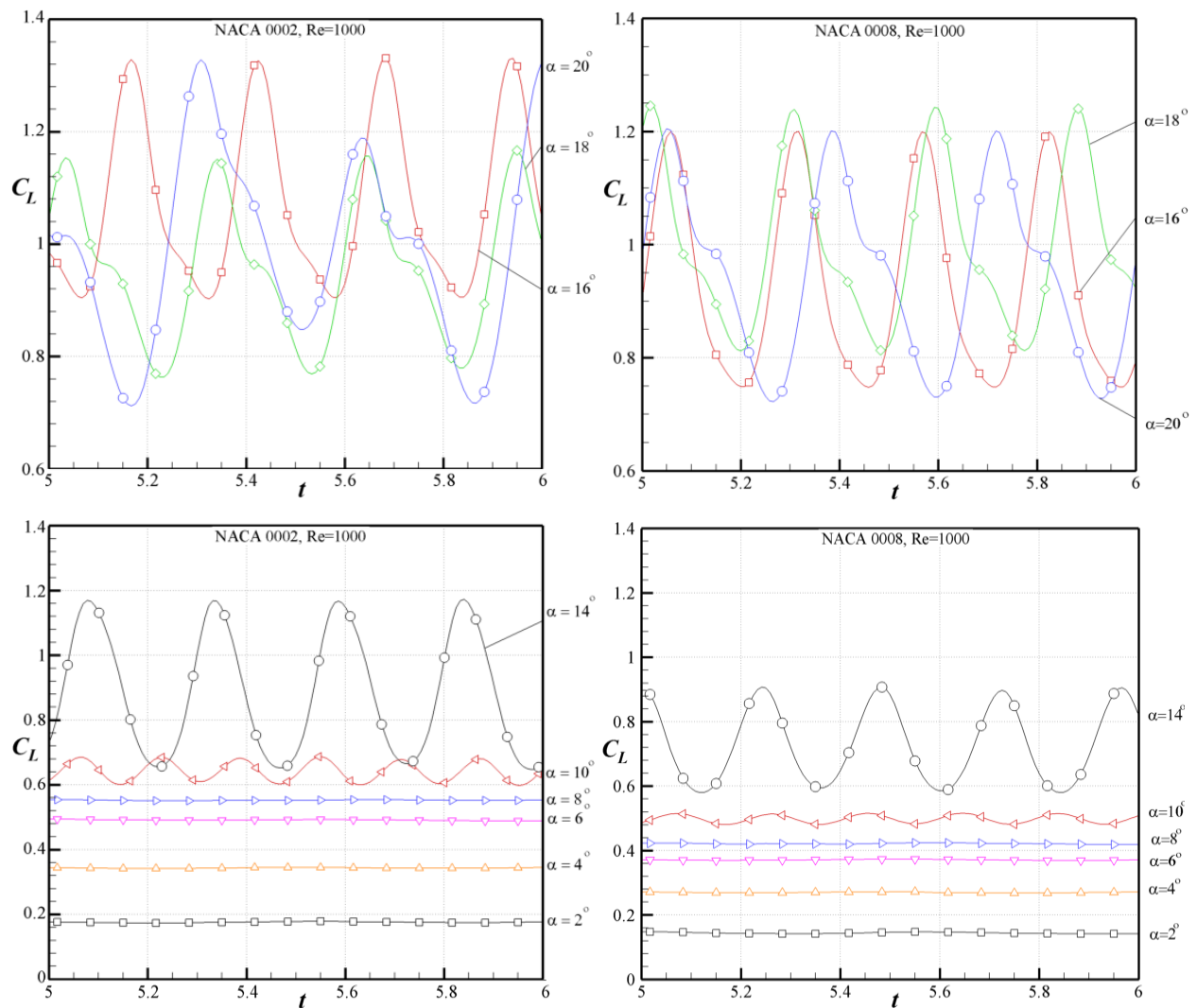


Figure 3.29 Influence of the airfoil thickness for symmetric airfoils. Comparison of the variations with the nondimensional time,  $t = t * U_\infty / c$ , of the lift coefficients,  $C_L$ , of NACA 0002 and 0008 airfoils for Reynolds number  $Re = 1000$ , at various angles of attack,  $\alpha$ .

From the Figures 3.27 and 3.29, it is noticeable that the amplitude of oscillations goes up by increasing the Reynolds number from 600 to 1000 for NACA 0002 airfoil. Also, the stall condition occurs in smaller angle of attack ( $\alpha = 18^\circ$ ) for higher Reynolds number.

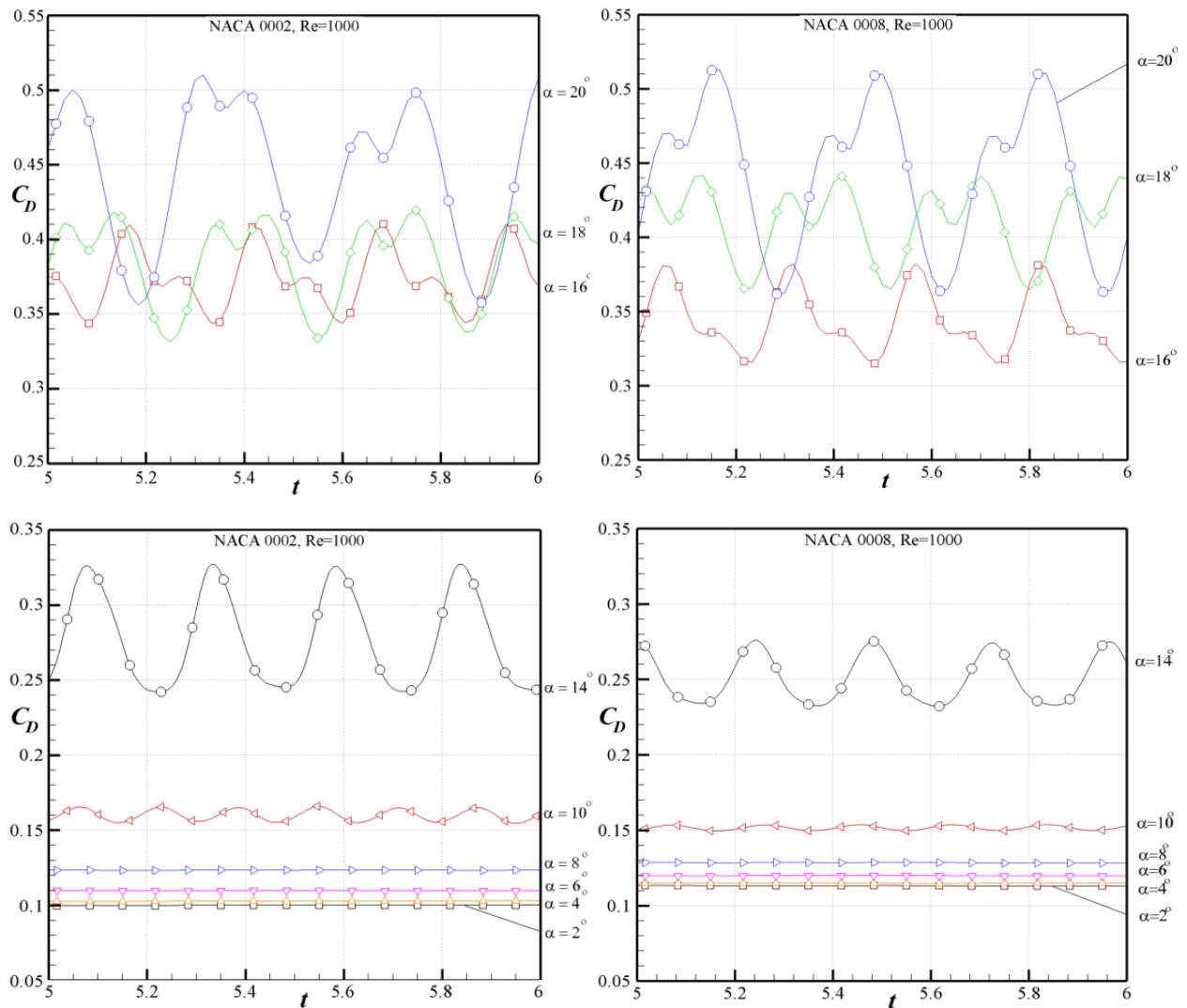


Figure 3.30 Influence of the airfoil thickness for symmetric airfoils. Comparison of the variations with the nondimensional time,  $t = t * U_{\infty} / c$ , of the drag coefficients,  $C_D$ , of NACA 0002 and 0008 airfoils for Reynolds number  $Re = 1000$ , at various angles of attack,  $\alpha$ .

### 3.5.3 Influence of the airfoil thickness for cambered airfoils

The influence of the relative thickness of the cambered airfoil on the unsteady effects generated by the unsteady flow separations at low Reynolds numbers can be studied by comparing the results shown in Figures 3.31 and 3.32 for the NACA 2402 and 2404 airfoils at  $Re = 600$ .

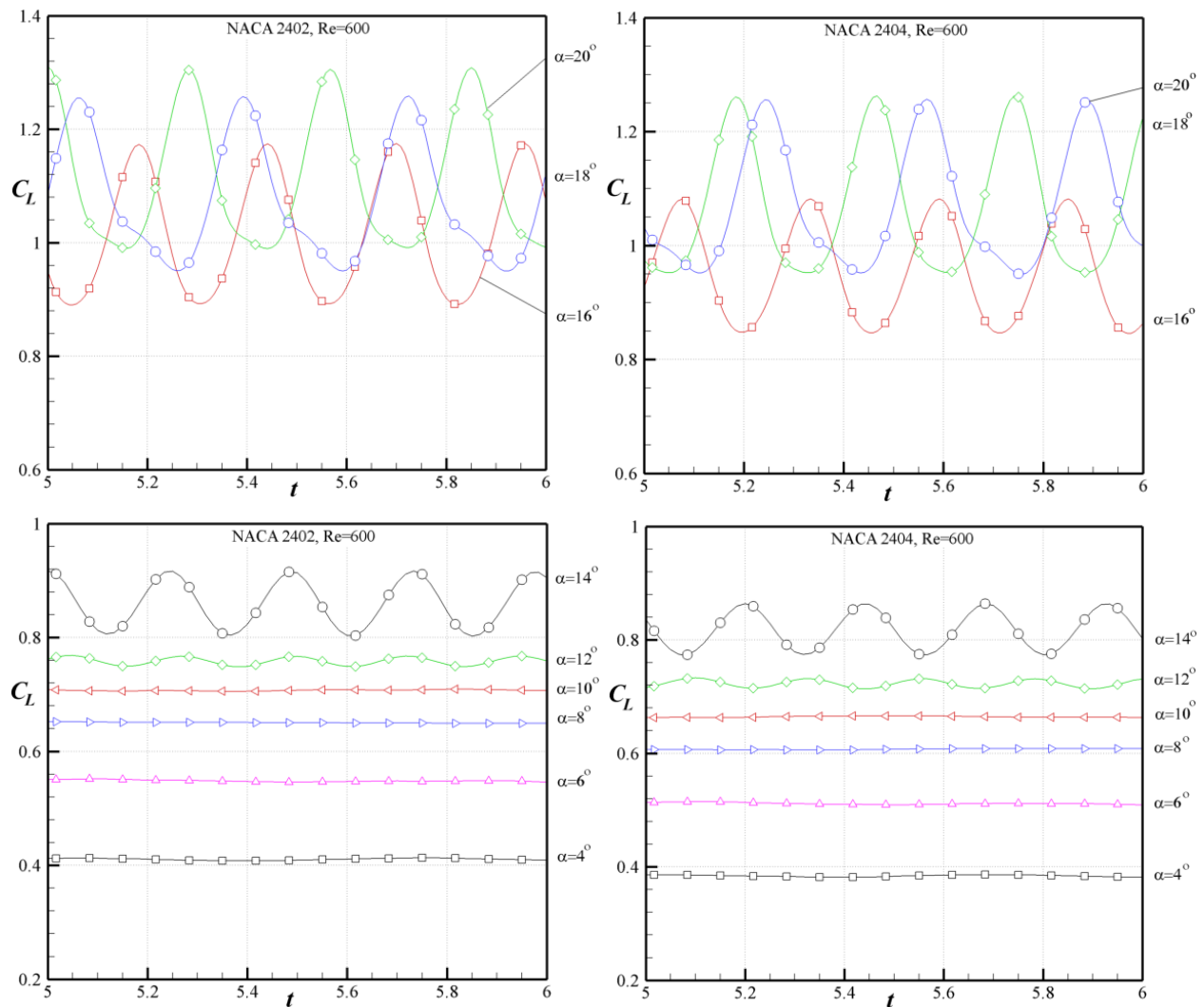


Figure 3.31 Influence of the airfoil thickness for cambered airfoils. Comparison of the variations with the nondimensional time,  $t = t^*U_\infty/c$ , of the lift coefficients,  $C_L$ , of NACA 2402 and 2404 airfoils for Reynolds number  $Re = 600$ , at various angles of attack,  $\alpha$ .

One can observe that, at the same angle of attack, the amplitudes of the oscillations in time of the aerodynamic coefficients are larger for the thinner airfoil, NACA 2402.

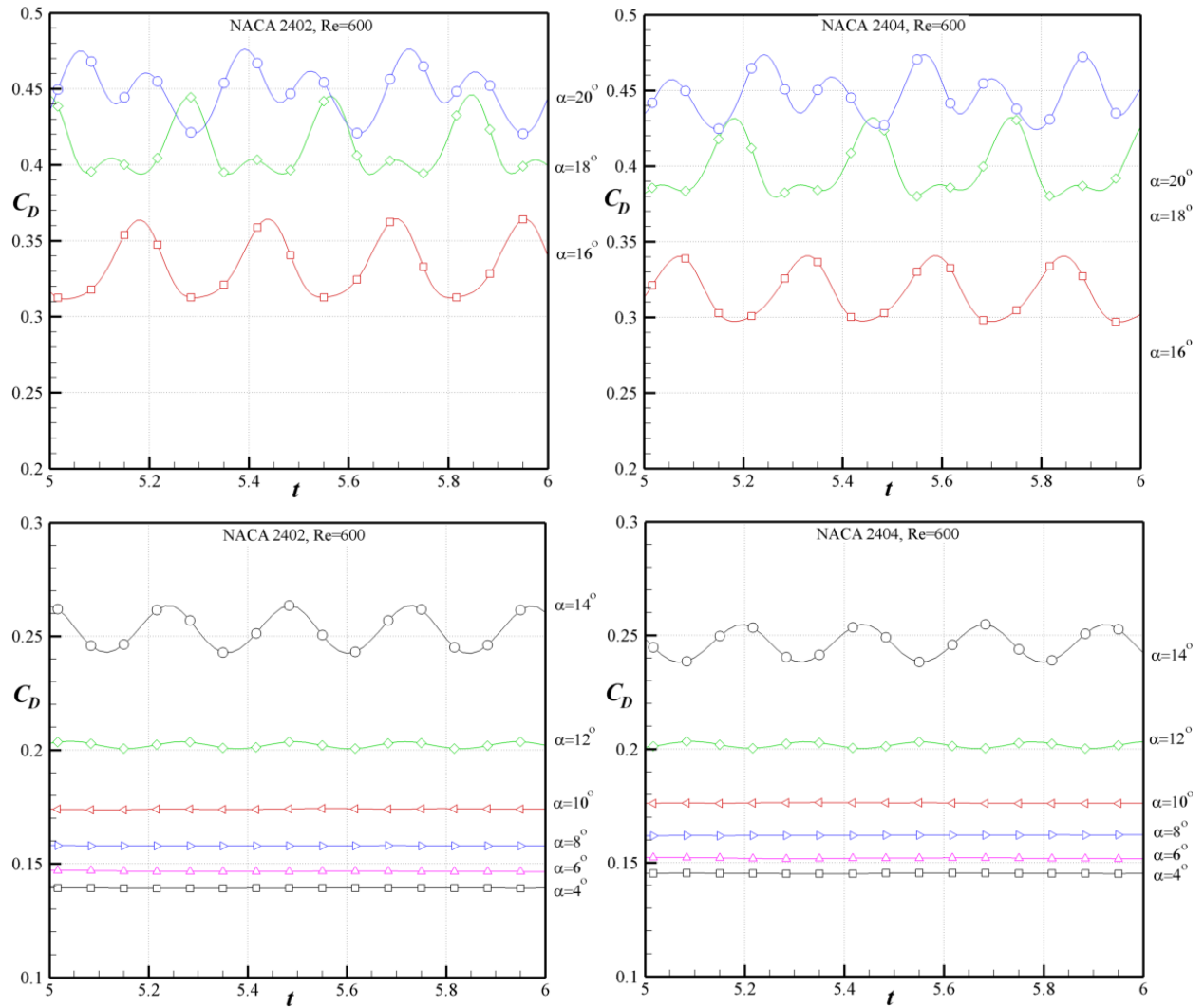


Figure 3.32 Influence of the airfoil thickness for cambered airfoils. Comparison of the variations with the nondimensional time,  $t = t * U_\infty / c$ , of the drag coefficients,  $C_D$ , of NACA 2402 and 2404 airfoils at Reynolds number  $Re = 600$ , for various angles of attack,  $\alpha$ .

### 3.5.4 Influence of the airfoil relative camber

The influence of the relative camber of the airfoil on the unsteady effects generated by the unsteady flow separations at low Reynolds numbers can be studied by comparing the results shown in Figures 3.33 and 3.34 for the cambered airfoils NACA 2404 and 4404.

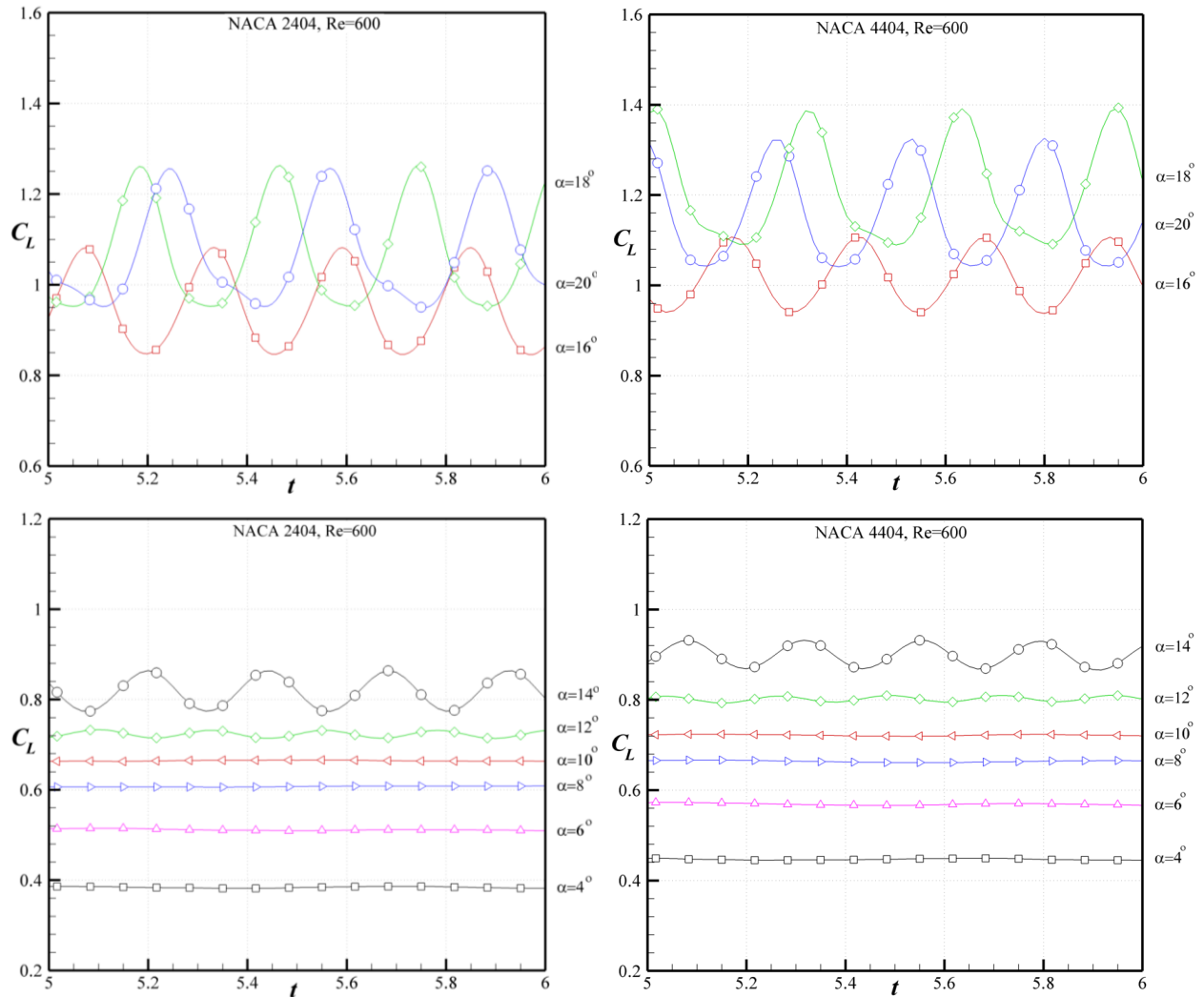


Figure 3.33 Influence of the airfoil relative camber. Comparison of the variations with the nondimensional time,  $t = t * U_\infty / c$ , of the lift coefficients,  $C_L$ , of NACA 2404 and 4404 airfoils for Reynolds number  $Re = 600$ , at various angles of attack,  $\alpha$ .

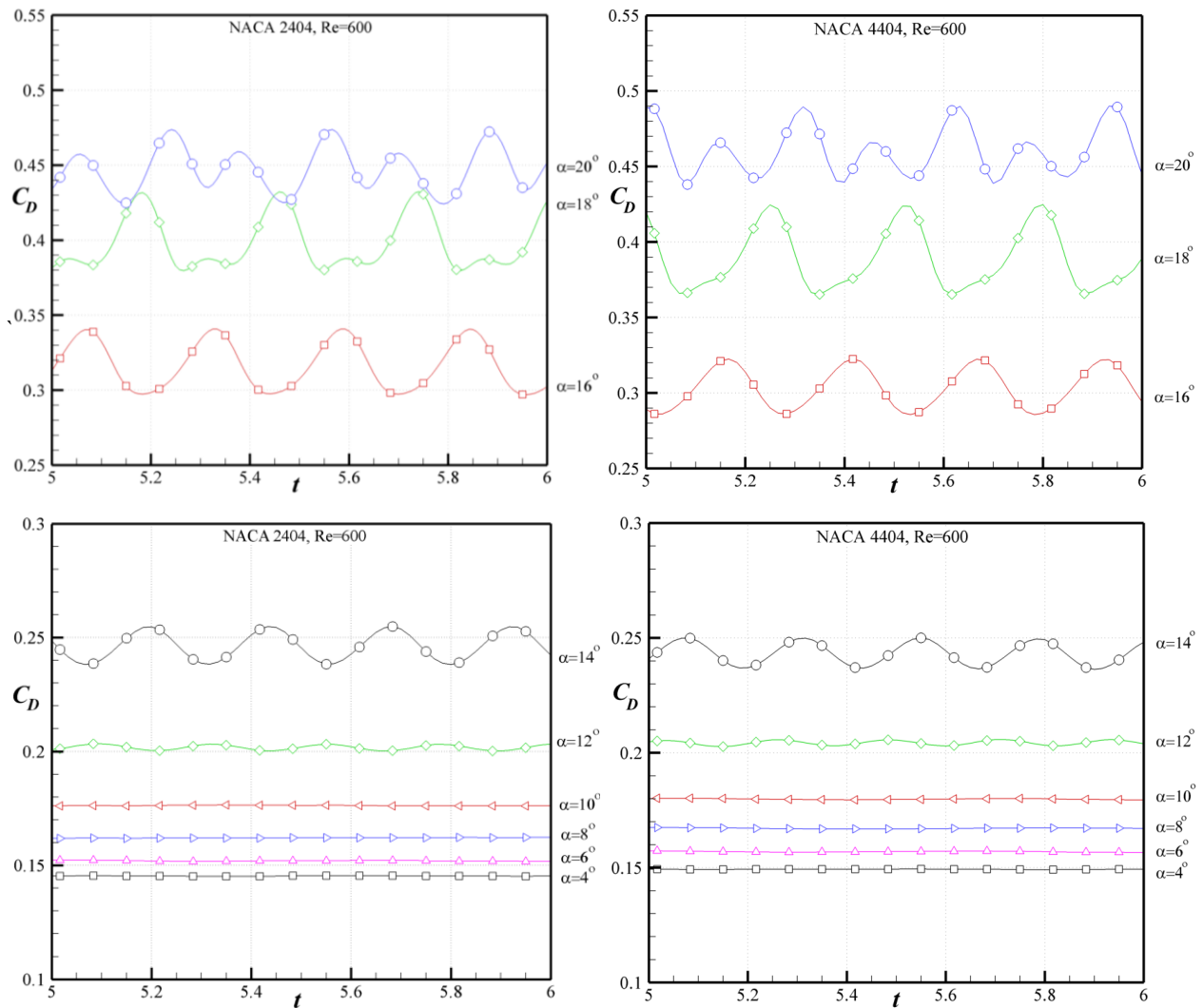


Figure 3.34 Influence of the airfoil relative camber. Comparison of the variations with the nondimensional time,  $t = t * U_{\infty} / c$ , of the lift coefficients,  $C_D$ , of NACA 2404 and 4404 airfoils for Reynolds number  $Re = 600$ , at various angles of attack,  $\alpha$ .

One can notice that, at the same angle of attack, the amplitudes of the oscillations in time of the aerodynamic coefficients are slightly smaller for the more cambered airfoil, NACA 4404.

### 3.6 Summary of findings

In this chapter the unsteady separations effects on the flow past stationary airfoils at low Reynolds numbers have been studied using an efficient time-accurate numerical method for the integration of the Navier-Stokes equations. This numerical method is based on a second-order

three-point-backward implicit scheme for the real time discretization and a pseudo-time relaxation procedure using artificial compressibility and a factored alternate-direction implicit scheme for the pseudo-time integration. A special decoupling procedure using the continuity equation reduces the problem to the solution of scalar-tridiagonal systems of equations, which enhances substantially the computational efficiency of the method.

The solutions obtained for the triangular airfoil were found in good agreement with the experimental results, before the effects of unsteady flow separations become important, since the experimental results were obtained only for steady flows.

This study indicated for the first time that the lift and drag coefficients of the stationary airfoil have oscillations in time generated by the unsteady flow separations on the upper surface of airfoil at low Reynolds numbers, which appear at relatively low angles of attack (about 8 degrees). These flow separations effects on the unsteady aerodynamic coefficients have been studied for various geometric and flow parameters, such as the angle of attack, relative thickness and camber, and Reynolds number.

The obtained results can be used for different engineering applications such as the design of micro aerial vehicles and unmanned aerial vehicles where the flow is relatively at low Reynolds numbers less than 6000.

## **Chapter 4**

### **Analysis of Steady and Unsteady Viscous Flows past Airfoils in the Proximity of the Ground**

The first part of this chapter is dedicated to study the steady and unsteady flows past oscillating airfoils at low Reynolds numbers (from 400 to 6000) in the proximity of the ground. There are many applications including military aircraft and Unmanned-Aerial Vehicles (UAVs) and very small aircrafts called Micro-Air Vehicles (MAVs) that can operate in various indoor or outdoor environments. To date, there are no published studies on steady or unsteady flows past airfoils in the proximity of the ground at these low Reynolds numbers.

The second part of this chapter is devoted to the analysis of unsteady flows past stationary airfoils, generated by the unsteady flow separations at low Reynolds numbers, in the proximity of the ground. It is interesting to analyze the effect of the ground proximity on these unsteady effects on the stationary airfoils at low Reynolds numbers. This study obtains solutions for the oscillations in time of the lift and drag coefficients of several symmetric and cambered airfoils in the proximity of the ground, which are generated by the unsteady flow separations developed on the airfoil upper surface at low Reynolds numbers.

This chapter presents the study of the ground effect on steady and unsteady flows past fixed and oscillating airfoils at low Reynolds numbers. This unsteady flow problem is solved in a rectangular computational domain, obtained from the physical domain by time-dependent coordinate transformations for various sub-domains, in which the boundary conditions are efficiently and rigorously implemented. Solutions for the airfoils in the proximity of the ground at low Reynolds numbers flows are obtained with an efficient numerical method developed by the author for the time-accurate solution of the Navier-Stokes equations, which is second-order accurate in both time and space. This method uses a pseudo-time relaxation procedure based on artificial compressibility, and a factored Alternate-Direction Implicit (ADI) scheme for integration in pseudo-time. A second-order central finite difference formulation is used on a stretched staggered grid, which avoids the odd-and-even points decoupling. A special decoupling procedure based on the continuity equation reduces the problem to the solution of scalar-

tridiagonal systems of equations, which enhances substantially the computational efficiency of the method.

This study analyzes the influence of various geometric and flow parameters, such as the distance to the ground, angle of attack, relative thickness and camber, and Reynolds number on the flow separations occurring on the airfoil upper surface and on the aerodynamic coefficients in the proximity of the ground.

#### 4.1 Problem formulation

Consider a cambered airfoil of chord  $c$  placed at a variable incidence  $\alpha(t)$  in a uniform stream of velocity  $U_\infty$  at a distance  $cH$  above the ground, as shown in Figure 4.1. The airfoil is referred to a Cartesian reference system of coordinates  $cx$  and  $cy$ , where  $x$  and  $y$  are nondimensional coordinates, with the  $x$ -axis along the airfoil chord and its origin at the airfoil leading edge. The airfoil upper and lower surfaces are defined by the equations (4.1).

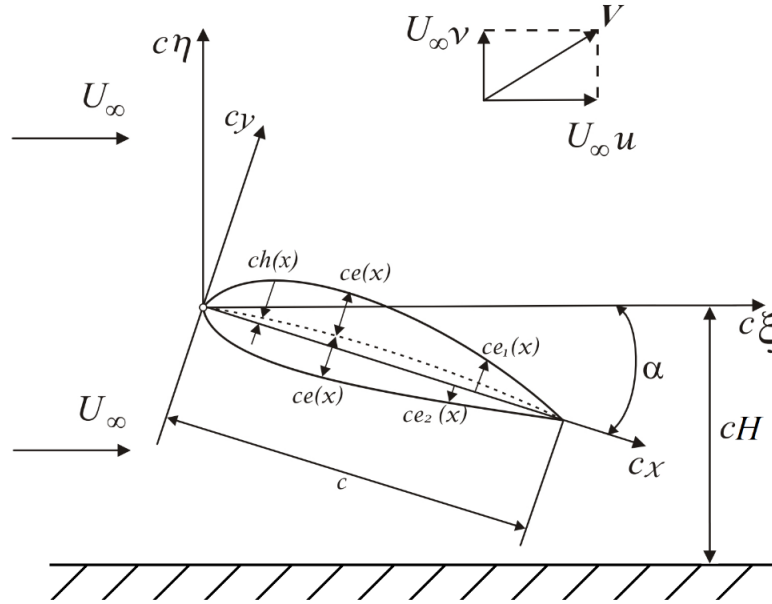


Figure 4.1 Geometry of an oscillating airfoil placed in a uniform flow at the variable incidence,  $\alpha(t) = \alpha_0 + \alpha_A \cos(\omega t)$ , in the proximity of the ground.

$$y = e_1(x) = h(x) + e(x), \quad \text{and} \quad y = -e_2(x) = h(x) - e(x), \quad (4.1)$$

where the subscripts 1 and 2 refer to the upper and lower surfaces, and where  $h(x)$  and  $e(x)$  define the camberline and the airfoil thickness variation along the airfoil chord, respectively. The special case of symmetric airfoils is characterized by  $e_1(x) = e_2(x) = e(x)$  and  $h(x) = 0$ .

The airfoil is assumed to execute harmonic pitching oscillations of frequency  $f$  about a hinge situated at the distance  $cx = ca$  from the leading edge, which is defined by the time variation of the angle attack with respect to the mean incidence  $\alpha_0$ , expressed as

$$\alpha(t) = \alpha_0 + \alpha_A \cos(\omega t), \quad (4.2)$$

where  $\alpha_A$  is the amplitude of oscillations,  $t = t^* U_\infty / c$  is a nondimensional time and  $\omega = 2\pi f c / U_\infty$  is the nondimensional frequency of the oscillations ( $\omega t = 2\pi f t^*$ ). In the steady case, the angle of attack is constant,  $\alpha(t) = \alpha_0 = \text{constant}$ .

The viscous fluid flow past the oscillating airfoil is referred to a fixed Cartesian reference system of coordinates  $c\xi$  and  $c\eta$  are defined by the equations

$$\xi = (x - a) \cos \alpha + y \sin \alpha, \quad \eta = -(x - a) \sin \alpha + y \cos \alpha, \quad (4.3)$$

where  $\xi$  and  $\eta$  are nondimensional coordinates with respect to the airfoil chord  $c$ , with the  $\xi$ -axis parallel to the uniform stream velocity  $U_\infty$  (inclined with the angle  $\alpha$  with respect to the airfoil chord) and with its origin at  $x = a$  (at the airfoil rotational hinge, as shown in Figure 4.1).

Let  $U_\infty u$  and  $U_\infty v$  denote the fluid velocity components along the fixed  $\xi$ - and  $\eta$ -axes, where  $u$  and  $v$  are the nondimensional velocity components with respect to  $U_\infty$ .

Applying the conservation of mass and Newton's second laws to an infinitesimal and fixed control volume yield the continuity and momentum equations in nondimensional conservation

$$\text{form as, } \frac{\partial \mathbf{V}}{\partial t} + \mathbf{Q}(\mathbf{V}, p) = \mathbf{0}, \quad \nabla \cdot \mathbf{V} = \frac{\partial u}{\partial \xi} + \frac{\partial v}{\partial \eta} = 0, \quad (4.4)$$

where  $t = t^* U_\infty / c$  is the nondimensional time ( $t^*$  is the dimensional time),  $\mathbf{V} = \{u, v\}^T$  represents the vector of the dimensionless velocity components and  $\mathbf{Q}(\mathbf{V}, p)$ , which includes the convective derivative, pressure and viscous terms, can be expressed in two-dimensional Cartesian coordinates in the form

$$Q_u(u, v, p) = \frac{\partial(uu)}{\partial \xi} + \frac{\partial(vu)}{\partial \eta} + \frac{\partial p}{\partial \xi} - \frac{1}{\text{Re}} \left( \frac{\partial^2 u}{\partial \xi^2} + \frac{\partial^2 u}{\partial \eta^2} \right), \quad (4.5)$$

$$Q_v(u, v, p) = \frac{\partial(uv)}{\partial\xi} + \frac{\partial(vv)}{\partial\eta} + \frac{\partial p}{\partial\eta} - \frac{1}{\text{Re}} \left( \frac{\partial^2 v}{\partial\xi^2} + \frac{\partial^2 v}{\partial\eta^2} \right), \quad (4.6)$$

$$\nabla \cdot \mathbf{V} = \frac{\partial u}{\partial\xi} + \frac{\partial v}{\partial\eta} \quad (4.7)$$

## 4.2 Method of solution

The problem is solved in a similar method that was explained in details in chapter 3. For an efficient and rigorous implementation of the moving boundary conditions, the problem is solved in a fixed rectangular computational domain with six sub-domains (indicated in Figure 4.2), which is obtained from the physical domain by a time-dependent geometrical transformation defined as

$$X = g(\xi, \eta, t), \quad Y = f(\xi, \eta, t), \quad t = t, \quad (4.8)$$

where  $g(\xi, \eta, t)$  and  $f(\xi, \eta, t)$  are defined for each domain in the following forms:

**Domain 1** (for  $x < 0$  and  $a \sin \alpha(t) < \eta < H_1$ ):

$$g(\xi, \eta, t) = \frac{\xi \cos \alpha(t) - \eta \sin \alpha(t) + a}{L_0 \cos \alpha(t) + \eta \sin \alpha(t) - a} L_0, \quad f(\xi, \eta, t) = \frac{\eta - a \sin \alpha(t)}{H_1 - a \sin \alpha(t)} H_1 \quad (4.9)$$

**Domain 2** (for  $x < 0$  and  $-H < \eta < a \sin \alpha(t)$ ):

$$g(\xi, \eta, t) = \frac{\xi \cos \alpha(t) - \eta \sin \alpha(t) + a}{L_0 \cos \alpha(t) + \eta \sin \alpha(t) - a} L_0, \quad f(\xi, \eta, t) = \frac{\eta - a \sin \alpha(t)}{H + a \sin \alpha(t)} H \quad (4.10)$$

**Domain 3** (for  $0 < x < 1$  and  $e_1(x) < y < H_1$ ):

$$g(\xi, \eta, t) = \xi \cos \alpha(t) - \eta \sin \alpha(t) + a, \\ f(\xi, \eta, t) = \frac{y - e_1(x)}{H_1 - e_1(x) \cos \alpha(t) + (x - a) \sin \alpha(t)} H_1 \cos \alpha(t) \quad (4.11)$$

**Domain 4** (for  $0 < x < 1$  and  $-H < y < -e_2(x)$ ):

$$g(\xi, \eta, t) = \xi \cos \alpha(t) - \eta \sin \alpha(t) + a, \\ f(\xi, \eta, t) = \frac{y + e_2(x)}{H - e_2(x) \cos \alpha(t) - (x - a) \sin \alpha(t)} H \cos \alpha(t) \quad (4.12)$$

**Domain 5** (for  $x > 1$  and  $-(1-a) \sin \alpha(t) < \eta < H_1$ ):

$$g(\xi, \eta, t) = \frac{\xi \cos \alpha(t) - \eta \sin \alpha(t) - 1 + a}{L_1 \cos \alpha(t) - \eta \sin \alpha(t) - 1 + a} (L_1 - 1) + 1,$$

$$f(\xi, \eta, t) = \frac{\eta + (1-a)\sin\alpha(t)}{H_1 + (1-a)\sin\alpha(t)} H_1 \quad (4.13)$$

**Domain 6** (for  $x > 1$  and  $-H < \eta < -(1-a)\sin\alpha(t)$ ):

$$g(\xi, \eta, t) = \frac{\xi \cos\alpha(t) - \eta \sin\alpha(t) - 1 + a}{L_1 \cos\alpha(t) - \eta \sin\alpha(t) - 1 + a} (L_1 - 1) + 1,$$

$$f(\xi, \eta, t) = \frac{\eta + (1-a)\sin\alpha(t)}{H - (1-a)\sin\alpha(t)} H \quad (4.14)$$

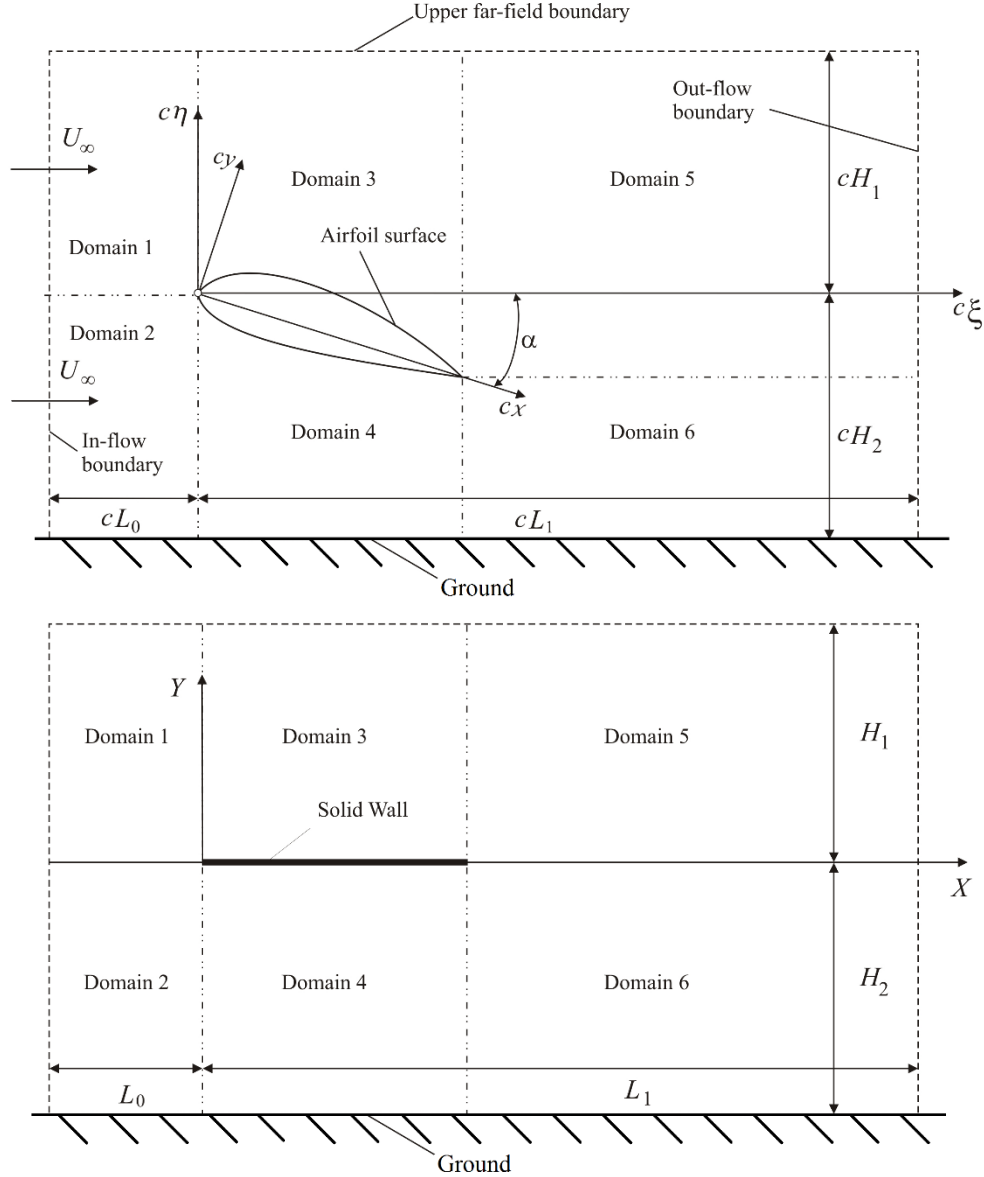


Figure 4.2 Geometry of the physical  $(\eta, \xi)$  and fixed computational domain  $(X, Y)$  defined by the time-dependent coordinate transformations from equations (4.8) to (4.14).

In equations 4.11 and 4.12,  $x$  and  $y$  are defined in function of the fixed coordinates  $\xi$  and  $\eta$  by the relations

$$x = \xi \cos \alpha - \eta \sin \alpha + a, \quad y = \xi \sin \alpha + \eta \cos \alpha \quad (4.15)$$

In these equations,  $\eta = H_1$  and  $\eta = -H_2 = H$  are the nondimensional physical coordinates of the upper and lower boundaries of the computational domain, and  $\xi = -L_0$ ,  $\xi = L_1$  are the nondimensional physical coordinates of the inflow and outflow boundaries, as shown in Figure 4.2.

In the computational domain  $(X, Y)$ , the upstream inflow and downstream outflow boundaries and the upper and lower boundaries are defined by the nondimensional coordinates  $X = -L_0$ ,  $X = L_1$  and  $Y = H_1$ ,  $Y = -H$ , respectively.

In this fixed computational domain, the Navier-Stokes and continuity equations can be expressed as

$$\frac{\partial \mathbf{V}}{\partial t} + \mathbf{G}(\mathbf{V}, p) = 0, \quad D\mathbf{V} = 0, \quad (4.16)$$

where

$$\mathbf{V} = \{u, v\}^T, \quad \mathbf{G}(\mathbf{V}, p) = \{G_u(u, v, p), G_v(u, v, p)\}^T, \quad (4.17)$$

$$G_u(u, v, p) = C_9 \frac{\partial u}{\partial X} + C_4 \frac{\partial u}{\partial Y} + C_7 \frac{\partial(uu)}{\partial X} + C_2 \frac{\partial(uu)}{\partial Y} + C_8 \frac{\partial(vu)}{\partial X} + C_3 \frac{\partial(vu)}{\partial Y} \\ + C_7 \frac{\partial p}{\partial X} + C_2 \frac{\partial p}{\partial Y} + C_1 \frac{\partial^2 u}{\partial X^2} + C_6 \frac{\partial^2 u}{\partial X \partial Y} + C_5 \frac{\partial^2 u}{\partial Y^2}, \quad (4.18)$$

$$G_v(u, v, p) = C_9 \frac{\partial v}{\partial X} + C_4 \frac{\partial v}{\partial Y} + C_7 \frac{\partial(vu)}{\partial X} + C_2 \frac{\partial(vu)}{\partial Y} + C_8 \frac{\partial(vv)}{\partial X} + C_3 \frac{\partial(vv)}{\partial Y} \\ + C_7 \frac{\partial p}{\partial X} + C_6 \frac{\partial p}{\partial Y} + C_1 \frac{\partial^2 v}{\partial X^2} + C_6 \frac{\partial^2 v}{\partial X \partial Y} + C_5 \frac{\partial^2 v}{\partial Y^2}, \quad (4.19)$$

$$D\mathbf{V} = C_7 \frac{\partial u}{\partial X} + C_2 \frac{\partial u}{\partial Y} + C_8 \frac{\partial v}{\partial X} + C_3 \frac{\partial v}{\partial Y}, \quad (4.20)$$

in which the expressions of the coefficients  $C_1, C_2, C_3, \dots, C_9$  are obtained for each domain from the time-dependent coordinate transformations (4.8) to (4.14). These coefficients are given in Appendix B.

No-slip boundary conditions are implemented on the airfoil contour and non-penetration condition (zero normal velocity component) are implemented on the upper and lower boundaries of the computational domain.

In a similar manner as it was explained in chapter 3, the equations (4.18) to (4.20) are further spatially discretized by central differencing on a stretched staggered grid, in which the flow variables  $u$ ,  $v$  and  $p$  are defined at different positions. By using ADI scheme the equations are transformed to a set of scalar equations in order to solve the problem more effectively.

### 4.3 Method validation for steady flows past airfoils far from the ground

The method has been first validated by comparison with the results obtained by Kunz and Kroo [28] and by Mateescu and Abdo [9, 10] for several NACA airfoils without the presence of the ground which were found in very good agreement with the present solutions for airfoils far from the ground ( $H = 12$ ). Two examples of validation results are presented in Figures 4.3 and 4.4 for the lift coefficient and for the pressure coefficient distribution.

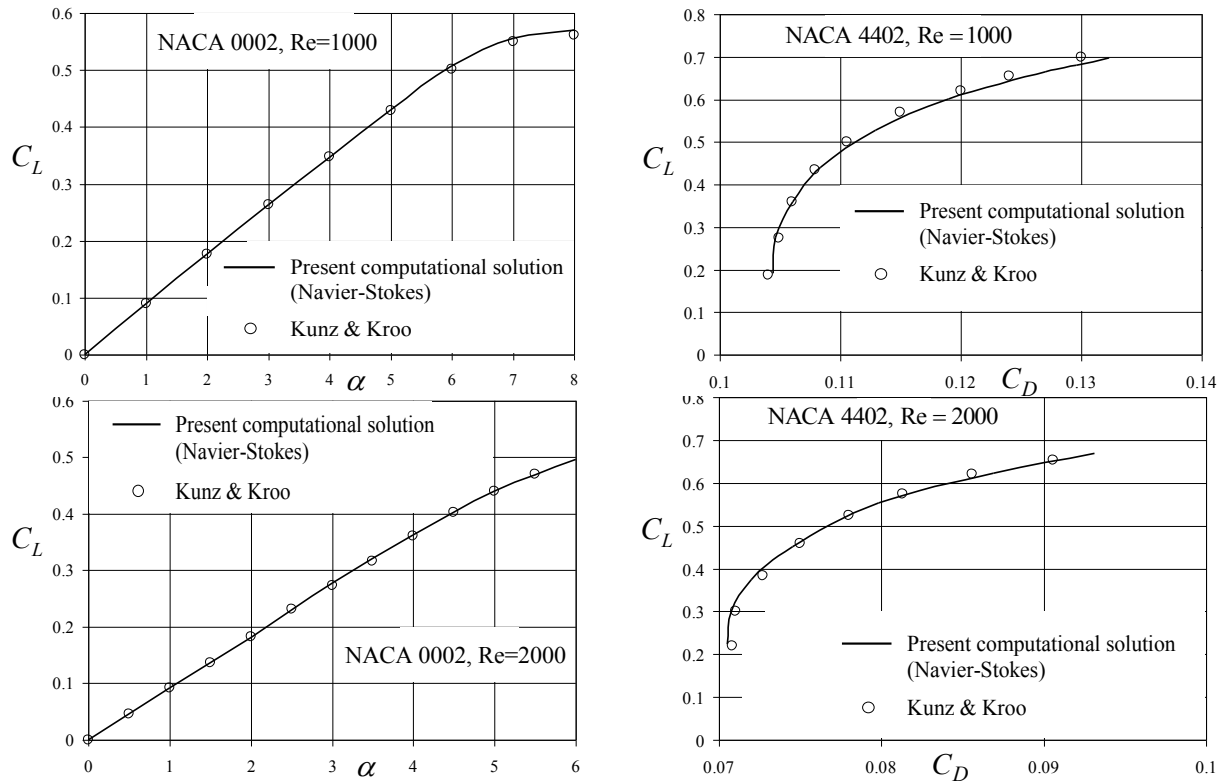


Figure 4.3 Present solutions for  $H = 12$  (no ground effect) for the lift coefficient of the isolated NACA 0002 and for the drag polar diagram for the isolated NACA 4402 airfoil for  $Re = 1000$  and 2000, compared with the results obtained by Kunz and Kroo [28].

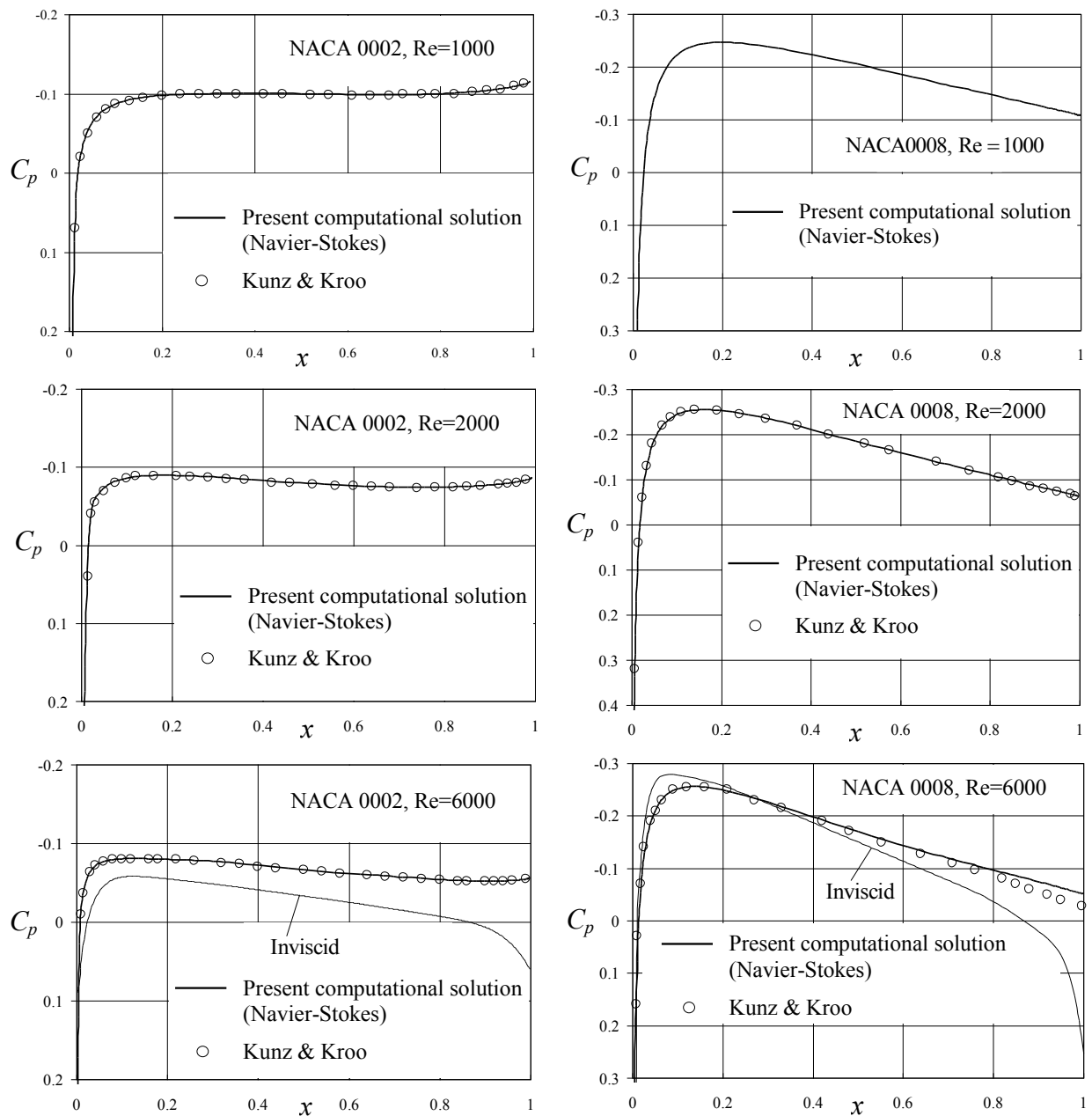


Figure 4.4 Present solutions obtained for  $H = 12$  (no ground effect) for the pressure coefficient distribution on the NACA 0002 and NACA 0008 airfoils at zero incidence for Reynolds numbers  $Re = 1000, 2000$  and  $6000$ , compared with results obtained by Kunz and Kroo [28] and by Mateescu and Abdo [9, 10] for inviscid flows.

#### 4.4 Ground effect on the steady flows past airfoils at low Reynolds numbers

The method of solution has been first applied to obtain solutions for the steady flows past airfoils in the proximity of the ground for various low Reynolds numbers and various distances to the ground.

The effect of the distance to the ground on the aerodynamic coefficients is illustrated in Figures 4.5 and 4.6, presenting the variations with the angle of attack  $\alpha$  of the lift and drag coefficients,  $C_L$  and  $C_D$ , and of the lift-to-drag ratio,  $C_L/C_D$ , for several symmetric and cambered NACA airfoils at several Reynolds numbers,  $Re$ , and for the distances to the ground  $H = 0.3$ ,  $H = 0.5$  and  $H = 12$  (no ground effect).

Figure 4.5 illustrates the influence of the Reynolds number on the ground effect for the lift and drag coefficients of the NACA 0004 airfoil at various low Reynolds numbers.

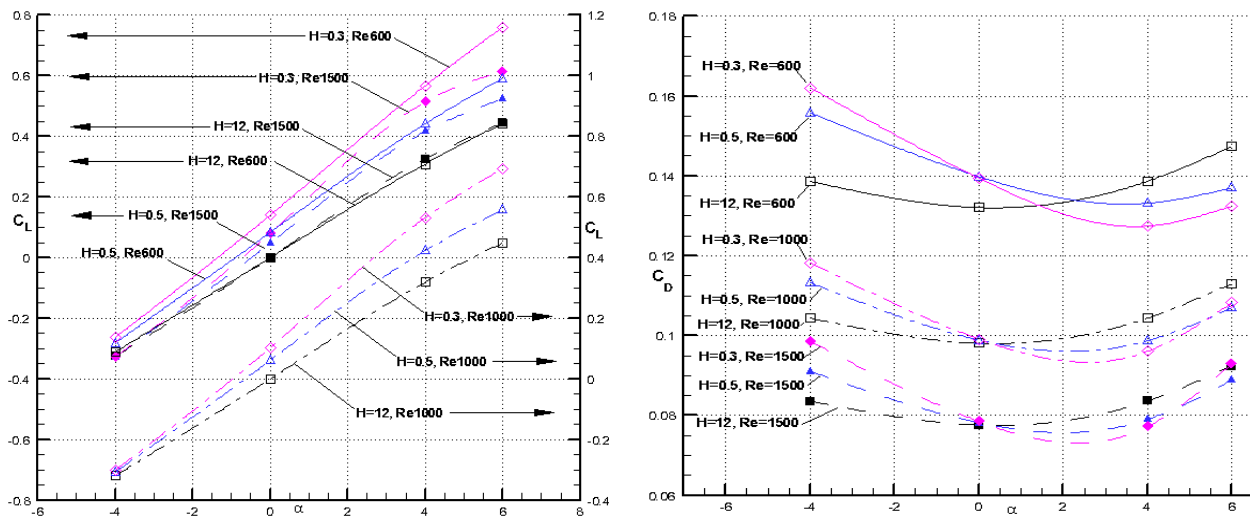


Figure 4.5 Influence of the Reynolds number. Typical variations of the lift and drag coefficients,  $C_L$  and  $C_D$ , with the angle of attack  $\alpha$  for NACA 0004 airfoil at  $Re = 600$ ,  $1000$  and  $1500$ , for three nondimensional distances to the ground:  $H = 0.3$ ,  $H = 0.5$  and  $H = 12$  (no ground effect).

The influence of the relative thickness and relative camber on the variations with the angle of attack  $\alpha$  of the lift and drag coefficients,  $C_L$  and  $C_D$ , and of the lift-to-drag ratio,  $C_L/C_D$ , is illustrated in Figure 4.6 for three symmetric airfoils NACA 0002, NACA 0004, NACA 0008 and three cambered airfoils NACA 2404, NACA 4404, NACA 6404 at  $Re = 1000$  for three nondimensional distances to the ground:  $H = 0.3$ ,  $H = 0.5$  and  $H = 12$  (no ground effect).

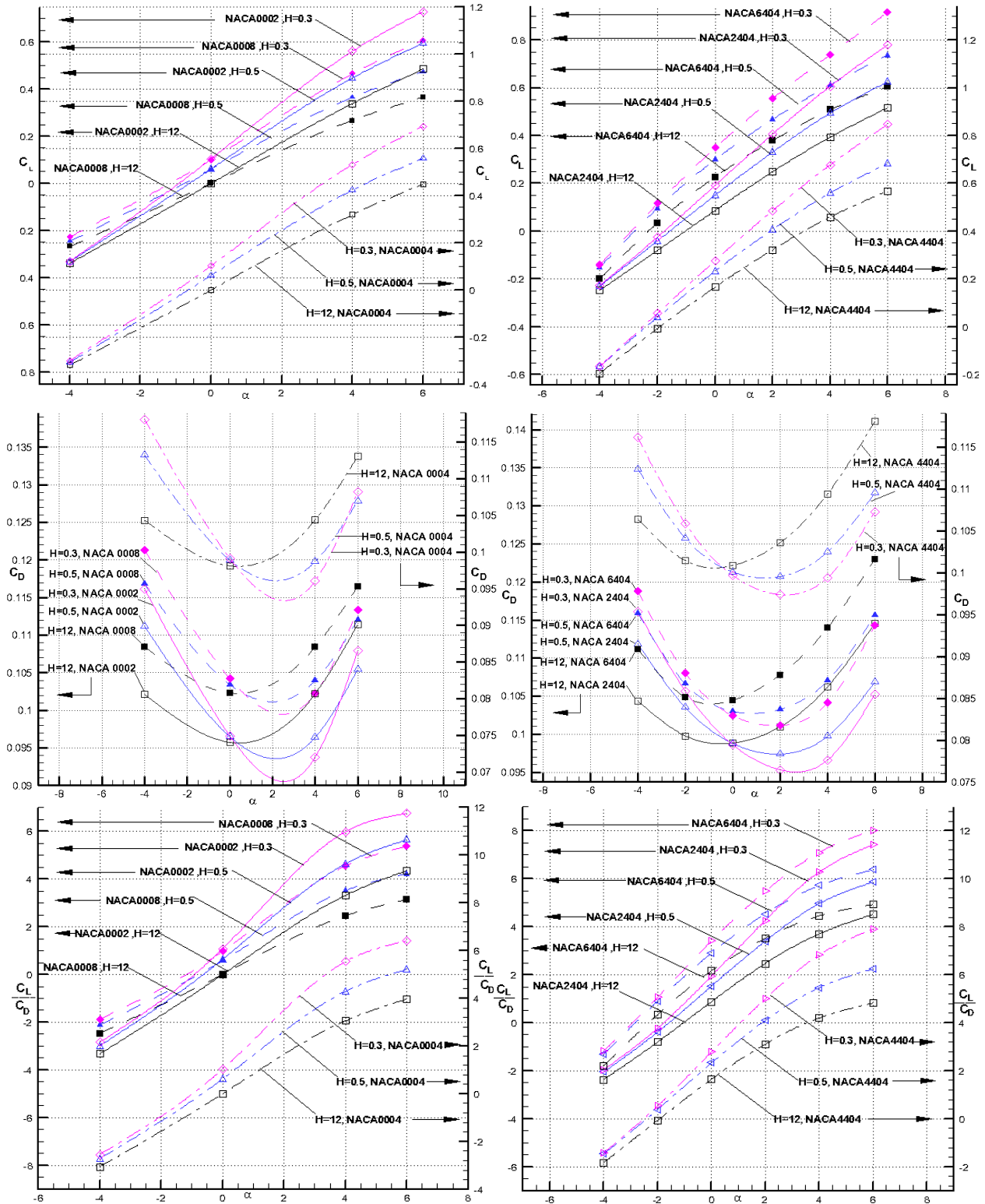


Figure 4.6 Lift and drag coefficients,  $C_L$ ,  $C_D$ , and the lift-to-drag ratio,  $C_L/C_D$ , versus the angle of attack  $\alpha$  for  $Re = 1000$  for the nondimensional distances to the ground  $H = 0.3$ ,  $H = 0.5$  and  $H = 12$  (no ground effect).

The analysis of the flow revealed that flow separations appear on the upper surface of the airfoil at lower angles of attack due to the proximity of the ground. This is seen in Figure 4.7 which illustrates the streamline pattern of the flow around three airfoils NACA 0002, NACA 0004 and NACA 0008 for Reynolds number,  $Re = 1000$ , and at the angle of attack  $\alpha = 6^\circ$ .

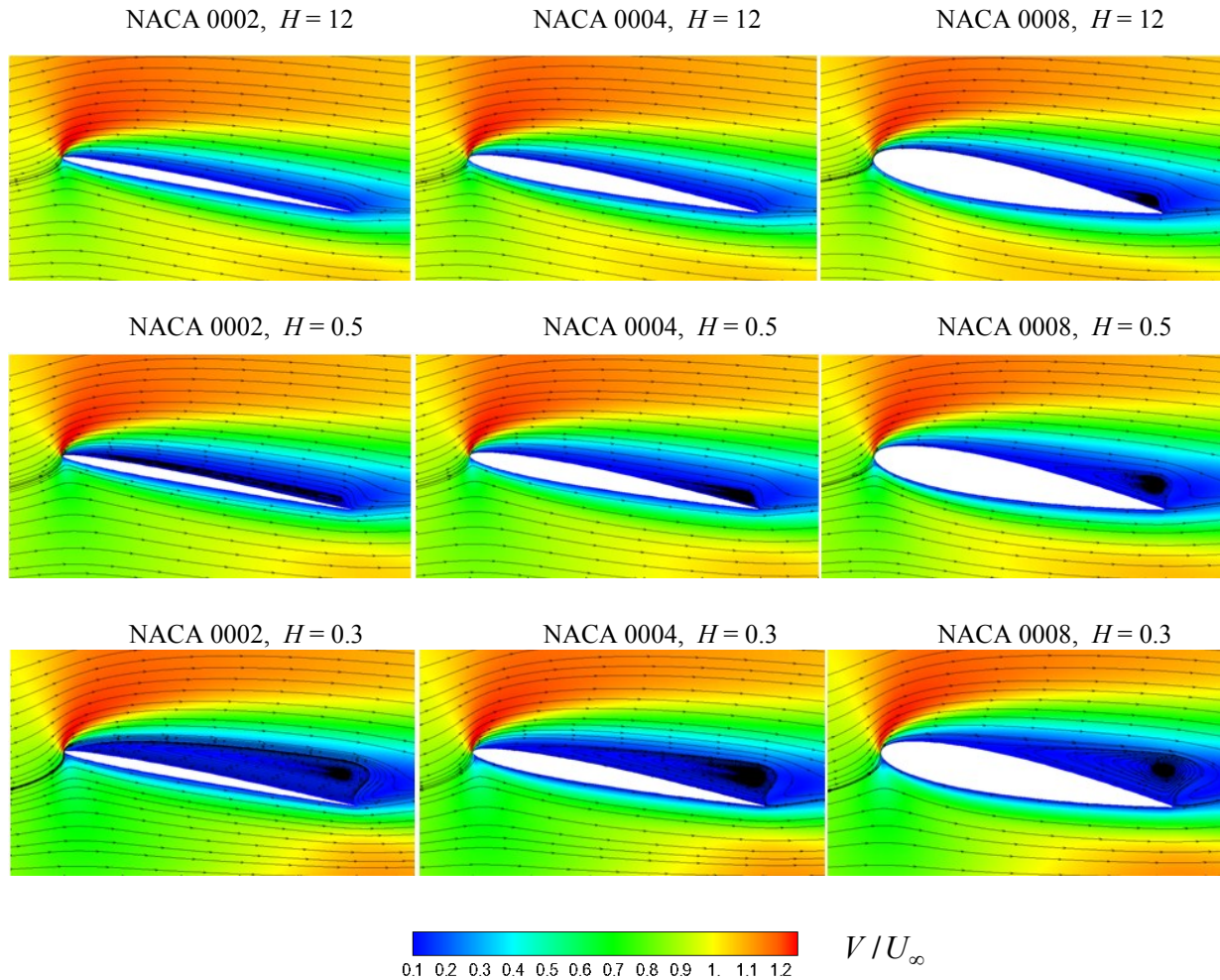


Figure 4.7 Illustration of the flow separation on the upper surface of three NACA airfoils at angle of attack  $\alpha = 6^\circ$  and Reynolds number  $Re = 1000$  for the several distances to the ground  $H = 0.3$ ,  $H = 0.5$  and  $H = 12$  (no ground effect). The lines show the streamline patterns of the flow around the airfoil and the color shades indicate the nondimensional velocity fields (with respect to the uniform stream velocity  $U_\infty$  )

It is noticeable that in the proximity of the ground (for  $H = 0.5$  and especially for  $H = 0.3$ ) there are important flow separation regions on the upper surface of the airfoils, while very far

from the ground ( $H = 12$ ) there is no flow separation for the thinner airfoils (NACA 0002 and 0004) and a smaller flow separation region for NACA 0008 airfoil.

The influence of the Reynolds number on the flow separation on the NACA 0004 airfoil at angle of attack  $\alpha = 6^\circ$  is illustrated in Figure 4.8 for three Reynolds numbers,  $Re = 600, 1000$  and  $1500$ . One can observe that the flow separation region becomes larger with the increase in the Reynolds number and in the closer proximity of the ground.

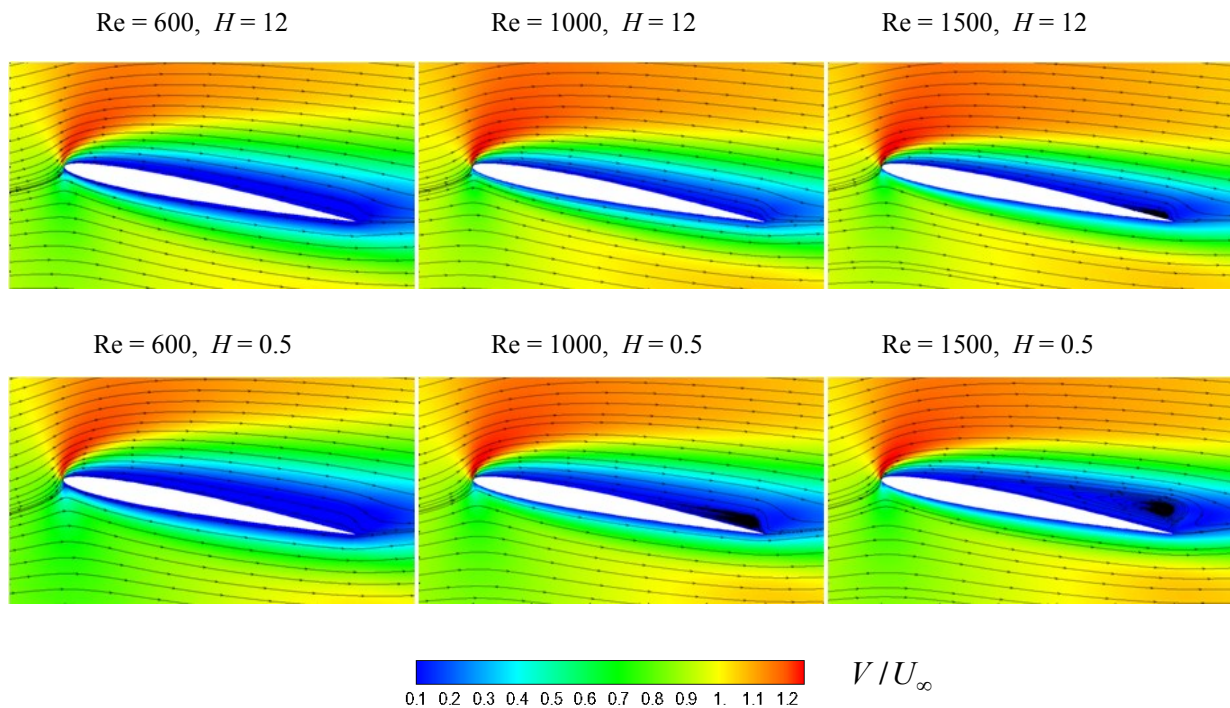


Figure 4.8 Illustration of the flow separation for NACA 0004 airfoil at angle of attack  $\alpha = 6^\circ$  for three Reynolds numbers,  $Re = 600, 1000$  and  $1500$  and for two distances to the ground:  $H = 0.5$  and  $H = 12$  (no ground effect)

## 4.5 Unsteady flow solutions for oscillating airfoils in the proximity of the ground at low Reynolds numbers

The numerical method presented in section 4.2 has been then applied to obtain solutions for the unsteady flows past airfoils executing pitching oscillations with respect to the leading edge ( $a = 0$ ) in the proximity of the ground for various low Reynolds numbers.

### 4.5.1 Influence of the Reynolds number

The influence of the Reynolds number and the distance to the ground on the unsteady lift and drag coefficients,  $C_L$ ,  $C_D$ , and on the unsteady lift-to-drag ratio  $C_L/C_D$ , is illustrated in Figures 4.9 and 4.10 for NACA 0002 and NACA 0004 airfoils executing pitching oscillations  $\alpha(t) = \alpha_0 + \alpha_A \cos(\omega t)$ , with  $\alpha_0 = 0^\circ$ ,  $\alpha_A = 4^\circ$  and  $\omega = 0.05$ , at  $Re = 600$  and  $1000$  for three distances to the ground:  $H = 0.3$ ,  $H = 0.5$  and  $H = 12$  (no ground effect).

The influence of the Reynolds number and the distance to the ground on the unsteady pitching moment coefficient,  $C_m$ , is illustrated in Figure 4.11 for NACA 0002 and NACA 0004 airfoils executing pitching oscillations  $\alpha(t) = \alpha_0 + \alpha_A \cos(\omega t)$ , with  $\alpha_0 = 0^\circ$ ,  $\alpha_A = 4^\circ$  and  $\omega = 0.05$ , at  $Re = 600$  and  $1000$  for three distances to the ground:  $H = 0.3$ ,  $H = 0.5$  and  $H = 12$  (no ground effect).

### 4.5.2 Influence of the airfoil relative thickness

The influence of the airfoil relative thickness and of the Reynolds number with the distance to the ground on the unsteady lift and drag coefficients,  $C_L$ ,  $C_D$  and on the lift-to-drag ratio  $C_L/C_D$ , is illustrated in Figure 4.12 for NACA 0002, NACA 0004 and NACA 0008 airfoils executing pitching oscillations  $\alpha(t) = \alpha_0 + \alpha_A \cos(\omega t)$ , with  $\alpha_0 = 0^\circ$ ,  $\alpha_A = 4^\circ$  and  $\omega = 0.05$ , at  $Re = 1000$  for three distances to the ground.

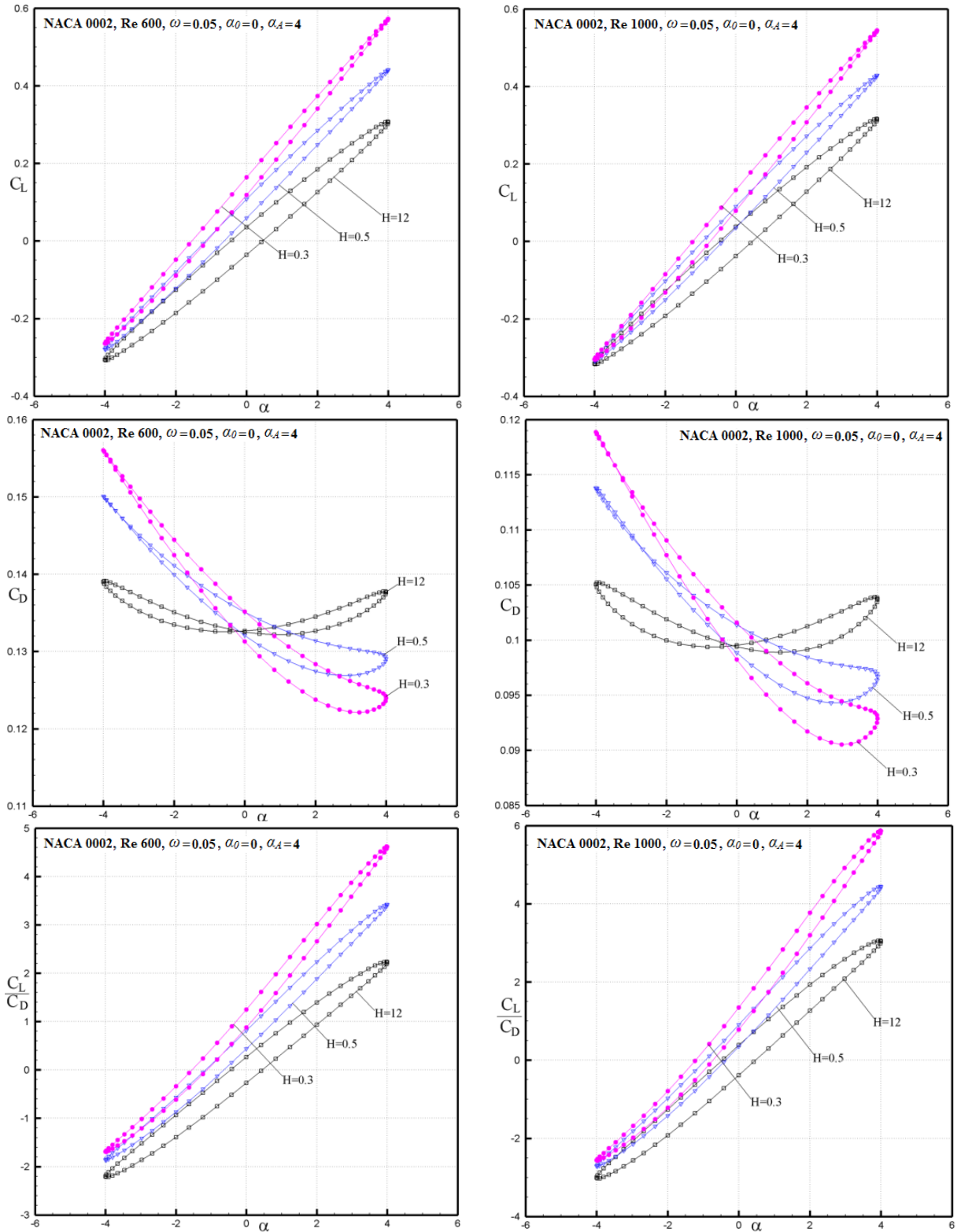


Figure 4.9 Influence of Reynolds number: Solutions for the unsteady lift and drag coefficients for a NACA 0002 airfoil executing pitching oscillations with  $\alpha_0 = 0^\circ$ ,  $\alpha_A = 4^\circ$ ,  $\omega = 0.05$ , at  $Re = 600$  and  $1000$  for three distances to the ground:  $H = 0.3$ ,  $H = 0.5$ ,  $H = 12$  (no ground effect).

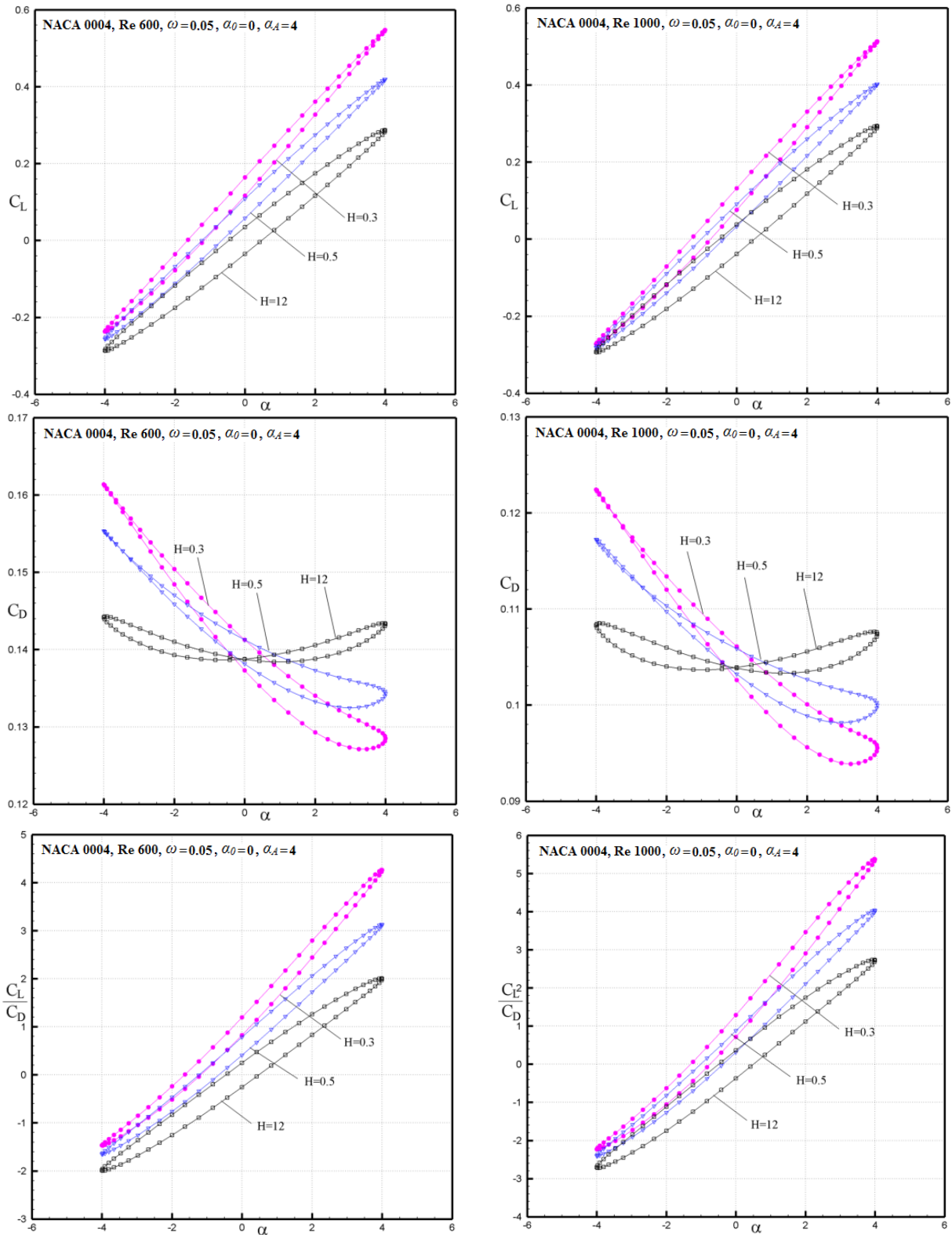


Figure 4.10 Influence of Reynolds number: Solutions for the unsteady lift and drag coefficients for a NACA 0004 airfoil executing pitching oscillations with  $\alpha_0 = 0^\circ$ ,  $\alpha_A = 4^\circ$ ,  $\omega = 0.05$ , at  $Re = 600$  and  $1000$  for three distances to the ground:  $H = 0.3$ ,  $H = 0.5$ ,  $H = 12$  (no ground effect).

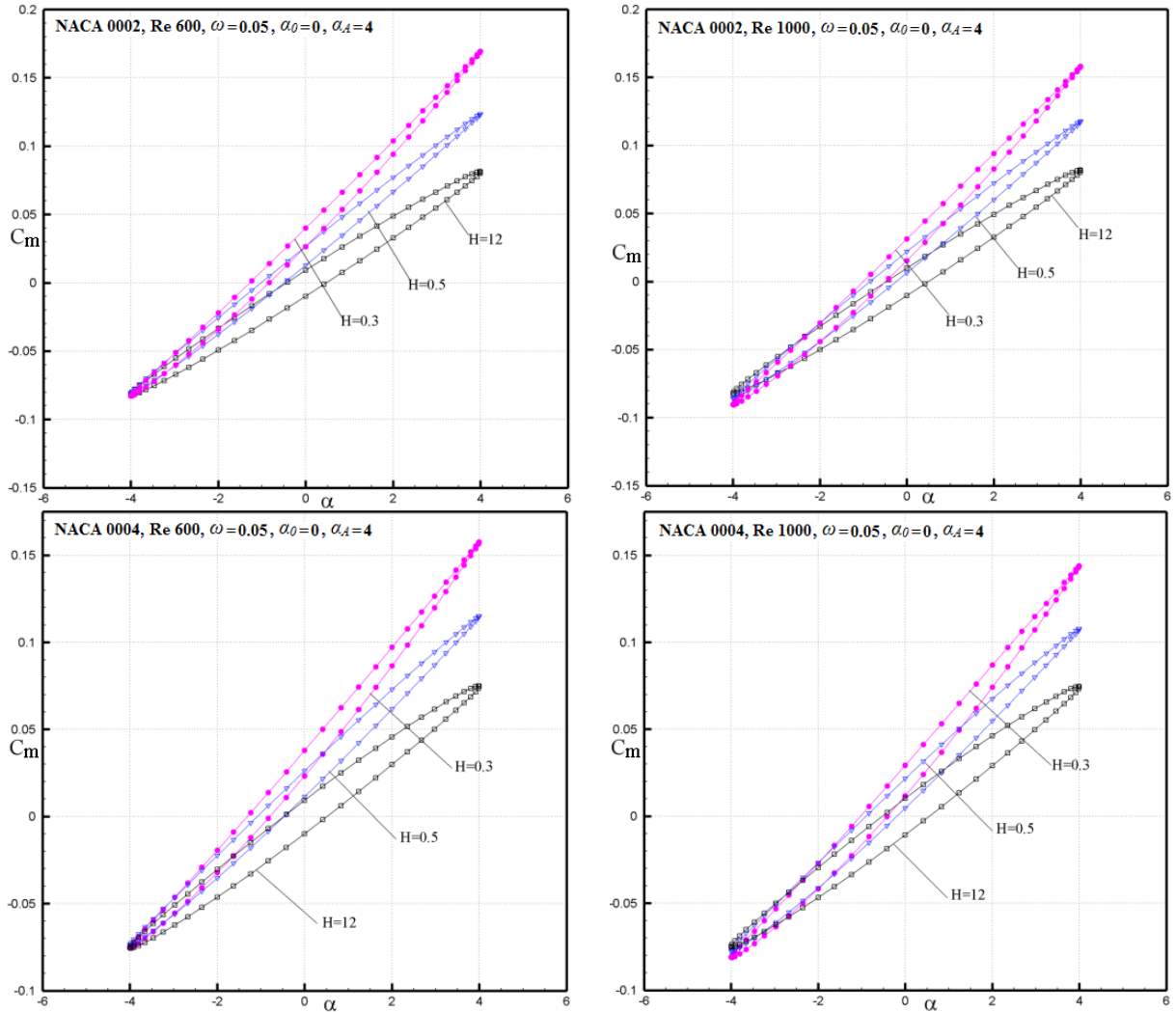


Figure 4.11 Influence of Reynolds number: Solutions for the unsteady pitching moment coefficient,  $C_m$ , for a NACA 0002 and NACA 0004 airfoils executing pitching oscillations, with  $\alpha_0 = 0^\circ$ ,  $\alpha_A = 4^\circ$ ,  $\omega = 0.05$ , at  $Re = 600$  and  $1000$  for three distances to the ground:  $H = 0.3$ ,  $H = 0.5$ ,  $H = 12$  (no ground effect).

### 4.5.3 Influence of the oscillation frequency

The influence of the oscillation frequency,  $\omega$ , and of the mean incidence,  $\alpha_0$ , with the distance to the ground on the unsteady lift and drag coefficients,  $C_L$  and  $C_D$ , and on the lift-to-drag ratio  $C_L/C_D$ , is illustrated in Figure 4.13 for NACA 0002 airfoil executing pitching oscillations  $\alpha(t) = \alpha_0 + \alpha_A \cos(\omega t)$ , with the oscillation amplitude  $\alpha_A = 4^\circ$ , for two oscillation frequencies  $\omega = 0.05$  and  $0.10$ , and for two values of the mean incidence  $\alpha_0 = 0^\circ$  and  $\alpha_0 = 2^\circ$ , at  $Re = 1000$  and for two distances to the ground:  $H = 0.3$  and  $H = 12$  (no ground effect).

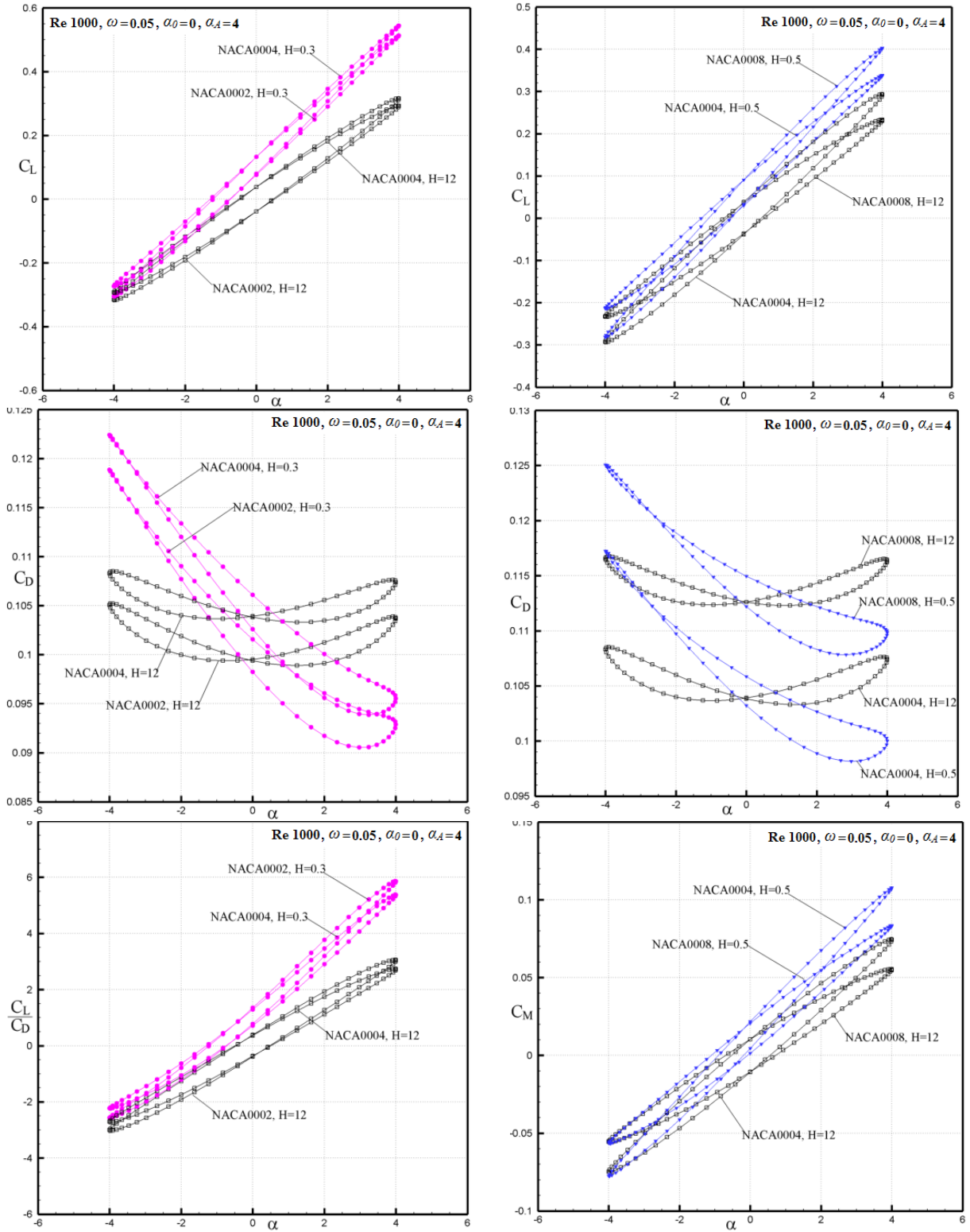


Figure 4.12 Influence of the airfoil thickness: The unsteady aerodynamic coefficients for NACA 0002, NACA 0004 and NACA 0008 airfoils executing pitching oscillations with  $\alpha_0 = 0^\circ$ ,  $\alpha_A = 4^\circ$ ,  $\omega = 0.05$ , at  $Re = 1000$  for three distances to the ground:  $H = 0.3$ ,  $H = 0.5$ ,  $H = 12$ .

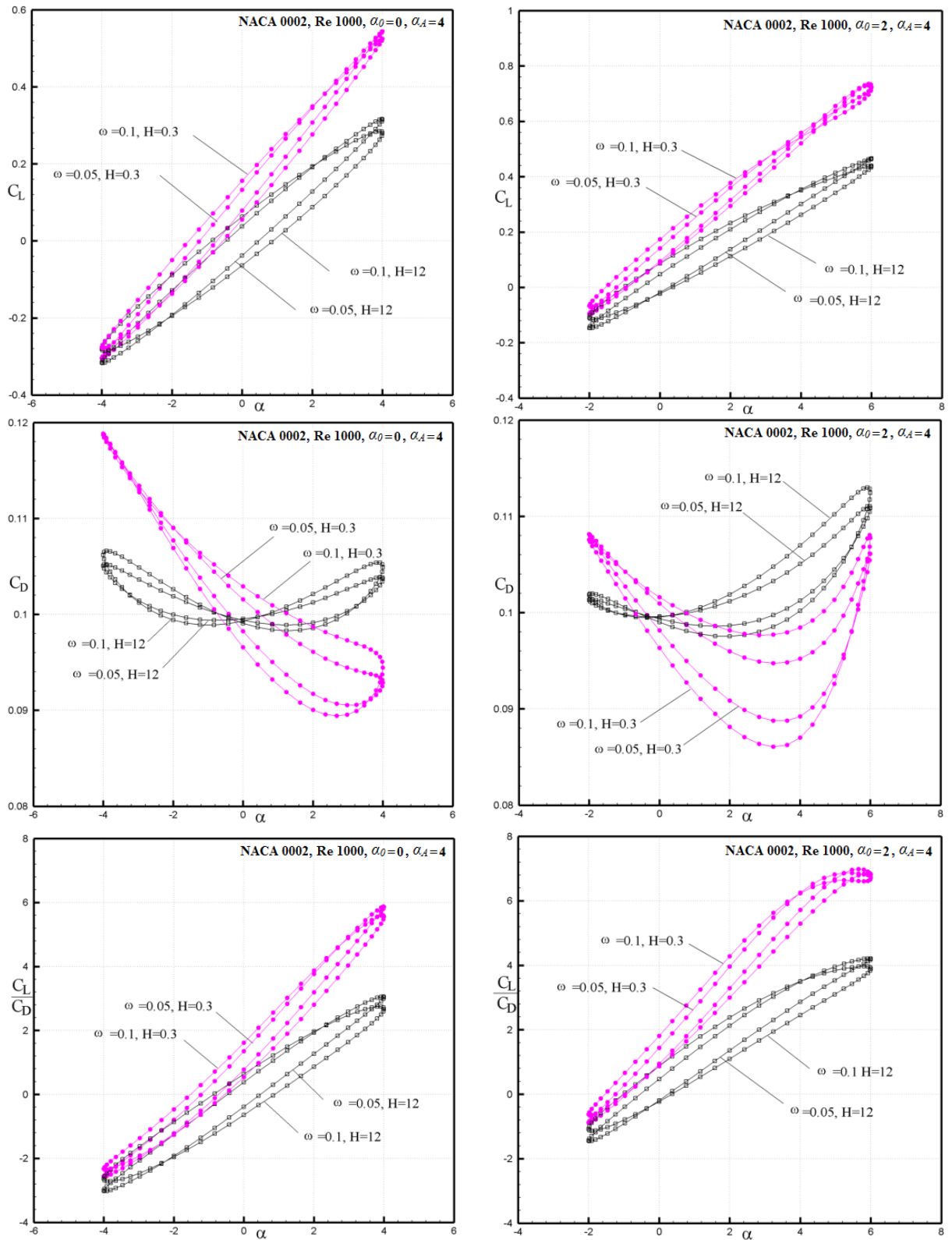


Figure 4.13 Influence of the oscillation frequency for NACA 0002 at two frequencies,  $\omega = 0.05$  and  $0.10$ , and for two values of the mean incidence  $\alpha_0 = 0^\circ$  and  $\alpha_0 = 2^\circ$ , at  $Re = 1000$  and for two distances to the ground:  $H = 0.3$  and  $H = 12$  (no ground effect).

One can be noted in Figure 4.13, that the shape of the hysteresis curve for the unsteady lift coefficient,  $C_L$ , in the case of pitching oscillations with  $\alpha_A = 2^\circ$ ,  $\alpha_A = 4^\circ$  and  $\omega = 0.1$  is significantly changed for the distance to the ground  $H = 0.3$  due to the flow separation region developed on the upper surface of the airfoil in this case.

#### 4.5.4 Typical variations of the unsteady pressure coefficient

The typical variations of the unsteady pressure coefficient along the chord at several moments during the oscillatory cycle,  $t/T$ , are illustrated in Figure 4.14 for NACA 0004 airfoil oscillating with  $\alpha_0 = 0^\circ$ ,  $\alpha_A = 4^\circ$ ,  $\omega = 0.05$ , and for NACA 0002 airfoil oscillating with  $\alpha_0 = 2^\circ$ ,  $\alpha_A = 4^\circ$ ,  $\omega = 0.05$ , at  $Re = 1000$  and for three distances to the ground:  $H = 0.3$ , and  $H = 12$  (no ground effect).

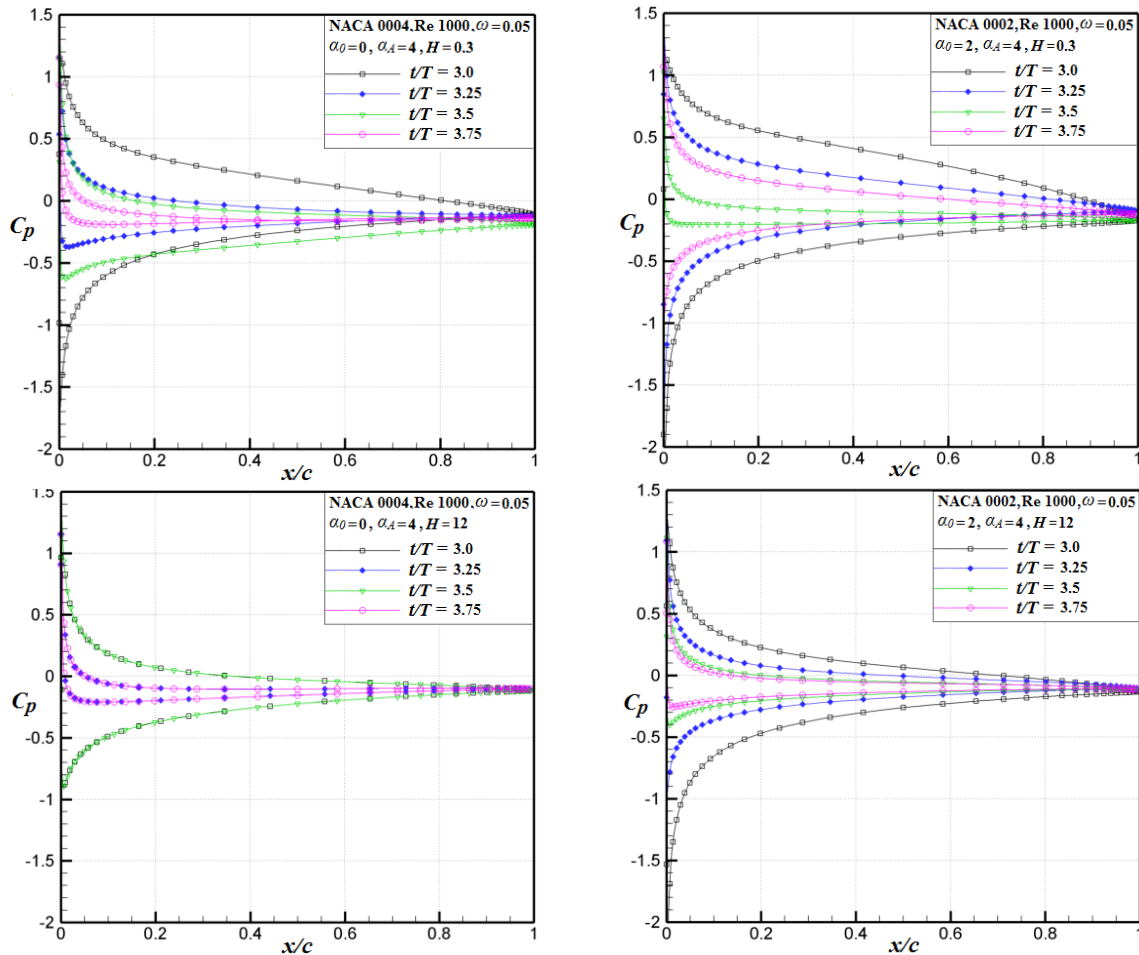


Figure 4.14 Variations of pressure coefficient along the chord during the oscillatory cycle,  $t/T$  : For NACA 0004 and NACA 0002 airfoils oscillating with  $\alpha_A = 4^\circ$ ,  $\omega = 0.05$ , and with  $\alpha_0 = 0^\circ$  and  $\alpha_0 = 2^\circ$ , respectively, at  $Re = 1000$  and for  $H = 0.3$ ,  $H = 0.5$ ,  $H = 12$  (no ground effect).

## 4.6 Solutions for unsteady flows past stationary airfoils in the proximity of the ground at low Reynolds numbers

This chapter also presents the numerical and experimental validation of computed solutions for unsteady flows past stationary airfoils in the proximity of the ground at low Reynolds numbers through the numerical method developed in section 4.2. The discussion is a novel contribution for the aerodynamics field that has not been identified in the literature review.

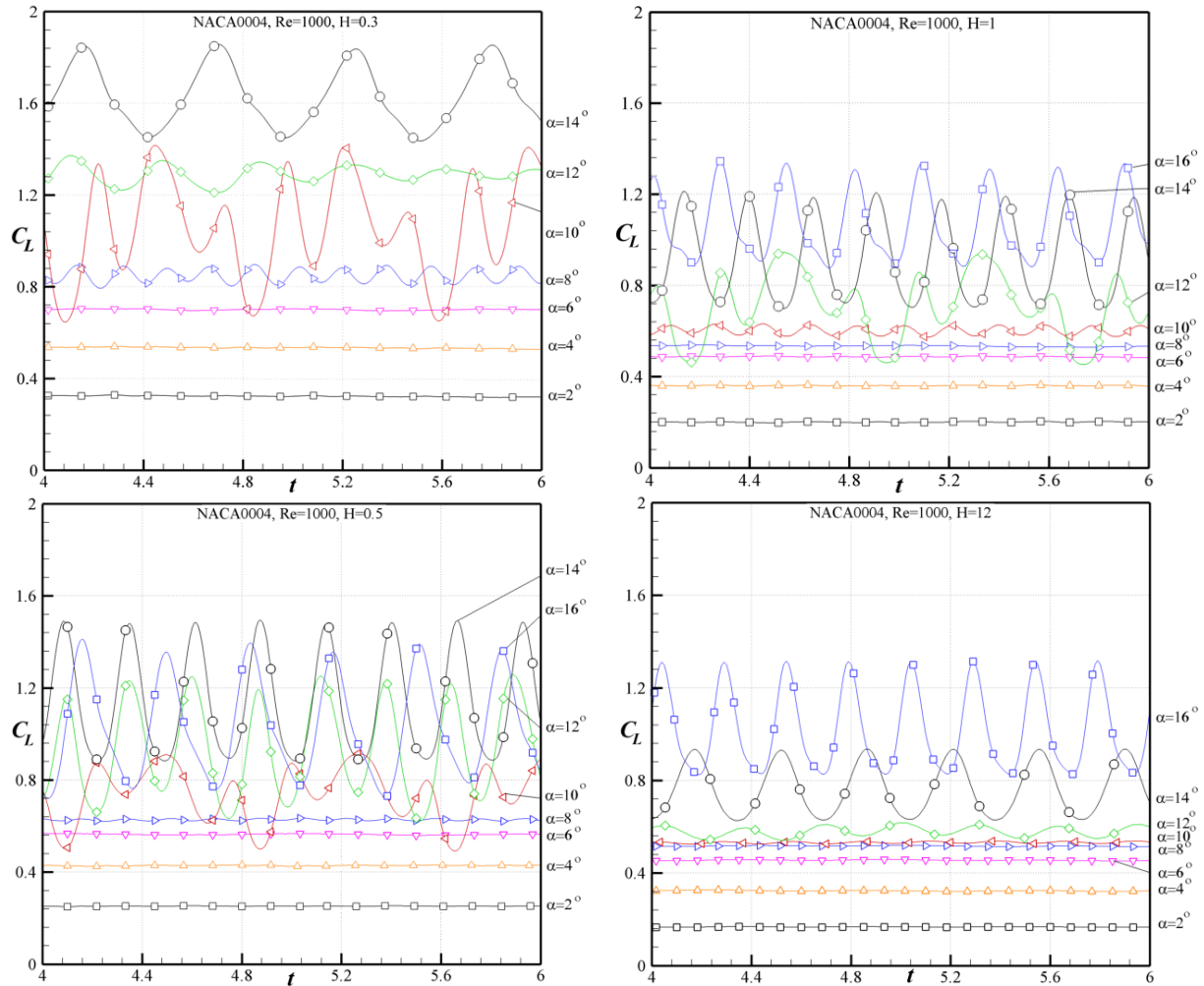


Figure 4.15 Influence of the distance to the ground,  $H$ : The variations with the nondimensional time,  $t = t^* U_\infty / c$ , of the lift coefficient,  $C_L$ , of the NACA 0004 airfoil for several nondimensional distances to the ground,  $H = 0.3, 0.5, 1.0$  and  $12$  (no ground effect), for  $Re = 1000$  and at various angles of attack,  $\alpha$ .

### 4.6.1 Influence of the distance to the ground

The aerodynamic coefficients of lift and drag,  $C_L$  and  $C_D$ , of the NACA 0004 airfoil are shown in Figures 4.15 and 4.16 for four distances to the ground,  $H = 0.3, 0.5, 1.0$  and  $12$  (no ground effect) for Reynolds number  $Re=1000$  and at various angles of attack,  $\alpha$ .

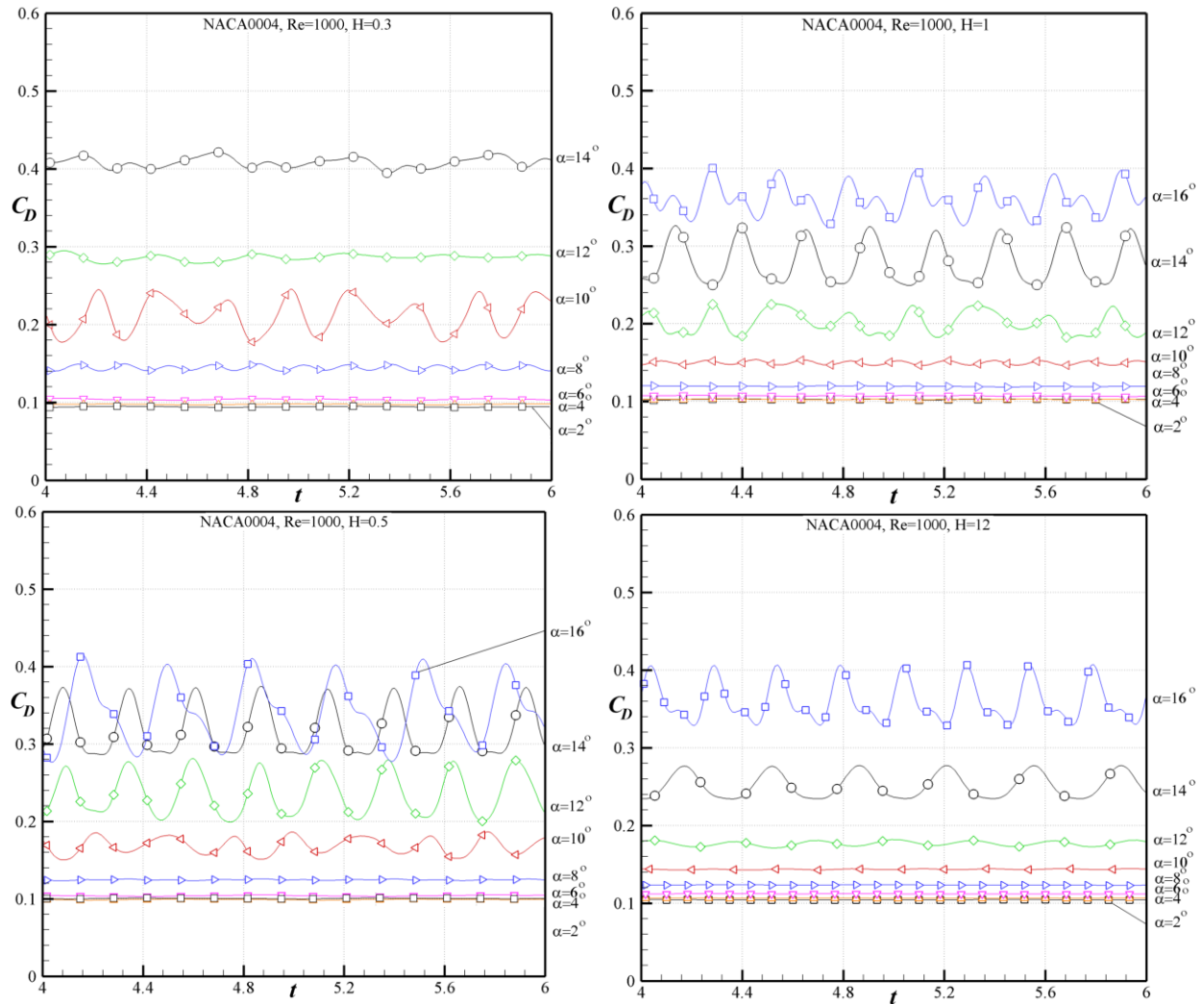


Figure 4.16 Influence of the distance to the ground,  $H$ : The variations with the nondimensional time,  $t = t * U_{\infty} / c$ , of the drag coefficient,  $C_D$ , of the NACA 0004 airfoil for several distances to the ground,  $H = 0.3, 0.5, 1.0$  and  $12$  (no ground effect), for Reynolds number,  $Re = 1000$ , and at various angles of attack,  $\alpha$ .

One can notice that the amplitude of the oscillations in time of the lift coefficient,  $C_L$ , increases with the decrease of the distance to the ground, and these oscillations appear at smaller angles of attack,  $\alpha$ , near the ground. A similar observation can be made for the drag coefficient.

One can also notice that close to the ground, at the nondimensional distance  $H = 0.5$ , the stall conditions are reached at  $\alpha = 14^\circ$ , and at  $\alpha = 16^\circ$  the lift coefficient becomes smaller, while the drag coefficient is larger than that at  $\alpha = 14^\circ$ . It is important to note that the oscillations in time of the aerodynamic coefficients, which are generated by the unsteady flow separations at low Reynolds numbers, start at much smaller angles of attack than the stall angle.

From Figures 4.15 and 4.16 it can be seen that up to  $\alpha = 6^\circ$  for  $Re = 1000$  and up to  $\alpha = 8^\circ$  for  $Re = 600$ , the aerodynamic coefficients are practically constant in time. With the increase in incidence, the lift and drag coefficients display periodic variations in time. The amplitude of these variations in time increases with the angle of attack, and for incidences larger than  $\alpha = 10^\circ$  these oscillations of the aerodynamic coefficients become more complex, due to an increasing complexity of the unsteady flow separations.

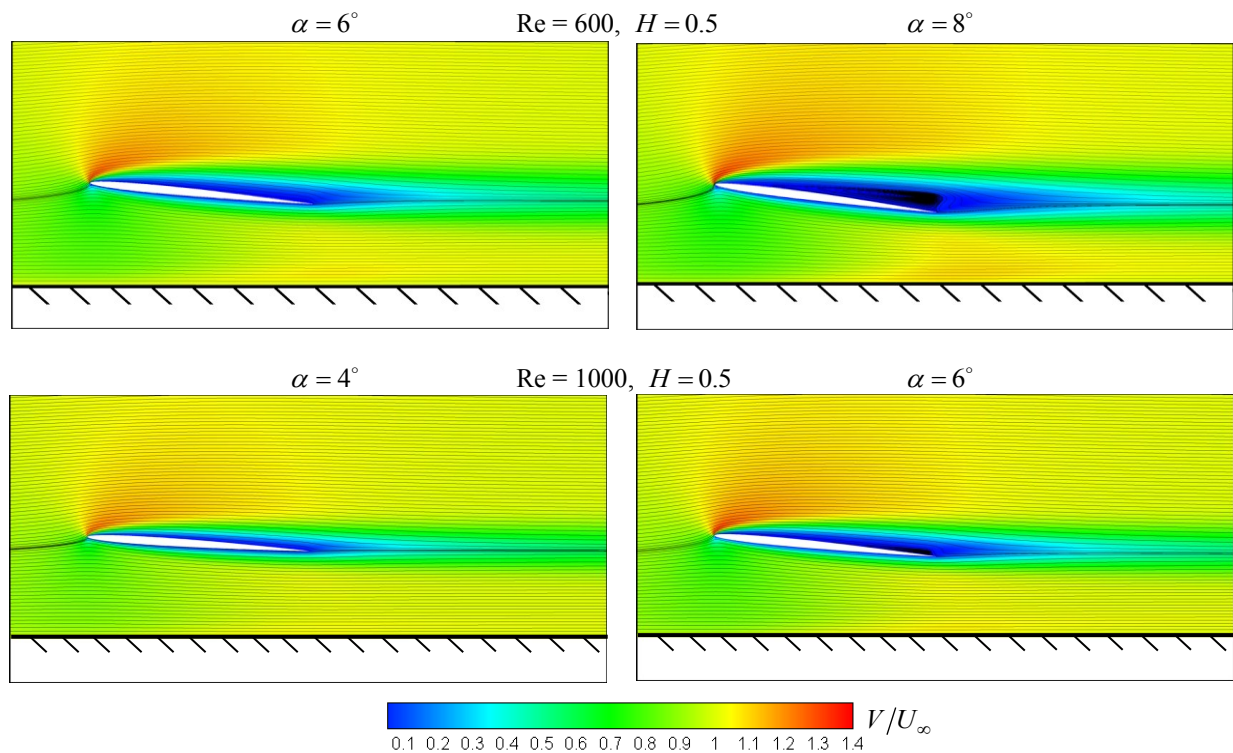


Figure 4.17 Illustrations of the steady flow separations for the NACA 0004 airfoil for two Reynolds numbers,  $Re = 600$  and  $1000$  and at three angles of attack,  $\alpha = 4^\circ$ ,  $\alpha = 6^\circ$  and  $\alpha = 8^\circ$  at the nondimensional distance to the ground  $H = 0.5$ .

This behavior is consistent with the results of the flow separation analysis, which revealed that for incidences smaller than  $\alpha = 8^\circ$ , the flow separation is well organized and does not present oscillations in time, as it can be observed in the flow visualizations shown in Figure 4.17.

In these flow visualizations, the streamlines are represented by continuous lines, and the flow velocity field is represented by color shades related to the non-dimensional velocity  $V/U_\infty$ .

At incidences larger than  $\alpha = 8^\circ$ , the complexity of the flow separations and their variations in time increase with the increase in the angle of attack,  $\alpha$ , and with decrease in the nondimensional distance to the ground,  $H$ . The most complex pattern of the flow separations is displayed closer to the ground and at larger angles of attack.

This can be seen in Figures 4.18 to 4.21 which present illustrations of the flow separations at various moments in the nondimensional time,  $t = t^*U_\infty/c$ , for the NACA 0004 airfoil at Reynolds number  $Re = 1000$  for various distances to the ground,  $H = 0.3, 0.5, 1.0$  and  $12$  (no ground effect), and at two angles of attack,  $\alpha = 10^\circ$  and  $\alpha = 12^\circ$ .

The influence of the angle of attack,  $\alpha$ , on the flow separations can be observed by comparing the flow visualizations shown in Figures 4.18 and 4.19 at  $\alpha = 10^\circ$  with the ones illustrated in Figures 4.20 and 4.21 for the same airfoil NACA 0004 at  $\alpha = 12^\circ$ . It can be seen that the unsteadiness of the flow separations increases with the increase in the angle of attack (for the same  $H$ ) and with the decrease in the nondimensional distance to the ground,  $H$ .

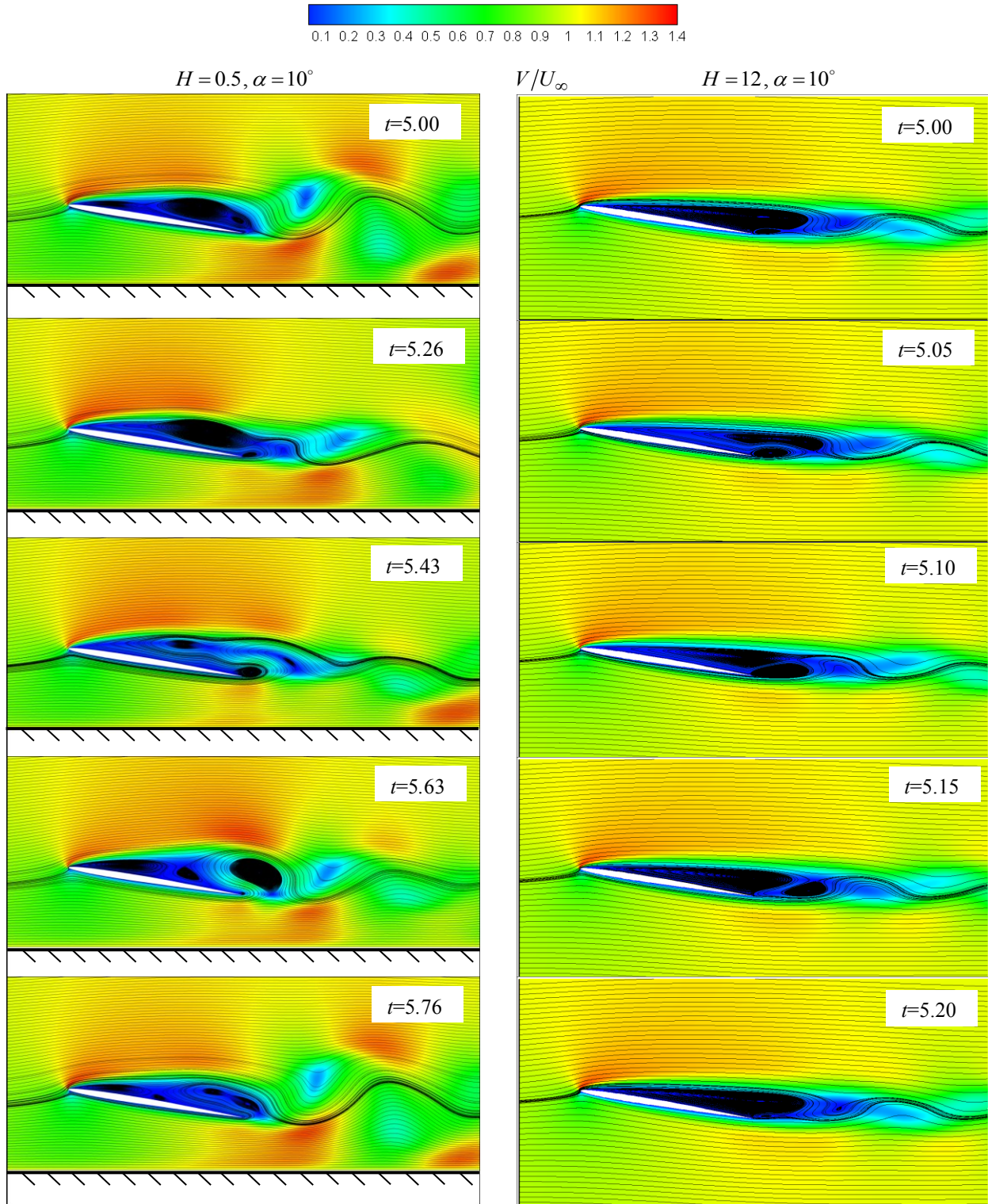


Figure 4.18 Illustration of the flow separations for the NACA 0004 airfoil at various moments in time,  $t = t^*U_\infty/c$ , comparison between two nondimensional distances to the ground,  $H = 0.5$  and  $H = 12$  (no ground effect), for  $Re = 1000$  and at  $\alpha = 10^\circ$ .

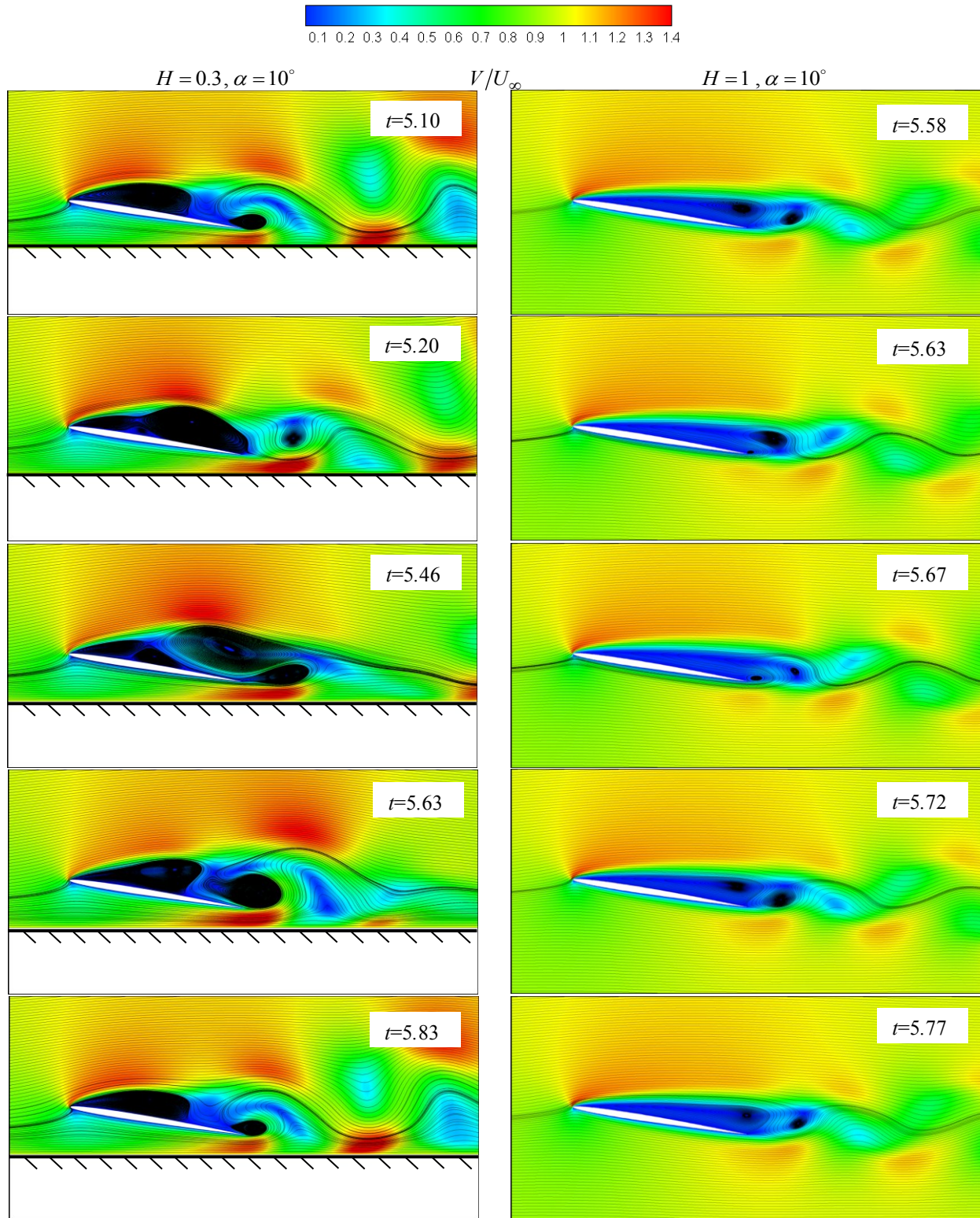


Figure 4.19 Illustration of the flow separations for the NACA 0004 airfoil at various moments in time,  $t = t^*U_\infty/c$ , comparison between two nondimensional distances to the ground,  $H = 0.3$  and  $H = 1$  (no ground effect), for  $Re = 1000$  and at  $\alpha = 10^\circ$ .

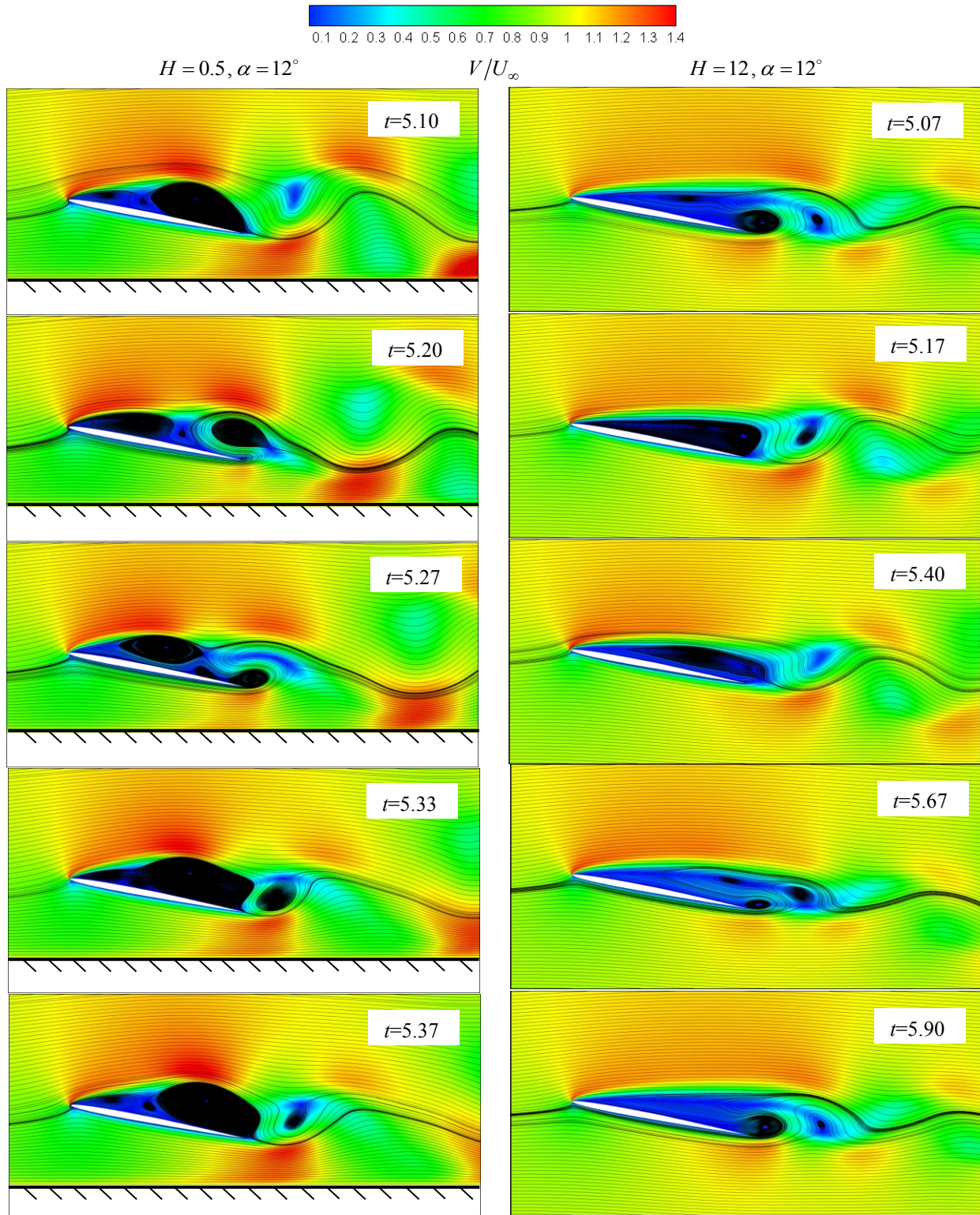


Figure 4.20 Illustration of the flow separations for the NACA 0004 airfoil at various moments in time,  $t = t^*U_\infty/c$ , comparison between two nondimensional distances to the ground,  $H = 0.5$  and  $H = 12$  (no ground effect), for  $Re = 1000$  and at  $\alpha = 12^\circ$ .

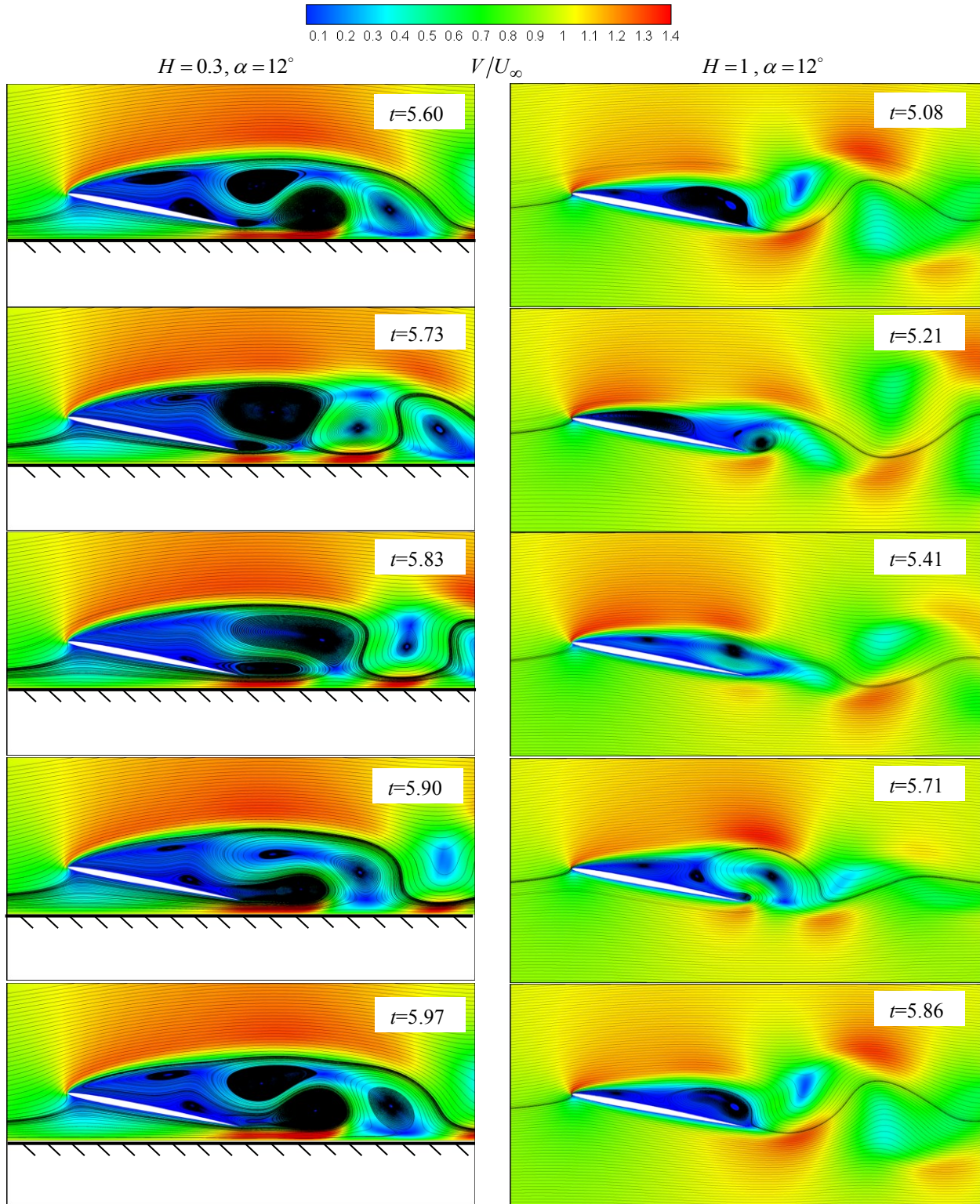


Figure 4.21 Illustration of the flow separations for the NACA 0004 airfoil at various moments in time,  $t = t^*U_\infty/c$ , comparison between two nondimensional distances to the ground,  $H = 0.3$  and  $H = 1$  (no ground effect), for  $Re = 1000$  and at  $\alpha = 12^\circ$ .

These illustrations of the variation in time of the flow separation pattern are consistent with the oscillatory variations in time of the aerodynamic coefficients shown in Figures 4.15 and 4.16, indicating that these unsteady flow separation structures, occurring in the flow past stationary airfoils at low Reynolds numbers, generate the oscillatory variations in time of the lift and drag coefficients.

#### 4.6.2 Influence of the Reynolds number

The influence of the Reynolds number on the unsteady effects generated by the unsteady flow separations at low Reynolds numbers is shown in Figure 4.22 for NACA 0002 airfoil at the

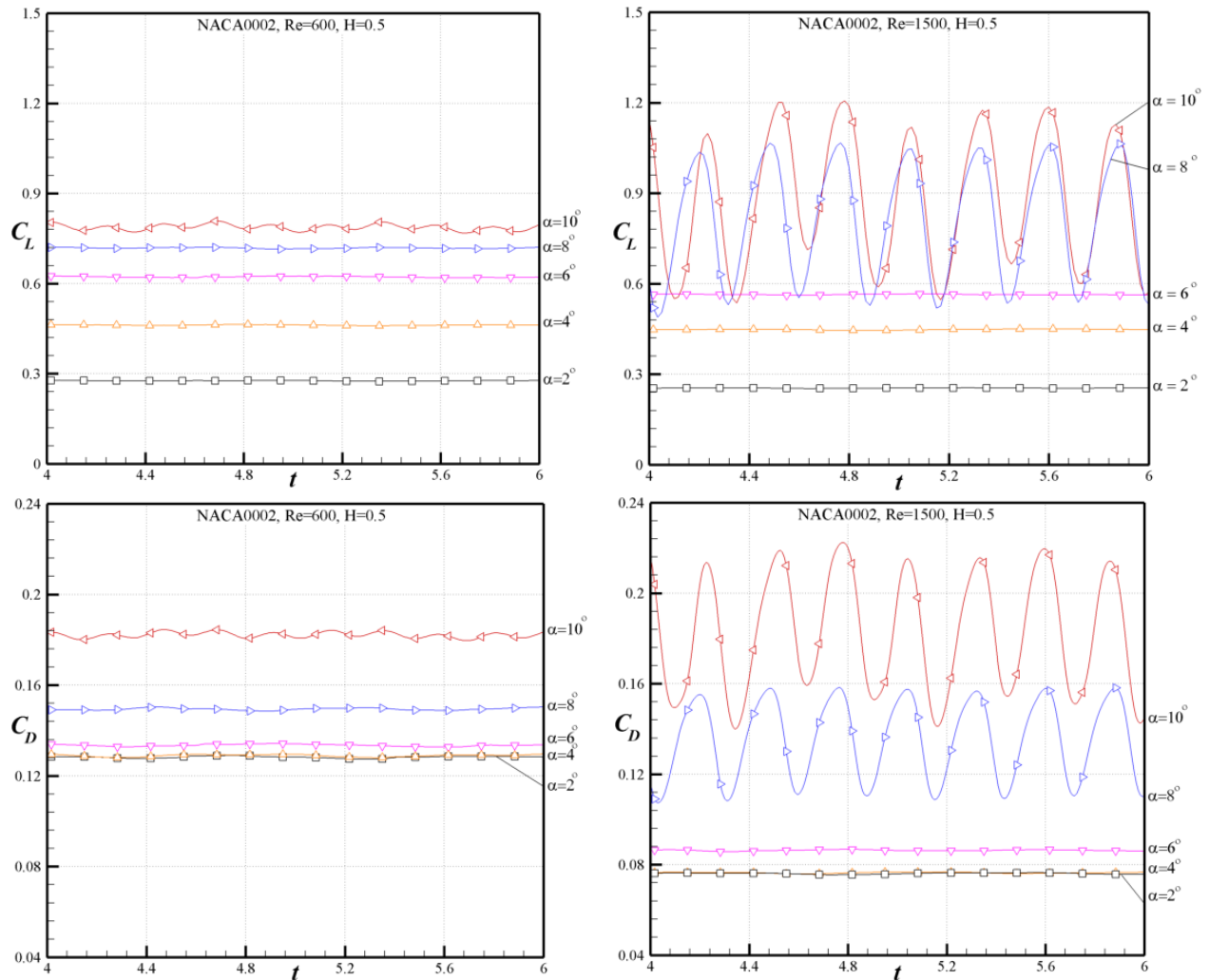


Figure 4.22 Influence of Reynolds number: Comparison of the variations with the nondimensional time,  $t = t^*U_\infty/c$ , of the lift and drag coefficients,  $C_L$  and  $C_D$ , for NACA 0002 airfoil for two Reynolds numbers,  $Re = 600$  and  $1500$ , at the distance to the ground  $H = 0.5$ , for various angles of attack,  $\alpha$ .

distance to the ground  $H = 0.5$  for two Reynolds numbers,  $Re = 600$  and  $1500$ , at several angles of attack, and in Figure 4.23 for the NACA 0004 airfoil for two Reynolds numbers,  $Re = 600$  and  $1000$ , at the same distance to the ground,  $H = 0.5$ .

One can notice that the amplitudes of the oscillations in time of the aerodynamic coefficients are increasing with the increase in the Reynolds number. This is more evident for the thinner airfoil, NACA 0002, in which the amplitudes of oscillations for both coefficients,  $C_L$  and  $C_D$ , are substantially larger for Reynolds number  $Re = 1500$  than those at  $Re = 600$ .

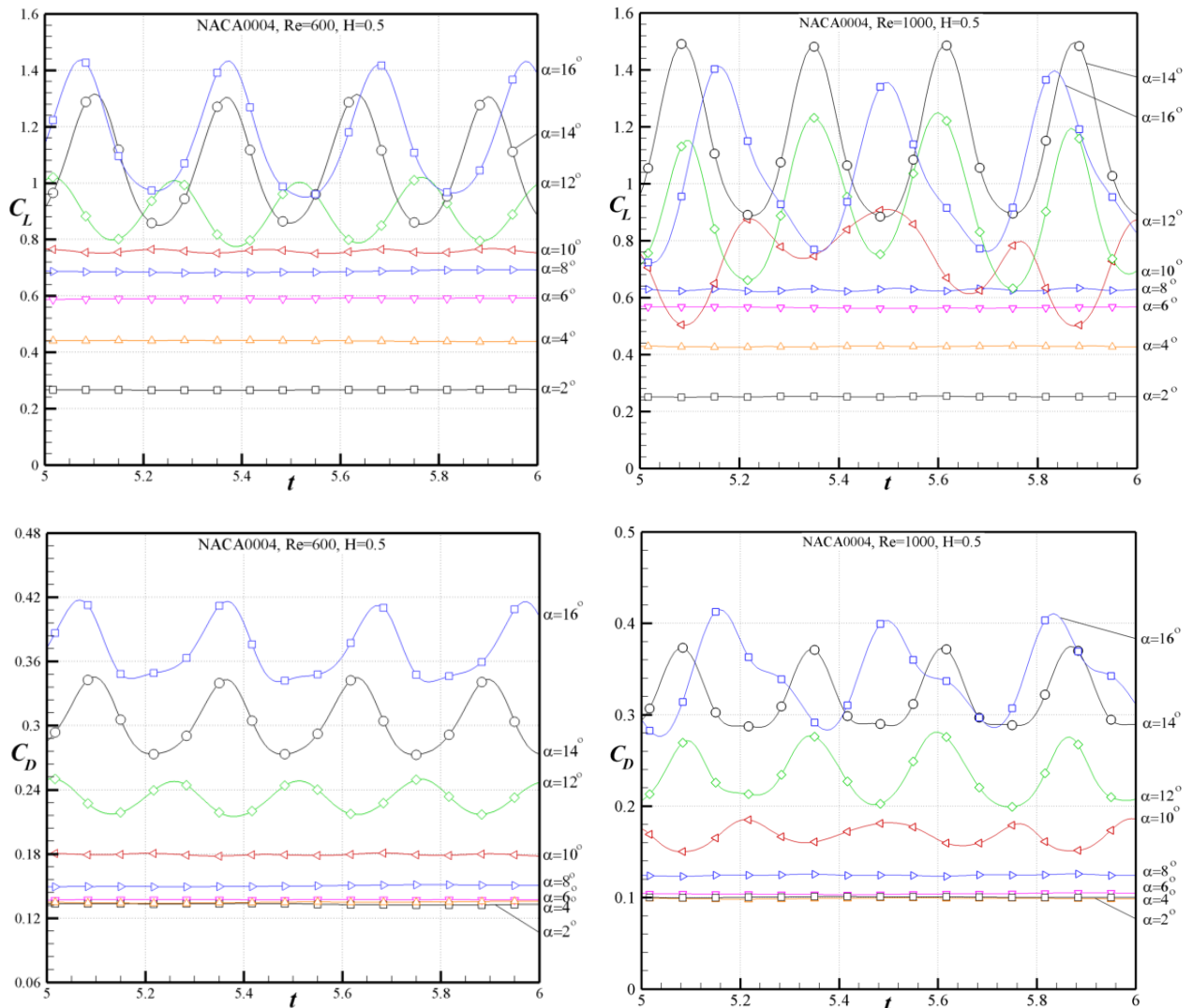


Figure 4.23 Influence of Reynolds number: Comparison of the variations with the nondimensional time,  $t = t^*U_\infty/c$ , of the lift and drag coefficients,  $C_L$  and  $C_D$ , for NACA 0004 airfoil for two Reynolds numbers,  $Re = 600$  and  $1000$ , at the distance to the ground  $H = 0.5$ , for various angles of attack,  $\alpha$ .

### 4.6.3 Influence of the airfoil thickness

The influence of the relative thickness of the airfoil on the unsteady effects generated by the unsteady flow separations at low Reynolds numbers in the proximity of the ground is shown in Figures 4.24 and 4.25 for two symmetric airfoils, NACA 0002 and 0008, for two Reynolds numbers,  $Re = 600$  and  $1000$ , and at the nondimensional distance to the ground  $H = 0.5$ .

One can observe that the amplitudes of the oscillations in time of the aerodynamic coefficients are larger for the thinner airfoil, NACA 0002, at the same angle of attack and at the same distance to the ground ( $H = 0.5$ ).

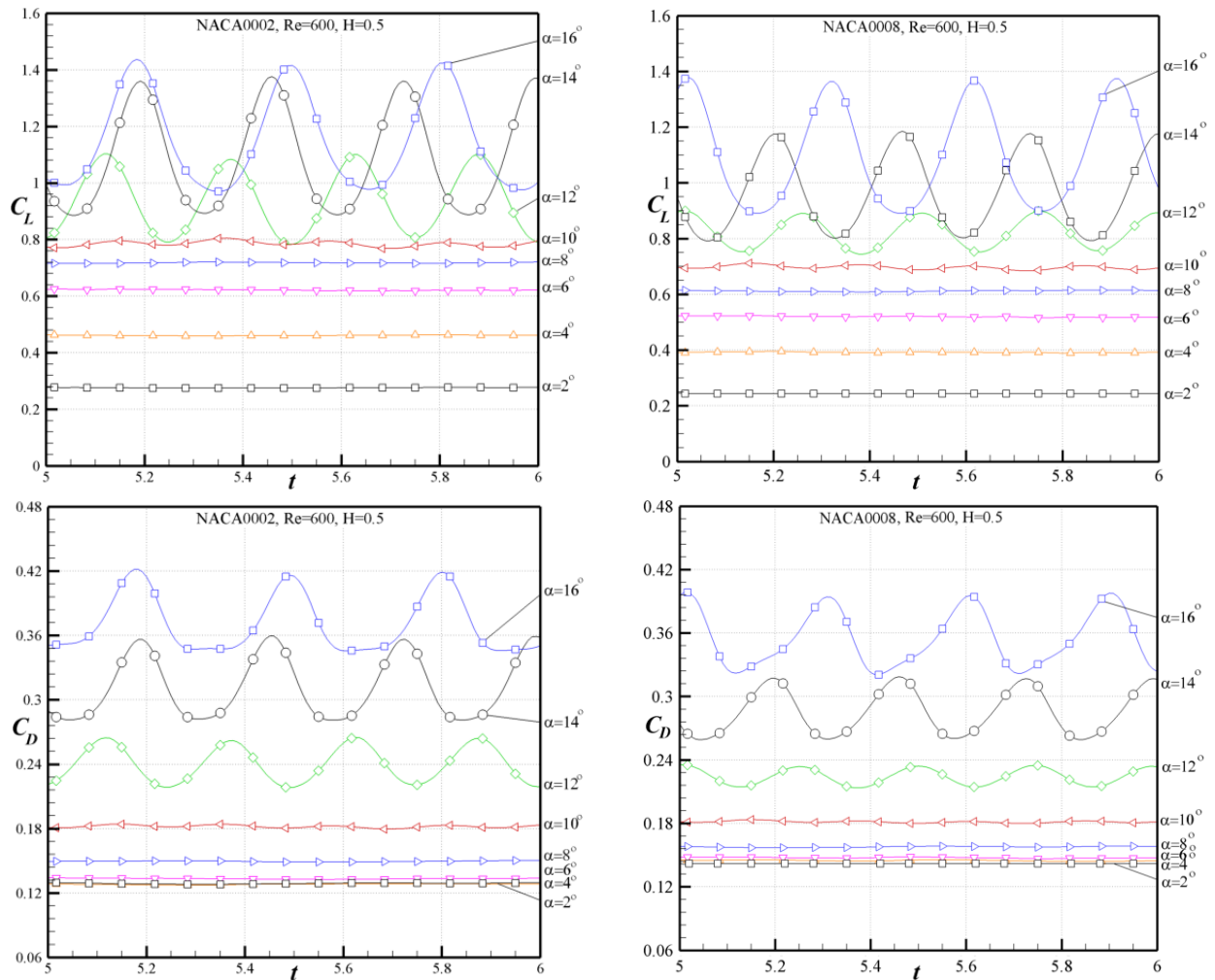


Figure 4.24 Influence of the airfoil thickness: Comparison of the variations with the nondimensional time,  $t = t^*U_\infty/c$ , of the lift coefficients,  $C_L$  and  $C_D$ , for two symmetric airfoils, NACA 0002 and NACA 0008 for Reynolds number,  $Re = 600$ , and the distance to the ground  $H = 0.5$ , for various angles of attack,  $\alpha$ .

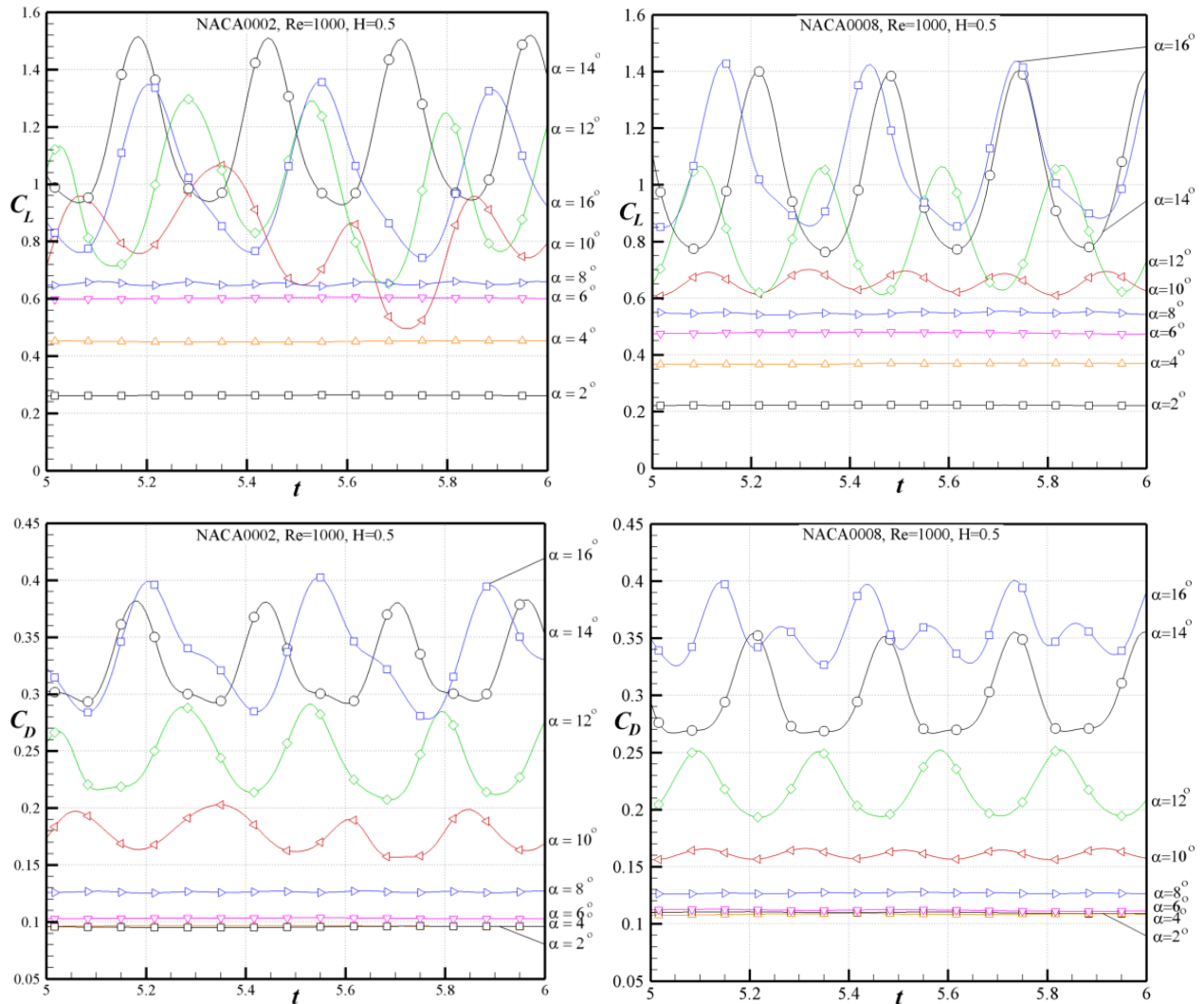


Figure 4.25 Influence of the airfoil thickness: Comparison of the variations with the nondimensional time,  $t = t^*U_\infty/c$ , of the lift coefficients,  $C_L$  and  $C_D$ , for two symmetric airfoils, NACA 0002 and NACA 0008 for Reynolds number,  $Re = 1000$ , and the distance to the ground  $H = 0.5$ , for various angles of attack,  $\alpha$ .

#### 4.6.4 Influence of the distance to the ground for cambered airfoils

The influence of the airfoil camber on the unsteady effects generated by the unsteady flow separations at low Reynolds numbers in the proximity of the ground is shown in Figures 4.26 and 4.27 for the cambered airfoil NACA 2404 at four nondimensional distances to the ground,  $H = 0.3, 0.5, 1.0$  and  $12$  (no ground effect) and at various angles of attack,  $\alpha$ .

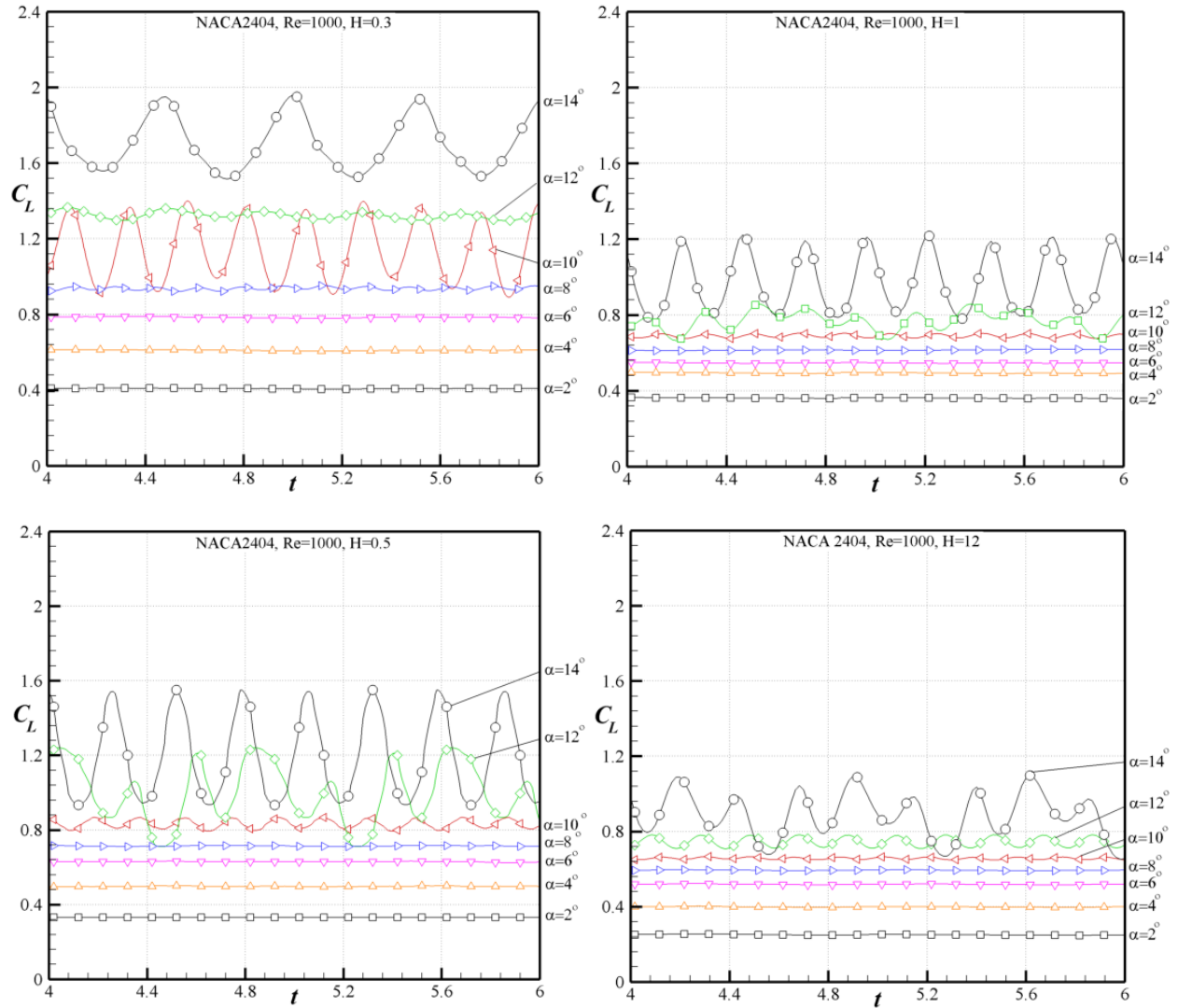


Figure 4.26 Influence of the distance to the ground,  $H$ , for a cambered airfoil: The variations with the nondimensional time,  $t = t^*U_\infty/c$ , of the lift coefficient,  $C_L$ , of the NACA 2404 airfoil for several nondimensional distances to the ground,  $H = 0.3, 0.5, 1.0$  and  $12$  (no ground effect), for Reynolds number,  $Re = 1000$ , and at various angles of attack,  $\alpha$ .

One can notice that the amplitudes of the oscillations in time of the aerodynamic coefficients become larger with the decrease of the distance to the ground for the cambered airfoil, NACA 2404, at the same angle of attack.

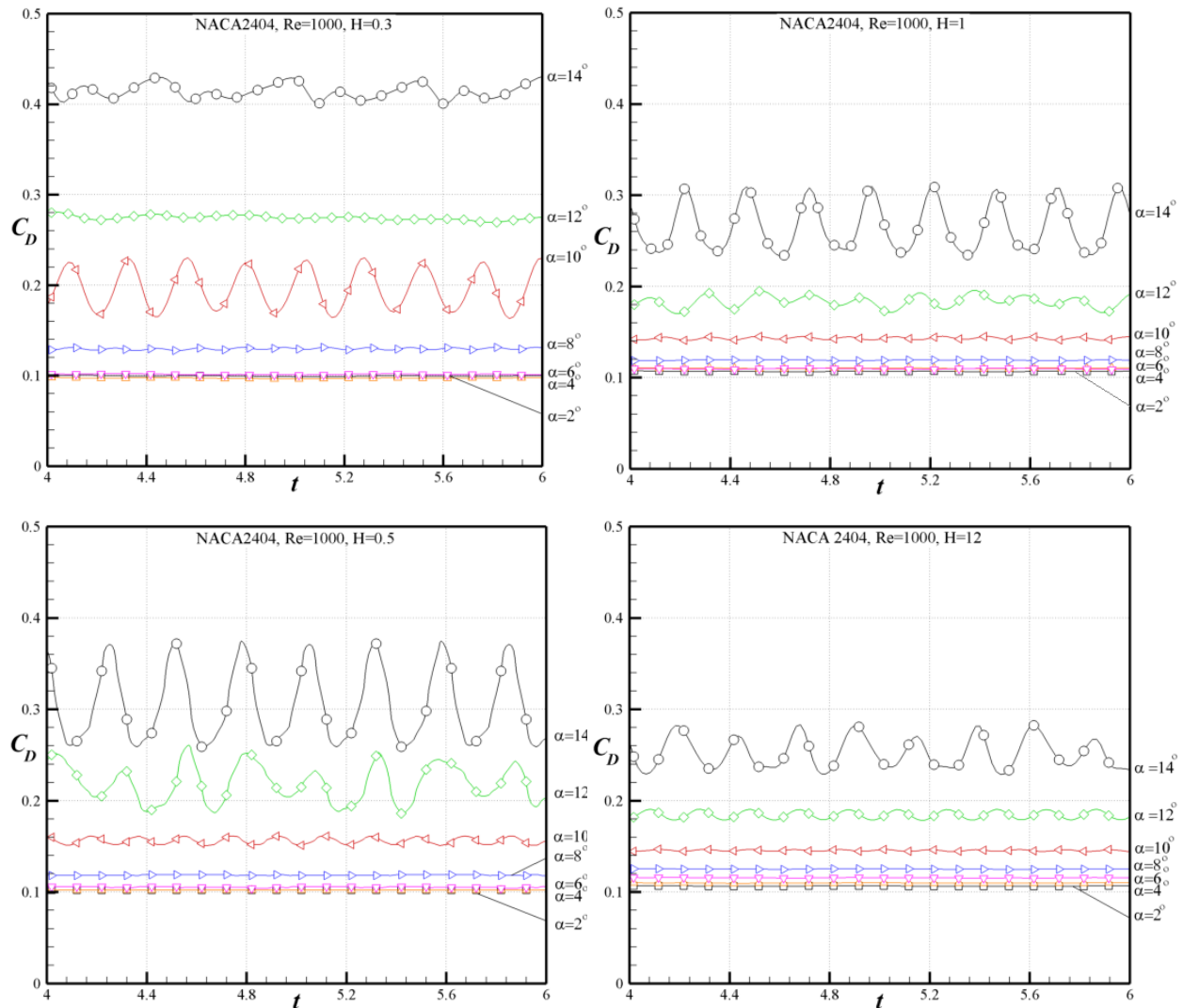


Figure 4.27 Influence of the distance to the ground,  $H$ , for a cambered airfoil: The variations with the nondimensional time,  $t = t \cdot U_\infty / c$ , of the drag coefficient,  $C_D$ , of the NACA 2404 airfoil for several nondimensional distances to the ground,  $H = 0.3, 0.5, 1.0$  and  $12$  (no ground effect), for Reynolds number,  $Re = 1000$ , and at various angles of attack,  $\alpha$ .

The above variations in time of the aerodynamic coefficients are consistent with the results of the flow separation analysis, which are shown in the flow visualizations illustrated in Figures 4.28 to 4.30 for the cambered airfoils NACA 2404 and NACA 4404 for Reynolds number,  $Re = 1000$ , and angle of attack  $\alpha = 10^\circ$ .

In these flow visualizations, the streamlines are represented by continuous lines, and the flow velocity field is represented by color shades related to the non-dimensional velocity  $V/U_\infty$ .

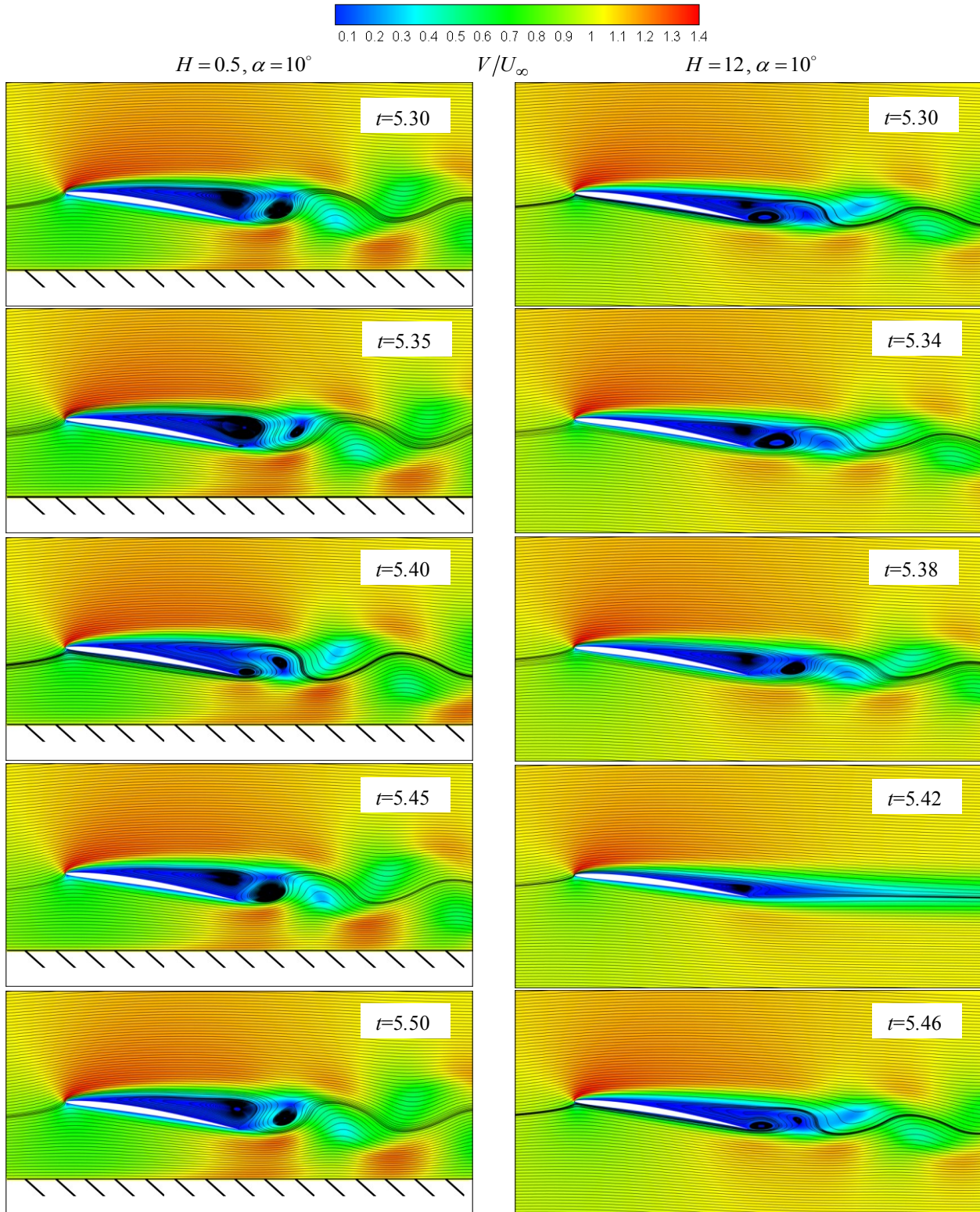


Figure 4.28 Illustration of the flow separations for NACA 2404 airfoil at various moments in time using the streamlines and the color shades indicating the nondimensional velocity field for  $H = 0.5$  and  $H = 12$ , for  $Re = 1000$  and at  $\alpha = 10^\circ$ .

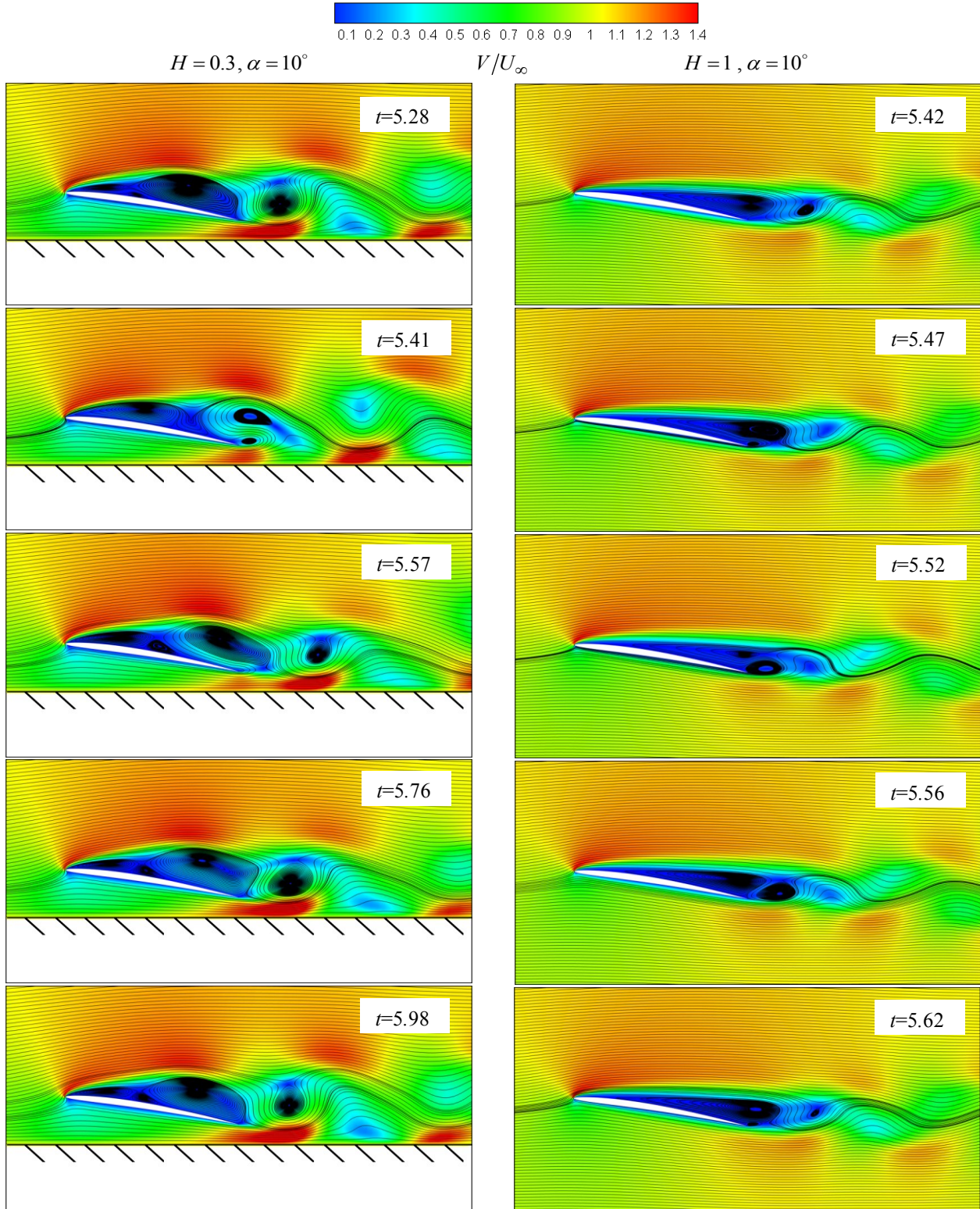


Figure 4.29 Illustration of the flow separations for NACA 2404 airfoil at various moments in time using the streamlines and the color shades indicating the nondimensional velocity field for  $H = 0.3$  and  $H = 1$ , for  $Re = 1000$  and at  $\alpha = 10^\circ$ .

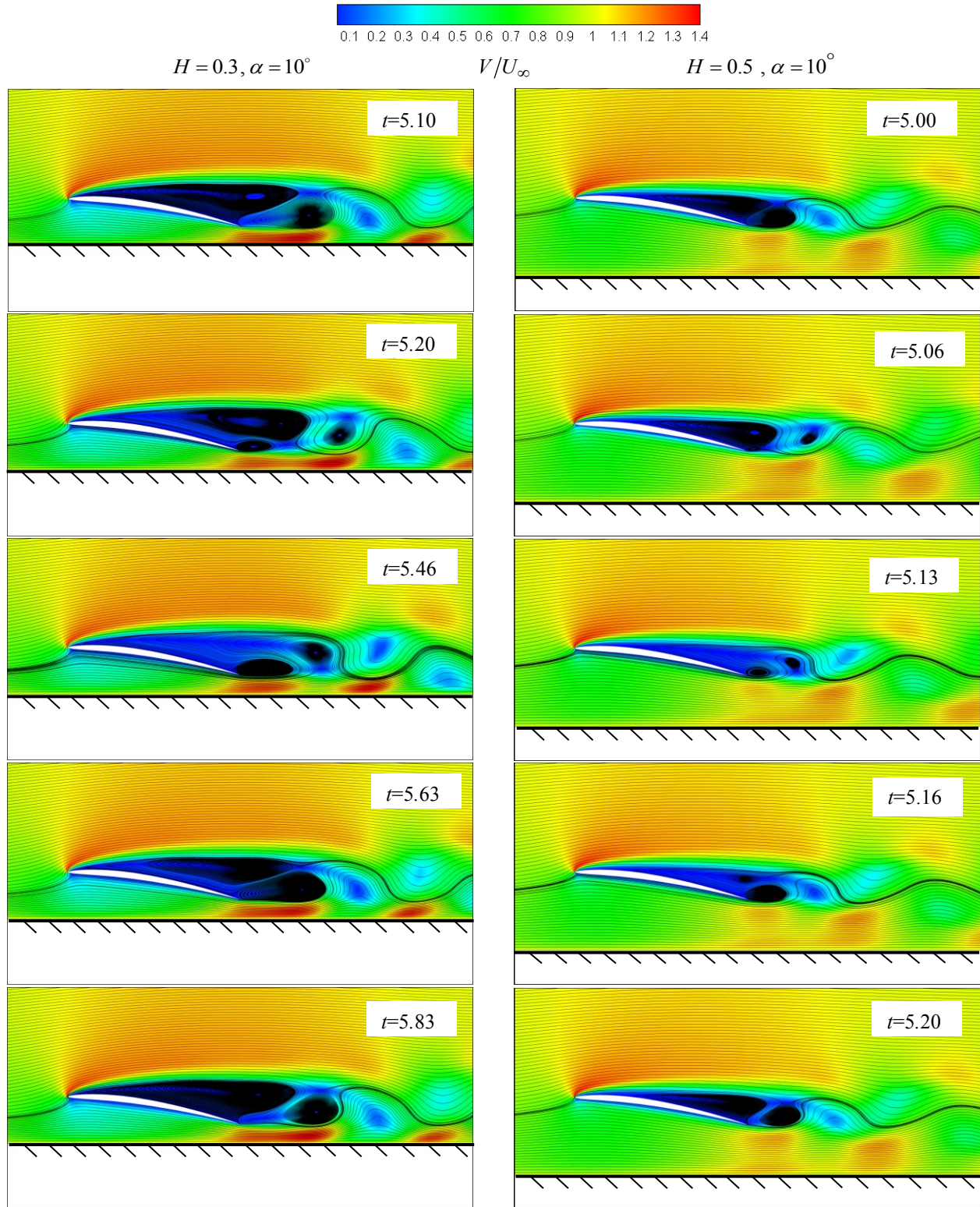


Figure 4.30 Illustration of the flow separations for NACA 4404 airfoil at various moments in time using the streamlines and the color shades indicating the nondimensional velocity field for  $H = 0.3$  and  $H = 0.5$ , for  $Re = 1000$  and at  $\alpha = 10^\circ$ .

### 4.6.5 Influence of the relative camber

The influence of the relative camber on the unsteady effects generated by the unsteady flow separations at low Reynolds numbers in the proximity of the ground can be seen in Figures 4.31 by comparing the results for NACA 4404 airfoil, and for NACA 2404 airfoil for  $H = 0.5$ .

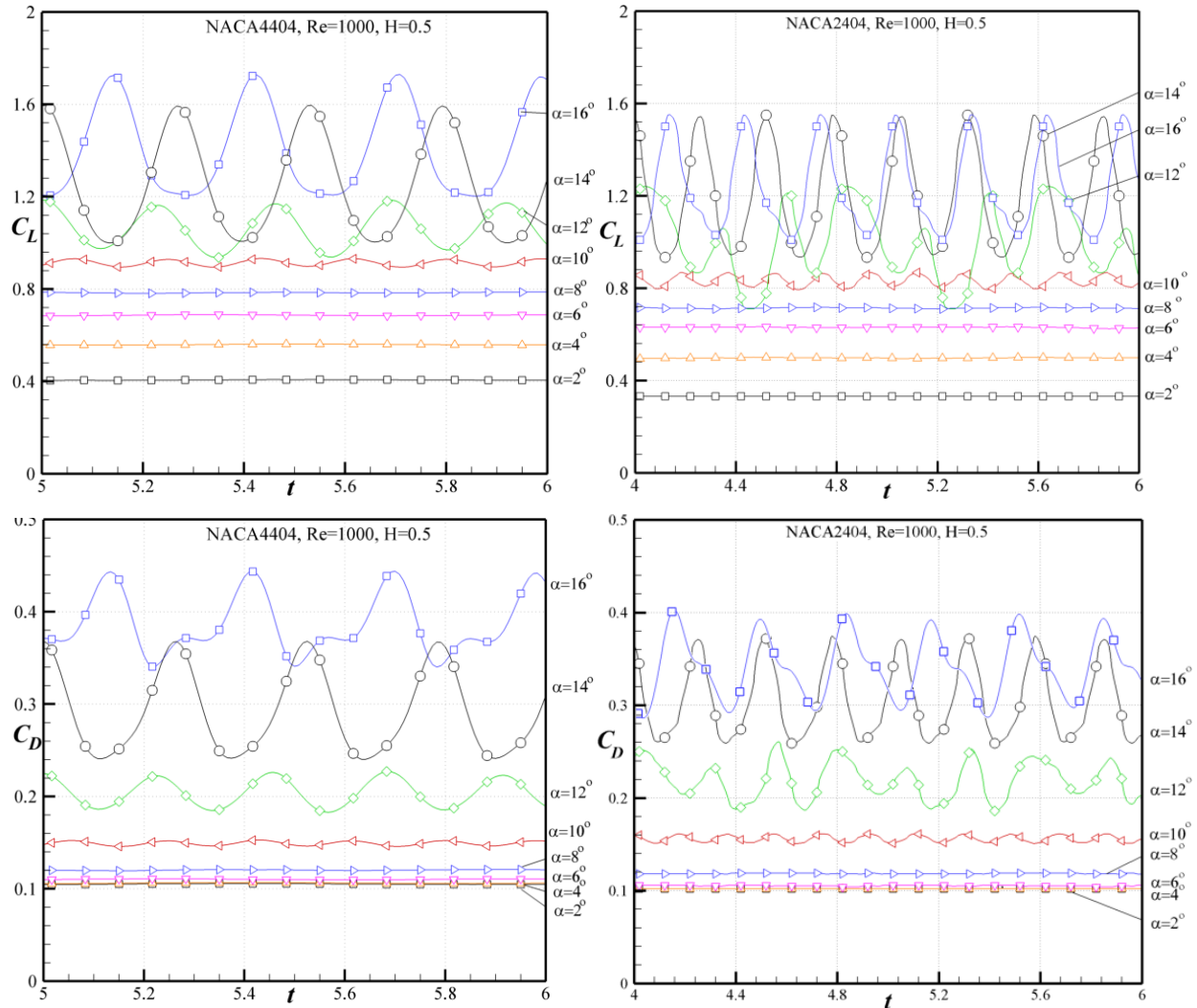


Figure 4.31 Influence of the relative camber for two cambered airfoil NACA 4404 and NACA 2404: The variations with the nondimensional time,  $t = t * U_\infty / c$ , of the lift and drag coefficients,  $C_L$  and  $C_D$ , for Reynolds number,  $Re = 1000$ , and distance to the ground,  $H = 0.5$  at various angles of attack,  $\alpha$ .

One can notice that the amplitudes of the oscillations in time of the aerodynamic coefficients increase with the relative camber, for the same angle of attack and distance to the ground. It

should be mentioned the stall condition for NACA 2404 airfoil occurs in an earlier incident  $\alpha = 16^\circ$ .

#### 4.6.6 Influence of the relative thickness for cambered airfoils

The influence of the relative thickness of cambered airfoils on the unsteady effects generated by the unsteady flow separations at low Reynolds numbers in the proximity of the ground is shown in Figure 4.32 for the NACA airfoils 2402 and 2404 for  $Re = 1000$ , and distance to the ground  $H = 0.5$  at various angles of attack,  $\alpha$ .

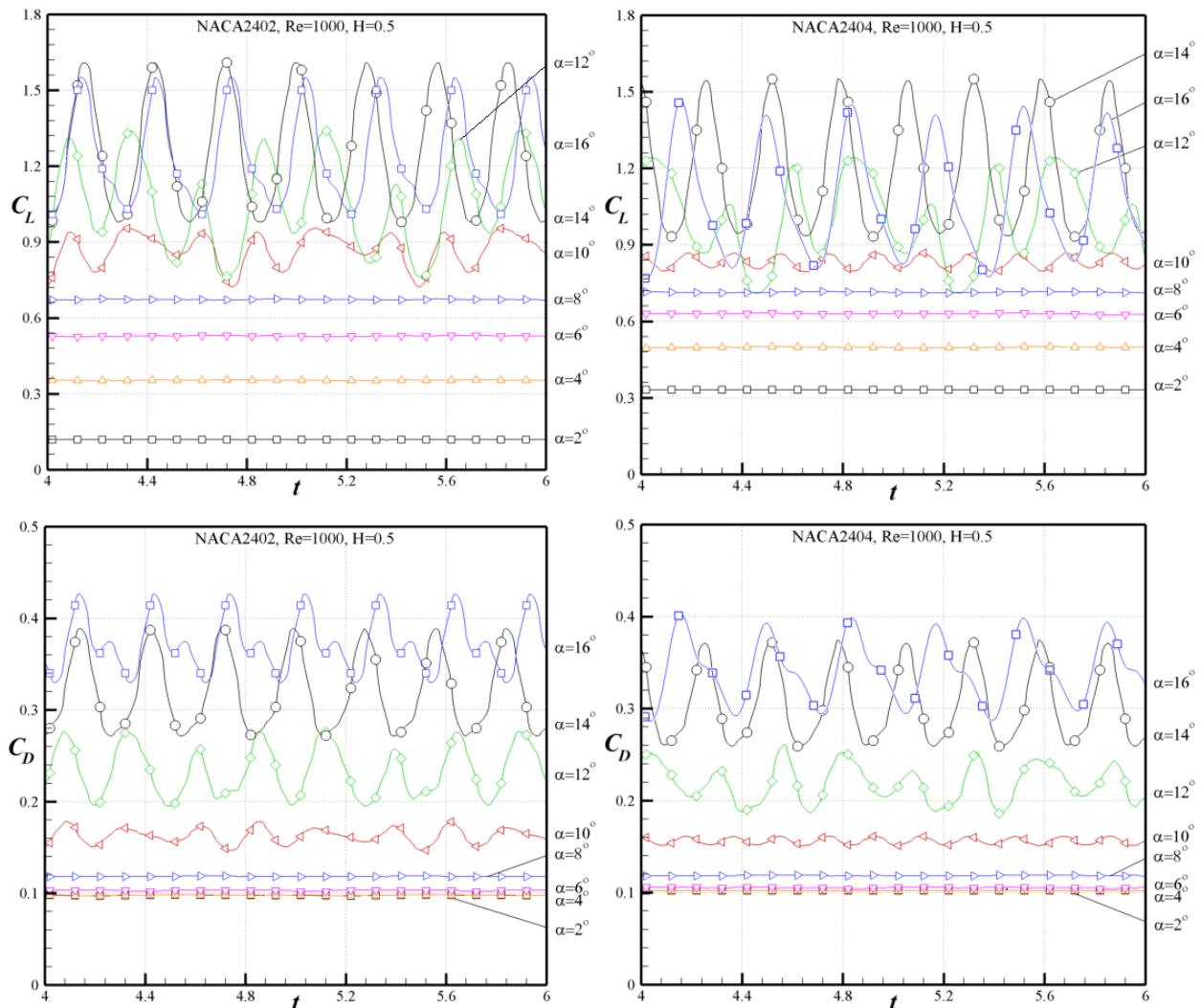


Figure 4.32 Influence of the airfoil thickness of cambered airfoils. Comparison of the variations with the nondimensional time,  $t = t * U_\infty / c$ , of the lift and drag coefficients,  $C_L$  and  $C_D$ , for two cambered airfoils, NACA 2402 and 2404 for Reynolds number,  $Re = 1000$ , and distance to the ground  $H = 0.5$  at various angles of attack,  $\alpha$ .

### 4.6.7 Influence of the maximum camber position

The influence of the maximum camber position on the unsteady effects generated by the unsteady flow separations at low Reynolds numbers in the proximity of the ground is shown in Figure 4.33 for the NACA 4404 and 4304 airfoils for  $Re = 1000$ , and distance to the ground  $H = 0.5$  at various angles of attack,  $\alpha$ .

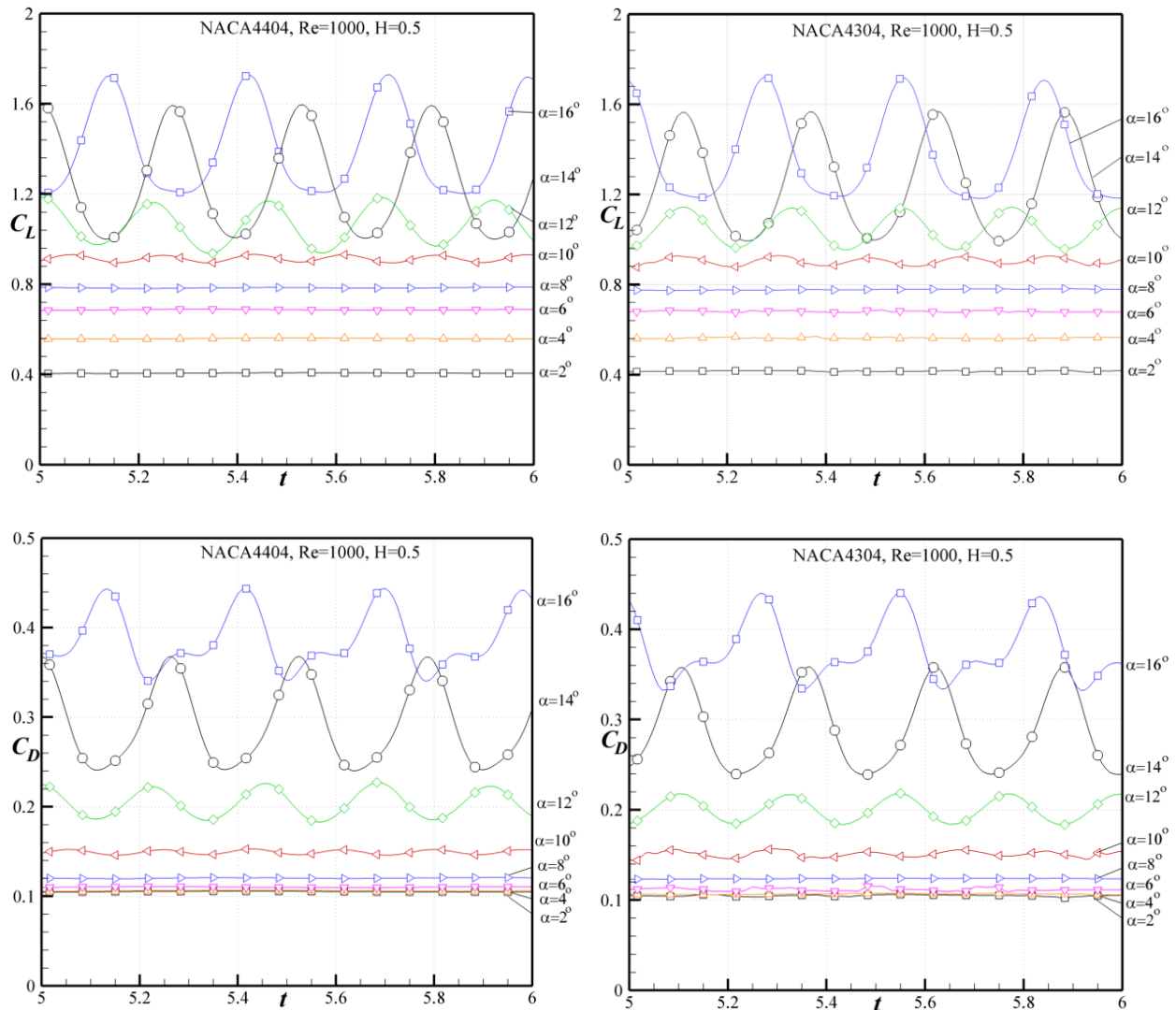


Figure 4.33 Influence of the maximum camber position. Comparison of the variations with the nondimensional time,  $t = t^*U_\infty/c$ , of the lift and drag coefficients,  $C_L$  and  $C_D$ , for two cambered airfoils, NACA 4404 and 4304 for Reynolds number,  $Re = 1000$ , and distance to the ground  $H = 0.5$  at various angles of attack,  $\alpha$ .

## **4.7 Summary of findings**

In this chapter the effect of the ground proximity on the steady and unsteady flows past airfoils has been thoroughly studied to solve the problems encountered by the micro-air-vehicles flying in the proximity of the ground or ceiling. The method developed in the previous case study has been extended to solve this problem.

The solutions for the lift and drag coefficients of the steady and unsteady flows for several symmetric and cambered NACA airfoils in the proximity of the ground are thoroughly analyzed in function of the distance to the ground. The unsteady flow separations on the airfoils are studied with the aid of flow visualizations illustrating the changes in the flow pattern at various moments in time.

This study revealed that the flow separations appear on the upper surface of the airfoil at lower angles of attack due to the proximity of the ground. It was also found that the flow separation regions developed on the upper surface of the airfoil increase with the getting closer to the ground, and for larger Reynolds numbers, thinner airfoils, and higher angles of attack.

## Chapter 5

# Analysis of Steady Viscous Flows Past Wings at Low Reynolds Numbers

The analysis of the flows past airfoils and wings at low Reynolds numbers received a special interest recently due to the development of the Unmanned-Aerial Vehicles (UAVs) and Micro-Air Vehicles (MAVs), which can operate at relatively low altitudes and low speeds [18, 19]. The flows past the airfoils and wings at these low Reynolds numbers ( $Re < 6000$ ) are laminar, and the fluid viscosity effect is dominant and vastly different from those at high Reynolds numbers, usually generating flow separations at their surfaces. Several studies have been published for the airfoil analysis at very low Reynolds numbers. Kunz and Kroo [28] found that many successful codes developed for the normal range of Reynolds numbers (in millions) are not appropriate for low Reynolds numbers. Kunz and Kroo in their computational study of low Reynolds number flow used the INS2D code developed at NASA Ames based on an upwind finite differencing scheme developed by Rogers and Kwak [29]. Later on, Mateescu and Abdo [10] studied the steady flows past airfoils at low Reynolds numbers with a method using artificial compressibility and a central finite difference formulation on stretched staggered grids.

Sunada *et al.* [70] conducted experiments for various rectangular wings of aspect ratio 7.25 at Reynolds number  $Re = 4000$ . Their study presents the experimental aerodynamic lift and drag coefficients obtained for these wings. The influence of the camber ratio, thickness ratio, and streamline shape has been shown in their research. The results presented in the form of lift and drag coefficients are used to validate the present numerical method.

This chapter presents the analysis of steady flow past wings at low Reynolds numbers. The problem is solved in a computational domain obtained from the physical flow domain using a coordinate transformation, in which the boundary conditions are rigorously and efficiently implemented. A pseudo-time relaxation procedure is used with artificial compressibility first introduced by Chorin [30]. A factored Alternate-Direction Implicit (ADI) scheme for the pseudo-time integration, and a special decoupling procedure is used to reduce the problem to the solutions of scalar-tridiagonal systems of equations, which increases significantly the

computational efficiency of the method. A second-order central finite difference formulation is implemented on a stretched staggered grid.

The solutions of the lift and drag coefficients of wings with several symmetric and cambered NACA airfoil sections at low Reynolds numbers are also presented in this chapter. The current numerical solutions are validated by comparison with the experimental results for aerodynamic lift and drag coefficients obtained by Sunada *et al.* [70].

The influence of various geometric and flow parameters, such as wing thickness, wing airfoil camber, angle of attack and Reynolds number, on the aerodynamic coefficients is also studied in this chapter.

## 5.1 Problem formulation and numerical method

Consider a wing with cambered airfoil of chord  $c$  and span  $b$  placed at an incidence  $\alpha$  in a uniform stream of velocity  $U_\infty$ , as shown in Figure 5.1 (the figure shows the half wing). The wing is referred to a Cartesian reference system of coordinates  $cx$ ,  $cy$ , and  $cz$ , where  $x$ ,  $y$  and  $z$  are nondimensional coordinates (with respect to the chord  $c$ ), with the  $x$ -axis along the wing chord and the  $y$ -axis along the wing span, and with the origin of the system situated at the leading edge of the wing root chord. The wing upper and lower surfaces are defined by the equations

$$z = e_1(x) = h(x) + e(x), \quad z = -e_2(x) = h(x) - e(x), \quad (5.1)$$

where the subscripts 1 and 2 refer to the upper and lower surfaces, and where  $h(x)$  and  $e(x)$  define, respectively, the camberline and the wing thickness variation along the wing chord. The special case of symmetric wing section is characterized by  $e_1(x) = e_2(x) = e(x)$  and  $h(x) = 0$ .

The viscous fluid flow past the wing is referred to a fixed Cartesian reference system of coordinates  $c\xi$ ,  $c\eta$ , and  $c\zeta$  defined by the equations

$$\xi = x \cos \alpha + y \sin \alpha, \quad \eta = y, \quad \zeta = -x \sin \alpha + y \cos \alpha, \quad (5.2)$$

where  $\xi$ ,  $\eta$ , and  $\zeta$  are nondimensional coordinates with respect to the wing chord  $c$ , with the  $\xi$ -axis parallel to the uniform stream velocity  $U_\infty$ , which is inclined with the angle  $\alpha$  with respect to the wing chord, the  $\eta$ -axis along the wing span, and the  $\zeta$ -axis perpendicular to the uniform stream velocity as shown in Figure 5.1.

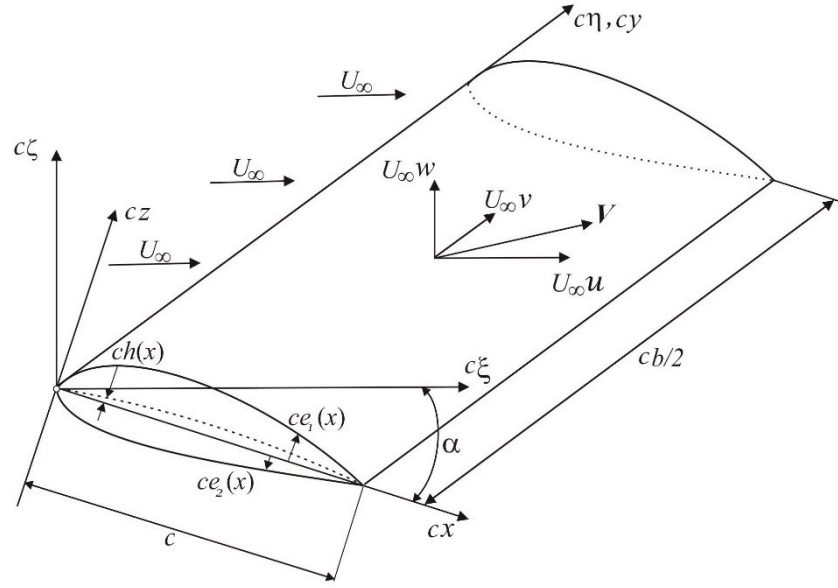


Figure 5.1. Geometry of a half rectangular wing placed in a uniform flow at the angle of attack  $\alpha$ .

Let  $U_\infty u$ ,  $U_\infty v$ , and  $U_\infty w$  denote the fluid velocity components along the fixed  $\xi$ -,  $\eta$ -, and  $\zeta$ -axes, where  $u$ ,  $v$ , and  $w$  are the nondimensional velocity components with respect to  $U_\infty$ .

The Navier-Stokes and continuity equations for the incompressible flow past a wing can be expressed in nondimensional conservation form as

$$\mathbf{Q}(\mathbf{V}, p) = 0, \quad \nabla \cdot \mathbf{V} = \frac{\partial u}{\partial \xi} + \frac{\partial v}{\partial \eta} + \frac{\partial w}{\partial \zeta} = 0, \quad (5.3)$$

where  $\mathbf{V} = \{u, v, w\}^T$  represents the vector of the dimensionless velocity components and  $\mathbf{Q}(\mathbf{V}, p)$ , which includes the convective derivative, pressure and viscous terms, can be expressed in three-dimensional Cartesian coordinates in the form

$$\mathbf{Q}(\mathbf{V}, p) = \{Q_u(u, v, w, p), Q_v(u, v, w, p), Q_w(u, v, w, p)\}^T, \quad (5.4)$$

$$Q_u(u, v, w, p) = \frac{\partial(uu)}{\partial \xi} + \frac{\partial(vu)}{\partial \eta} + \frac{\partial(wu)}{\partial \zeta} + \frac{\partial p}{\partial \xi} - \frac{1}{\text{Re}} \left( \frac{\partial^2 u}{\partial \xi^2} + \frac{\partial^2 u}{\partial \eta^2} + \frac{\partial^2 u}{\partial \zeta^2} \right), \quad (5.5a)$$

$$Q_v(u, v, w, p) = \frac{\partial(uv)}{\partial \xi} + \frac{\partial(vv)}{\partial \eta} + \frac{\partial(wv)}{\partial \zeta} + \frac{\partial p}{\partial \eta} - \frac{1}{\text{Re}} \left( \frac{\partial^2 v}{\partial \xi^2} + \frac{\partial^2 v}{\partial \eta^2} + \frac{\partial^2 v}{\partial \zeta^2} \right), \quad (5.5b)$$

$$Q_w(u, v, w, p) = \frac{\partial(uw)}{\partial\xi} + \frac{\partial(vw)}{\partial\eta} + \frac{\partial(ww)}{\partial\zeta} + \frac{\partial p}{\partial\zeta} - \frac{1}{\text{Re}} \left( \frac{\partial^2 w}{\partial\xi^2} + \frac{\partial^2 w}{\partial\eta^2} + \frac{\partial^2 w}{\partial\zeta^2} \right), \quad (5.5c)$$

$$\nabla \cdot \mathbf{V} = \frac{\partial u}{\partial\xi} + \frac{\partial v}{\partial\eta} + \frac{\partial w}{\partial\zeta}, \quad (5.6)$$

where  $p$  is the dimensionless pressure, nondimensionalized with respect to  $\rho U_\infty^2$ , and  $\text{Re} = cU_\infty/\nu$  is the Reynolds number based on the chord length,  $c$  ( $\rho$  and  $\nu$  are the fluid density and kinematic viscosity).

The problem is solved for a half wing in a fixed computational domain  $(X, Y, Z)$ , which is obtained from the physical flow domain  $(\xi, \eta, \zeta)$ , indicated in Figure 5.2. In this computational domain, the half wing is transformed into a flat plate by geometrical transformation expressed as

$$X = g(\xi, \eta, \zeta), \quad Y = q(\eta) \quad Z = f(\xi, \eta, \zeta), \quad (5.7)$$

where  $g(\xi, \eta, \zeta)$ ,  $q(\eta)$ , and  $f(\xi, \eta, \zeta)$  are defined for each of the six sub-domains in the following forms

**Domain 1** (for  $\xi < 0$ ,  $0 < \eta < b/2 + S$ , and  $-H_2 < \zeta < H_1$ ) :

$$X = \frac{\xi \cos \alpha - \zeta \sin \alpha}{L_0 \cos \alpha + \zeta \sin \alpha} L_0, \quad Y = \eta, \quad Z = \zeta, \quad (5.8a)$$

**Domain 2** (for  $0 < \xi < 1$ ,  $0 < \eta < b/2$ , and  $e_1(x) < \zeta < H_1$ ) :

$$X = \xi \cos \alpha - \zeta \sin \alpha, \quad Y = \eta, \quad Z = \frac{z - ce_1(x)}{H_1 + x \sin \alpha - ce_1(x) \cos \alpha} H_1 \cos \alpha, \quad (5.8b)$$

**Domain 3** (for  $0 < \xi < 1$ ,  $0 < \eta < b/2$ , and  $-H_2 < \zeta < -e_2(x)$ ) :

$$X = \xi \cos \alpha - \zeta \sin \alpha, \quad Y = \eta, \quad Z = \frac{z + ce_2(x)}{H_2 - x \sin \alpha - ce_2(x) \cos \alpha} H_2 \cos \alpha, \quad (5.8c)$$

**Domain 4** (for  $0 < \xi < 1$ ,  $b/2 < \eta < b/2 + S$ , and  $-H_2 < \zeta < H_1$ ) :

$$X = \frac{\xi \cos \alpha - \zeta \sin \alpha}{L_0 \cos \alpha + \zeta \sin \alpha} L_0, \quad Y = \eta, \quad Z = \zeta, \quad (5.8d)$$

**Domain 5** (for  $\xi > 1$ ,  $0 < \eta < b/2 + S$ , and  $-\sin \alpha < \zeta < H_1$ ) :

$$X = \frac{\xi \cos \alpha - \zeta \sin \alpha - 1}{L_1 \cos \alpha - \zeta \sin \alpha - 1} (L_1 - 1) + 1, \quad Y = \eta, \quad Z = \frac{\zeta + \sin \alpha}{H_1 + \sin \alpha} H_1, \quad (5.8e)$$



**Domain 6** (for  $\xi > 1$ ,  $0 < \eta < b/2 + S$ , and  $-H_2 < \zeta < -\sin \alpha$ ) :

$$X = \frac{\xi \cos \alpha - \zeta \sin \alpha - 1}{L_1 \cos \alpha - \zeta \sin \alpha - 1} (L_1 - 1) + 1, \quad Y = \eta, \quad Z = \frac{\zeta + \sin \alpha}{H_2 + \sin \alpha} H_2, \quad (5.8f)$$

In equations (5.8b) and (5.8c),  $x$  and  $z$  are defined in the function of the coordinates  $\xi$  and  $\zeta$  by the relations

$$x = \xi \cos \alpha - \zeta \sin \alpha, \quad z = \xi \sin \alpha + \zeta \cos \alpha, \quad (5.9)$$

where,  $\xi = -L_0$  and  $\xi = L_1$  are the nondimensional physical coordinates of the inflow and outflow boundaries, while,  $\eta = 0$  and  $\eta = b/2 + S$  are the nondimensional physical coordinates of lateral boundaries, and  $\zeta = H_1$ ,  $\zeta = -H_2$  are the nondimensional physical coordinates of the upper and lower boundaries, illustrated in Figure 5.2.

In the computational domain  $(X, Y, Z)$ , the upstream inflow and downstream outflow boundaries, lateral boundaries, and the upper and lower boundaries are defined by the same nondimensional coordinates  $X = -L_0$ ,  $X = L_1$ , and  $Y = 0$ ,  $Y = b/2 + S$ , and  $Z = H_1$ ,  $Z = -H_2$ , respectively.

The Navier-Stokes and continuity equations can be expressed in the computational domain, as

$$\mathbf{G}(\mathbf{V}, p) = 0, \quad \mathbf{D}\mathbf{V} = 0, \quad (5.10)$$

where,

$$\mathbf{V} = \{u, v, w\}^T, \quad \mathbf{G}(\mathbf{V}, p) = \{G_u(u, v, w, p), G_v(u, v, w, p), G_w(u, v, w, p)\}^T, \quad (5.11)$$

$$\begin{aligned} G_u(u, v, w, p) = & C_7 \frac{\partial(uu)}{\partial X} + C_1 \frac{\partial^2 u}{\partial X^2} + C_2 \frac{\partial(uu)}{\partial Z} + \frac{\partial(vu)}{\partial Y} + C_3 \frac{\partial(wu)}{\partial Z} + C_4 \frac{\partial u}{\partial Z} \\ & + C_7 \frac{\partial p}{\partial X} + C_8 \frac{\partial(wu)}{\partial X} + C_9 \frac{\partial u}{\partial X} + C_2 \frac{\partial p}{\partial Z} + C_5 \frac{\partial^2 u}{\partial Z^2} + C_6 \frac{\partial^2 u}{\partial Z \partial X} + C_{10} \frac{\partial^2 u}{\partial Y^2}, \end{aligned} \quad (5.12a)$$

$$\begin{aligned} G_v(u, v, w, p) = & C_7 \frac{\partial(uv)}{\partial X} + C_1 \frac{\partial^2 v}{\partial X^2} + C_2 \frac{\partial(uv)}{\partial Z} + \frac{\partial(vv)}{\partial Y} + C_3 \frac{\partial(wv)}{\partial Z} + C_4 \frac{\partial v}{\partial Z} + \frac{\partial p}{\partial Y} \\ & + C_8 \frac{\partial wv}{\partial X} + C_9 \frac{\partial v}{\partial X} + C_5 \frac{\partial^2 v}{\partial Z^2} + C_6 \frac{\partial^2 v}{\partial Z \partial X} + C_{10} \frac{\partial^2 v}{\partial Y^2}, \end{aligned} \quad (5.12b)$$

$$\begin{aligned}
G_w(u, v, w, p) = & C_7 \frac{\partial(uw)}{\partial X} + C_1 \frac{\partial^2 w}{\partial X^2} + C_2 \frac{\partial(uw)}{\partial Z} + \frac{\partial(vw)}{\partial Y} + C_3 \frac{\partial(ww)}{\partial Z} + C_4 \frac{\partial w}{\partial Z} \\
& + C_8 \frac{\partial w w}{\partial X} + C_9 \frac{\partial w}{\partial X} + C_3 \frac{\partial p}{\partial Z} + C_8 \frac{\partial p}{\partial X} + C_5 \frac{\partial^2 w}{\partial Z^2} + C_6 \frac{\partial^2 w}{\partial Z \partial X} + C_{10} \frac{\partial^2 w}{\partial Y^2}, \tag{5.12c}
\end{aligned}$$

$$D\mathbf{V} = C_7 \frac{\partial u}{\partial X} + \frac{\partial v}{\partial Y} + C_2 \frac{\partial u}{\partial Z} + C_3 \frac{\partial w}{\partial Z} + C_8 \frac{\partial w}{\partial X}, \tag{5.13}$$

in which the expressions of the coefficients  $C_1, C_2, C_3, \dots, C_9$ , and  $C_{10}$  are obtained for each domain from the coordinate transformations (5.7) to (5.8), the details are explained in Appendix C.

## 5.2 Method of solution

An iterative pseudo-time relaxation procedure with artificial compressibility is then used in order to solve this steady flow problem

$$\frac{\partial \check{\mathbf{V}}}{\partial \tau} + \check{\mathbf{G}}(\mathbf{V}, p) = 0, \quad \delta \frac{\partial \check{p}}{\partial \tau} + D\check{\mathbf{V}} = 0, \tag{5.14}$$

where  $\check{\mathbf{V}}(\tau)$  and  $\check{p}(\tau)$  denote the pseudo-functions corresponding to the variable velocity and pressure at pseudo-time  $\tau$ , and  $\delta$  represents an artificially-added compressibility.

An implicit Euler scheme is then used to discretize equations (5.14) between the pseudo-time levels  $\tau^\nu$  and  $\tau^{\nu+1} = \tau^\nu + \Delta\tau$ , and the resulting equations are expressed in terms of the pseudo-time variations  $\Delta\check{u} = \check{u}^{\nu+1} - \check{u}^\nu$ ,  $\Delta\check{v} = \check{v}^{\nu+1} - \check{v}^\nu$ ,  $\Delta\check{w} = \check{w}^{\nu+1} - \check{w}^\nu$ , and  $\Delta\check{p} = \check{p}^{\nu+1} - \check{p}^\nu$ , in the matrix form

$$[\mathbf{I} + \Delta\tau(\mathbf{D}_X + \mathbf{D}_Y + \mathbf{D}_Z)]\Delta\mathbf{f} = \Delta\tau \mathbf{R}, \tag{5.15}$$

where  $\Delta\mathbf{f} = [\Delta\check{u}, \Delta\check{v}, \Delta\check{w}, \Delta\check{p}]^T$ ,  $\mathbf{I}$  is the identity matrix, and

$$\mathbf{D}_X = \begin{bmatrix} M & 0 & 0 & C_7 \frac{\partial}{\partial X} \\ 0 & M & 0 & 0 \\ 0 & 0 & M & 0 \\ \frac{C_7}{\delta} \frac{\partial}{\partial X} & 0 & \frac{C_8}{\delta} \frac{\partial}{\partial X} & 0 \end{bmatrix}, \quad \mathbf{D}_Y = \begin{bmatrix} N & 0 & 0 & 0 \\ 0 & N & 0 & 0 \\ 0 & 0 & N & 0 \\ 0 & \frac{\partial}{\partial Y} & 0 & 0 \end{bmatrix}, \tag{5.16}$$

$$\mathbf{D}_Z = \begin{bmatrix} L & 0 & 0 & C_2 \frac{\partial}{\partial Z} \\ 0 & L & 0 & 0 \\ 0 & 0 & L & C_3 \frac{\partial}{\partial Z} \\ \frac{C_2}{\delta} \frac{\partial}{\partial Z} & 0 & \frac{C_3}{\delta} \frac{\partial}{\partial Z} & 0 \end{bmatrix}, \quad \mathbf{R} = \begin{bmatrix} -G_u^v \\ -G_v^v \\ -G_w^v \\ -(1/\delta) D \check{\mathbf{V}}^v \end{bmatrix}, \quad (5.17)$$

in which the differential operators  $M$ ,  $N$ , and  $L$  are defined as

$$M = C_9 \frac{\partial \phi}{\partial X} + C_7 \frac{\partial(\bar{u}^v \phi)}{\partial X} + C_8 \frac{\partial(\bar{w}^v \phi)}{\partial X} + C_1 \frac{\partial^2 \phi}{\partial X^2}, \quad (5.18)$$

$$N = \frac{\partial(\bar{v}^v \phi)}{\partial Y} + C_{10} \frac{\partial^2 \phi}{\partial Y^2}, \quad (5.19)$$

$$L = C_2 \frac{\partial(\bar{u}^v \phi)}{\partial Z} + C_3 \frac{\partial(\bar{w}^v \phi)}{\partial Z} + C_4 \frac{\partial \phi}{\partial Z} + C_5 \frac{\partial^2 \phi}{\partial Z^2} + C_6 \frac{\partial^2 \phi}{\partial X \partial Z}, \quad (5.20)$$

where  $\phi$  can be  $\Delta \bar{u}$ ,  $\Delta \bar{v}$ ,  $\Delta \bar{w}$ , or  $\Delta \bar{p}$ .

The optimal value of the artificial compressibility,  $\delta$ , and the size of the pseudo-time step,  $\Delta \tau$ , are determined, in a similar manner to that used in the previous studies by the author [1, 3, 6].

A factored ADI scheme is then applied to separate equation (5.15) into three successive sweeps in the  $Z$ ,  $Y$  and  $X$  directions, defined by the equation

$$[\mathbf{I} + \Delta \tau (\mathbf{D}_X + \mathbf{D}_Y + \mathbf{D}_Z)] \Delta \mathbf{f} = [\mathbf{I} + \Delta \tau \mathbf{D}_X][\mathbf{I} + \Delta \tau \mathbf{D}_Y][\mathbf{I} + \Delta \tau \mathbf{D}_Z] \Delta \mathbf{f}. \quad (5.21)$$

This ADI scheme can produce some convergence issues when  $\Delta \tau$  takes large values. Therefore, to have a faster convergence it is important to keep  $\Delta \tau$  sufficiently small.

The ADI scheme is reduced to the solution of several sets of scalar-tridiagonal systems of equations. Thus, equation (5.15) changes to

$$[\mathbf{I} + \Delta \tau \mathbf{D}_X][\mathbf{I} + \Delta \tau \mathbf{D}_Y][\mathbf{I} + \Delta \tau \mathbf{D}_Z] \Delta \mathbf{f} = \Delta \tau \mathbf{R} \quad (5.22)$$

The ADI method requires the introduction of the intermediate variables  $\Delta \mathbf{f}^*$  and  $\Delta \bar{\mathbf{f}}$  to solve the linear implicit system of equations. The variable  $\Delta \mathbf{f}^*$  has the components  $\Delta u^*$ ,  $\Delta v^*$ ,  $\Delta w^*$  and  $\Delta p^*$ , which are calculated in the  $Z$ -sweep as

$$[\mathbf{I} + \Delta \tau \mathbf{D}_Z] \Delta \mathbf{f}^* = \Delta \tau \mathbf{R}, \quad (5.23)$$

and the variable  $\Delta \bar{\mathbf{f}}$  has the components  $\Delta \bar{u}$ ,  $\Delta \bar{v}$ ,  $\Delta \bar{w}$  and  $\Delta \bar{p}$ , which are computed in the  $Y$ -sweep as

$$[\mathbf{I} + \Delta \tau \mathbf{D}_Y] \Delta \bar{\mathbf{f}} = \Delta \mathbf{f}^*, \quad (5.24)$$

then,  $\Delta \mathbf{f}$  are obtained in the  $X$ -sweep as

$$[\mathbf{I} + \Delta \tau \mathbf{D}_Y] \Delta \mathbf{f} = \Delta \bar{\mathbf{f}}, \quad (5.25)$$

Hence, after the factored ADI scheme is applied, the scalar form of  $Z$ -sweep,  $Y$ -sweep, and  $X$ -sweep are obtained by replacing the equations (5.16) to (5.20) into (5.23), (5.24) and (5.25).

The  $Z$ -sweep,  $Y$ -sweep, and  $X$ -sweep equations are further spatially discretized by central differencing on a stretched staggered grid, in which the flow variables  $u$ ,  $v$ ,  $w$  and pressure,  $p$  are defined at different positions, as shown in Figure 5.3. By using a staggered grid, this method avoids the odd-and-even point decoupling while preserving the second-order accuracy in space of the method. The grid stretching is defined by hyperbolic sine functions in the  $X$ ,  $Y$ , and  $Z$  directions.

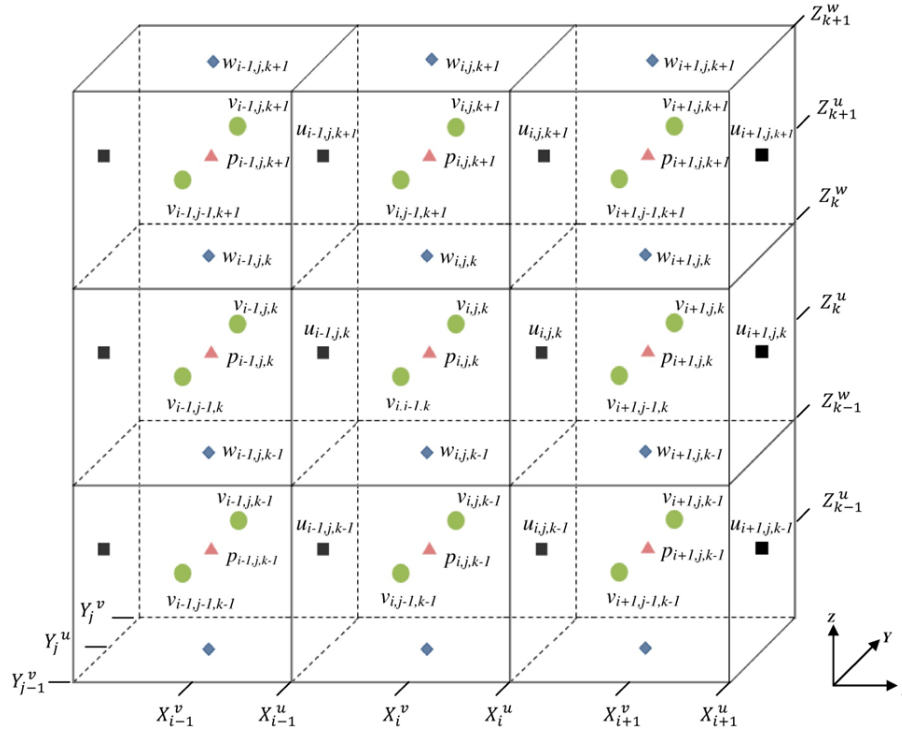


Figure 5.3. Geometry of the staggered grid.

A special decoupling procedure [9, 10, 11], based on the utilization of the continuity equation is used for each sweep to eliminate the pressure from the momentum equations. For example, for the Z-sweep the corresponding relation from continuity equation can be used:

$$\Delta p^* = -\frac{\Delta \tau}{\delta} \left( D\tilde{V}^v + C_2 \frac{\partial(\Delta u^*)}{\partial Z} + C_3 \frac{\partial(\Delta w^*)}{\partial Z} \right), \quad \Delta p = \Delta p^* - \frac{\Delta \tau}{\delta} \frac{\partial(\Delta u)}{\partial X} \quad (5.26)$$

In this manner, the problem is reduced to the solution of three sets of decoupled scalar-tridiagonal systems of equations, for each sweep. As a result, this method is characterized by excellent computational efficiency and accuracy.

### 5.3 Lift and drag coefficients of the rectangular wings

The aerodynamic lift and drag forces are generated by the pressure and the shear stress acting perpendicular and tangential on the upper wing surface,  $p_u$  and  $\tau_u$ , and on its lower surface,  $p_l$  and  $\tau_l$ . The wing upper and lower surfaces are each divided, by planes of constant  $y$  and planes of constant  $x$ , into very small area elements of elemental areas  $\delta\sigma_{wu,i,j}$  and  $\delta\sigma_{wl,i,j}$ , respectively, where  $i$  varies from 1 to  $m$  along the chord, and  $j$  varies from  $-n$  to  $n$  along the wing span.

Consider a strip element of the wing of constant width  $\delta y_j$  (from the leading edge to the trailing edge), the normal force,  $N$ , and tangential force,  $A$ , on this strip is

$$N_j = -\sum_{i=1}^{i=m} (p_{u,i,j} \cos \theta_{u,i,j} + \tau_{u,i,j} \sin \theta_{u,i,j}) \delta\sigma_{wu,i,j} + \sum_{i=1}^{i=m} (p_{l,i,j} \cos \theta_{l,i,j} - \tau_{l,i,j} \sin \theta_{l,i,j}) \delta\sigma_{wl,i,j}, \quad (5.27a)$$

$$A_j = \sum_{i=1}^{i=m} (-p_{u,i,j} \sin \theta_{u,i,j} + \tau_{u,i,j} \cos \theta_{u,i,j}) \delta\sigma_{wu,i,j} + \sum_{i=1}^{i=m} (p_{l,i,j} \sin \theta_{l,i,j} - \tau_{l,i,j} \cos \theta_{l,i,j}) \delta\sigma_{wl,i,j}, \quad (5.27b)$$

where  $\theta_{u,i,j}$  and  $\theta_{l,i,j}$  are the inclination angles of the upper and lower wing surfaces with respect to the  $x$ -axis.

As a result, the normal and tangential force coefficients for the spanwise wing strip are expressed in terms of the pressure coefficient  $C_p$  and the skin friction coefficients  $C_f$  in the form

$$C_{n,j} = - \sum_{i=1}^{i=m} \left( C_{p_{u,i,j}} - C_{p_{l,i,j}} \right) + \sum_{i=1}^{i=m} \left( C_{f_{u,i,j}} \sin \theta_{u,i,j} + C_{f_{l,i,j}} \sin \theta_{l,i,j} \right), \quad (5.28a)$$

$$C_{a,j} = \sum_{i=1}^{i=m} \left( C_{p_{u,i,j}} \sin \theta_{u,i,j} + C_{p_{l,i,j}} \sin \theta_{l,i,j} \right) + \sum_{i=1}^{i=m} \left( C_{f_{u,i,j}} - C_{f_{l,i,j}} \right). \quad (5.28b)$$

Then, the lift and drag coefficients for each strip of the wing along the span can be expressed in the form

$$C_{l,j} = C_{n,j} \cos \alpha - C_{a,j} \sin \alpha, \quad (5.29a)$$

$$C_{d,j} = C_{n,j} \sin \alpha + C_{a,j} \cos \alpha \quad (5.29b)$$

To obtain the total lift and drag coefficients of the wing, the lift and drag forces for each wing strip are summed up along the span and divided to the total area of the wing as

$$C_L = \sum_{j=-n}^n \left[ C_{l,j} \sigma_{w,j} \right] \frac{1}{S_w}, \quad (5.30a)$$

$$C_D = \sum_{j=-n}^n \left[ C_{d,j} \sigma_{w,j} \right] \frac{1}{S_w}, \quad (5.30b)$$

where  $S_w$  is the total area of rectangular wing and  $\sigma_{w,j}$  is the area of each strip.

## 5.4 Method validation

The numerical solutions for the lift and drag coefficients obtained by this method for the steady flow past the wing are validated in Figure 5.4 by comparison with the experimental results reported by Sunada *et al.* [70] for the rectangular wing with NACA 0006 airfoil of aspect ratio 7.25 for Reynolds number  $Re = 4000$  at several incidences.

Very good agreement can be noticed in Figure 5.4 between the present solutions of the lift and drag coefficients and the experimental results for angle of attack up to  $\alpha = 5.7^\circ$ . After this incidence, the flow becomes unsteady, due to the unsteady flow separations, and the comparison deteriorates.

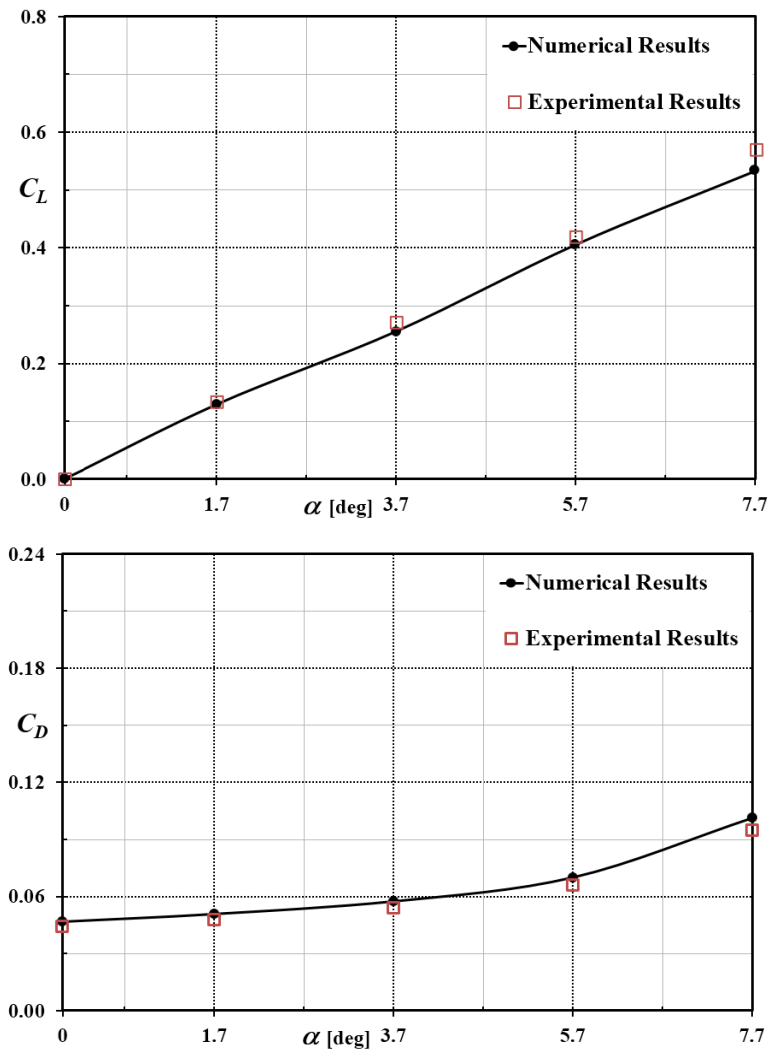


Figure 5.4. The variation with the angle of attack,  $\alpha$ , for the lift and drag coefficients,  $C_L$  and  $C_D$ , of the rectangular wing with NACA0006 airfoil and aspect ratio 7.25 at Reynolds number  $Re = 4000$ . Comparison between:

- Present steady solutions
- Experimental steady results obtained by Sunada *et al.* [70].

## 5.5 Grid sensitivity analysis

The grid sensitivity has been evaluated for the presented numerical solution through the mesh refinement applied to a steady flow past the rectangular wing. Through the geometry analysis, it is found the length of domain 1 and domain 5, 6 (as shown in Figure 5.2) along the wing chord should be at least  $L_0 = 10$ , and  $L_I = 30$ , the length of upper and lower boundaries are  $H_I = 10$ , and

$H_2 = -10$ , and the length of domain 4 along the span should be at least  $S_1 = 8$ , and  $S_2 = -8$ . Beyond these lengths the numerical results are not affected.

To find the ideal grid points, the solution is solved for a steady viscous flow past rectangular wing with NACA 0004 airfoil section for  $Re = 1500$  at angle of attack,  $\alpha = 4^\circ$ .

The criteria of comparison are based on the aerodynamic coefficients such as the total lift and drag coefficients of the rectangular wing,  $C_L$  and  $C_D$ .

The results of the grid sensitivity test are shown in Table 5.1. It can be seen there is no discrepancy between the solution obtained by using  $300 \times 120 \times 175$  grid points and the fully converged solution obtained with  $350 \times 145 \times 200$  grid points. Beyond this grid density, the numerical solution is not influenced by the grid refinement.

Number of grid points	$C_L$	$C_D$
100 x 20 x 75	0.203	0.079
150 x 45 x 100	0.221	0.087
200 x 70 x 125	0.234	0.089
250 x 95 x 150	0.236	0.090
300 x 120 x 175	0.237	0.091
350 x 145 x 200	0.237	0.091

Table 5.1 Grid sensitivity of the numerical solution for steady flow past rectangular wing with NACA 0004 airfoil section for  $Re = 1500$  at angle of attack,  $\alpha = 4^\circ$  based on the computed aerodynamic coefficients,  $C_L$  and  $C_D$ .

The computational time varies for each study case, however, in general the finally converged solution for steady viscous flow over a rectangular wing for a fine mesh with  $300 \times 120 \times 175$  grid points requires 0.2 minutes per iteration computing time on a PC (Intel dual core- i7 CPU) using FORTRAN 90.

## 5.6 Solutions of the steady viscous flows past rectangular wings

The numerical method presented in section 5.2 is used to obtain solutions of the flow past wings with symmetric and cambered NACA airfoil sections at low Reynolds numbers. The results are shown for different Reynolds numbers, and several angles of attack. The influence of Reynolds number, and wing thickness is also presented for several aerodynamic characteristics

including total lift and drag coefficients, and variations of lift and drag coefficients along the wing span.

### 5.6.1 Influence of the Reynolds number

The influence of Reynolds number on the aerodynamic lift and drag coefficients,  $C_L$  and  $C_D$ , of a rectangular wing with NACA 0002 airfoil section and aspect ratio 8 for two Reynolds numbers  $Re = 600$  and  $1000$  is shown in Figure 5.5. In addition, the influence of Reynolds number for a rectangular wing with NACA 0004 airfoil section, and the same aspect ratio for two values of Reynolds numbers  $Re = 600$  and  $1500$  is illustrated in Figure 5.6. These results are presented for the lift and drag coefficients at various angles of attack.

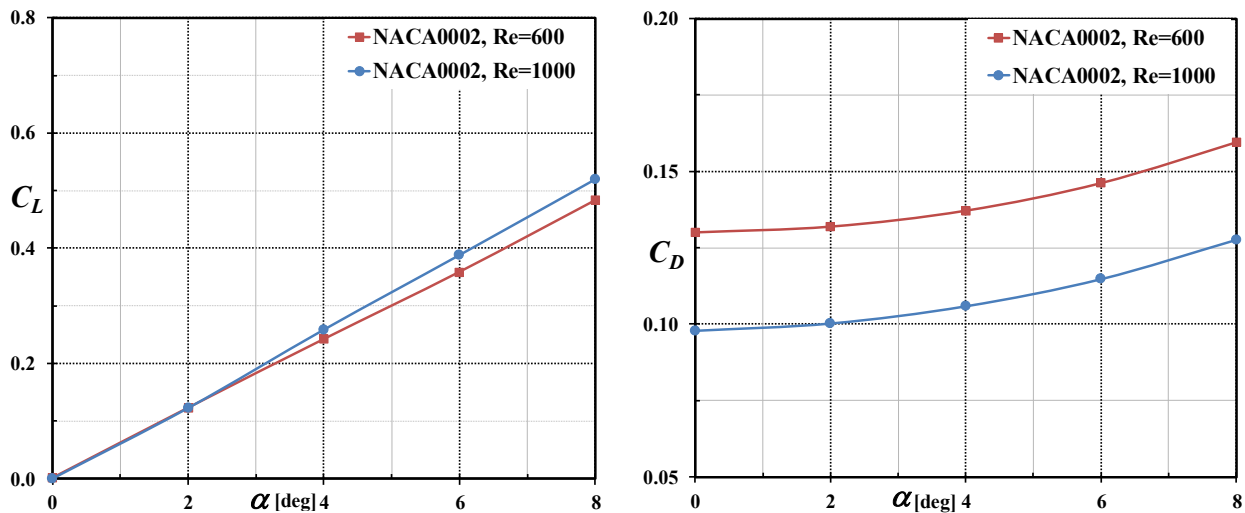


Figure 5.5. Influence of the Reynolds number on the aerodynamic coefficients: Comparison of the lift and drag coefficients,  $C_L$  and  $C_D$ , for a rectangular wing with NACA0002 airfoil section of aspect ratio 8 for two Reynolds numbers,  $Re = 600$  and  $1000$ , at several angles of attack,  $\alpha$ .

One can notice that the lift coefficient is increasing as the Reynolds number increases. However, when the Reynolds number rise, the drag coefficient shows an opposite behavior and it decreases.

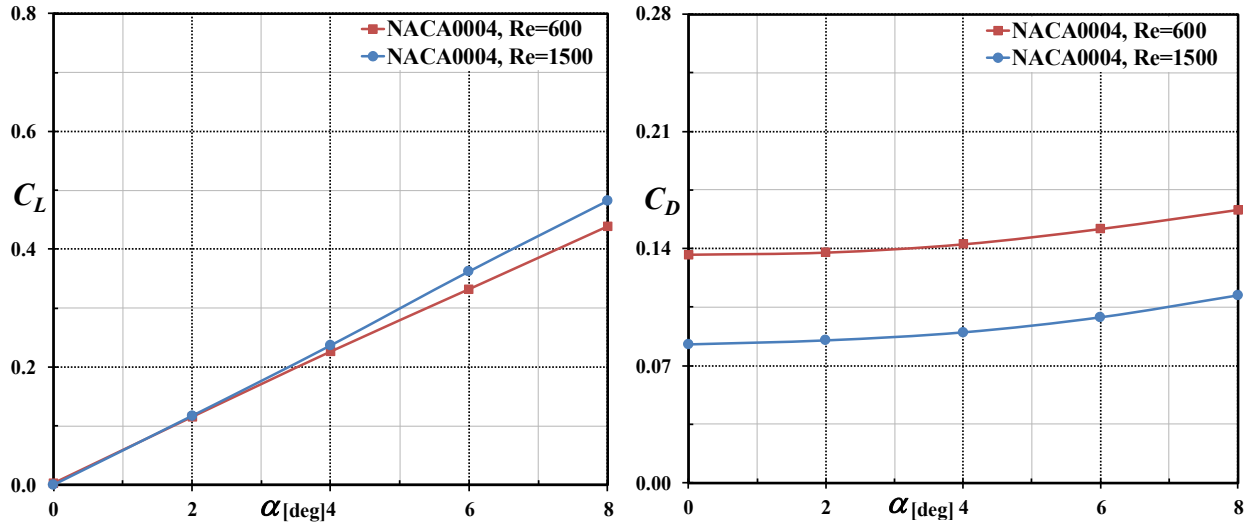


Figure 5.6. Influence of the Reynolds number on the aerodynamic coefficients: Comparison of the lift and drag coefficients,  $C_L$  and  $C_D$ , for a rectangular wing with NACA 0004 airfoil section and aspect ratio 8 for two Reynolds numbers,  $Re = 600$  and  $1500$ , at several angles of attack,  $\alpha$ .

### 5.6.2 Influence of the wing thickness

The influence of the wing thickness with NACA 0002 and NACA 0008 airfoil sections, and aspect ratio 8 on the aerodynamic characteristics,  $C_L$  and  $C_D$ , is shown in Figure 5.7 for  $Re = 600$ , and in Figure 5.8 for  $Re = 1000$ .

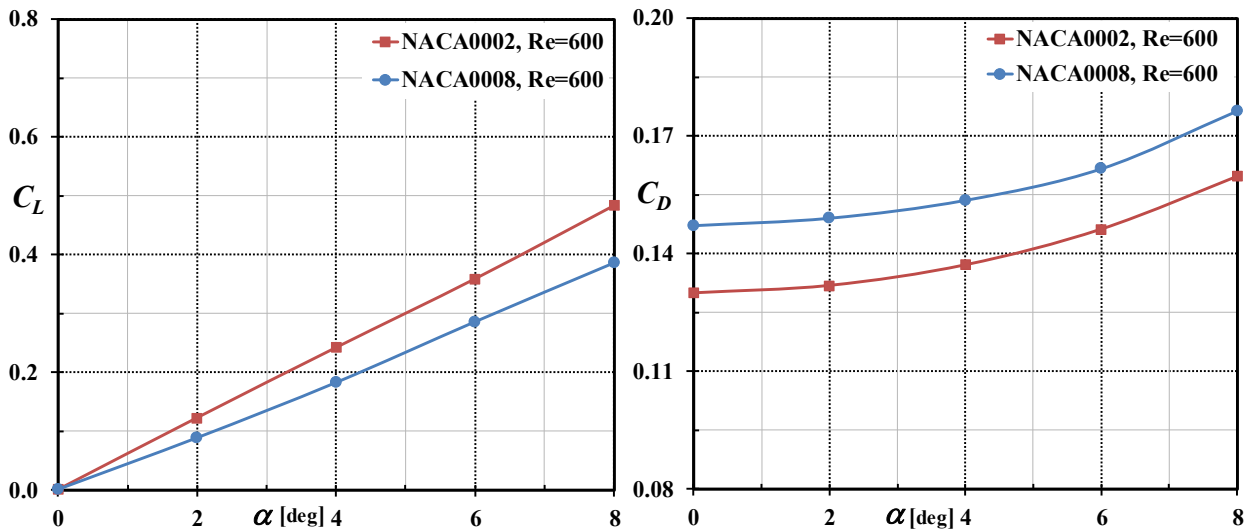


Figure 5.7. Influence of the wing thickness on the aerodynamic coefficients: Comparison of the lift and drag coefficients,  $C_L$  and  $C_D$ , for a rectangular wing with NACA0002 and NACA0008 airfoil sections and aspect ratio 8 for Reynolds number  $Re = 600$  at several angles of attack,  $\alpha$ .

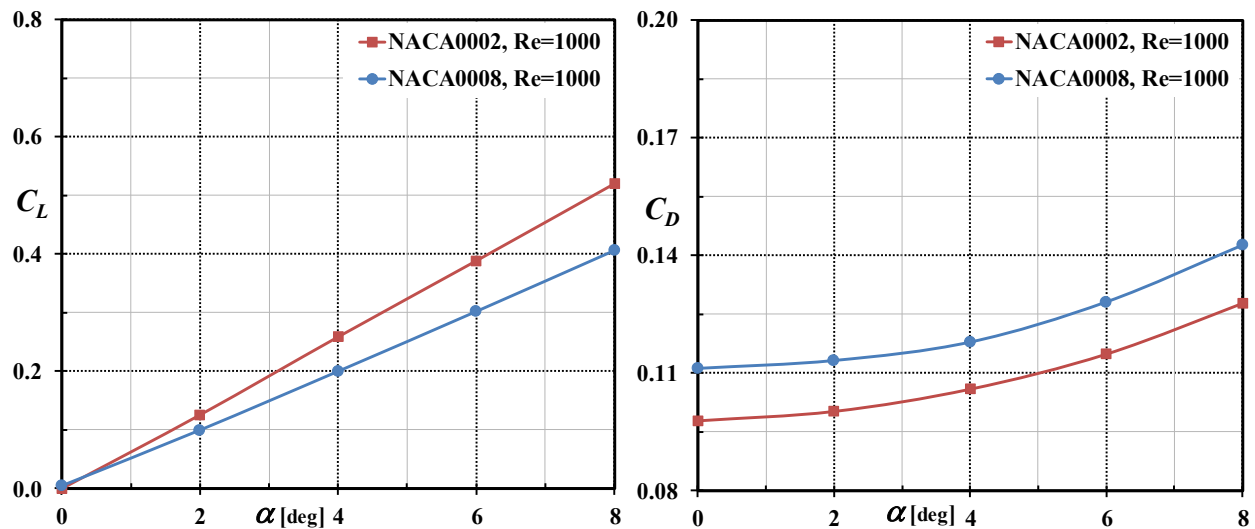


Figure 5.8. Influence of the wing thickness on the aerodynamic coefficients: Comparison of the lift and drag coefficients,  $C_L$  and  $C_D$ , for a rectangular wing with NACA0002 and NACA0008 airfoil sections and aspect ratio 8 for Reynolds number  $Re = 1000$  at several angles of attack,  $\alpha$ .

In the above figures, one can notice that the lift coefficient decreases for thicker wings at the same Reynolds number. In other words, the lift coefficient is smaller for the wing with NACA 0008 airfoil section than for NACA 0002 airfoil section at the same Reynolds number.

However, the drag coefficient increases for thicker wings at the same Reynolds number, such that the drag coefficient of wing with NACA 0008 airfoil section is larger than that of the wing with NACA 0002 airfoil section at the same Reynolds number.

### 5.6.3 Influence of Reynolds number and wing thickness on the variations of the local lift and drag coefficients along the semi-span of the wing

In order to study the variations of the local lift and drag coefficients,  $C_l$  and  $C_d$ , along the semi-span of the wing, three rectangular wings with NACA 0002, NACA 0004, and NACA0008 airfoil sections are selected. The influence of the Reynolds number on these variations can be seen in Figure 5.9 for the half wing with NACA 0004 airfoil section for two Reynolds numbers,  $Re = 600$  and  $1500$  at the angles of attack 6 and 8 degrees.

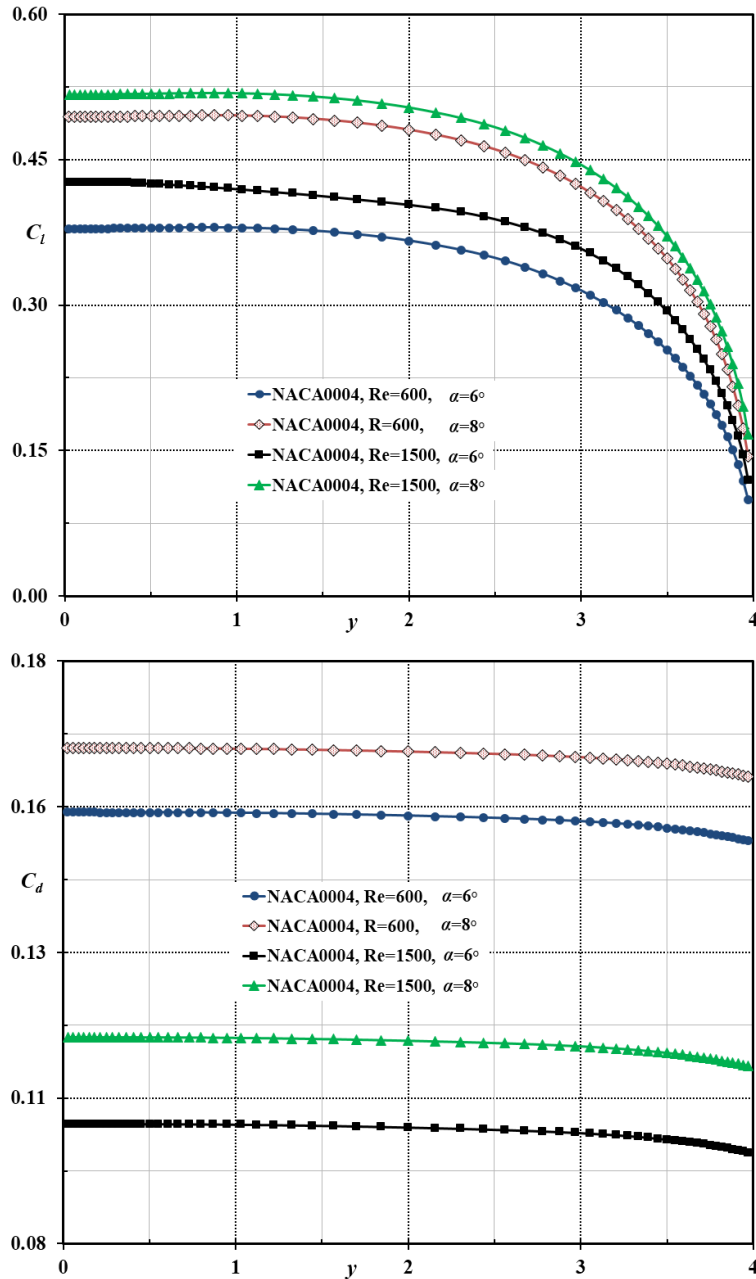


Figure 5.9. Influence of the Reynolds number on the variation of the local aerodynamic coefficients along the wing semi-span: Comparison of  $C_l$  and  $C_d$  for a rectangular wing with NACA 0004 airfoil section of aspect ratio 8 for two Reynolds numbers,  $Re = 600$  and  $1500$ , at angles of attack  $\alpha = 6^\circ$  and  $8^\circ$ .

One can notice that as the angle of attack increases, the local lift and drag coefficients,  $C_l$  and  $C_d$ , are larger. At the same angle of attack and NACA airfoil section, the local lift coefficient becomes larger when the Reynolds number increases.

The influence of the wing thickness on the local lift and drag coefficients variations along the semi-span for rectangular wings with NACA 0002, and NACA 0008 airfoil sections for  $Re = 600$  at the angles of attack  $2$  and  $4$  degrees is shown in the Figure 5.10.

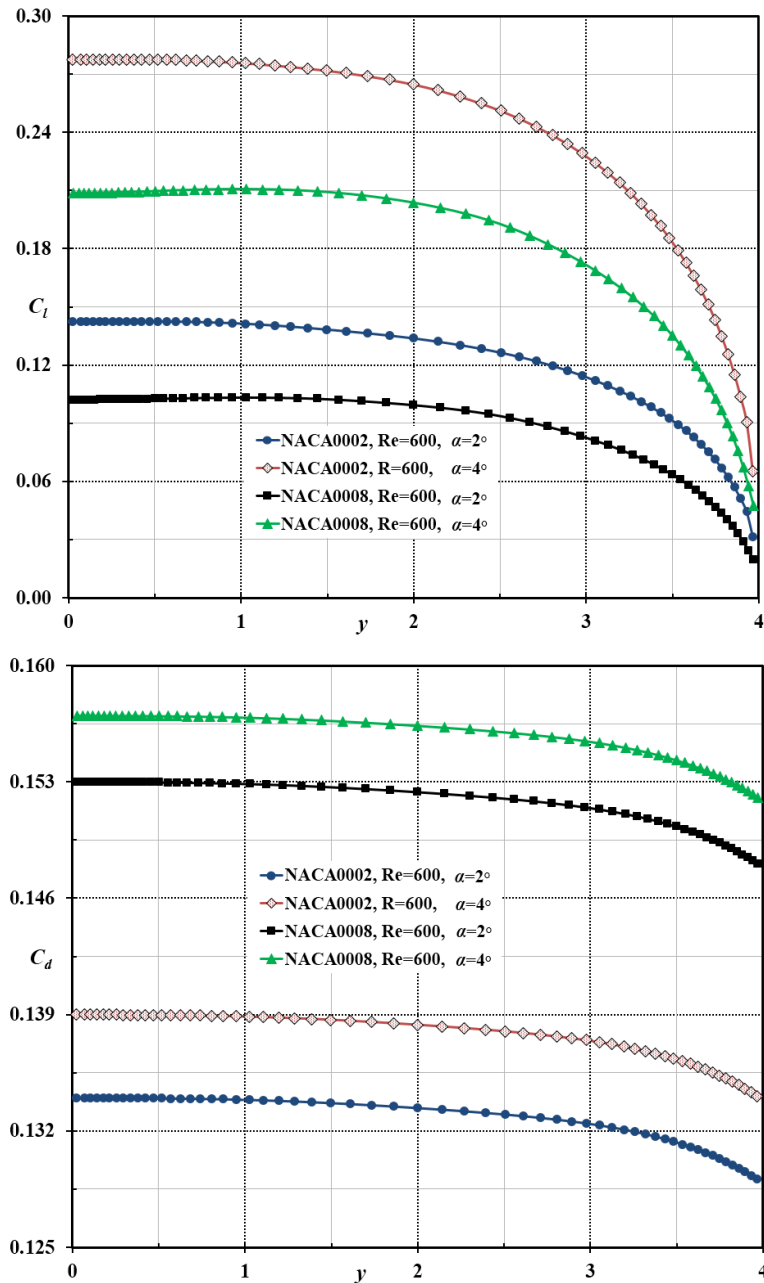


Figure 5.10. Influence of the wing thickness on the variation of the aerodynamic coefficients along the semi-span of the wing: Comparison of  $C_l$  and  $C_d$ , for two rectangular wings with NACA 0002 and NACA 0008 airfoil sections, aspect ratio 8 for  $Re = 600$  at the angles of attack  $\alpha = 2^\circ$  and  $4^\circ$ .

One can notice that the thinner wing with NACA 0002 airfoil section has a larger local lift coefficient and a smaller drag coefficient than the thicker wing with NACA 0008 airfoil section.

### 5.6.4 Influence of the wing camber

The influence of the airfoil camber of the rectangular wing with aspect ratio 8 for  $Re = 1000$  on the wing lift and drag coefficients can be seen in Figure 5.11 by comparing the results for the wing with NACA 2404 airfoil section and the wing with NACA 4404 airfoil section.

One can notice that the wing lift and drag coefficients,  $C_L$  and  $C_D$ , are larger for the more cambered wing.

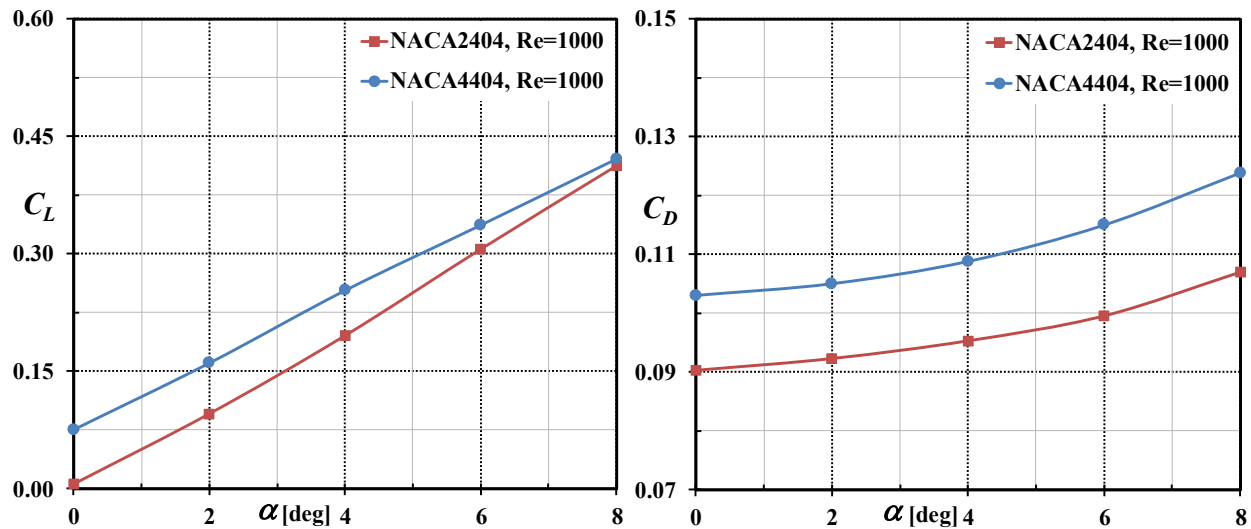


Figure 5.11. Influence of the wing camber on the aerodynamic coefficients: Comparison of the wing lift and drag coefficients,  $C_L$  and  $C_D$ , for two rectangular wings with NACA 2404 and NACA 4404 airfoil section, aspect ratio 8 for  $Re = 1000$  at several incidences.

### 5.6.5 Streamline and flow pattern for steady viscous flows past wings

The typical front views ( $\xi, \zeta$  planes) of the flow past a wing with NACA 0008 airfoil section as viewed from the longitudinal planes  $y = 0$ ,  $y = 0.25(b/2)$ ,  $y = 0.5(b/2)$ , and  $y = 0.75(b/2)$  towards the wing tip ( $y=b/2$ ) are illustrated in Figure 5.12 for  $Re = 1000$  at angle of attack  $\alpha = 8^\circ$  by using the streamlines (represented by continuous lines). The color shades show the magnitude of the nondimensional flow velocity with respect to the mean flow velocity,  $U_\infty$ , according to the scale indicated in the figure.

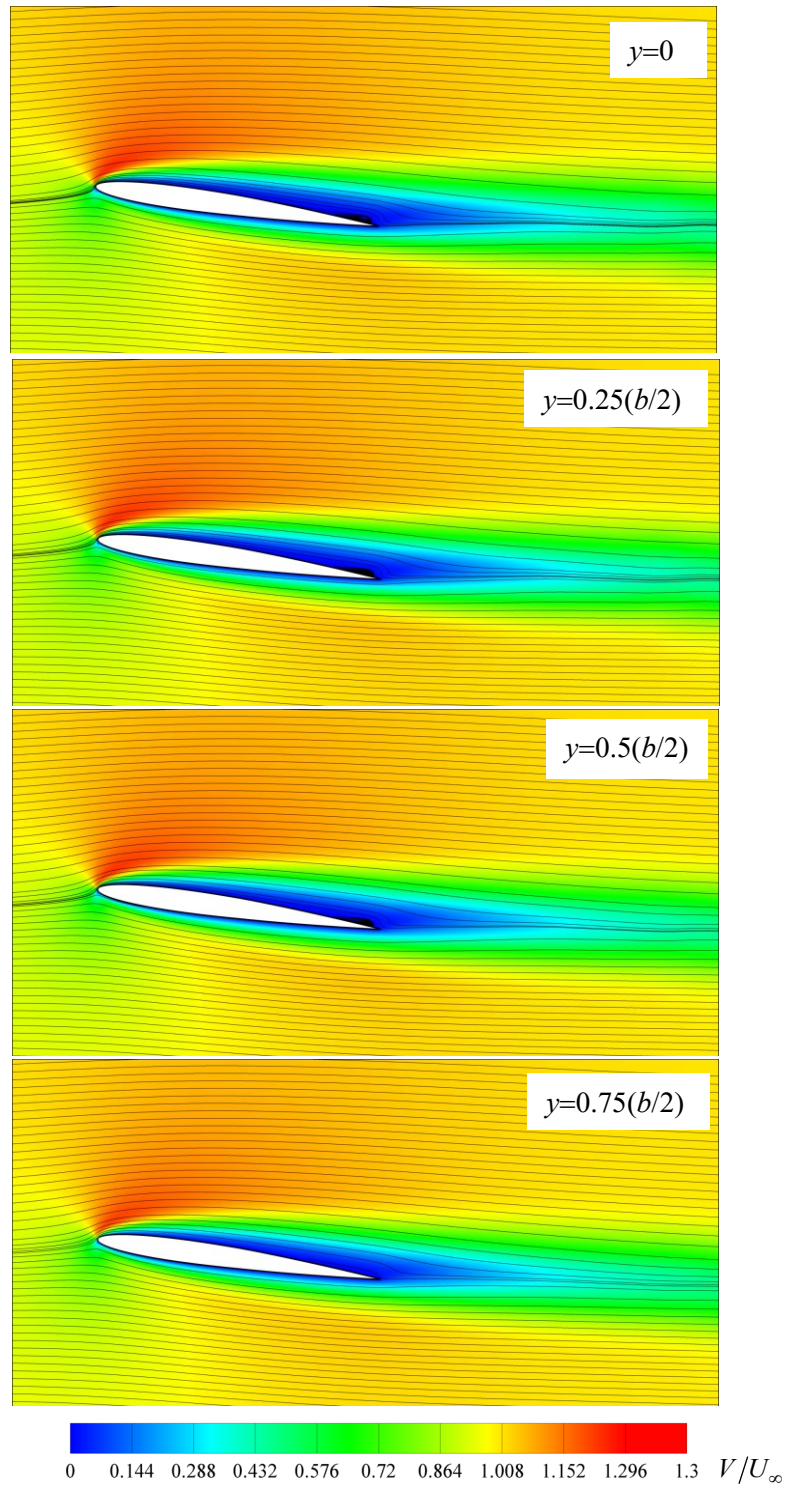


Figure 5.12. Illustration of the velocity contours and streamlines indicating the nondimensional velocity for the wing with NACA 0008 airfoil section for  $Re = 1000$  and angle of attack  $\alpha = 8^\circ$  at various spanwise locations  $y = 0$ ,  $y = 0.25(b/2)$ ,  $y = 0.5(b/2)$ , and  $y = 0.75(b/2)$ .

One can notice, the flow separation is appearing at the trailing edge on the upper surface of the wing as illustrated in Figure 5.12. It is interesting to see that the flow separation is decreasing as moving towards to the wing tip and finally vanishing.

Typical velocity contours of steady flow past the wing with NACA 0008 airfoil section is shown in Figure 5.13 for  $Re = 1000$  at the angle of attack,  $\alpha = 8^\circ$ .

Moreover, the streamlines pattern are illustrated in Figure 5.14 at the plane  $(\eta, \zeta)$ . It is clearly noticeable that a vorticity occurs at the tip of the rectangular wing.

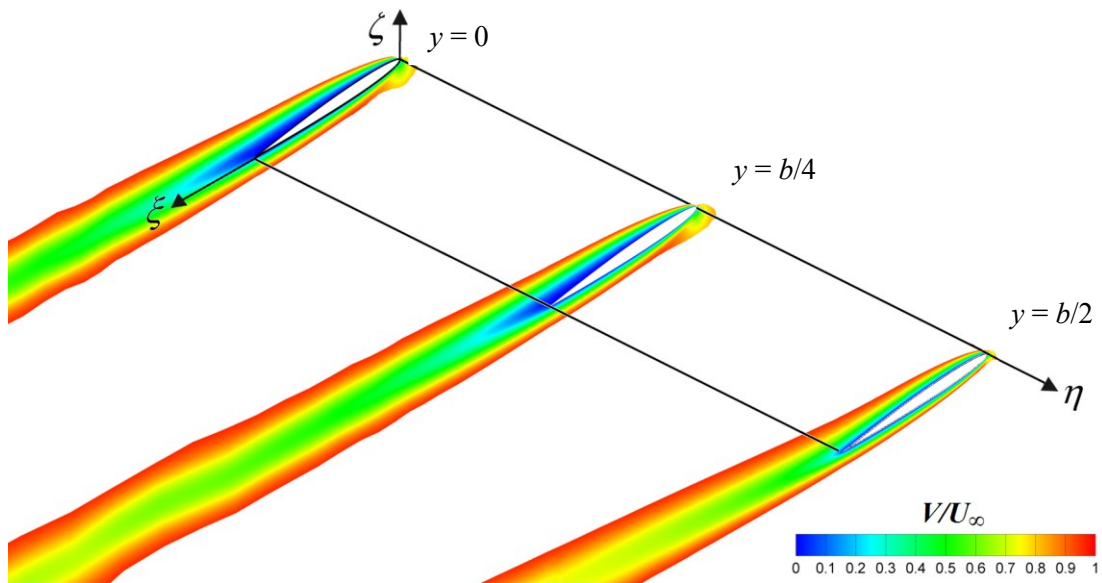


Figure 5.13. Isometric view of the velocity contours in a flow past a half-wing with NACA 0008 airfoil section for  $Re = 1000$  at angle of attack  $\alpha = 8^\circ$  illustrated in the physical domain  $(\xi, \eta, \zeta)$ .

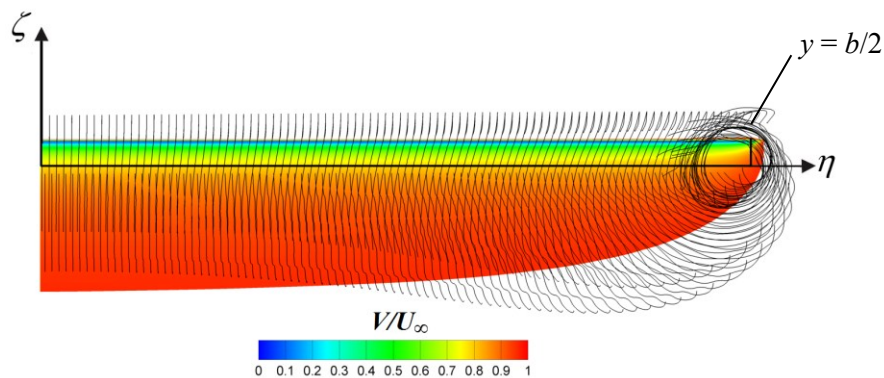


Figure 5.14. Velocity contours and streamlines in the  $(\eta, \zeta)$  plane (side view) of a flow past a wing with NACA 0008 airfoil section for  $Re = 1000$  at angle of attack  $\alpha = 8^\circ$ .

## 5.7 Summary of findings

An efficient numerical method has been developed to solve the Navier-Stokes equations for incompressible flows past rectangular wings at low Reynolds numbers. The problem is solved in a computational domain obtained from the physical flow domain by a coordinate transformation, and using a pseudo-time relaxation procedure with artificial compressibility, a factored alternate-direction implicit scheme, and a special decoupling procedure to reduce the problem to the solutions of scalar-tridiagonal systems of equations, which improves significantly the computational efficiency of the method.

The numerical solutions of the aerodynamic lift and drag coefficients obtained by this method are validated with the experimental results for rectangular wings. The influence of various geometric and flow parameters on the aerodynamic coefficients, such as the wing thickness, wing airfoil camber, angle of attack and Reynolds number is thoroughly studied.

It is interesting to note that for the micro-air vehicles applications, the chord length is between 5 and 20 cm, Reynolds number is between 600 and 4000 and the Mach number is less than 0.03, which justifies the numerical method used in this thesis based on incompressible flows in comparison with the few solutions obtained with compressible flow solvers.

## Chapter 6

### Conclusions

The main conclusions of this thesis are presented below in several categories corresponding to the chapters 2 through 5. Several suggestions for future work are also given at the end of this chapter.

#### 6.1 Three-dimensional confined viscous flows at low Reynolds numbers

Chapter 2 presents the analysis of the steady and unsteady three-dimensional confined viscous flows with fixed and oscillating walls and variable inflow velocity. This analysis is performed with a time-accurate numerical method developed by the author for the solution of the Navier-Stokes equations for unsteady laminar flows. The problem is solved in a fixed computational domain obtained by a time-dependent coordinate transformation from the physical domain, which converts the physical oscillating wall into a fixed wall in the computational domain. This numerical method is second-order-accurate based on a finite difference formulation on a staggered grid and uses a pseudo-time relaxation procedure with artificial compressibility. An Alternate-Direction Implicit (ADI) scheme is used in conjunction with a special decoupling procedure, which eliminates the pressure based on the continuity equation. This procedure reduces the problem to the efficient solution of several sets of decoupled scalar-tridiagonal systems of equations, which enhances substantially the computational efficiency of the method.

The method was successfully validated by comparison with the theoretical solutions for the case of uniform rectangular channels of various aspect ratios and by comparison with experimental results for the three-dimensional confined flows with multiple separation regions in a channel with a downstream-facing step. It is confirmed for the first time that the discrepancy between the two-dimensional numerical solutions and the experimental results is due to the three-dimensional effects introduced by the lateral walls of the experimental configuration, in contrast to the rigorous two-dimensional character of the two-dimensional computational solutions.

This method is then used to obtain solutions for the three-dimensional steady and unsteady flows past a downstream-facing step with oscillating walls and variable inflow velocities. The

variation of the flow separation and reattachment locations on the upper and lower walls along the span of the channel has been thoroughly studied.

The chapter presents a detailed study of the unsteady flow separation regions, including the study of the influence of various geometric and flow parameters, such as the channel aspect ratio, step height, Reynolds number, amplitudes of the wall oscillation and inflow velocity variation, and oscillation frequency, on the formation and duration of the flow separation regions.

## **6.2 Unsteady flow separations on stationary airfoils at low Reynolds numbers**

Chapter 3 presents the unsteady flow analysis of the stationary airfoils at low Reynolds numbers, aiming to study the unsteady effects on the aerodynamic coefficients generated by the unsteadiness of the flow separations. It was found that the aerodynamic coefficients of lift and drag have periodic variations in time at incidences larger than 6 or 8 degrees depending on the airfoil shape and the Reynolds number.

Solutions are presented for the unsteady lift and drag coefficients of several symmetric and cambered airfoils, which incorporate the effect of the unsteady flow separations. These unsteady solutions are obtained with an efficient time-accurate numerical method developed by the author for the solution of the Navier-Stokes equations at low Reynolds numbers, which is second-order-accurate in time and space. Comparison with available experimental results successfully validates the numerical method.

The influence of various geometric and flow parameters, such as the angle of attack, the airfoil relative thickness and camber, and the Reynolds number on the unsteady aerodynamic coefficients has been studied for several symmetric and cambered NACA airfoils.

The flow separation is also studied with the aid of the flow visualizations illustrating the changes in the flow pattern at various moments in time. It was found that the unsteadiness of the flow separations is consistent with the oscillations in time of the aerodynamic coefficients, which are generated by the unsteady flow separations occurring at low Reynolds numbers.

## **6.3 Steady and unsteady viscous flows past airfoils in the proximity of the ground**

The steady and unsteady flow past airfoils in the proximity of the ground at low Reynolds numbers has been studied in Chapter 4. The unsteady flow problem is solved in a rectangular computational domain, obtained from the physical domain by time-dependent coordinate

transformations for various sub-domains, in which the boundary conditions are efficiently and rigorously implemented. The numerical method developed in Chapter 3 for the integration of the Navier-Stokes equations was extended to study these flows in the proximity of the ground.

The numerical method was validated by comparing the steady flow solutions obtained for a larger distance to the ground with the available experimental results for isolated airfoils at low Reynolds numbers.

Solutions are first presented for the aerodynamic coefficients of several NACA airfoils in steady flows for various low Reynolds numbers at several distances to the ground. The effect of the proximity of the ground on the aerodynamic coefficients has been studied for various Reynolds numbers and several symmetric and cambered NACA airfoils. The analysis of the steady flow on these airfoils revealed that flow separations appear on the upper surface of the airfoil at lower angles of attack are due to the proximity of the ground. It was also found that the flow separation regions developed on the upper surface of the airfoil increase with the getting closer to the ground, and for larger Reynolds numbers, thicker airfoils, and higher angles of attack.

Solutions are also presented for the unsteady aerodynamic coefficients of several NACA airfoils executing pitching oscillations for various low Reynolds numbers at several distances to the ground. The influence of different parameters, such as the Reynolds number, relative thickness of the airfoil and oscillation frequency, on the ground effect in the unsteady flows at low Reynolds numbers has also been studied.

The unsteady flow separations effects on the stationary airfoils at low Reynolds numbers in the proximity of the ground has also been presented in this chapter. It was found that the aerodynamic coefficients of lift and drag have periodic variations in time at incidences larger than 6 or 8 degrees depending on the airfoil shape, the Reynolds number and the distance to the ground.

The amplitude of the oscillations in time of the lift coefficient was found to increase with the decrease of the distance to the ground, and these oscillations appear at smaller angles of attack near the ground. A similar observation can be made for the drag coefficient.

The flow separations on the stationary airfoils in the proximity of the ground are also studied with the aid of the flow visualizations illustrating the changes in the flow pattern at various moments in time.

## **6.4 Steady viscous flows past wings at low Reynolds numbers**

The steady viscous flows past rectangular wings with different NACA airfoil sections at low Reynolds numbers has been studied in Chapter 5 with an efficient numerical method developed by the author for the steady solution of the Navier-Stokes equations for laminar incompressible flows, which is second-order accurate in space. The steady flow problem is solved in a rectangular computational domain, obtained from the physical domain obtained by geometrical coordinate transformations for various sub-domains, in which the boundary conditions are efficiently and rigorously implemented. This method uses a pseudo-time relaxation procedure based on artificial compressibility, and a factored alternate-direction implicit scheme for the integration in pseudo-time. A second-order central finite differencing formulation is used on a stretched staggered grid.

The method was successfully validated by comparing the present flow solutions with the previous experimental results for the rectangular wing with NACA 0006 airfoil section of aspect ratio 7.25 at Reynolds number  $Re = 4000$  at various angles of attack.

The influence of various flow and geometrical parameters, such as the Reynolds number, wing thickness, wing camber and angle of attack on the aerodynamic characteristics such as the total lift and drag coefficients of the rectangular wing has been studied. In addition, typical streamlines and velocity contours of the flow past rectangular wings with a NACA airfoil section at low Reynolds numbers are also illustrated in this chapter.

## **6.5 Future work**

As a suggestion for future work, the numerical method developed in Chapter 5 for solving the steady viscous flows past rectangular wings can be extended to study of the unsteady flows past trapezoidal wings executing pitching oscillations at low Reynolds numbers. The author will continue these studies in the near future.

## LIST OF REFERENCES

- [1] Mateescu, D., **Panahi, A.**, and Wang, C., “Unsteady Effects on Airfoils in the Ground Proximity due to Unsteady Flow Separations at Low Reynolds Numbers”, *32nd AIAA Applied Aerodynamics Conference, AIAA Aviation Forum Aerodynamics Conference*, Atlanta, Georgia, June 2014, AIAA Paper 2014-2015, pp. 1-27.
- [2] Mateescu, D., **Panahi, A.**, and Roy, V., “Analysis of the Flow past Airfoils with Gurney Flaps at Low Reynolds Numbers”, *52nd Aerospace Sciences Meeting, ScieTech 2014*, National Harbor, Maryland, January 2014, AIAA Paper 2014-0040, pp. 1-25.
- [3] Mateescu, D., **Panahi, A.**, and Wang, C., “Unsteady Effects on Stationary Airfoils due to Unsteady Flow Separations at Low Reynolds Numbers”, *31st Applied Aerodynamics Conference*, San Diego, California, June 2013, AIAA Paper 2013-2527, pp. 1-30.
- [4] Mateescu, D., **Panahi, A.**, “Analysis of unsteady three-dimensional confined flows with oscillating walls and variable inflow velocity”, *51st AIAA Aerospace Sciences Meeting, AIAA Applied Aerodynamics Conference*, Grapevine, Texas, USA, 7-10 January 2013, AIAA Paper 2013-0063, pp. 1-18.
- [5] **Panahi, A.**, Mateescu, D., “Steady and unsteady three-dimensional flows in confined configurations with constant and variable inflow velocity”, *Proceedings of the ASME 2012 International Mechanical Engineering Congress and Exposition IMECE2012*, Houston, Texas, November 2012.
- [6] Mateescu, D., **Panahi, A.**, Wang, C., and Scholz, O., “Analysis of steady and unsteady flows past airfoils in the proximity of the ground at low Reynolds numbers”, *30th Applied Aerodynamics Conference*, New Orleans, Louisiana, June 2012, AIAA Paper 2012-3028, pp. 1-20.
- [7] Mateescu, D., **Panahi, A.**, and Roy, V., “Analysis of three-dimensional confined laminar flows with multiple flow separation regions”, *50th AIAA Aerospace Sciences Meeting, AIAA Applied Aerodynamics Conference*, Nashville, Tennessee, January 2012, AIAA Paper 2012-0703, pp. 1-13.
- [8] Mateescu, D., **Panahi, A.**, and Roy, V., “Study of three-dimensional confined laminar flows”, *23rd Canadian Congress of Applied Mechanics 2011 CANCAM 2011*, Vancouver, British Columbia, June 2011.
- [9] Mateescu, D., and Abdo, M., “Aerodynamic analysis of airfoils at very low Reynolds numbers”, *AIAA Paper 2004-1053*, Reno, January 2004.

- [10] Mateescu, D. and Abdo, M., “Analysis of flows past airfoils at very low Reynolds numbers” *J. Aerospace Engineering*. Vol. 224, pp. 757-775, 2010.
- [11] Mateescu, D., Munoz, M. and Olivier, S., “Analysis of unsteady confined viscous flows with variable inflow velocity and oscillating walls”, *J. Fluids Engineering*, vol. 132, 2010, pp. 1-9.
- [12] Mateescu, D., and Venditti, D., “Unsteady confined viscous flows with oscillating walls and multiple separation regions over a downstream-facing step”, *J. Fluids and Structures*, vol. 15, 2001, pp. 1187-1205.
- [13] Lee, T., and Mateescu, D., “Experimental and numerical investigation of 2-D backward-facing step flow”, *J. Fluids and Structures*, vol. 12, 1998, pp. 703-716.
- [14] Mateescu, D., Munoz, M., and Scholz, O., “Unsteady flows past Oscillating airfoils at low Reynolds numbers”, *29th Applied Aerodynamics Conference*, Honolulu, Hawaii, AIAA Paper 2011-3657, June 2011, pp. 1-15.
- [15] Mateescu, D., Scholz, O., and Wang, C., “Aerodynamics of airfoils at low Reynolds numbers in the proximity of the ground”, *12th Pan American Congress of Applied Mechanics - PACAM XII*, Port of Spain, Trinidad, January 2012, pp. 1-6.
- [16] Mateescu, D., Munoz, M., and Scholz, O., “Analysis of unsteady confined viscous flows with variable inflow velocity and oscillating walls,” *ASME J. Fluids Engineering*, Vol. 132, Issue 4, 2010, pp. 1-9.
- [17] Mueller, T. J., “Aerodynamic measurements at low Reynolds numbers for fixed wing micro-air vehicles”, *Development and Operation of UAVs for Military and Civil applications*, VKI, Belgium, 1999, pp. 1-32.
- [18] Davis, W. R., Kosicki, B. B., Boroson, D. M., and Kostishack, “Micro air vehicles for optical surveillance”, *Linc. Lab. Journal*, vol. 9, Issue 2, 1996, pp. 197–213.
- [19] Iima, M., “A two-dimensional aerodynamic model of freely flying insects”, *Journal of Theoretical Biology*, 2007, 247, 657–671.
- [20] Velazquez, A., Arias, J. R., and Mendez, B., “Laminar heat transfer enhancement downstream of a backward facing step by using a pulsating flow”, *International J. Heat and Mass Transfer*, vol. 51, Issues 7-8, 2008, pp. 2075-2089.
- [21] Gerber, A. G., Holloway, A. G., and Ng, C., “A model of the unsteady response of a backward-facing compliant step”, *International J. Numerical Methods in Fluids*, vol. 55, Issue 1, 2007, pp 57-80.

- [22] Inada, F., and Hayama, S., “A study on leakage-flow-induced vibrations”, *J. Fluids and Structures*, vol. 4, 1990, pp. 395-412.
- [23] Mateescu, D., Païdoussis, M. P., and Bélanger, F., “A theoretical model compared with experiments for the unsteady pressure on a cylinder oscillating in a turbulent annular flow”, *J. Sound and Vibrations*, vol. 135, Issue 3, 1989, pp. 487-498.
- [24] Mateescu, D., Païdoussis, M. P., and Bélanger, F., “Unsteady pressure measurements on an oscillating cylinder in narrow annular flow”, *J. Fluids and Structures*, vol. 2, 1988, pp. 615-628.
- [25] Mateescu, D., Pottier, T., Perotin, L., and Granger, S., “Three-dimensional unsteady flows between oscillating eccentric cylinders by an enhanced hybrid spectral method”, *J. Fluids and Structures*, vol. 9, Issue 6, 1995, pp. 671-695.
- [26] Abbott, D. E., and Kline, S. J., “Experimental investigations of subsonic turbulent flow over single and double backward-facing steps”, *ASME J. Basic Engineering*, vol. 84, 1962, pp. 317-325.
- [27] Eaton, J. K., Jeans, A. H., Ashjaee, J., and Johnston, J. P., “A wall-flow-direction probe for use in separating and reattaching flows”, *ASME J. of Fluids Engineering*, vol. 101, 1979, pp. 364-366.
- [28] Kunz, P., and Kroo, L., “Analysis and design of airfoils for use at ultra-low Reynolds numbers”, *In Proceedings of the AIAA Rotating Wing Conference*, June 2000, pp. 35–60.
- [29] Rogers, S., and Kwak, D., “An upwind differencing scheme for the time-accurate incompressible Navier–Stokes equations”, *AIAA Journal*, vol. 28, 1990, pp. 253–262.
- [30] Chorin, A., “A numerical method for solving incompressible viscous flow problems”, *J. Computational Physics*, 1967, 2, 12–26.
- [31] Armaly, B. F., Durst, F., Pereira, J. C. F., and Schonung, B., “Experimental and theoretical investigation of Backward-facing step flow”, *J. Fluid Mechanics*, vol. 127, 1983, pp. 1026–1033.
- [32] Goldstein, R. J., Eriksen, V., Olson, R. M., and Eckert, G., “Laminar separation, reattachment and transition of the flow over a downstream-facing step”, *ASME J. of Basic Engineering*, vol. 92, 1970, pp. 732-741.
- [33] Eaton, J. K., and Johnston, J. P., “A review of research on subsonic turbulent flow reattachment”, *AIAA Journal*, vol. 19, 1981, pp.1093-1100.
- [34] Kim, J. and Moin, P., “Application of a fractional-step method to incompressible Navier-Stokes equations”, *J. Computational Physics*, vol. 59, 1985, pp. 308-323.

- [35] Grant, I., Owens, E., Yan, Y., and Shen, X., “Particle image velocimetry measurements of the separated flow behind a rearward facing step”, *Experiments in Fluids*, vol. 12, 1992, pp. 238-244.
- [36] Gartling, D.K., “A test problem for outflow boundary conditions - Flow over a backward-facing step”, *International J. Numerical Methods in Fluids*, vol. 11, 1990, pp. 953-967.
- [37] Williams, P. T., and Baker, A. J., “Numerical simulations of laminar flow over a 3D backward-facing step”, *International J. Numerical Methods in Fluids*. vol. 24, 1997, pp. 1159–1183.
- [38] Chiang, T. P., Sheu, Tony W. H., “Time evolution of laminar flow over a three-dimensional backward-facing step”, *International J. Numerical Methods in Fluids*, vol. 31, Issue 4, 1999, pp. 721-745.
- [39] Nie, J. H., Armaly, B. F., “Three-dimensional convective flow adjacent to backward-facing step - effects of step height”, *International J. Heat Transfer*, vol. 45, 2002, pp. 2431-2438.
- [40] Eppler, R., and Somers, D. M., “Low speed airfoil design and analysis”, *Advanced Technology Airfoil Research*, 1979, vol. I, pp. 73-100.
- [41] Eppler, R., and Somers, D. M., “A Computer Program for the Design and Analysis of Low-Speed Airfoils”, *Technical Report*, 1981.
- [42] Eppler, R., and Somers, D. M., “Airfoil design for Reynolds numbers between 50,000 and 500,000”, *Conference on Low Reynolds Number Airfoil Aerodynamics*, pp. 1-14, 1985.
- [43] Ladson, C. L., Brooks, C. W., Hill, Jr., A. S., and Sproles, D. W., “Computer program to obtain ordinates for NACA airfoils”, *Technical report*, NASA, 1996.
- [44] Lissaman, P. B. S., “Low-Reynolds number airfoils”, Preprint, 1983.
- [45] Werle, H., “Le tunnel hydrodynamique au service de la recherche aérospatiale”, *Publication No 156. ONERA*, Office National d’études et de recherches aérospaciales, 1974.
- [46] Hanf. Piv, E. S., “Application in advanced low Reynolds number facility”, *IEE Transactions on Aerospace and Electronic Systems*, vol. 40, pp. 310-319, 2004.
- [47] Suwa, T., Nose, K., Numata, D., Nagai. H. and Asai, K., Compressibility Effects on Airfoil Aerodynamics at Low Reynolds Number. 30th Applied Aerodynamics Conference, New Orleans, Louisiana, June 2012, AIAA Paper 2012-3029, pp. 1-13.
- [48] Suwa, T. and Asai, K., Private Communication, August 2012.

- [49] Yilei He, Qiulin Qu, and Agarwall R. K., “Shape Optimization of an Airfoil in Ground Effect for Application to WIG Craft”, *Journal of Aerodynamics*, vol. 2014, December 2014, pp. 1-11.
- [50] Anderson J. D., “Fundamentals of Aerodynamics”, second edition., McGraw-Hill, New York, 1991.
- [51] [49] Carafoli E., Mateescu D., Nastase A., “Wing Theory in Supersonic Flow”, Pergamon Press, Oxford, 1969.
- [52] Kuethe, A. M., Chow, C. Y., “Foundations of Aerodynamics”, Wiley, New York, 1986.
- [53] Milne-Thomson L.M., “Theoretical Aerodynamics”, Dover, New York, 1966.
- [54] Thwaites B., “Incompressible Aerodynamics”, Oxford Univ. Press, Oxford, UK, 1960.
- [55] Glauert H., “The Elements of Aerofoil and Airscrew Theory”, Cambridge Univ. Press, Cambridge, UK, 1959.
- [56] Anderson J. D., “Computational Fluid Dynamics”, McGraw-Hill, New York, 1985.
- [57] Drela M., Giles M. B., “Viscous-inviscid analysis of transonic and low Reynolds number airfoils”, *AIAA Journal*, vol. 25, Issue 10, 1987, pp. 1347–1355.
- [58] Drela M., Giles M. B., “ISES – a two-dimensional viscous aerodynamic design and analysis code”, AIAA Paper 87-0424, January 1987.
- [59] Jameson A., Schmidt W., Turkel E., “Numerical solution of the Euler equations by finite volume methods using Runge–Kutta time stepping schemes”, AIAA Paper 81-1259, June 1981.
- [60] Elrefaee M. M., Wu J. C., S.G., “Lekoudis, Solutions of the compressible Navier–Stokes equations using the integral method”, *AIAA Journal*, vol. 20, Issue 3, 1982, pp. 356–362.
- [61] Nelson T. E., Zingg D. W., Johnston G. W., “Compressible Navier–Stokes computations of multielement airfoils flows using multiblock grids”, *AIAA Journal*, vol. 1994, pp. 506–511.
- [62] Mateescu D., Stanescu D., “A biased flux method for solving the Euler equations in subsonic, transonic and supersonic flows, in: Computational Methods and Experimental Measurements VII”, *Computational Mechanics Publications*, Southampton, 1995, pp. 327–335.
- [63] Cebeci T., “An Engineering Approach to the Calculation of Aerodynamic Flows”, Springer-Verlag, Berlin, 1999.
- [64] Peterson, R., “The boundary-layer and stalling characteristics of the NACA 64A010 airfoil section,” *NACA Technical Report 2235*, NACA, Nov. 1950.

- [65] Derkesen, R. W., Agelinchaab, M., and Tachie, M., “Characteristics of the flow over a NACA 0012 airfoil at low Reynolds numbers,” *Advances in Fluid Mechanics*, vol. VII, 2008, pp. 143-152.
- [66] Maughmer, M. D., and Coder, J. G., “Comparison of theoretical method for predicting airfoil aerodynamic characteristics,” *U.S. Army Research, Development and Engineering Command*, RDECOM TR 10-D-106, August 2010.
- [67] Chorin, A., “A numerical method for solving incompressible viscous flow problems,” *Journal of Computational Physics*, vol. 135, 1997, pp. 118-125.
- [68] Chorin, A., “A numerical solution of the Navier-Stokes equations,” *Mathematics of Computation*, vol. 22, 1968, pp. 745-762.
- [69] Broering, T. M., Lian, Y. S., “The effect of phase angle and wing spacing on tandem flapping wings”, *Acta Mechanica Sinica*, vol. 28, Issue 6, December 2012, pp. 1557–1571.
- [70] Sunada, S., Yasuda, T., Yasuda, K., and Kawachi, K., “Comparison of Wing Characteristics at an Ultralow Reynolds Number”, *Journal of Aircraft*, vol. 39, No. 2, March–April 2002, pp. 331-338.
- [71] White, F.M., “Viscous fluid flow”, Second Edition, New York, McGraw-Hill, 1991.
- [72] Soh, W., “Time-marching solution of incompressible Navier-Stokes equations for internal flows,” *Journal of Computational Physics*, Vol. 70, 1987, pp. 232-252.
- [73] Soh, W., and Goodrich, J., “Unsteady solution of incompressible Navier-Stokes equations,” *Journal of Computational Physics*, Vol. 79, 1988, pp. 113-134.
- [74] Munday, M., and Taira, K. “Nonlinear lift on a triangular airfoil in low Reynolds number compressible flow”, *Journal of Aircraft*, vol. 52, No. 3, May–June 2015.

## **APPENDICES**

## Appendix A

### Alternating-Direction Implicit (ADI) scheme:

By replacing the equations (2.53) to (2.55) into (2.58), (2.59) and (2.60), the scalar form of Z-sweep, X-sweep and Y-sweep are as follows

**Z-sweep:**

$$\begin{aligned}
 & \begin{bmatrix} \Delta\bar{u} \\ \Delta\bar{v} \\ \Delta\bar{w} \\ \Delta\bar{p} \end{bmatrix} + \Delta\tau \begin{bmatrix} C_2 \frac{\partial(\tilde{u}^v \Delta\bar{u})}{\partial Z} + C_3 \frac{\partial(\tilde{w}^v \Delta\bar{u})}{\partial Z} + C_4 \frac{\partial(\Delta\bar{u})}{\partial Z} + C_2 \frac{\partial(\Delta\bar{p})}{\partial Z} + C_5 \frac{\partial^2 \Delta\bar{u}}{\partial Z^2} + C_6 \frac{\partial^2 \Delta\bar{u}}{\partial Z \partial X} \\ C_2 \frac{\partial(\tilde{u}^v \Delta\bar{v})}{\partial Z} + C_3 \frac{\partial(\tilde{w}^v \Delta\bar{v})}{\partial Z} + C_4 \frac{\partial(\Delta\bar{v})}{\partial Z} + C_5 \frac{\partial^2 \Delta\bar{v}}{\partial Z^2} + C_6 \frac{\partial^2 \Delta\bar{v}}{\partial Z \partial X} \\ C_2 \frac{\partial(\tilde{u}^v \Delta\bar{w})}{\partial Z} + C_3 \frac{\partial(\tilde{w}^v \Delta\bar{w})}{\partial Z} + C_4 \frac{\partial(\Delta\bar{w})}{\partial Z} + C_3 \frac{\partial(\Delta\bar{p})}{\partial Z} + C_5 \frac{\partial^2 \Delta\bar{w}}{\partial Z^2} + C_6 \frac{\partial^2 \Delta\bar{w}}{\partial Z \partial X} \\ C_2 \frac{1}{\delta} \frac{\partial \Delta\bar{u}}{\partial Z} + C_3 \frac{1}{\delta} \frac{\partial \Delta\bar{w}}{\partial Z} \end{bmatrix} \\
 & = \Delta\tau \begin{bmatrix} -\tilde{G}^v_u \\ -\tilde{G}^v_v \\ -\tilde{G}^v_w \\ -\frac{1}{\delta} \nabla \cdot \tilde{V}^v \end{bmatrix} \tag{A.1}
 \end{aligned}$$

**X-sweep:**

$$\begin{aligned}
 & \begin{bmatrix} \Delta u^* \\ \Delta v^* \\ \Delta w^* \\ \Delta p^* \end{bmatrix} + \Delta\tau \begin{bmatrix} \frac{\partial(\tilde{u}^v \Delta u^*)}{\partial X} + C_1 \frac{\partial^2 \Delta u^*}{\partial X^2} + \frac{\partial(\Delta p^*)}{\partial X} \\ \frac{\partial(\tilde{u}^v \Delta v^*)}{\partial X} + C_1 \frac{\partial^2 \Delta v^*}{\partial X^2} \\ \frac{\partial(\tilde{u}^v \Delta w^*)}{\partial X} + C_1 \frac{\partial^2 \Delta w^*}{\partial X^2} \\ \frac{1}{\delta} \frac{\partial \Delta u^*}{\partial X} \end{bmatrix} = \begin{bmatrix} \Delta\bar{u} \\ \Delta\bar{v} \\ \Delta\bar{w} \\ \Delta\bar{p} \end{bmatrix} \tag{A.2}
 \end{aligned}$$

**Y-sweep:**

$$\begin{bmatrix} \Delta u \\ \Delta v \\ \Delta w \\ \Delta p \end{bmatrix} + \Delta \tau \begin{bmatrix} \frac{\partial(\tilde{v}^v \Delta u)}{\partial Y} + C_1 \frac{\partial^2 \Delta u}{\partial Y^2} \\ \frac{\partial(\tilde{v}^v \Delta v)}{\partial Y} + C_1 \frac{\partial^2 \Delta v}{\partial Y^2} + \frac{\partial(\Delta p)}{\partial Y} \\ \frac{\partial(\tilde{v}^v \Delta w)}{\partial Y} + C_1 \frac{\partial^2 \Delta w}{\partial Y^2} \\ \frac{1}{\delta} \frac{\partial \Delta v}{\partial Y} \end{bmatrix} = \begin{bmatrix} \Delta u^* \\ \Delta v^* \\ \Delta w^* \\ \Delta p^* \end{bmatrix} \quad (\text{A. 3})$$

**Spatial discretization of momentums:**

The central and backward difference operators, which denotes the difference between the primary grid points and the secondary grid points are defined as:

$$\begin{aligned} \Delta X_i^u &= X_{i+1}^v - X_i^v & \Delta X_i^v &= X_i^u - X_{i-1}^u \\ \Delta Y_j^u &= Y_j^v - Y_{j-1}^v & \Delta Y_j^v &= Y_{j+1}^u - Y_j^u \\ \Delta Z_k^u &= Z_k^w - Z_{k-1}^w & \Delta Z_k^w &= Z_{k+1}^u - Z_k^u \end{aligned}$$

$$\begin{aligned} \nabla X_i^u &= X_i^u - X_i^v & \nabla X_i^v &= X_i^v - X_{i-1}^u \\ \nabla Y_j^u &= Y_j^u - Y_{j-1}^v & \nabla Y_j^v &= Y_j^v - Y_j^u \\ \nabla Z_k^u &= Z_k^u - Z_{k-1}^w & \nabla Z_k^w &= Z_k^w - Z_k^u \end{aligned}$$

**X-Momentum:**

$$\begin{aligned} G_u(u, v, w, p) &= \frac{\partial(uu)}{\partial X} + C_1 \frac{\partial^2 u}{\partial X^2} + C_2 \frac{\partial(uu)}{\partial Z} + \frac{\partial(vu)}{\partial Y} + C_3 \frac{\partial(wu)}{\partial Z} + C_4 \frac{\partial u}{\partial Z} + \frac{\partial p}{\partial X} \\ &+ C_2 \frac{\partial p}{\partial Z} + C_5 \frac{\partial^2 u}{\partial Z^2} + C_6 \frac{\partial^2 u}{\partial Z \partial X} + C_1 \frac{\partial^2 u}{\partial Y^2} \end{aligned} \quad (\text{A. 4})$$

After spatial discretization:

$$\begin{aligned}
G^u_{i,j,k} = & \frac{1}{\Delta X_i^u} \left[ (u_u^{X+})^2 - (u_u^{X-})^2 + C_1 \left( \frac{u_{i+1,j,k} - u_{i,j,k}}{\Delta X_{i+1}^v} - \frac{u_{i,j,k} - u_{i-1,j,k}}{\Delta X_i^v} \right) \right. \\
& \left. + (p_{i+1,j,k} - p_{i,j,k}) \right] \\
& + \frac{1}{\Delta Y_j^u} \left[ (u_u^{Y+} v_u^{Y+} - u_u^{Y-} v_u^{Y-}) + C_1 \left( \frac{u_{i,j+1,k} - u_{i,j,k}}{\Delta Y_j^v} - \frac{u_{i,j,k} - u_{i,j-1,k}}{\Delta Y_{j-1}^v} \right) \right] \\
& + \frac{1}{\Delta Z_k^u} \left[ C_2 [(u_u^{Z+})^2 - (u_u^{Z-})^2] + C_3 (u_u^{Z+} w_u^{Z+} - u_u^{Z-} w_u^{Z-}) \right. \\
& + C_4 (u_u^{Z+} - u_u^{Z-}) + C_2 (p_{i,j,k+1} - p_{i,j,k}) \\
& + C_5 \left( \frac{u_{i,j,k+1} - u_{i,j,k}}{\Delta Z_k^w} - \frac{u_{i,j,k} - u_{i,j,k-1}}{\Delta Z_{k-1}^w} \right) \\
& \left. + C_6 \left( \frac{u_w^{p+} - u_w^{m+}}{\Delta X_i^u} - \frac{u_w^{p-} - u_w^{m-}}{\Delta X_i^u} \right) \right] \tag{A.5}
\end{aligned}$$

where, the following linear interpolates of the velocity components of the staggered grid are used:

$$\begin{aligned}
u_{u,i,j,k}^{X-} &= \frac{\nabla X_i^v \cdot u_{i,j,k} + \nabla X_i^u u_{i-1,j,k}}{\Delta X_i^v}, & \text{and} & & u_{u,i,j,k}^{X+} &= u_{u_{i+1,j,k}}^{X-} \\
u_{u,i,j,k}^{Z-} &= \frac{\nabla Z_{k-1}^w \cdot u_{i,j,k} + \nabla Z_k^u u_{i,j,k-1}}{\Delta Z_{k-1}^w}, & \text{and} & & u_{u,i,j,k}^{Z+} &= \check{u}_{u_{i,j,k+1}}^{Z-} \\
v_{u,i,j,k}^{Y-} &= \frac{\nabla X_i^u \cdot v_{i+1,j-1,k} + \nabla X_{i+1}^v v_{i,j-1,k}}{\Delta X_i^u}, & \text{and} & & v_{u,i,j,k}^{Y+} &= v_{u_{i,j+1,k}}^{Y-} \\
u_{u,i,j,k}^{Y-} &= \frac{\nabla Y_{j-1}^v \cdot u_{i,j,k} + \nabla Y_j^u u_{i,j-1,k}}{\Delta Y_{j-1}^v}, & \text{and} & & u_{u,i,j,k}^{Y+} &= u_{u_{i,j+1,k}}^{Y-} \\
w_{u,i,j,k}^{Z-} &= \frac{\nabla X_i^u \cdot w_{i+1,j,k-1} + \nabla X_{i+1}^v w_{i,j,k-1}}{\Delta X_i^u}, & \text{and} & & w_{u,i,j,k}^{Z+} &= \check{w}_{u_{i,j,k+1}}^{Z-} \\
u_{11} &= \frac{\nabla X_i^u \cdot u_{i-1,j,k-1} + \nabla X_i^v \cdot u_{i,j,k-1}}{\Delta X_i^v}, & \text{and} & & u_{12} &= \frac{\nabla X_i^u \cdot u_{i-1,j,k} + \nabla X_i^v \cdot u_{i,j,k}}{\Delta X_i^v} \\
u|_{w_{i,j,k}}^{m-} &= \frac{\nabla Z_k^u \cdot u_{11} + \nabla Z_{k-1}^w \cdot u_{12}}{\Delta Z_{k-1}^w}, & \text{and} & & u|_{w_{i,j,k-1}}^{m+} &= u|_{w_{i,j,k}}^{m-}, \\
u|_{w_{i-1,j,k}}^{p-} &= u|_{w_{i,j,k}}^{m-}, & \text{and} & & u|_{w_{i-1,j,k-1}}^{p+} &= u|_{w_{i,j,k}}^{m-}
\end{aligned}$$

## y-Momentum:

$$\begin{aligned}
G_v(u, v, w, p) = & \frac{\partial(uv)}{\partial X} + C_1 \frac{\partial^2 v}{\partial X^2} + C_2 \frac{\partial(uv)}{\partial Z} + \frac{\partial(vv)}{\partial Y} + C_3 \frac{\partial(wv)}{\partial Z} + C_4 \frac{\partial v}{\partial Z} + \frac{\partial p}{\partial Y} \\
& + C_5 \frac{\partial^2 w}{\partial Z^2} + C_6 \frac{\partial^2 w}{\partial Z \partial X} + C_1 \frac{\partial^2 w}{\partial Y^2}
\end{aligned} \tag{A.6}$$

After spatial discretization:

$$\begin{aligned}
G_v^{i,j,k} = & \frac{1}{\Delta X_i^v} \left[ (v_v^{X+} u_v^{X+} - v_v^{X-} u_v^{X-}) + C_1 \left( \frac{v_{i+1,j,k} - v_{i,j,k}}{\Delta X_i^u} - \frac{v_{i,j,k} - v_{i-1,j,k}}{\Delta X_{i-1}^u} \right) \right] \\
& + \frac{1}{\Delta Y_j^v} \left[ (v_v^{Y+})^2 - (v_v^{Y-})^2 + C_1 \left( \frac{v_{i,j+1,k} - v_{i,j,k}}{\Delta Y_{j+1}^u} - \frac{v_{i,j,k} - v_{i,j-1,k}}{\Delta Y_j^u} \right) \right] \\
& + (p_{i,j+1,k} - p_{i,j,k}) \\
& + \frac{1}{\Delta Z_k^u} \left[ C_2 (v_v^{Z+} w_v^{Z+} - v_v^{Z-} w_v^{Z-}) + C_3 (v_v^{Z+} w_v^{Z+} - v_v^{Z-} w_v^{Z-}) \right. \\
& + C_4 (v_v^{Z+} - v_v^{Z-}) + C_5 \left( \frac{v_{i,j,k+1} - v_{i,j,k}}{\Delta Z_k^w} - \frac{v_{i,j,k} - v_{i,j,k-1}}{\Delta Z_{k-1}^w} \right) \\
& \left. + C_6 \left( \frac{v_u^{p+} - v_u^{m+}}{\Delta X_i^v} - \frac{v_u^{p-} - v_u^{m-}}{\Delta X_i^v} \right) \right]
\end{aligned} \tag{A.7}$$

where, the following linear interpolates of the velocity components of the staggered grid are used:

$$\begin{aligned}
u_{v_{i,j,k}}^{X-} &= \frac{\nabla Y_j^v \cdot u_{i-1,j+1,k} + \nabla Y_{j+1}^u \cdot u_{i-1,j,k}}{\Delta Y_j^v}, \quad \text{and} \quad u_{v_{i,j,k}}^{X+} = u_{v_{i+1,j,k}}^{X-} \\
v_{v_{i,j,k}}^{X-} &= \frac{\nabla X_{i-1}^u \cdot v_{i,j,k} + \nabla X_i^v \cdot v_{i-1,j,k}}{\Delta X_{i-1}^u}, \quad \text{and} \quad v_{v_{i,j,k}}^{X+} = v_{v_{i+1,j,k}}^{X-} \\
v_{v_{i,j,k}}^{Z-} &= \frac{\nabla Z_{k-1}^w \cdot v_{i,j,k} + \nabla Z_k^u \cdot v_{i,j,k-1}}{\Delta Z_{k-1}^w}, \quad \text{and} \quad v_{v_{i,j,k}}^{Z+} = \check{v}_{v_{i,j,k+1}}^{Z-} \\
v_{v_{i,j,k}}^{Y-} &= \frac{\nabla Y_j^u \cdot v_{i,j,k} + \nabla Y_j^v \cdot v_{i,j-1,k}}{\Delta Y_j^u}, \quad \text{and} \quad v_{v_{i,j,k}}^{Y+} = v_{v_{i,j+1,k}}^{Y-} \\
v_{21} &= \frac{\nabla X_i^v \cdot v_{i-1,j-1,k} + \nabla X_{i-1}^u \cdot v_{i,j-1,k}}{\Delta X_{i-1}^u}, \quad \text{and} \quad v_{22} = \frac{\nabla X_i^v \cdot v_{i-1,j,k} + \nabla X_{i-1}^u \cdot v_{i,j,k}}{\Delta X_{i-1}^u} \\
v|_{u_{i,j,k}}^{m-} &= \frac{\nabla Y_j^v \cdot v_{21} + \nabla Y_j^u \cdot v_{22}}{\Delta Y_j^u}, \quad \text{and} \quad v|_{u_{i-1,j,k}}^{p-} = v|_{u_{i,j,k}}^{m-}
\end{aligned}$$

$$v|_{u_{i,j-1,k}}^{m+} = v|_{u_{i,j,k}}^{m-}, \quad \text{and} \quad v|_{u_{i-1,j-1,k}}^{p+} = v|_{u_{i,j,k}}^{m-}$$

### z-Momentum:

$$\begin{aligned} G_w(u, v, w, p) = & \frac{\partial(uw)}{\partial X} + C_1 \frac{\partial^2 w}{\partial X^2} + C_2 \frac{\partial(uw)}{\partial Z} + \frac{\partial(vw)}{\partial Y} + C_3 \frac{\partial(ww)}{\partial Z} + C_4 \frac{\partial w}{\partial Z} + C_5 \frac{\partial p}{\partial Z} \\ & + C_5 \frac{\partial^2 w}{\partial Z^2} + C_6 \frac{\partial^2 w}{\partial Z \partial X} + C_1 \frac{\partial^2 w}{\partial Y^2} \end{aligned} \quad (\text{A.8})$$

After spatial discretization:

$$\begin{aligned} G_w^{i,j,k} = & \frac{1}{\Delta X_i^v} \left[ (w_w^{X+} u_w^{X+} - w_w^{X-} u_w^{X-}) + C_1 \left( \frac{w_{i+1,j,k} - w_{i,j,k}}{\Delta X_i^u} - \frac{w_{i,j,k} - w_{i-1,j,k}}{\Delta X_{i-1}^u} \right) \right] \\ & + \frac{1}{\Delta Y_j^u} \left[ (w_w^{Y+} v_w^{Y+} - w_w^{Y-} v_w^{Y-}) + C_1 \left( \frac{w_{i,j+1,k} - w_{i,j,k}}{\Delta Y_j^v} - \frac{w_{i,j,k} - w_{i,j-1,k}}{\Delta Y_{j-1}^v} \right) \right] \\ & + \frac{1}{\Delta Z_k^w} \left[ C_2 (w_w^{Z+} u_w^{Z+} - w_w^{Z-} u_w^{Z-}) \right. \\ & + C_3 [(w_w^{Z+})^2 - (w_w^{Z-})^2 + (p_{i,j,k+1} - p_{i,j,k})] + C_4 (w_w^{Z+} - w_w^{Z-}) \\ & + C_5 \left( \frac{w_{i,j,k+1} - w_{i,j,k}}{\Delta Z_{k+1}^u} - \frac{w_{i,j,k} - w_{i,j,k-1}}{\Delta Z_k^u} \right) \\ & \left. + C_6 \left( \frac{w_u^{p+} - w_u^{m+}}{\Delta X_i^v} - \frac{w_u^{p-} - w_u^{m-}}{\Delta X_i^v} \right) \right] \end{aligned} \quad (\text{A.9})$$

where, the following linear interpolates of the velocity components of the staggered grid are used:

$$w_{w_{i,j,k}}^{X-} = \frac{\nabla X_{i-1}^u \cdot w_{i,j,k} + \nabla X_i^v \cdot w_{i-1,j,k}}{\Delta X_{i-1}^u}, \quad \text{and} \quad w_{w_{i,j,k}}^{X+} = w_{w_{i+1,j,k}}^{X-}$$

$$u_{w_{i,j,k}}^{X-} = \frac{\nabla Z_k^w \cdot u_{i-1,j,k+1} + \nabla Z_{k+1}^u \cdot u_{i-1,j,k}}{\Delta Z_k^w}, \quad \text{and} \quad u_{w_{i,j,k}}^{X+} = u_{w_{i+1,j,k}}^{X-}$$

$$w_{w_{i,j,k}}^{Z-} = \frac{\nabla Z_k^u \cdot w_{i,j,k} + \nabla Z_k^w \cdot w_{i,j,k-1}}{\Delta Z_k^u}, \quad \text{and} \quad w_{w_{i,j,k}}^{Z+} = w_{w_{i,j,k+1}}^{Z-}$$

$$u_{w_{i,j,k}}^{Z-} = u_{u_{i,j,k}}^{X-}, \quad \text{and} \quad u_{w_{i,j,k}}^{Z+} = u_{u_{i,j,k+1}}^{Z-}$$

$$w_{w_{i,j,k}}^{Y-} = \frac{\nabla Y_{j-1}^v \cdot w_{i,j,k} + \nabla Y_j^u \cdot w_{i,j-1,k}}{\Delta Y_{j-1}^v}, \quad \text{and} \quad w_{w_{i,j,k}}^{Y+} = w_{w_{i,j+1,k}}^{Y-}$$

$$v_{w_{i,j,k}}^{Y-} = \frac{\nabla Z_k^w \cdot v_{i,j-1,k+1} + \nabla Z_{k+1}^u \cdot v_{i,j-1,k}}{\Delta Z_k^w}, \text{ and}$$

$$v_{w_{i,j,k}}^{Y+} = \check{v}_{w_{i,j+1,k}}^{Y-}$$

$$w_{11} = \frac{\nabla X_i^v \cdot w_{i-1,j,k-1} + \nabla X_{i-1}^u \cdot w_{i,j,k-1}}{\Delta X_{i-1}^u}, \text{ and}$$

$$w_{12} = \frac{\nabla X_i^v \cdot w_{i-1,j,k} + \nabla X_{i-1}^u \cdot w_{i,j,k}}{\Delta X_{i-1}^u}$$

$$w|_{u_{i,j,k}}^{m-} = \frac{\nabla Z_k^w \cdot w_{11} + \nabla Z_k^u \cdot w_{12}}{\Delta Z_k^u}, \text{ and}$$

$$w|_{u_{i,j,k-1}}^{m+} = w|_{u_{i,j,k}}^{m-}$$

$$w|_{u_{i-1,j,k}}^{p-} = w|_{u_{i,j,k}}^{m-}, \text{ and}$$

$$w|_{u_{i-1,j,k-1}}^{p+} = w|_{u_{i,j,k}}^{m-}$$

### Continuity equation:

$$\nabla \cdot V = C_7 \frac{\partial u}{\partial X} + C_2 \frac{\partial u}{\partial Z} + \frac{\partial v}{\partial Y} + C_8 \frac{\partial w}{\partial X} + C_3 \frac{\partial w}{\partial Z} \quad (\text{A. 10})$$

Continuity equation can be spatially discretized as

$$\begin{aligned} \nabla \cdot V = & \frac{1}{\Delta X_i^v} \left( C_7 (u_{i,j,k} - u_{i-1,j,k}) + C_8 (w|_{u_{i,j,k}}^{m+} - w|_{u_{i,j,k}}^{m-}) \right) + \frac{1}{\Delta Y_j^u} [(v_{i,j,k} - v_{i,j-1,k})] \\ & + \frac{1}{\Delta Z_k^u} \left( C_2 (u|_{w_{i,j,k}}^{m+} - u|_{w_{i,j,k}}^{m-}) + C_3 (w_{i,j,k} - w_{i,j,k-1}) \right) \end{aligned} \quad (\text{A. 11})$$

### Spatial discretization of three successive sweeps:

Theses sweeps can be spatially discretized as following

#### Z-sweep:

#### X-Momentum:

$$\overline{\Delta u} + \alpha \Delta \tau \left( C_2 \frac{\partial u \overline{\Delta u}}{\partial Z} + C_3 \frac{\partial w \overline{\Delta u}}{\partial Z} + C_4 \frac{\partial \overline{\Delta u}}{\partial Z} + C_5 \frac{\partial^2 \overline{\Delta u}}{\partial Z^2} + C_6 \frac{\partial^2 \overline{\Delta u}}{\partial X \partial Z} + C_2 \frac{\partial \overline{\Delta p}}{\partial Z} \right) = \Delta \tau R_u \quad (\text{A. 12})$$

$$\begin{aligned}
& \left. \left\{ \frac{\alpha \Delta \tau}{\Delta Z_k^u} \left[ \begin{aligned} & C_2 \left( -\check{u}_{u,i,j,k}^{Z-} \left( \frac{\nabla Z_k^u}{\Delta Z_{k-1}^w} \right) \right) \\ & -C_3 \left( \check{w}_{u,i,j,k}^{Z-} \left( \frac{\nabla Z_k^u}{\Delta Z_{k-1}^w} \right) \right) \\ & -C_4 \left( \frac{\nabla Z_k^u}{\Delta Z_{k-1}^w} \right) \\ & +C_5 \left( \frac{1}{\Delta Z_{k-1}^w} \right) \end{aligned} \right] \right\} \\
& + \overline{\Delta u}_{i,j,k} \cdot \left\{ 1 + \frac{\alpha \Delta \tau}{\Delta Z_k^u} \left[ \begin{aligned} & C_2 \cdot \left( \check{u}_{u,i,j,k}^{Z+} \left( \frac{\nabla Z_{k+1}^u}{\Delta Z_k^w} \right) - \check{u}_{u,i,j,k}^{Z-} \left( \frac{\nabla Z_{k-1}^w}{\Delta Z_{k-1}^w} \right) \right) \\ & +C_3 \left( \check{w}_{u,i,j,k}^{Z+} \left( \frac{\nabla Z_{k+1}^u}{\Delta Z_k^w} \right) - \check{w}_{u,i,j,k}^{Z-} \left( \frac{\nabla Z_{k-1}^w}{\Delta Z_{k-1}^w} \right) \right) \\ & +C_4 \left( \left( \frac{\nabla Z_{k+1}^u}{\Delta Z_k^w} \right) - \left( \frac{\nabla Z_{k-1}^w}{\Delta Z_{k-1}^w} \right) \right) \\ & +C_5 \left( \frac{-1}{\Delta Z_k^w} + \frac{-1}{\Delta Z_{k-1}^w} \right) \end{aligned} \right] \right\} \\
& + \overline{\Delta u}_{i,j,k+1} \cdot \left\{ \frac{\alpha \Delta \tau}{\Delta Z_k^u} \left[ \begin{aligned} & C_2 \cdot \left( \check{u}_{u,i,j,k}^{Z+} \left( \frac{\nabla Z_k^w}{\Delta Z_k^w} \right) \right) \\ & +C_3 \left( \check{w}_{u,i,j,k}^{Z+} \left( \frac{\nabla Z_k^w}{\Delta Z_k^w} \right) \right) \\ & +C_4 \left( \frac{\nabla Z_k^w}{\Delta Z_k^w} \right) \\ & +C_5 \left( \frac{1}{\Delta Z_k^w} \right) \end{aligned} \right] \right\}
\end{aligned}$$

$$= \Delta \tau R_u - \frac{C_6}{\Delta X_i^u} \frac{\alpha \Delta \tau}{\Delta Z_k^u} \left( \overline{\Delta u}|_{w,i,j,k}^{p+} - \overline{\Delta u}|_{w,i,j,k}^{m+} - \overline{\Delta u}|_{w,i,j,k}^{p-} + \overline{\Delta u}|_{w,i,j,k}^{m-} \right) \quad (\text{A. 13})$$

**Y-Momentum:**

$$\overline{\Delta v} + \alpha \Delta \tau \left( C_2 \frac{\partial u \overline{\Delta v}}{\partial Z} + C_3 \frac{\partial w \overline{\Delta v}}{\partial Z} + C_4 \frac{\partial \overline{\Delta v}}{\partial Z} + C_5 \frac{\partial^2 \overline{\Delta v}}{\partial Z^2} + C_6 \frac{\partial^2 \overline{\Delta v}}{\partial X \partial Z} \right) = \Delta \tau R_v \quad (\text{A. 14})$$

$$\begin{aligned} & \overline{\Delta v}_{i,j,k-1} \left\{ \frac{\alpha \Delta \tau}{\Delta Z_k^u} \left[ \begin{array}{l} C_2 \left( -u_{v,i,j,k}^{Z-} \cdot \left( \frac{\nabla Z_k^u}{\Delta Z_{k-1}^w} \right) \right) \\ -C_3 \left( w_{v,i,j,k}^{Z-} \cdot \left( \frac{\nabla Z_k^u}{\Delta Z_{k-1}^w} \right) \right) \\ -C_4 \left( \frac{\nabla Z_k^u}{\Delta Z_{k-1}^w} \right) \\ +C_5 \left( \frac{1}{\Delta Z_{k-1}^w} \right) \end{array} \right] \right\} \\ & + \overline{\Delta v}_{i,j,k} \cdot \left\{ 1 + \frac{\alpha \Delta \tau}{\Delta Z_k^u} \left[ \begin{array}{l} C_2 \left( u_{v,i,j,k}^{Z+} \cdot \left( \frac{\nabla Z_{k+1}^u}{\Delta Z_k^w} \right) - u_{v,i,j,k}^{Z-} \cdot \left( \frac{\nabla Z_{k-1}^w}{\Delta Z_{k-1}^w} \right) \right) \\ +C_3 \left( w_{v,i,j,k}^{Z+} \cdot \left( \frac{\nabla Z_{k+1}^u}{\Delta Z_k^w} \right) - w_{v,i,j,k}^{Z-} \cdot \left( \frac{\nabla Z_{k-1}^w}{\Delta Z_{k-1}^w} \right) \right) \\ +C_4 \left( \frac{\nabla Z_{k+1}^u}{\Delta Z_k^w} - \frac{\nabla Z_{k-1}^w}{\Delta Z_{k-1}^w} \right) \\ +C_5 \left( \frac{-1}{\Delta Z_k^w} + \frac{-1}{\Delta Z_{k-1}^w} \right) \end{array} \right] \right\} \\ & + \overline{\Delta v}_{i,j,k+1} \left\{ \frac{\alpha \Delta \tau}{\Delta Z_k^u} \left[ \begin{array}{l} C_2 \left( u_{v,i,j,k}^{Z+} \cdot \left( \frac{\nabla Z_k^w}{\Delta Z_k^w} \right) \right) \\ +C_3 \left( w_{v,i,j,k}^{Z+} \cdot \left( \frac{\nabla Z_k^w}{\Delta Z_k^w} \right) \right) \\ +C_4 \left( \frac{\nabla Z_k^w}{\Delta Z_k^w} \right) \\ +C_5 \left( \frac{1}{\Delta Z_k^w} \right) \end{array} \right] \right\} \\ & = \Delta \tau R_v - \frac{C_6}{\Delta X_i^v} \frac{\alpha \Delta \tau}{\Delta Z_k^u} \left( \overline{\Delta v}|_{u,i,j,k}^{p+} - \overline{\Delta v}|_{u,i,j,k}^{m+} - \overline{\Delta v}|_{u,i,j,k}^{p-} + \overline{\Delta v}|_{u,i,j,k}^{m-} \right) \quad (\text{A. 15}) \end{aligned}$$

**Z-Momentum:**

$$\begin{aligned} \overline{\Delta w}(1 + \Delta\tau) + \alpha\Delta\tau \left( C_2 \frac{\partial u \overline{\Delta w}}{\partial Z} + C_3 \frac{\partial w \overline{\Delta w}}{\partial Z} + C_4 \frac{\partial \overline{\Delta w}}{\partial Z} + C_5 \frac{\partial^2 \overline{\Delta w}}{\partial Z^2} + C_6 \frac{\partial^2 \overline{\Delta w}}{\partial X \partial Z} + C_3 \frac{\partial \overline{\Delta p}}{\partial Z} \right) \\ = \Delta\tau R_w \end{aligned} \quad (\text{A.16})$$

$$\begin{aligned} \overline{\Delta w}_{i,j,k-1} & \left\{ \frac{\alpha\Delta\tau}{\Delta Z_k^w} \left[ \begin{aligned} & C_2 \cdot \left( -u_{w_{i,j,k}}^{Z-} \left( \frac{\nabla Z_k^w}{\Delta Z_k^u} \right) \right) \\ & -C_3 \left( w_{w_{i,j,k}}^{Z-} \left( \frac{\nabla Z_k^w}{\Delta Z_k^u} \right) \right) \\ & -C_4 \left( \frac{\nabla Z_k^w}{\Delta Z_k^u} \right) \\ & +C_5 \left( \frac{1}{\Delta Z_k^u} \right) \\ & -C_{3w} \cdot C_{3p} \frac{\Delta\tau}{\delta} \left( \frac{1}{\Delta Z_k^u} \right) \end{aligned} \right] \right\} \\ +\overline{\Delta w}_{i,j,k} & \left\{ 1 + \Delta\tau + \frac{\alpha\Delta\tau}{\Delta Z_k^w} \left[ \begin{aligned} & C_2 \left( u_{w_{i,j,k}}^{Z+} \cdot \frac{\nabla Z_{k+1}^w}{\Delta Z_{k+1}^u} - u_{w_{i,j,k}}^{Z-} \cdot \frac{\nabla Z_k^u}{\Delta Z_k^u} \right) \\ & +C_3 \left( w_{w_{i,j,k}}^{Z+} \cdot \frac{\nabla Z_{k+1}^w}{\Delta Z_{k+1}^u} - w_{w_{i,j,k}}^{Z-} \cdot \frac{\nabla Z_k^u}{\Delta Z_k^u} \right) \\ & +C_4 \left( \frac{\nabla Z_{k+1}^w}{\Delta Z_{k+1}^u} - \frac{\nabla Z_k^u}{\Delta Z_k^u} \right) \\ & +C_5 \left( \frac{-1}{\Delta Z_{k+1}^u} + \frac{-1}{\Delta Z_k^u} \right) \\ & -C_{3w} \cdot C_{3p} \frac{\Delta\tau}{\delta} \left( \frac{-1}{\Delta Z_{k+1}^u} + \frac{-1}{\Delta Z_k^u} \right) \end{aligned} \right] \right\} \end{aligned}$$

$$\begin{aligned}
& + \overline{\Delta w}_{i,j,k+1} \left\{ \frac{\alpha \Delta \tau}{\Delta Z_k^w} \left[ \begin{aligned} & C_2 \left( u_{w_{i,j,k}}^{Z+} \cdot \frac{\nabla Z_{k+1}^u}{\Delta Z_{k+1}^u} \right) \\ & + C_3 \left( w_{w_{i,j,k}}^{Z+} \cdot \frac{\nabla Z_{k+1}^u}{\Delta Z_{k+1}^u} \right) \\ & + C_4 \left( \frac{\nabla Z_{k+1}^u}{\Delta Z_{k+1}^u} \right) \\ & + C_5 \left( \frac{1}{\Delta Z_{k+1}^u} \right) \\ & - C_{3w} \cdot C_{3p} \frac{\Delta \tau}{\delta} \left( \frac{1}{\Delta Z_{k+1}^u} \right) \end{aligned} \right] \right\} \\
& = \Delta \tau R_w - C_6 \alpha \frac{\Delta \tau}{\Delta Z_k^w} \left( \frac{\overline{\Delta w}|_{u_{i,j,k}}^{p+} - \overline{\Delta w}|_{u_{i,j,k}}^{m+}}{\Delta X_i^v} - \frac{\overline{\Delta w}|_{u_{i,j,k}}^{p-} - \overline{\Delta w}|_{u_{i,j,k}}^{m-}}{\Delta X_i^v} \right) \\
& \quad + C_{3w} \alpha \frac{\Delta \tau}{\Delta Z_k^w} \frac{\Delta \tau}{\delta} (\nabla \cdot V_{i,j,k+1} - \nabla \cdot V_{i,j,k}) \\
& \quad + C_{3w} \cdot C_{2p} \alpha \frac{\Delta \tau}{\Delta Z_k^w} \frac{\Delta \tau}{\delta} \left[ \left( \frac{\overline{\Delta u}|_{w_{i,j,k+1}}^{m+} - \overline{\Delta u}|_{w_{i,j,k+1}}^{m-}}{\Delta Z_{k+1}^u} \right) \right. \\
& \quad \left. - \left( \frac{\overline{\Delta u}|_{w_{i,j,k}}^{m+} - \overline{\Delta u}|_{w_{i,j,k}}^{m-}}{\Delta Z_k^u} \right) \right] \tag{A.17}
\end{aligned}$$

**Continuity equation:**

$$\frac{\Delta \tau}{\delta} \left( C_2 \frac{\partial \overline{\Delta u}}{\partial Z} + C_3 \frac{\partial \overline{\Delta w}}{\partial Z} \right) + \overline{\Delta p} = \Delta \tau R_p \tag{A.18}$$

$$\overline{\Delta p}_{i,j,k} = -\frac{\Delta \tau}{\delta} \nabla \cdot V_{i,j,k} - \frac{\Delta \tau}{\delta} \left[ C_2 \left( \frac{\overline{\Delta u}|_{w_{i,j,k}}^{m+} - \overline{\Delta u}|_{w_{i,j,k}}^{m-}}{\Delta Z_k^u} \right) + C_3 \left( \frac{\overline{\Delta w}_{i,j,k} - \overline{\Delta w}_{i,j,k-1}}{\Delta Z_k^u} \right) \right] \tag{A.19}$$

**X-sweep:**

**X-Momentum:**

$$\Delta u^*(1 + \Delta\tau) + \alpha\Delta\tau \left( C_9 \frac{\partial \Delta u^*}{\partial X} + C_7 \frac{\partial u \Delta u^*}{\partial X} + C_8 \frac{\partial w \Delta u^*}{\partial X} + C_1 \frac{\partial^2 \Delta u^*}{\partial X^2} + C_7 \frac{\partial \Delta p^*}{\partial X} \right) = \overline{\Delta u} \quad (\text{A. 20})$$

$$\begin{aligned} & \Delta u^*_{i-1,j,k} \cdot \left\{ \frac{\alpha\Delta\tau}{\Delta X_i^u} \left[ \begin{array}{l} -C_7 \left( \tilde{u}_{u_{i,j,k}}^{X-} \left( \frac{\nabla X_i^u}{\Delta X_i^v} \right) \right) \\ -C_8 \left( \tilde{w}_{u_{i,j,k}}^{X-} \left( \frac{\nabla X_i^u}{\Delta X_i^v} \right) \right) \\ +C_1 \left( \frac{1}{\Delta x_i^v} \right) \\ -\frac{\Delta\tau}{\delta} C_{7u} C_{7p} \left( \frac{1}{\Delta x_i^v} \right) \end{array} \right] \right\} \\ & + \Delta u^*_{i+1,j,k} \cdot \left\{ \frac{\alpha\Delta\tau}{\Delta X_i^u} \left[ \begin{array}{l} +C_7 \left( \tilde{u}_{u_{i,j,k}}^{X+} \left( \frac{\nabla X_{i+1}^v}{\Delta X_{i+1}^v} \right) \right) \\ +C_8 \left( \tilde{w}_{u_{i,j,k}}^{X+} \left( \frac{\nabla X_{i+1}^v}{\Delta X_{i+1}^v} \right) \right) \\ +C_1 \left( \frac{1}{\Delta x_{i+1}^v} \right) \\ -\frac{\Delta\tau}{\delta} C_{7u} C_{7p} \left( \frac{1}{\Delta x_{i+1}^v} \right) \end{array} \right] \right\} \\ & + \Delta u^*_{i,j,k} \cdot \left\{ 1 + \Delta\tau + \frac{\alpha\Delta\tau}{\Delta X_i^u} \left[ \begin{array}{l} +C_7 \left( \tilde{u}_{u_{i,j,k}}^{X+} \left( \frac{\nabla X_{i+1}^u}{\Delta X_{i+1}^v} \right) - \tilde{u}_{u_{i,j,k}}^{X-} \left( \frac{\nabla X_i^v}{\Delta X_i^v} \right) \right) \\ +C_8 \left( \tilde{w}_{u_{i,j,k}}^{X+} \left( \frac{\nabla X_{i+1}^u}{\Delta X_{i+1}^v} \right) - \tilde{w}_{u_{i,j,k}}^{X-} \left( \frac{\nabla X_i^v}{\Delta X_i^v} \right) \right) \\ +C_1 \left( \frac{-1}{\Delta x_{i+1}^v} + \frac{-1}{\Delta x_i^v} \right) \\ -\frac{\Delta\tau}{\delta} C_{7u} C_{7p} \left( \frac{-1}{\Delta x_{i+1}^v} + \frac{-1}{\Delta x_i^v} \right) \end{array} \right] \right\} \\ & = \overline{\Delta u} - C_{7u} \alpha \frac{\Delta\tau}{\Delta X_i^u} (\overline{\Delta p}_{i+1,j,k} - \overline{\Delta p}_{i,j,k}) \\ & \quad + \alpha \frac{\Delta\tau}{\Delta X_i^u} \frac{\Delta\tau}{\delta} C_{7u} C_{8p} \left( \frac{\Delta w^*|_{u_{i+1,j,k}}^{m+} - \Delta w^*|_{u_{i+1,j,k}}^{m-}}{\Delta X_{i+1}^v} - \frac{\Delta w^*|_{u_{i,j,k}}^{m+} - \Delta w^*|_{u_{i,j,k}}^{m-}}{\Delta X_i^v} \right) \quad (\text{A. 21}) \end{aligned}$$

**Y-Momentum:**

$$\Delta v^* + \alpha \Delta \tau \left( C_9 \frac{\partial \Delta v^*}{\partial X} + C_7 \frac{\partial u \Delta v^*}{\partial X} + C_8 \frac{\partial w \Delta v^*}{\partial X} + C_1 \frac{\partial^2 \Delta v^*}{\partial X^2} \right) = \overline{\Delta v} \quad (\text{A.22})$$

$$\begin{aligned} & \left\{ \frac{\alpha \Delta \tau}{\Delta X_i^v} \left[ \begin{array}{c} -C_9 \left( \frac{\nabla X_i^v}{\Delta X_{i-1}^u} \right) \\ -C_7 \left( u_{v_{i+1},j,k}^{X-} \left( \frac{\nabla X_i^v}{\Delta X_{i-1}^u} \right) \right) \\ -C_8 \left( w_{v_{i+1},j,k}^{X-} \left( \frac{\nabla X_i^v}{\Delta X_{i-1}^u} \right) \right) \\ +C_1 \left( \frac{1}{\Delta x_{i-1}^u} \right) \end{array} \right] \right\} \\ & + \Delta v^*_{i,j,k} \cdot \left\{ 1 + \frac{\alpha \Delta \tau}{\Delta X_i^v} \left[ \begin{array}{c} C_9 \left( \frac{\nabla X_{i+1}^v}{\Delta X_i^u} - \frac{\nabla X_{i-1}^u}{\Delta X_{i-1}^u} \right) \\ +C_7 \left( u_{v_{i+1},j,k}^{X+} \left( \frac{\nabla X_{i+1}^v}{\Delta X_i^u} \right) - u_{v_{i+1},j,k}^{X-} \left( \frac{\nabla X_{i-1}^u}{\Delta X_{i-1}^u} \right) \right) \\ +C_8 \left( w_{v_{i+1},j,k}^{X+} \left( \frac{\nabla X_{i+1}^v}{\Delta X_i^u} \right) - w_{v_{i+1},j,k}^{X-} \left( \frac{\nabla X_{i-1}^u}{\Delta X_{i-1}^u} \right) \right) \\ +C_1 \left( \frac{-1}{\Delta x_i^u} + \frac{-1}{\Delta x_{i-1}^u} \right) \end{array} \right] \right\} \\ & + \Delta v^*_{i+1,j,k} \cdot \left\{ \frac{\alpha \Delta \tau}{\Delta X_i^v} \left[ \begin{array}{c} C_9 \left( \frac{\nabla X_i^u}{\Delta X_i^u} \right) \\ +C_7 \left( u_{v_{i+1},j,k}^{X+} \left( \frac{\nabla X_i^u}{\Delta X_i^u} \right) \right) \\ +C_8 \left( w_{v_{i+1},j,k}^{X+} \left( \frac{\nabla X_i^u}{\Delta X_i^u} \right) \right) \\ +C_1 \left( \frac{1}{\Delta x_i^u} \right) \end{array} \right] \right\} = \overline{\Delta v}_{i,j,k} \quad (\text{A.23}) \end{aligned}$$

**Z-Momentum:**

$$\Delta w^* + \alpha \Delta \tau \left( C_9 \frac{\partial \Delta w^*}{\partial X} + C_7 \frac{\partial u \Delta w^*}{\partial X} + C_8 \frac{\partial w \Delta w^*}{\partial X} + C_1 \frac{\partial^2 \Delta w^*}{\partial X^2} \right) = \overline{\Delta w} \quad (\text{A. 24})$$

$$\begin{aligned} & \left. \left. \left. \Delta w^*_{i-1,j,k} \cdot \left\{ \frac{\alpha \Delta \tau}{\Delta X_i^v} \left[ \begin{array}{c} -C_9 \left( \frac{\nabla X_i^v}{\Delta X_{i-1}^u} \right) \\ -C_7 \left( u_{w_{i,j,k}}^{X-} \cdot \left( \frac{\nabla X_i^v}{\Delta X_{i-1}^u} \right) \right) \\ -C_8 \left( w_{w_{i,j,k}}^{X-} \cdot \left( \frac{\nabla X_i^v}{\Delta X_{i-1}^u} \right) \right) \\ +C_1 \left( \frac{1}{\Delta x_{i-1}^u} \right) \end{array} \right] \right\} \right. \right. \\ & \left. \left. \left. + \Delta w^*_{i,j,k} \cdot \left\{ \frac{\alpha \Delta \tau}{\Delta X_i^v} \left[ \begin{array}{c} 1 + C_9 \left( \frac{\nabla X_{i+1}^v}{\Delta X_i^u} - \frac{\nabla X_{i-1}^u}{\Delta X_{i-1}^u} \right) \\ +C_7 \left( u_{w_{i,j,k}}^{X+} \cdot \left( \frac{\nabla X_{i+1}^v}{\Delta X_i^u} \right) - u_{w_{i,j,k}}^{X-} \cdot \left( \frac{\nabla X_{i-1}^u}{\Delta X_{i-1}^u} \right) \right) \\ +C_8 \left( w_{w_{i,j,k}}^{X+} \cdot \left( \frac{\nabla X_{i+1}^v}{\Delta X_i^u} \right) - w_{w_{i,j,k}}^{X-} \cdot \left( \frac{\nabla X_{i-1}^u}{\Delta X_{i-1}^u} \right) \right) \\ +C_1 \left( \frac{-1}{\Delta x_i^u} + \frac{-1}{\Delta x_{i-1}^u} \right) \end{array} \right] \right\} \right. \right. \\ & \left. \left. \left. + \Delta w^*_{i+1,j,k} \cdot \left\{ \frac{\alpha \Delta \tau}{\Delta X_i^v} \left[ \begin{array}{c} C_9 \left( \frac{\nabla X_i^u}{\Delta X_i^u} \right) \\ +C_7 \left( u_{w_{i,j,k}}^{X+} \cdot \left( \frac{\nabla X_i^u}{\Delta X_i^u} \right) \right) \\ +C_8 \left( w_{w_{i,j,k}}^{X+} \cdot \left( \frac{\nabla X_i^u}{\Delta X_i^u} \right) \right) \\ +C_1 \left( \frac{1}{\Delta x_i^u} \right) \end{array} \right] \right\} = \overline{\Delta w}_{i,j,k} \right. \quad (\text{A. 25}) \end{aligned}$$

**Continuity equation:**

$$\frac{\Delta\tau}{\delta} \left( C_7 \frac{\partial \Delta u^*}{\partial X} + C_8 \frac{\partial \Delta w^*}{\partial X} \right) + \Delta p^* = \overline{\Delta p} \quad (\text{A. 26})$$

$$\Delta p^*_{i,j,k} = \overline{\Delta p}_{i,j,k} - \frac{\Delta\tau}{\delta} \left( C_7 \frac{\Delta u^*_{i,j,k} - \Delta u^*_{i-1,j,k}}{\Delta X_i^v} + C_8 \frac{\Delta w^*_{i,j,k}^{m+} - \Delta w^*_{i,j,k}^{m-}}{\Delta X_i^v} \right) \quad (\text{A. 27})$$

**Y-sweep:**

**X-Momentum:**

$$\Delta u + \alpha \Delta\tau \left( \frac{\partial v \Delta u}{\partial Y} + C_1 \frac{\partial^2 \Delta u}{\partial Y^2} \right) = \Delta u^* \quad (\text{A. 28})$$

$$\begin{aligned} \Delta u_{i,j-1,k} \cdot \left\{ \frac{\alpha \Delta\tau}{\Delta Y_j^u} \left[ \begin{array}{c} -\check{v}_{u,i,j,k}^{Y-} \cdot \left( \frac{\nabla Y_j^u}{\Delta Y_{j-1}^v} \right) \\ + C_1 \left( \frac{1}{\Delta Y_{j-1}^v} \right) \end{array} \right] \right\} + \Delta u_{i,j,k} \cdot \left\{ 1 + \frac{\alpha \Delta\tau}{\Delta Y_j^u} \left[ \begin{array}{c} \check{v}_{u,i,j,k}^{Y+} \cdot \left( \frac{\nabla Y_{j+1}^u}{\Delta Y_j^v} \right) - \check{v}_{u,i,j,k}^{Y-} \cdot \left( \frac{\nabla Y_{j-1}^u}{\Delta Y_{j-1}^v} \right) \\ + C_1 \left( \frac{-1}{\Delta Y_j^v} + \frac{-1}{\Delta Y_{j-1}^v} \right) \end{array} \right] \right\} \\ + \Delta u_{i,j+1,k} \cdot \left\{ \frac{\alpha \Delta\tau}{\Delta Y_j^u} \left[ \begin{array}{c} \check{v}_{u,i,j,k}^{Y+} \cdot \left( \frac{\nabla Y_j^u}{\Delta Y_j^v} \right) \\ + C_1 \left( \frac{1}{\Delta Y_j^v} \right) \end{array} \right] \right\} = \Delta u^* \end{aligned} \quad (\text{A. 29})$$

**Y-Momentum:**

$$\Delta v(1 + \Delta\tau) + \alpha \Delta\tau \left( \frac{\partial v \Delta v}{\partial Y} + C_{10} \frac{\partial^2 \Delta v}{\partial Y^2} + \frac{\partial \Delta p}{\partial Y} \right) = \Delta v^* \quad (\text{A. 30})$$

$$\begin{aligned} \Delta v_{i,j-1,k} \cdot \left\{ \frac{\alpha \Delta\tau}{\Delta Y_j^v} \left[ \begin{array}{c} -\check{v}_{v,i,j,k}^{Y-} \cdot \left( \frac{\nabla Y_j^v}{\Delta Y_j^u} \right) \\ + C_1 \left( \frac{1}{\Delta Y_j^u} \right) - \frac{\Delta\tau}{\Delta Y_j^u} \end{array} \right] \right\} + \Delta v_{i,j,k} \cdot \left\{ 1 + \Delta\tau + \frac{\alpha \Delta\tau}{\Delta Y_j^v} \left[ \begin{array}{c} \check{v}_{v,i,j,k}^{Y+} \cdot \left( \frac{\nabla Y_{j+1}^v}{\Delta Y_{j+1}^u} \right) - \check{v}_{v,i,j,k}^{Y-} \cdot \left( \frac{\nabla Y_j^v}{\Delta Y_j^u} \right) \\ + C_1 \left( \frac{-1}{\Delta Y_{j+1}^u} + \frac{-1}{\Delta Y_j^u} \right) \\ + \frac{\Delta\tau}{\Delta Y_{j+1}^u} + \frac{\Delta\tau}{\Delta Y_j^u} \end{array} \right] \right\} + \\ \Delta v_{i,j+1,k} \cdot \left\{ \frac{\alpha \Delta\tau}{\Delta Y_j^v} \left[ \begin{array}{c} \check{v}_{v,i,j,k}^{Y+} \cdot \left( \frac{\nabla Y_{j+1}^v}{\Delta Y_{j+1}^u} \right) \\ + C_1 \left( \frac{1}{\Delta Y_{j+1}^u} \right) - \frac{\Delta\tau}{\Delta Y_{j+1}^u} \end{array} \right] \right\} = \Delta v^*_{i,j,k} - \alpha \frac{\Delta\tau}{\Delta Y_j^v} \left( \Delta p^*_{i,j+1,k} - \Delta p^*_{i,j,k} \right) \end{aligned} \quad (\text{A. 31})$$

**Z-Momentum:**

$$\Delta w + \alpha \Delta \tau \left( \frac{\partial v \Delta w}{\partial Y} + C_1 \frac{\partial^2 \Delta w}{\partial Y^2} \right) = \Delta w^* \quad (\text{A. 32})$$

$$\begin{aligned} \Delta w_{i,j-1,k} \cdot \left\{ \frac{\alpha \Delta \tau}{\Delta Y_j^u} \left[ -\check{v}_{w_{i,j,k}}^{Y-} \cdot \left( \frac{\nabla Y_j^u}{\Delta Y_{j-1}^v} \right) \right] \right\} + \Delta w_{i,j,k} \cdot \left\{ 1 + \frac{\alpha \Delta \tau}{\Delta Y_j^u} \left[ \check{v}_{w_{i,j,k}}^{Y+} \cdot \left( \frac{\nabla Y_{j+1}^u}{\Delta Y_j^v} \right) - \check{v}_{w_{i,j,k}}^{Y-} \cdot \left( \frac{\nabla Y_{j-1}^v}{\Delta Y_{j-1}^v} \right) \right] \right\} \\ + \Delta w_{i,j+1,k} \cdot \left\{ \frac{\alpha \Delta \tau}{\Delta Y_j^u} \left[ \check{v}_{w_{i,j,k}}^{Y+} \cdot \left( \frac{\nabla Y_j^v}{\Delta Y_j^v} \right) \right] \right\} = \Delta w^*_{i,j,k} \end{aligned} \quad (\text{A. 33})$$

**Continuity equation:**

$$\Delta \tau \frac{\partial \Delta v}{\partial Y} + \Delta p = \Delta p^* \quad (\text{A. 34})$$

$$\Delta p_{i,j,k} = \Delta p^*_{i,j,k} - \frac{\Delta \tau}{\Delta Y_j^u} (\Delta v_{i,j,k} - \Delta v_{i,j-1,k}) \quad (\text{A. 35})$$

## Appendix B

### Steady and unsteady flows past airfoils

The Navier-Stokes equations can be expressed in the computational domain by using geometrical transformation

$$G_u(u, v, p) = C_7 \frac{\partial(uu)}{\partial X} + C_2 \frac{\partial(uu)}{\partial Y} + C_4 \frac{\partial(vu)}{\partial X} + C_3 \frac{\partial(vu)}{\partial Y} + C_7 \frac{\partial p}{\partial X} + C_2 \frac{\partial p}{\partial Y} + C_1 \frac{\partial^2 u}{\partial X^2} + C_6 \frac{\partial^2 u}{\partial X \partial Y} + C_5 \frac{\partial^2 u}{\partial Y^2} \quad (\text{B.1})$$

$$G_v(u, v, p) = C_7 \frac{\partial(vu)}{\partial X} + C_2 \frac{\partial(vu)}{\partial Y} + C_4 \frac{\partial(vv)}{\partial X} + C_3 \frac{\partial(vv)}{\partial Y} + C_4 \frac{\partial p}{\partial X} + C_3 \frac{\partial p}{\partial Y} + C_1 \frac{\partial^2 v}{\partial X^2} + C_6 \frac{\partial^2 v}{\partial X \partial Y} + C_5 \frac{\partial^2 v}{\partial Y^2} \quad (\text{B.2})$$

$$DV = C_7 \frac{\partial u}{\partial X} + C_2 \frac{\partial u}{\partial Y} + C_4 \frac{\partial v}{\partial X} + C_3 \frac{\partial v}{\partial Y} \quad , \quad (\text{B.3})$$

### Time-dependent coordinate transformation coefficients

The time-dependent coordinate transformation coefficients for each domain can be defined as

#### Domain 1, 2, 5 and 6

$$C_1 = -\frac{1}{\text{Re}} \left[ \left( \frac{\partial X}{\partial \xi} \right)^2 + \left( \frac{\partial X}{\partial \eta} \right)^2 \right] \quad (\text{B.4})$$

$$C_2 = 0 \quad (\text{B.5})$$

$$C_3 = \frac{\partial Y}{\partial \eta} \quad (\text{B.6})$$

$$C_4 = \frac{\partial Y}{\partial \alpha} \frac{d\alpha}{dt} + \frac{\partial Y}{\partial h} \frac{dh}{dt} \quad (\text{B.7})$$

$$C_5 = \left( -\frac{1}{\text{Re}} \right) \left( \frac{\partial Y}{\partial \eta} \right)^2 \quad (\text{B.8})$$

$$C_6 = -\frac{2}{\text{Re}} \frac{\partial X}{\partial \eta} \frac{\partial Y}{\partial \eta} \quad (\text{B.9})$$

$$C_7 = \frac{\partial X}{\partial \xi} \quad (\text{B.10})$$

$$C_8 = \frac{\partial X}{\partial \eta} \quad (\text{B.11})$$

$$C_9 = \frac{\partial X}{\partial \alpha(t)} \frac{d\alpha(t)}{dt} + \frac{\partial X}{\partial h} \frac{dh}{dt} - \frac{1}{\text{Re}} \frac{\partial^2 X}{\partial \eta^2} \quad (\text{B.12})$$

**Domain 3 and 4**

$$C_1 = -\frac{1}{\text{Re}} \left[ \left( \frac{\partial X}{\partial x} \frac{\partial x}{\partial \xi} \right)^2 \left( \frac{\partial X}{\partial x} \frac{\partial x}{\partial \eta} \right)^2 \right] \quad (\text{B.13})$$

$$C_2 = \frac{\partial Y}{\partial x} \frac{\partial x}{\partial \xi} + \frac{\partial Y}{\partial y} \frac{\partial y}{\partial \xi} + \frac{\partial Y}{\partial e} \frac{de}{dx} \frac{\partial x}{\partial \xi} \quad (\text{B.14})$$

$$C_3 = \frac{\partial Y}{\partial x} \frac{\partial x}{\partial \eta} + \frac{\partial Y}{\partial y} \frac{\partial y}{\partial \eta} + \frac{\partial Y}{\partial e} \frac{de}{dx} \frac{\partial x}{\partial \eta} \quad (\text{B.15})$$

$$\begin{aligned} C_4 = & \left\{ \frac{\partial Y}{\partial x} \left[ \frac{\partial x}{\partial \alpha(t)} \frac{d\alpha(t)}{dt} + \frac{\partial x}{\partial h} \frac{dh}{dt} \right] + \frac{\partial Y}{\partial y} \left[ \frac{\partial y}{\partial \alpha(t)} \frac{d\alpha(t)}{dt} + \frac{\partial y}{\partial h} \frac{dh}{dt} \right] + \right. \\ & \left. + \frac{\partial Y}{\partial \alpha(t)} \frac{d\alpha(t)}{dt} + \frac{\partial Y}{\partial h} \frac{dh}{dt} + \frac{\partial Y}{\partial e} \frac{de}{dx} \left[ \frac{\partial x}{\partial \alpha(t)} \frac{d\alpha(t)}{dt} + \frac{\partial x}{\partial h} \frac{dh}{dt} \right] \right\} - \\ & - \frac{1}{\text{Re}} \left[ \left[ \left( \frac{\partial^2 Y}{\partial x^2} + 2 \left( \frac{\partial^2 Y}{\partial x \partial e} \frac{de}{dx} \right) + \frac{\partial^2 Y}{\partial e^2} \left( \frac{de}{dx} \right)^2 + \frac{\partial Y}{\partial e} \frac{d^2 e}{dx^2} \right) \left( \frac{\partial x}{\partial \xi} \right)^2 + \right. \right. \\ & \left. \left. + \left( \frac{\partial^2 Y}{\partial x \partial y} + \frac{\partial^2 Y}{\partial e \partial y} \frac{de}{dx} \right) \frac{\partial y}{\partial \xi} \frac{\partial x}{\partial \xi} + \frac{\partial^2 Y}{\partial y \partial x} \frac{\partial x}{\partial \xi} \frac{\partial y}{\partial \xi} + \frac{\partial^2 Y}{\partial y \partial e} \frac{de}{dx} \frac{\partial x}{\partial \xi} \frac{\partial y}{\partial \xi} \right] + \right. \\ & \left. + \left[ \left( \frac{\partial^2 Y}{\partial x^2} + 2 \left( \frac{\partial^2 Y}{\partial x \partial e} \frac{de}{dx} \right) + \frac{\partial^2 Y}{\partial e^2} \left( \frac{de}{dx} \right)^2 + \frac{\partial Y}{\partial e} \frac{d^2 e}{dx^2} \right) \left( \frac{\partial x}{\partial \eta} \right)^2 + \right. \right. \end{aligned}$$

$$+ \left[ \left( \frac{\partial^2 Y}{\partial x \partial y} + \frac{\partial^2 Y}{\partial e \partial y} \frac{de}{dx} \right) \frac{\partial y}{\partial \eta} \frac{\partial x}{\partial \eta} + \frac{\partial^2 Y}{\partial y \partial x} \frac{\partial x}{\partial \eta} \frac{\partial y}{\partial \eta} + \frac{\partial^2 Y}{\partial y \partial e} \frac{de}{dx} \frac{\partial x}{\partial \eta} \frac{\partial y}{\partial \eta} \right] \quad (\text{B.16})$$

$$C_5 = -\frac{1}{\text{Re}} \left[ \left( \left( \frac{\partial Y}{\partial x} + \frac{\partial Y}{\partial e} \frac{de}{dx} \right) \frac{\partial x}{\partial \xi} + \frac{\partial Y}{\partial y} \frac{\partial y}{\partial \xi} \right)^2 + \left( \left( \frac{\partial Y}{\partial x} + \frac{\partial Y}{\partial e} \frac{de}{dx} \right) \frac{\partial x}{\partial \eta} + \frac{\partial Y}{\partial y} \frac{\partial y}{\partial \eta} \right)^2 \right] \quad (\text{B.17})$$

$$C_6 = -\frac{2}{\text{Re}} \left[ \left( \left( \frac{\partial Y}{\partial x} + \frac{\partial Y}{\partial e} \frac{de}{dx} \right) \frac{\partial x}{\partial \xi} + \frac{\partial Y}{\partial y} \frac{\partial y}{\partial \xi} \right) \left( \frac{\partial X}{\partial x} \frac{\partial x}{\partial \xi} \right) + \left( \left( \frac{\partial Y}{\partial x} + \frac{\partial Y}{\partial e} \frac{de}{dx} \right) \frac{\partial x}{\partial \eta} + \frac{\partial Y}{\partial y} \frac{\partial y}{\partial \eta} \right) \left( \frac{\partial X}{\partial x} \frac{\partial x}{\partial \eta} \right) \right] \quad (\text{B.18})$$

$$C_7 = \frac{\partial X}{\partial x} \frac{\partial x}{\partial \xi} \quad (\text{B.19})$$

$$C_8 = \frac{\partial X}{\partial x} \frac{\partial x}{\partial \eta} \quad (\text{B.20})$$

$$C_9 = \frac{\partial X}{\partial x} \left[ \frac{\partial x}{\partial \alpha} \frac{d\alpha}{dt} + \frac{\partial x}{\partial h} \frac{dh}{dt} \right] \quad (\text{B.21})$$

### Alternating-direction implicit scheme

Continuity and momentum equations can be arranged in the global matrix form:

$$[I + \alpha \cdot \Delta t (D_x + D_y)] \Delta \Phi = \Delta \tau \cdot S \quad (\text{B.22})$$

where,

$$D_x = \begin{bmatrix} M + 1/\alpha & 0 & C_7 \frac{\partial}{\partial X} \\ 0 & M & C_8 \frac{\partial}{\partial X} \\ \frac{1}{\alpha} \frac{C_7}{\delta} \frac{\partial}{\partial X} & \frac{1}{\alpha} \frac{C_8}{\delta} \frac{\partial}{\partial X} & 0 \end{bmatrix} \quad (\text{B.23})$$

$$D_y = \begin{bmatrix} N & 0 & C_2 \frac{\partial}{\partial Y} \\ 0 & N + 1/\alpha & C_3 \frac{\partial}{\partial Y} \\ \frac{1}{\alpha} \frac{C_2}{\delta} \frac{\partial}{\partial Y} & \frac{1}{\alpha} \frac{C_3}{\delta} \frac{\partial}{\partial Y} & 0 \end{bmatrix} \quad (\text{B.24})$$

and,

$$\Delta\Phi = \begin{bmatrix} \Delta u \\ \Delta v \\ \Delta p \end{bmatrix} \quad S = \begin{bmatrix} F_u^n - \tilde{u}^v - \alpha \cdot \tilde{G}_u^v \\ F_v^n - \tilde{v}^v - \alpha \cdot \tilde{G}_v^v \\ -1/\delta \cdot \nabla \tilde{V}^v \end{bmatrix} \quad (\text{B.25})$$

with,

$$\begin{cases} M\Phi = C_7 \frac{\partial(\tilde{u}^v\Phi)}{\partial X} + C_8 \frac{\partial(\tilde{v}^v\Phi)}{\partial X} + C_1 \frac{\partial^2\Phi}{\partial X^2} + C_9 \frac{\partial\Phi}{\partial X} \\ N\Phi = C_2 \frac{\partial(\tilde{u}^v\Phi)}{\partial Y} + C_3 \frac{\partial(\tilde{v}^v\Phi)}{\partial Y} + C_4 \frac{\partial\Phi}{\partial Y} + C_5 \frac{\partial^2\Phi}{\partial Y^2} + C_6 \frac{\partial^2\Phi}{\partial Y\partial X} \end{cases} \quad (\text{B.26})$$

Using ADI scheme results in two successive sweeps in  $y$  and  $x$  directions:

$$\left[ I + \alpha \cdot \Delta t \cdot D_y \right] \Delta\Phi^* = \Delta t \cdot S \quad \left[ I + \alpha \cdot \Delta t \cdot D_x \right] \cdot \Delta\Phi = \Delta\Phi^* \quad (\text{B.27})$$

## Spatial discretization for momentums

Spatial discretizations are made by using central differences:

$$\left. \frac{df}{dx} \right|_{x=x_i} = \frac{f_{i+1} - f_{i-1}}{x_{i+1} - x_{i-1}} \quad \text{or} \quad \left. \frac{df}{dx} \right|_{x=x_i} = \frac{f_{i+1/2} - f_{i-1/2}}{x_{i+1/2} - x_{i-1/2}} \quad (\text{B.28})$$

$$\left. \frac{d^2f}{dx^2} \right|_{x=x_i} = \frac{1}{x_{i+1/2} - x_{i-1/2}} \left[ \frac{f_{i+1} - f_i}{x_{i+1} - x_i} - \frac{f_i - f_{i-1}}{x_i - x_{i-1}} \right] \quad (\text{B.29})$$

The central and backward difference operators, which denotes the difference between the primary grid points and the secondary grid points are defined as:

$$\begin{aligned} \Delta x_i^u &= x_{i+1}^v - x_i^v & \Delta x_i^v &= x_i^u - x_{i-1}^u \\ \Delta y_j^u &= y_j^v - y_{j-1}^v & \Delta y_j^v &= y_{j+1}^u - y_j^u \\ \nabla x_i^u &= x_i^u - x_i^v & \nabla x_i^v &= x_i^v - x_{i-1}^u \\ \nabla y_j^u &= y_j^u - y_{j-1}^v & \nabla y_j^v &= y_j^v - y_j^u \end{aligned}$$

The following linear interpolates of the velocity components of the staggered mesh are used :

$$\begin{aligned}
u_u^{x+} &= \frac{\nabla x_{i+1}^u \cdot u_{i,j} + \nabla x_{i+1}^v \cdot u_{i+1,j}}{\Delta x_{i+1}^v} , & u_u^{x-} &= \frac{\nabla x_i^u \cdot u_{i-1,j} + \nabla x_i^v \cdot u_{i,j}}{\Delta x_i^v} \\
u_u^{y+} &= \frac{\nabla y_{j+1}^u \cdot u_{i,j} + \nabla y_j^v \cdot u_{i,j+1}}{\Delta y_j^v} , & u_u^{y-} &= \frac{\nabla y_j^u \cdot u_{i,j-1} + \nabla y_{j-1}^v \cdot u_{i,j}}{\Delta y_{j-1}^v} \\
v_u^{y+} &= \frac{\nabla x_{i+1}^v \cdot v_{i,j} + \nabla x_i^u \cdot v_{i+1,j}}{\Delta x_i^u} , & v_u^{y-} &= \frac{\nabla x_{i+1}^v \cdot v_{i,j-1} + \nabla x_i^u \cdot v_{i+1,j-1}}{\Delta x_i^u} \\
v_v^{x+} &= \frac{\nabla x_{i+1}^v \cdot v_{i,j} + \nabla x_i^u \cdot v_{i+1,j}}{\Delta x_i^u} , & v_v^{x-} &= \frac{\nabla x_i^v \cdot v_{i-1,j} + \nabla x_{i-1}^u \cdot v_{i,j}}{\Delta x_{i-1}^u} \\
v_v^{y+} &= \frac{\nabla y_{j+1}^v \cdot v_{i,j} + \nabla y_{j+1}^u \cdot v_{i,j+1}}{\Delta y_{j+1}^u} , & v_v^{y-} &= \frac{\nabla y_j^v \cdot v_{i,j-1} + \nabla y_j^u \cdot v_{i,j}}{\Delta y_j^u} \\
u_v^{x+} &= \frac{\nabla y_{j+1}^u \cdot u_{i,j} + \nabla y_j^v \cdot v_{i,j+1}}{\Delta y_j^v} , & u_v^{x-} &= \frac{\nabla y_{j+1}^u \cdot u_{i-1,j} + \nabla y_j^v \cdot u_{i-1,j+1}}{\Delta y_j^v} \\
p_{u_{i,j}}^{y+} &= \frac{\nabla y_{j+1}^u \cdot p_1 + \nabla y_j^v \cdot p_2}{\Delta y_j^v} , & p_{u_{i,j+1}}^{y-} &= p_{u_{i,j}}^{y+} \\
p_1 &= \frac{\nabla x_{i+1}^v \cdot p_{i,j} + \nabla x_i^u \cdot p_{i+1,j}}{\Delta x_i^u} , & p_2 &= \frac{\nabla x_{i+1}^v \cdot p_{i,j+1} + \nabla x_i^u \cdot p_{i+1,j+1}}{\Delta x_i^u} \\
u_{v_{i,j}}^{m-} &= \frac{\nabla y_j^u \cdot u_1 + \nabla y_{j-1}^v \cdot u_2}{\Delta y_{j-1}^v} \\
u_1 &= \frac{\nabla x_i^u \cdot u_{i-1,j-1} + \nabla x_i^v \cdot u_{i,j-1}}{\Delta x_i^v} , & u_2 &= \frac{\nabla x_i^u \cdot u_{i-1,j} + \nabla x_i^v \cdot u_{i,j}}{\Delta x_i^v} \\
u_{v_{i-1,j}}^{p-} &= u_{v_{i,j}}^{m-} & u_{v_{i,j-1}}^{m+} &= u_{v_{i,j}}^{m-} & u_{v_{i-1,j-1}}^{p+} &= u_{v_{i,j}}^{m-}
\end{aligned}$$

**X-Momentum:**

$$G_u(u, v, p) = C_7 \frac{\partial u^2}{\partial X} + C_2 \frac{\partial uu}{\partial Y} + C_8 \frac{\partial uv}{\partial X} + C_3 \frac{\partial uv}{\partial Y} + C_7 \frac{\partial p}{\partial X} + C_2 \frac{\partial p}{\partial Y} + C_1 \frac{\partial^2 u}{\partial X^2} \quad (\text{B.30})$$

$$+ C_6 \frac{\partial^2 u}{\partial X \partial Y} + C_5 \frac{\partial^2 u}{\partial Y^2} + C_4 \frac{\partial u}{\partial Y} + C_9 \frac{\partial u}{\partial X}$$

$$G_u|_{i,j} = \frac{1}{\Delta x_i^u} \cdot \left[ \begin{aligned} & C_7 \cdot \left( (u_u^{x+})^2 - (u_u^{x-})^2 \right) + C_8 \cdot (v_{v_{i+1}}^{y-} \cdot u_u^{x+} - v_v^{y-} \cdot u_u^{x-}) + C_7 \cdot (p_{i+1,j} - p_{i,j}) \dots \\ & + C_1 \cdot \left( \frac{u_{i+1,j} - u_{i,j}}{\Delta x_{i+1}^v} - \frac{u_{i,j} - u_{i-1,j}}{\Delta x_i^v} \right) + C_9 \cdot (u_u^{x+} - u_u^{x-}) \end{aligned} \right] \quad (\text{B.31})$$

$$+ \frac{1}{\Delta y_j^u} \cdot \left[ \begin{aligned} & C_2 \cdot \left( (u_u^{y+})^2 - (u_u^{y-})^2 \right) + C_2 \cdot (p_u^{y+} - p_u^{y-}) + C_6 \cdot \left( \frac{u_v^{p+} - u_v^{m+}}{\Delta x_i^u} - \frac{u_v^{p-} - u_v^{m-}}{\Delta x_i^u} \right) \dots \\ & + C_5 \cdot \left( \frac{u_{i,j+1} - u_{i,j}}{\Delta y_j^v} - \frac{u_{i,j} - u_{i,j-1}}{\Delta y_{j-1}^v} \right) + C_4 \cdot (u_u^{y+} - u_u^{y-}) + C_3 \cdot (v_u^{y+} u_u^{y+} - v_u^{y-} u_u^{y-}) \end{aligned} \right]$$

**Y-Momentum:**

$$G_v(u, v, p) = C_8 \frac{\partial vv}{\partial X} + C_3 \frac{\partial vv}{\partial Y} + C_7 \frac{\partial uv}{\partial X} + C_3 \frac{\partial uv}{\partial Y} + C_2 \frac{\partial uv}{\partial Y} + C_8 \frac{\partial p}{\partial X} + C_3 \frac{\partial p}{\partial Y} + C_1 \frac{\partial^2 v}{\partial X^2} \quad (\text{B.32})$$

$$+ C_6 \frac{\partial^2 v}{\partial X \partial Y} + C_5 \frac{\partial^2 v}{\partial Y^2} + C_4 \frac{\partial v}{\partial Y} + C_9 \frac{\partial v}{\partial X}$$

$$G_v|_{i,j} = \frac{1}{\Delta x_i^v} \cdot \left[ \begin{aligned} & C_8 \cdot \left( (v_v^{x+})^2 - (v_v^{x-})^2 \right) + C_7 \cdot (u_v^{x+} v_v^{x+} - u_v^{x-} v_v^{x-}) + C_8 \cdot (p_v^{x+} - p_v^{x-}) \\ & + C_9 \cdot (v_v^{x+} - v_v^{x-}) + C_1 \cdot \left( \frac{v_{i+1,j} - v_{i,j}}{\Delta x_i^u} - \frac{v_{i,j} - v_{i-1,j}}{\Delta x_{i-1}^u} \right) \end{aligned} \right]$$

$$+ \frac{1}{\Delta y_j^v} \cdot \left[ \begin{aligned} & C_3 \cdot \left( (v_v^{y+})^2 - (v_v^{y-})^2 \right) + C_2 \cdot (u_v^{y+} v_v^{y+} - u_v^{y-} v_v^{y-}) + C_3 \cdot (p_{i,j+1} - p_{i,j}) \\ & + C_5 \cdot \left( \frac{v_{i,j+1} - v_{i,j}}{\Delta y_{j+1}^u} - \frac{v_{i,j} - v_{i,j-1}}{\Delta y_j^u} \right) + C_4 \cdot (v_v^{y+} - v_v^{y-}) + C_6 \cdot \left( \frac{v_u^{p+} - v_u^{m+}}{\Delta x_i^v} - \frac{v_u^{p-} - v_u^{m-}}{\Delta x_i^v} \right) \end{aligned} \right]$$

(B.12)

## Spatial discretization of two successive sweeps

### Y-sweep:

#### X-Momentum:

$$\begin{aligned} & \Delta u_{i,j-1}^* \cdot \left[ \frac{\alpha \cdot \Delta t}{\Delta y_j^u} \cdot \left( -C_2 \cdot \tilde{u}^v \Big|_u^{y^-} \cdot \frac{\nabla y_j^u}{\Delta y_{j-1}^v} - C_3 \cdot \tilde{v}^v \Big|_u^{y^-} \cdot \frac{\nabla y_j^u}{\Delta y_{j-1}^v} - C_4 \cdot \frac{\nabla y_j^u}{\Delta y_{j-1}^v} + C_5 \cdot \frac{1}{\Delta y_{j-1}^v} \right) \right] + \\ & \Delta u_{i,j}^* \cdot \left[ 1 + \frac{\alpha \cdot \Delta t}{\Delta y_j^u} \cdot \left( C_2 \cdot \left( \tilde{u}^v \Big|_u^{y^+} \cdot \frac{\nabla y_{j+1}^u}{\Delta y_j^v} - \tilde{u}^v \Big|_u^{y^-} \cdot \frac{\nabla y_{j-1}^u}{\Delta y_{j-1}^v} \right) + C_3 \cdot \left( \tilde{v}^v \Big|_u^{y^+} \cdot \frac{\nabla y_{j+1}^u}{\Delta y_j^v} - \tilde{v}^v \Big|_u^{y^-} \cdot \frac{\nabla y_{j-1}^u}{\Delta y_{j-1}^v} \right) \dots \right) \right. \\ & \quad \left. + C_4 \cdot \left( \frac{\nabla y_{j+1}^u}{\Delta y_j^v} - \frac{\nabla y_{j-1}^u}{\Delta y_{j-1}^v} \right) + C_5 \cdot \left( -\frac{1}{\Delta y_j^v} - \frac{1}{\Delta y_{j-1}^v} \right) \right] + \end{aligned} \quad (\text{B.33})$$

$$\Delta u_{i,j+1}^* \cdot \left[ \frac{\alpha \cdot \Delta t}{\Delta y_j^u} \cdot \left( C_2 \cdot \tilde{u}^v \Big|_u^{y^+} \cdot \frac{\nabla y_j^v}{\Delta y_j^v} + C_3 \cdot \tilde{v}^v \Big|_u^{y^+} \cdot \frac{\nabla y_j^v}{\Delta y_j^v} + C_4 \cdot \frac{\nabla y_j^v}{\Delta y_j^v} + C_5 \cdot \frac{1}{\Delta y_j^v} \right) \right]$$

$$= \Delta t \cdot S_u \Big|_{i,j}$$

#### Y-Momentum:

$$\begin{aligned} & \Delta v_{i,j-1}^* \cdot \left[ \frac{\alpha \cdot \Delta t}{\Delta y_j^v} \cdot \left( -C_2 \cdot \tilde{u}^v \Big|_v^{y^-} \cdot \frac{\nabla y_j^v}{\Delta y_j^u} - C_3 \cdot \tilde{v}^v \Big|_v^{y^-} \cdot \frac{\nabla y_j^v}{\Delta y_j^u} - C_4 \cdot \frac{\nabla y_j^v}{\Delta y_j^u} + C_5 \cdot \frac{1}{\Delta y_j^u} - C_3^p \cdot \frac{C_3}{\delta} \cdot \frac{\Delta t}{\Delta y_j^u} \right) \right] + \\ & \Delta v_{i,j}^* \cdot \left[ 1 + \Delta t + \frac{\alpha \cdot \Delta t}{\Delta y_j^v} \cdot \left( C_2 \cdot \left( \tilde{u}^v \Big|_v^{y^+} \cdot \frac{\nabla y_{j+1}^v}{\Delta y_{j+1}^u} - \tilde{u}^v \Big|_v^{y^-} \cdot \frac{\nabla y_j^v}{\Delta y_j^u} \right) + C_3 \cdot \left( \tilde{v}^v \Big|_v^{y^+} \cdot \frac{\nabla y_{j+1}^v}{\Delta y_{j+1}^u} - \tilde{v}^v \Big|_v^{y^-} \cdot \frac{\nabla y_j^v}{\Delta y_j^u} \right) \dots \right) \right. \\ & \quad \left. + C_4 \cdot \left( \frac{\nabla y_{j+1}^v}{\Delta y_{j+1}^u} - \frac{\nabla y_j^v}{\Delta y_j^u} \right) + C_5 \cdot \left( -\frac{1}{\Delta y_{j+1}^u} - \frac{1}{\Delta y_j^u} \right) + C_3^p \cdot C_3 \cdot \frac{\Delta t}{\delta} \cdot \left( \frac{1}{\Delta y_{j+1}^u} + \frac{1}{\Delta y_j^u} \right) \right] + \end{aligned}$$

$$\Delta v_{i,j+1}^* \cdot \left[ \frac{\alpha \cdot \Delta t}{\Delta y_j^v} \cdot \left( C_2 \cdot \tilde{u}^v \Big|_v^{y^+} \cdot \frac{\nabla y_{j+1}^u}{\Delta y_{j+1}^u} + C_3 \cdot \tilde{v}^v \Big|_v^{y^+} \cdot \frac{\nabla y_{j+1}^u}{\Delta y_{j+1}^u} + C_4 \cdot \frac{\nabla y_{j+1}^u}{\Delta y_{j+1}^u} + C_5 \cdot \frac{1}{\Delta y_{j+1}^u} - C_3^p \cdot C_3 \cdot \frac{\Delta t}{\delta} \cdot \frac{\Delta t}{\Delta y_{j+1}^u} \right) \right]$$

$$= S_v \Big|_{i,j}$$

$$- \frac{\alpha \cdot \Delta t}{\Delta y_j^v} \cdot C_3 \cdot \left[ -\frac{\Delta t}{\delta} (\nabla \tilde{v}_{i,j+1}^v - \nabla \tilde{v}_{i,j}^v) - \frac{\Delta t}{\delta} \cdot C_2^p \cdot \left( \frac{\Delta u_{i,j+1}^* \Big|_{v,i,j+1}^{m+} - \Delta u_{i,j+1}^* \Big|_{v,i,j+1}^{m-}}{\Delta y_{j+1}^u} - \frac{\Delta u_{i,j}^* \Big|_{v,i,j}^{m+} - \Delta u_{i,j}^* \Big|_{v,i,j}^{m-}}{\Delta y_j^u} \right) \right] \quad (\text{B.34})$$

**Continuity equation:**

$$\Delta p_{i,j}^* = -\frac{\Delta t}{\delta} \cdot \nabla \tilde{V}_{i,j}^v - \frac{\Delta t}{\delta} \frac{1}{\Delta y_j^u} \left( C_2^p \cdot \left( \Delta u_{i,j}^{*|m+} - \Delta u_{i,j}^{*|m-} \right) + C_3^p \cdot \left( \Delta v_{i,j}^* - \Delta v_{i,j-1}^* \right) \right) \quad (\text{B.35})$$

**X-sweep:**

**X-Momentum:**

$$\begin{aligned} & \left[ \frac{\alpha \cdot \Delta t}{\Delta x_i^u} \cdot \left( C_7 \cdot \left( -\tilde{u}^v \Big|_u^{x+} \cdot \frac{\nabla x_i^u}{\Delta x_i^v} \right) - C_8 \cdot \left( \tilde{v}^v \Big|_v^{y-} \cdot \frac{\nabla x_i^u}{\Delta x_i^v} \right) + C_1 \cdot \frac{1}{\Delta x_i^v} - C_7 \cdot C_7^p \cdot \frac{\Delta t}{\delta} \cdot \frac{1}{\Delta x_i^v} - C_9 \cdot \nabla x_i^u \right) \right] \cdot \Delta u_{i-1,j} \\ & + \left[ 1 + \Delta t + \frac{\alpha \cdot \Delta t}{\Delta x_i^u} \cdot \left( C_7 \cdot \left( \tilde{u}^v \Big|_u^{x+} \cdot \frac{\nabla x_{i+1}^u}{\Delta x_{i+1}^v} - \tilde{u}^v \Big|_u^{x-} \cdot \frac{\nabla x_i^u}{\Delta x_i^v} \right) + C_1 \cdot \left( -\frac{1}{\Delta x_i^v} - \frac{1}{\Delta x_{i+1}^v} \right) + C_7 \cdot C_7^p \cdot \frac{\Delta t}{\delta} \cdot \left( \frac{1}{\Delta x_i^v} + \frac{1}{\Delta x_{i+1}^v} \right) \dots \right) \right. \\ & \quad \left. + C_8 \cdot \left( \tilde{v}^v \Big|_v^{y-} \cdot \frac{\nabla x_{i+1}^u}{\Delta x_{i+1}^v} - \tilde{v}^v \Big|_v^{y-} \cdot \frac{\nabla x_i^u}{\Delta x_i^v} \right) + C_9 \cdot \left( \frac{\nabla x_{i+1}^u}{\Delta x_{i+1}^v} - \frac{\nabla x_i^u}{\Delta x_i^v} \right) \right] \cdot \Delta u_{i,j} \\ & + \left[ \frac{\alpha \cdot \Delta t}{\Delta x_i^u} \cdot \left( C_7 \cdot \tilde{u}^v \Big|_u^{x+} \cdot \frac{\nabla x_{i+1}^v}{\Delta x_{i+1}^v} + C_8 \cdot \tilde{v}^v \Big|_v^{y-} \cdot \frac{\nabla x_{i+1}^v}{\Delta x_{i+1}^v} + C_1 \cdot \frac{1}{\Delta x_{i+1}^v} - C_7 \cdot C_7^p \cdot \frac{\Delta t}{\delta} \cdot \frac{1}{\Delta x_{i+1}^v} + C_9 \cdot \nabla x_{i+1}^v \right) \right] \cdot \Delta u_{i+1,j} \\ & = \Delta u_{i,j}^* - \frac{\alpha \cdot \Delta t}{\Delta x_i^u} \cdot \left[ \Delta p_{i+1,j}^* - \Delta p_{i,j}^* - C_8^p \cdot \frac{\Delta t}{\delta} \cdot \left( \frac{\Delta v_{u_{i+1},j}^{p-} - \Delta v_{u_{i+1},j}^{m-}}{\Delta x_{i+1}^v} \right) + C_8^p \cdot \frac{\Delta t}{\delta} \cdot \left( \frac{\Delta v_{u_{i,j}}^{p-} - \Delta v_{u_{i,j}}^{m-}}{\Delta x_i^v} \right) \right] \end{aligned} \quad (\text{B.36})$$

**Y-Momentum:**

$$\begin{aligned} & \left[ \frac{\alpha \cdot \Delta t}{\Delta x_i^v} \cdot \left( C_7 \cdot \left( -\tilde{u}^v \Big|_v^{x-} \right) \frac{\nabla x_i^v}{\Delta x_{i-1}^u} + C_1 \frac{1}{\Delta x_{i-1}^u} - C_8 \cdot \frac{\tilde{v}^v \Big|_v^{x-}}{\Delta x_{i-1}^u} - C_9 \cdot \nabla x_i^v \right) \right] \cdot \Delta v_{i-1,j} \\ & + \left[ 1 + \frac{\alpha \cdot \Delta t}{\Delta x_i^v} \cdot \left( C_7 \cdot \left( \tilde{u}^v \Big|_v^{x+} \cdot \frac{\nabla x_{i+1}^v}{\Delta x_i^u} - \tilde{u}^v \Big|_v^{x-} \cdot \frac{\nabla x_{i-1}^v}{\Delta x_{i-1}^u} \right) + C_8 \cdot \left( \tilde{v}^v \Big|_v^{x+} \cdot \frac{\nabla x_{i+1}^v}{\Delta x_i^u} - \tilde{v}^v \Big|_v^{x-} \cdot \frac{\nabla x_{i-1}^v}{\Delta x_{i-1}^u} \right) \dots \right) \right. \\ & \quad \left. + C_1 \cdot \left( -\frac{1}{\Delta x_i^u} - \frac{1}{\Delta x_{i-1}^u} \right) + C_9 \cdot \left( \frac{\nabla x_{i+1}^v}{\Delta x_i^u} - \frac{\nabla x_{i-1}^v}{\Delta x_{i-1}^u} \right) \right] \cdot \Delta v_{i,j} \quad (\text{B.37}) \\ & + \left[ \frac{\alpha \cdot \Delta t}{\Delta x_i^v} \cdot \left( C_7 \cdot \tilde{u}^v \Big|_v^{x+} \cdot \frac{\nabla x_i^u}{\Delta x_i^u} + C_8 \cdot \tilde{v}^v \Big|_v^{x+} \cdot \frac{\nabla x_i^u}{\Delta x_i^u} + C_1 \cdot \frac{1}{\Delta x_i^u} + C_9 \cdot \nabla x_i^u \right) \right] \cdot \Delta v_{i+1,j} = \Delta v_{i,j}^* \end{aligned}$$

**Continuity equation:**

$$\Delta p_{i,j} = \Delta p_{i,j}^* - \frac{\Delta t}{\delta} \cdot \left[ C_7^p \cdot \left( \frac{\Delta u_{i,j} - \Delta u_{i-1,j}}{\Delta x_i^v} \right) + C_8^p \cdot \left( \frac{\Delta v_{u_{i,j}}^{p-} - \Delta v_{u_{i,j}}^{m-}}{\Delta x_i^v} \right) \right] \quad (\text{B.38})$$

## Appendix C

### Steady viscous flows past wings

The Navier-Stokes and continuity equations for the incompressible steady flow past the wing can be expressed in nondimensional conservation form as

$$\mathbf{G}(\mathbf{V}, p) = \mathbf{0}, \quad \nabla \cdot \mathbf{V} = \frac{\partial u}{\partial \xi} + \frac{\partial v}{\partial \eta} + \frac{\partial w}{\partial \zeta} = 0, \quad (\text{C.1})$$

$$\begin{aligned} G_u(u, v, w, p) = & C_7 \frac{\partial uu}{\partial X} + C_2 \frac{\partial uu}{\partial Z} + \frac{\partial vu}{\partial Y} + C_8 \frac{\partial wu}{\partial X} + C_3 \frac{\partial wu}{\partial Z} + C_7 \frac{\partial p}{\partial X} + C_2 \frac{\partial p}{\partial Z} + C_1 \frac{\partial^2 u}{\partial X^2} \\ & + C_4 \frac{\partial u}{\partial Z} + C_{10} \frac{\partial^2 u}{\partial Y^2} + C_5 \frac{\partial^2 u}{\partial Z^2} + C_9 \frac{\partial u}{\partial X} + C_6 \frac{\partial^2 u}{\partial X \partial Z} \end{aligned} \quad (\text{C.2})$$

$$\begin{aligned} G_v(u, v, w, p) = & C_7 \frac{\partial uv}{\partial X} + C_2 \frac{\partial uv}{\partial Z} + \frac{\partial vv}{\partial Y} + C_8 \frac{\partial wv}{\partial X} + C_3 \frac{\partial wv}{\partial Z} + \frac{\partial p}{\partial Y} + C_1 \frac{\partial^2 v}{\partial X^2} + C_4 \frac{\partial v}{\partial Z} \\ & + C_{10} \frac{\partial^2 v}{\partial Y^2} + C_5 \frac{\partial^2 v}{\partial Z^2} + C_9 \frac{\partial v}{\partial X} + C_6 \frac{\partial^2 v}{\partial X \partial Z} \end{aligned} \quad (\text{C.3})$$

$$\begin{aligned} G_w(u, v, w, p) = & C_7 \frac{\partial uw}{\partial X} + C_2 \frac{\partial uw}{\partial Z} + \frac{\partial vw}{\partial Y} + C_8 \frac{\partial ww}{\partial X} + C_3 \frac{\partial ww}{\partial Z} + C_8 \frac{\partial p}{\partial X} + C_3 \frac{\partial p}{\partial Z} + C_1 \frac{\partial^2 w}{\partial X^2} + C_4 \frac{\partial w}{\partial Z} \\ & + C_{10} \frac{\partial^2 w}{\partial Y^2} + C_5 \frac{\partial^2 w}{\partial Z^2} + C_9 \frac{\partial w}{\partial X} + C_6 \frac{\partial^2 w}{\partial X \partial Z} \end{aligned} \quad (\text{C.4})$$

$$C_7 \frac{\partial u}{\partial X} + C_2 \frac{\partial u}{\partial Z} + \frac{\partial v}{\partial Y} + C_8 \frac{\partial w}{\partial X} + C_3 \frac{\partial w}{\partial Z} = 0 \quad (\text{C.5})$$

### Geometrical coordinate transformation coefficients:

Geometrical coordinate transformation coefficients for each domain can be defined as

#### Domain 1, 4, 5 and 6

$$C_1 = -\frac{1}{\text{Re}} \left[ \left( \frac{\partial X}{\partial \xi} \right)^2 + \left( \frac{\partial X}{\partial \eta} \right)^2 + \left( \frac{\partial X}{\partial \zeta} \right)^2 \right] \quad (\text{C.6})$$

$$C_2 = 0 \quad (\text{C.7})$$

$$C_3 = \frac{\partial Z}{\partial \zeta} \quad (\text{C.8})$$

$$C_4 = -\frac{1}{\text{Re}} \left[ \frac{\partial^2 Z}{\partial \eta^2} \right] \quad (\text{C.9})$$

$$C_5 = -\frac{1}{\text{Re}} \left[ \left( \frac{\partial Z}{\partial \eta} \right)^2 + \left( \frac{\partial Z}{\partial \zeta} \right)^2 \right] \quad (\text{C. 10})$$

$$C_6 = -\frac{2}{\text{Re}} \left( \frac{\partial Z}{\partial \eta} \frac{\partial X}{\partial \eta} + \frac{\partial Z}{\partial \zeta} \frac{\partial X}{\partial \zeta} \right) \quad (\text{C. 11})$$

$$C_7 = \frac{\partial X}{\partial \bar{\xi}} \quad (\text{C. 12})$$

$$C_8 = \frac{\partial X}{\partial \bar{\zeta}} \quad (\text{C. 13})$$

$$C_9 = -\frac{1}{\text{Re}} \left[ \frac{\partial^2 X}{\partial \eta^2} + \frac{\partial^2 X}{\partial \zeta^2} \right] \quad (\text{C. 14})$$

$$C_{10} = -\frac{1}{\text{Re}} \quad (\text{C. 15})$$

**Domain 2 and 3**

$$C_1 = -\frac{1}{\text{Re}} \left[ \left( \frac{\partial X}{\partial x} \right)^2 \left( \frac{\partial x}{\partial \bar{\xi}} \right)^2 + \left( \frac{\partial X}{\partial \eta} \right)^2 + \left( \frac{\partial X}{\partial x} \right)^2 \left( \frac{\partial x}{\partial \bar{\zeta}} \right)^2 \right] \quad (\text{C. 16})$$

$$C_2 = \left[ \frac{\partial Z}{\partial z} \frac{\partial z}{\partial \bar{\xi}} + \frac{\partial Z}{\partial x} \frac{\partial x}{\partial \bar{\xi}} + \frac{\partial Z}{\partial e(\bar{x})} \frac{\partial e(\bar{x})}{\partial \bar{x}} \frac{\partial \bar{x}}{\partial x} \frac{\partial x}{\partial \bar{\xi}} \right] \quad (\text{C. 17})$$

$$C_3 = \left[ \frac{\partial Z}{\partial z} \frac{\partial z}{\partial \bar{\zeta}} + \frac{\partial Z}{\partial x} \frac{\partial x}{\partial \bar{\zeta}} + \frac{\partial Z}{\partial e(\bar{x})} \frac{\partial e(\bar{x})}{\partial \bar{x}} \frac{\partial \bar{x}}{\partial x} \frac{\partial x}{\partial \bar{\zeta}} \right] \quad (\text{C. 18})$$

$$\begin{aligned} C_4 = & -\frac{1}{\text{Re}} \left[ \left( \frac{\partial^2 Z}{\partial x^2} + 2 \left( \frac{\partial^2 Z}{\partial x \partial e(\bar{x})} \frac{\partial e(\bar{x})}{\partial \bar{x}} \right) + \frac{\partial^2 Z}{\partial e(\bar{x})^2} \left( \frac{\partial e(\bar{x})}{\partial x} \right)^2 + \frac{\partial Z}{\partial e(\bar{x})} \frac{\partial^2 e(\bar{x})}{\partial \bar{x}^2} \right) \left( \frac{\partial x}{\partial \bar{\xi}} \right)^2 \right. \\ & + \left( 2 \frac{\partial^2 Z}{\partial x \partial z} + 2 \left( \frac{\partial^2 Z}{\partial z \partial e(\bar{x})} \frac{\partial e(\bar{x})}{\partial \bar{x}} \right) \right) \left( \frac{\partial z}{\partial \bar{\xi}} \frac{\partial x}{\partial \bar{\xi}} \right) \\ & + \left( \frac{\partial^2 Z}{\partial x^2} + 2 \left( \frac{\partial^2 Z}{\partial x \partial e(\bar{x})} \frac{\partial e(\bar{x})}{\partial \bar{x}} \right) + \frac{\partial^2 Z}{\partial e(\bar{x})^2} \left( \frac{\partial e(\bar{x})}{\partial x} \right)^2 + \frac{\partial Z}{\partial e(\bar{x})} \frac{\partial^2 e(\bar{x})}{\partial \bar{x}^2} \right) \left( \frac{\partial x}{\partial \bar{\zeta}} \right)^2 \\ & \left. + \left( 2 \frac{\partial^2 Z}{\partial x \partial z} + 2 \left( \frac{\partial^2 Z}{\partial z \partial e(\bar{x})} \frac{\partial e(\bar{x})}{\partial \bar{x}} \right) \right) \left( \frac{\partial z}{\partial \bar{\zeta}} \frac{\partial x}{\partial \bar{\zeta}} \right) \right] \quad (\text{C. 19}) \end{aligned}$$

$$\begin{aligned}
C_5 = & -\frac{1}{\text{Re}} \left[ \left( \frac{\partial Z}{\partial z} \right)^2 \left( \frac{\partial z}{\partial \xi} \right)^2 + 2 \left( \frac{\partial Z}{\partial x} \frac{\partial x}{\partial \xi} \frac{\partial Z}{\partial z} \frac{\partial z}{\partial \xi} \right) + 2 \left( \frac{\partial Z}{\partial e(\bar{x})} \frac{\partial e(\bar{x})}{\partial \bar{x}} \frac{\partial \bar{x}}{\partial x} \frac{\partial x}{\partial \xi} \frac{\partial Z}{\partial z} \frac{\partial z}{\partial \xi} \right) + \left( \frac{\partial Z}{\partial x} \right)^2 \left( \frac{\partial x}{\partial \xi} \right)^2 \right. \\
& + 2 \left( \frac{\partial Z}{\partial e(\bar{x})} \frac{\partial e(\bar{x})}{\partial \bar{x}} \frac{\partial \bar{x}}{\partial x} \frac{\partial Z}{\partial x} \left( \frac{\partial x}{\partial \xi} \right)^2 \right) + \left( \frac{\partial Z}{\partial e(\bar{x})} \right)^2 \left( \frac{\partial e(\bar{x})}{\partial X} \right)^2 \left( \frac{\partial \bar{x}}{\partial x} \right)^2 \left( \frac{\partial x}{\partial \xi} \right)^2 \\
& + \left( \frac{\partial Z}{\partial z} \right)^2 \left( \frac{\partial z}{\partial \zeta} \right)^2 + 2 \left( \frac{\partial Z}{\partial x} \frac{\partial x}{\partial \zeta} \frac{\partial Z}{\partial z} \frac{\partial z}{\partial \zeta} \right) + 2 \left( \frac{\partial Z}{\partial e(\bar{x})} \frac{\partial e(\bar{x})}{\partial \bar{x}} \frac{\partial \bar{x}}{\partial x} \frac{\partial x}{\partial \zeta} \frac{\partial Z}{\partial z} \frac{\partial z}{\partial \zeta} \right) \\
& + \left( \frac{\partial Z}{\partial x} \right)^2 \left( \frac{\partial x}{\partial \zeta} \right)^2 + 2 \left( \frac{\partial Z}{\partial e(\bar{x})} \frac{\partial e(\bar{x})}{\partial \bar{x}} \frac{\partial \bar{x}}{\partial x} \frac{\partial Z}{\partial x} \left( \frac{\partial x}{\partial \zeta} \right)^2 \right) \\
& \left. + \left( \frac{\partial Z}{\partial e(\bar{x})} \right)^2 \left( \frac{\partial e(\bar{x})}{\partial X} \right)^2 \left( \frac{\partial \bar{x}}{\partial x} \right)^2 \left( \frac{\partial x}{\partial \zeta} \right)^2 \right] \tag{C.20}
\end{aligned}$$

$$\begin{aligned}
C_6 = & -\frac{1}{\text{Re}} \left[ 2 \left( \frac{\partial Z}{\partial z} \frac{\partial z}{\partial \xi} \frac{\partial X}{\partial x} \frac{\partial x}{\partial \xi} \right) + 2 \left( \frac{\partial Z}{\partial x} \left( \frac{\partial x}{\partial \xi} \right)^2 \frac{\partial X}{\partial x} \right) + 2 \left( \frac{\partial Z}{\partial e(\bar{x})} \frac{\partial e(\bar{x})}{\partial x} \frac{\partial \bar{x}}{\partial x} \frac{\partial X}{\partial x} \left( \frac{\partial x}{\partial \xi} \right)^2 \right) \right. \\
& + 2 \left( \frac{\partial X}{\partial x} \left( \frac{\partial x}{\partial \xi} \right)^2 \frac{\partial Z}{\partial x} \right) + 2 \left( \frac{\partial Z}{\partial e(x)} \frac{\partial e(x)}{\partial x} \frac{\partial x}{\partial \eta} \frac{\partial X}{\partial \eta} \right) + 2 \left( \frac{\partial Z}{\partial z} \frac{\partial z}{\partial \zeta} \frac{\partial X}{\partial x} \frac{\partial x}{\partial \zeta} \right) \\
& \left. + 2 \left( \frac{\partial Z}{\partial e(x)} \frac{\partial e(x)}{\partial x} \left( \frac{\partial X}{\partial x} \right)^2 \left( \frac{\partial x}{\partial \zeta} \right)^2 \right) \right] \tag{C.21}
\end{aligned}$$

$$C_7 = \frac{\partial X}{\partial x} \frac{\partial x}{\partial \xi} \tag{C.22}$$

$$C_8 = \frac{\partial X}{\partial x} \frac{\partial x}{\partial \zeta} \tag{C.23}$$

$$C_9 = -\frac{4}{\text{Re}} \left[ \frac{\partial^2 X}{\partial \eta^2} \right] \tag{C.24}$$

$$C_{10} = -\frac{1}{\text{Re}} \tag{C.25}$$

### Alternating-Direction Implicit (ADI) scheme:

Continuity and momentum equations can be arranged in the global matrix form:

$$[\mathbf{I} + \Delta\tau(\mathbf{D}_X + \mathbf{D}_Y + \mathbf{D}_Z)]\Delta\mathbf{f} = \Delta\tau \mathbf{R} \tag{C.26}$$

where,

$$\begin{aligned}
\mathbf{D}_X &= \begin{bmatrix} M & 0 & 0 & C_7 \frac{\partial}{\partial X} \\ 0 & M & 0 & 0 \\ 0 & 0 & M & 0 \\ \frac{C_7}{\delta} \frac{\partial}{\partial X} & 0 & \frac{C_8}{\delta} \frac{\partial}{\partial X} & 0 \end{bmatrix}, & \mathbf{D}_Y &= \begin{bmatrix} N & 0 & 0 & 0 \\ 0 & N & 0 & 0 \\ 0 & 0 & N & 0 \\ 0 & \frac{\partial}{\partial Y} & 0 & 0 \end{bmatrix}, \\
\mathbf{D}_Z &= \begin{bmatrix} L & 0 & 0 & C_2 \frac{\partial}{\partial Z} \\ 0 & L & 0 & 0 \\ 0 & 0 & L & C_3 \frac{\partial}{\partial Z} \\ \frac{C_2}{\delta} \frac{\partial}{\partial Z} & 0 & \frac{C_3}{\delta} \frac{\partial}{\partial Z} & 0 \end{bmatrix}, & \mathbf{R} &= \begin{bmatrix} -G_u^v \\ -G_v^v \\ -G_w^v \\ -(1/\delta) D \check{\mathbf{V}}^v \end{bmatrix}, & & (C.27)
\end{aligned}$$

in which the differential operators  $M$ ,  $N$ , and  $L$  are defined as

$$M = C_9 \frac{\partial \phi}{\partial X} + C_7 \frac{\partial(\bar{u}^v \phi)}{\partial X} + C_8 \frac{\partial(\bar{w}^v \phi)}{\partial X} + C_1 \frac{\partial^2 \phi}{\partial X^2}, \quad (C.28)$$

$$N = \frac{\partial(\bar{v}^v \phi)}{\partial Y} + C_{10} \frac{\partial^2 \phi}{\partial Y^2}, \quad (C.29)$$

$$L = C_2 \frac{\partial(\bar{u}^v \phi)}{\partial Z} + C_3 \frac{\partial(\bar{w}^v \phi)}{\partial Z} + C_4 \frac{\partial \phi}{\partial Z} + C_5 \frac{\partial^2 \phi}{\partial Z^2} + C_6 \frac{\partial^2 \phi}{\partial X \partial Z}, \quad (C.30)$$

Using ADI scheme results in three successive sweeps in  $Z$ ,  $Y$  and  $X$  directions:

$$[\mathbf{I} + \alpha \Delta \tau \mathbf{D}_Z] \Delta \mathbf{f}^* = \Delta \tau \mathbf{R} \quad Z\text{-Sweep}$$

$$[\mathbf{I} + \alpha \Delta \tau \mathbf{D}_Y] \Delta \bar{\mathbf{f}} = \Delta \mathbf{f}^* \quad Y\text{-Sweep}$$

$$[\mathbf{I} + \alpha \Delta \tau \mathbf{D}_X] \Delta \mathbf{f} = \Delta \bar{\mathbf{f}} \quad X\text{-Sweep}$$

## Spatial discretization for momentums:

Spatial discretizations on momentum equations are made by using central differences:

$$\left. \frac{df}{dx} \right|_{x=x_i} = \frac{f_{i+1} - f_{i-1}}{x_{i+1} - x_{i-1}} \quad \text{or} \quad \left. \frac{df}{dx} \right|_{x=x_i} = \frac{f_{i+1/2} - f_{i-1/2}}{x_{i+1/2} - x_{i-1/2}} \quad (\text{C.31})$$

$$\left. \frac{d^2 f}{dx^2} \right|_{x=x_i} = \frac{1}{x_{i+1/2} - x_{i-1/2}} \left[ \frac{f_{i+1} - f_i}{x_{i+1} - x_i} - \frac{f_i - f_{i-1}}{x_i - x_{i-1}} \right] \quad (\text{C.32})$$

The central and backward difference operators, which denotes the difference between the primary grid points and the secondary grid points are defined as:

$$\begin{aligned} \Delta x_i^u &= x_{i+1}^v - x_i^v & \Delta x_i^v &= x_i^u - x_{i-1}^u \\ \Delta y_j^u &= y_j^v - y_{j-1}^v & \Delta y_j^v &= y_{j+1}^u - y_j^u \\ \Delta z_k^u &= z_k^w - z_{k-1}^w & \Delta z_k^w &= z_{k+1}^u - z_k^u \\ \nabla x_i^u &= x_i^u - x_i^v & \nabla x_i^v &= x_i^v - x_{i-1}^u \\ \nabla y_j^u &= y_j^u - y_{j-1}^v & \nabla y_j^v &= y_j^v - y_j^u \\ \nabla z_k^u &= z_k^u - z_{k-1}^w & \nabla z_k^w &= z_k^w - z_k^u \end{aligned}$$

The following interpolates are needed to discretize momentum equations (C.2) to (C.5)

### Interpolations for $G_u$

$$\tilde{u}_{u,i,j,k}^{X-} = \frac{\nabla X_i^v \cdot u_{i,j,k} + \nabla X_i^u u_{i-1,j,k}}{\Delta X_i^v} \quad \text{and} \quad \tilde{u}_{u,i,j,k}^{X+} = \tilde{u}_{u_{i+1,j,k}}^{X-}$$

$$\tilde{u}_{u,i,j,k}^{Z-} = \frac{\nabla Z_{k-1}^w \cdot u_{i,j,k} + \nabla Z_k^u u_{i,j,k-1}}{\Delta Z_{k-1}^w} \quad \text{and} \quad \tilde{u}_{u,i,j,k}^{Z+} = \tilde{u}_{u_{i,j,k+1}}^{Z-}$$

$$v_{u,i,j,k}^{X-} = \frac{\nabla Y_j^v \cdot v_{i,j-1,k} + \nabla Y_j^u v_{i,j,k}}{\Delta Y_j^u} \quad \text{and} \quad v_{u_{i-1,j,k}}^{X+} = v_{u_{i,j,k}}^{X-}$$

$$\tilde{u}_{u,i,j,k}^{Y-} = \frac{\nabla Y_{j-1}^v \cdot u_{i,j,k} + \nabla Y_j^u u_{i,j-1,k}}{\Delta Y_{j-1}^v} \quad \text{and} \quad \tilde{u}_{u_{i,j,k}}^{Y+} = \tilde{u}_{u_{i,j+1,k}}^{Y-}$$

$$\tilde{w}_{u,i,j,k}^{X-} = \frac{\nabla Z_k^u \cdot w_{i,j,k} + \nabla Z_k^w w_{i,j,k-1}}{\Delta Z_k^u} \quad \text{and} \quad \tilde{w}_{u_{i-1,j,k}}^{X+} = \tilde{w}_{u_{i,j,k}}^{X-}$$

$$\tilde{w}_{u,i,j,k}^{Z-} = \frac{\nabla X_i^u \cdot w_{i+1,j,k-1} + \nabla X_{i+1}^v w_{i,j,k-1}}{\Delta X_i^u} \quad \text{and} \quad \tilde{w}_{u_{i,j,k}}^{Z+} = \tilde{w}_{u_{i,j,k+1}}^{Z-}$$

$$p_{1,i,j,k} = \frac{\nabla X_{i+1}^v \cdot p_{i,j,k} + \nabla X_i^u p_{i+1,j,k}}{\Delta X_i^u} \quad \text{and} \quad p_{2,i,j,k} = \frac{\nabla X_{i+1}^v \cdot p_{i,j,k+1} + \nabla X_i^u p_{i+1,j,k+1}}{\Delta X_i^u}$$

$$\check{p}_{u_{i,j,k}}^{Z+} = \frac{\nabla Z_{k+1}^u \cdot p_{1,i,j,k} + \nabla Z_k^w \cdot p_{2,i,j,k-1}}{\Delta Z_k^w} \quad \text{and} \quad \check{p}_{u_{i,j,k}}^{Z-} = \check{p}_{u_{i,j,k-1}}^{Z+}$$

$$u_{11} = \frac{\nabla X_i^u \cdot u_{i-1,j,k-1} + \nabla X_i^v \cdot u_{i,j,k-1}}{\Delta X_i^v} \quad \text{and} \quad u_{12} = \frac{\nabla X_i^u \cdot u_{i-1,j,k} + \nabla X_i^v \cdot u_{i,j,k}}{\Delta X_i^v}$$

$$u|_{w_{i,j,k}}^{m-} = \frac{\nabla Z_k^u \cdot u_{11} + \nabla Z_{k-1}^w \cdot u_{12}}{\Delta Z_{k-1}^w}, \quad u|_{w_{i,j,k-1}}^{m+} = u|_{w_{i,j,k}}^{m-},$$

$$u|_{w_{i-1,j,k}}^{p-} = u|_{w_{i,j,k}}^{m-}, \quad u|_{w_{i-1,j,k-1}}^{p+} = u|_{w_{i,j,k}}^{m-}$$

### Interpolations for $G_v$

$$\check{u}_{v_{i,j,k}}^{X-} = \frac{\nabla Y_j^v \cdot u_{i-1,j+1,k} + \nabla Y_{j+1}^u \cdot u_{i-1,j,k}}{\Delta Y_j^v} \quad \text{and} \quad \check{u}_{v_{i,j,k}}^{X+} = \check{u}_{v_{i+1,j,k}}^{X-}$$

$$v_{v_{i,j,k}}^{X-} = \frac{\nabla X_{i-1}^u \cdot v_{i,j,k} + \nabla X_i^v \cdot v_{i-1,j,k}}{\Delta X_{i-1}^u} \quad \text{and} \quad v_{v_{i,j,k}}^{X+} = v_{v_{i+1,j,k}}^{X-}$$

$$\check{v}_{v_{i,j,k}}^{Z-} = \frac{\nabla Z_{k-1}^w \cdot v_{i,j,k} + \nabla Z_k^u \cdot v_{i,j,k-1}}{\Delta Z_{k-1}^w} \quad \text{and} \quad \check{v}_{v_{i,j,k}}^{Z+} = \check{v}_{v_{i,j,k+1}}^{Z-}$$

$$v_{v_{i,j,k}}^{Y-} = \frac{\nabla Y_j^u \cdot v_{i,j,k} + \nabla Y_j^v \cdot v_{i,j-1,k}}{\Delta Y_j^u} \quad \text{and} \quad v_{v_{i,j,k}}^{Y+} = v_{v_{i,j+1,k}}^{Y-}$$

$$w_{v_{i,j,k}}^{Z-} = \frac{\nabla Y_j^v \cdot w_{i,j+1,k-1} + \nabla Y_{j+1}^u \cdot w_{i,j,k-1}}{\Delta Y_j^v} \quad \text{and} \quad w_{v_{i,j,k}}^{Z+} = w_{v_{i,j,k+1}}^{Z-}$$

$$v_{11} = \frac{\nabla X_i^v \cdot v_{i-1,j,k-1} + \nabla X_{i-1}^u \cdot v_{i,j,k-1}}{\Delta X_{i-1}^u} \quad \text{and} \quad v_{12} = \frac{\nabla X_i^v \cdot v_{i-1,j,k} + \nabla X_{i-1}^u \cdot v_{i,j,k}}{\Delta X_{i-1}^u}$$

$$v|_{c_{i,j,k}}^{m-} = \frac{\nabla Z_k^u \cdot v_{11} + \nabla Z_{k-1}^w \cdot v_{12}}{\Delta Z_{k-1}^w}, \quad \text{and} \quad v|_{c_{i,j,k-1}}^{m+} = v|_{c_{i,j,k}}^{m-},$$

$$v|_{c_{i-1,j,k}}^{p-} = v|_{c_{i,j,k}}^{c-}, \quad \text{and} \quad v|_{c_{i-1,j,k-1}}^{p+} = v|_{c_{i,j,k}}^{c-}$$

### Interpolations for $G_w$

$$w_{w_{i,j,k}}^{X-} = \frac{\nabla X_{i-1}^u \cdot w_{i,j,k} + \nabla X_i^v \cdot w_{i-1,j,k}}{\Delta X_{i-1}^u} \quad \text{and} \quad w_{w_{i,j,k}}^{X+} = w_{w_{i+1,j,k}}^{X-}$$

$$u_{w_{i,j,k}}^{X-} = \frac{\nabla Z_k^w \cdot u_{i-1,j,k+1} + \nabla Z_{k+1}^u \cdot u_{i-1,j,k}}{\Delta Z_k^w} \quad \text{and} \quad u_{w_{i,j,k}}^{X+} = u_{w_{i+1,j,k}}^{X-}$$

$$w_{w_{i,j,k}}^{Z-} = \frac{\nabla Z_k^u \cdot w_{i,j,k} + \nabla Z_k^w \cdot w_{i,j,k-1}}{\Delta Z_k^u} \quad \text{and} \quad w_{w_{i,j,k}}^{Z+} = w_{w_{i,j,k+1}}^{Z-}$$

$$u_{w_{i,j,k}}^{Z-} = u_{u_{i,j,k}}^{X-}, \quad \text{and} \quad u_{w_{i,j,k}}^{Z+} = u_{w_{i,j,k+1}}^{Z-}$$

$$\check{v}_{w_{i,j,k}}^{X-} = \check{v}_{u_{i-1,j,k}}^{Z+} \quad \text{and} \quad \check{v}_{w_{i-1,j,k}}^{X+} = \check{v}_{w_{i,j,k}}^{X-}$$

$$\check{v}_{w_{i,j,k}}^{Z-} = \check{v}_{v_{i,j,k}}^{Y-} \quad \text{and} \quad \check{v}_{w_{i,j,k-1}}^{Z+} = \check{v}_{w_{i,j,k}}^{Z-}$$

$$\check{w}_{w_{i,j,k}}^{Y-} = \frac{\nabla Y_{j-1}^v \cdot w_{i,j,k} + \nabla Y_j^u \cdot w_{i,j-1,k}}{\Delta Y_{j-1}^v} \quad \text{and} \quad w_{w_{i,j,k}}^{Y+} = w_{w_{i,j+1,k}}^{Y-}$$

$$w_{11} = \frac{\nabla X_i^v \cdot w_{i-1,j,k-1} + \nabla X_{i-1}^u \cdot w_{i,j,k-1}}{\Delta X_{i-1}^u} \quad \text{and} \quad w_{12} = \frac{\nabla X_i^v \cdot w_{i-1,j,k} + \nabla X_{i-1}^u \cdot w_{i,j,k}}{\Delta X_{i-1}^u}$$

$$w|_{u_{i,j,k}}^{m-} = \frac{\nabla Z_k^w \cdot w_{11,i,j,k} + \nabla Z_k^u \cdot w_{12,i,j,k}}{\Delta Z_k^u}, \quad w|_{u_{i,j,k-1}}^{m+} = w|_{u_{i,j,k}}^{m-},$$

$$w|_{u_{i-1,j,k}}^{p-} = w|_{u_{i,j,k}}^{m-}, \quad w|_{u_{i-1,j,k-1}}^{p+} = w|_{u_{i,j,k}}^{m-}$$

After rearranging equations (C.1) to (C.5), the discretized momentum equations are as follows

$$G_u(u, v, w, p) = \frac{1}{\Delta X_i^u} \left[ \begin{aligned} & C_7 \cdot \left( (\check{u}_{u_{i,j,k}}^{X+})^2 - (\check{u}_{u_{i,j,k}}^{X-})^2 \right) \\ & + C_8 \left( \check{w}_{u_{i,j,k}}^{X+} \cdot \check{u}_{u_{i,j,k}}^{X+} - \check{w}_{u_{i,j,k}}^{X-} \cdot \check{u}_{u_{i,j,k}}^{X-} \right) \\ & + C_7 (p_{i+1,j,k} - p_{i,j,k}) \\ & + C_1 \left( \frac{u_{i+1,j,k} - u_{i,j,k}}{\Delta x_{i+1}^v} - \frac{u_{i,j,k} - u_{i-1,j,k}}{\Delta x_i^v} \right) \\ & + C_9 \left( u_{u_{i,j,k}}^{X+} - u_{u_{i,j,k}}^{X-} \right) \end{aligned} \right] \\ + \frac{1}{\Delta Y_j^u} \left[ \begin{aligned} & \left( \check{v}_{u_{i,j,k}}^{Y+} \cdot \check{u}_{u_{i,j,k}}^{Y+} - \check{v}_{u_{i,j,k}}^{Y-} \cdot \check{u}_{u_{i,j,k}}^{Y-} \right) \\ & + C_{10} \left( \frac{u_{i,j+1,k} - u_{i,j,k}}{\Delta Y_j^v} - \frac{u_{i,j,k} - u_{i,j-1,k}}{\Delta Y_{j-1}^v} \right) \end{aligned} \right] \\ + \frac{1}{\Delta Z_k^u} \left[ \begin{aligned} & C_2 \left( (\check{u}_{u_{i,j,k}}^{Z+})^2 - (\check{u}_{u_{i,j,k}}^{Z-})^2 \right) \\ & + C_3 \left( \check{w}_{u_{i,j,k}}^{Z+} \cdot \check{u}_{u_{i,j,k}}^{Z+} - \check{w}_{u_{i,j,k}}^{Z-} \cdot \check{u}_{u_{i,j,k}}^{Z-} \right) \\ & + C_2 \left( p_{u_{i,j,k}}^{Z+} - p_{u_{i,j,k}}^{Z-} \right) \\ & + C_5 \left( \frac{u_{i,j,k+1} - u_{i,j,k}}{\Delta z_k^w} - \frac{u_{i,j,k} - u_{i,j,k-1}}{\Delta z_{k-1}^w} \right) \\ & + C_4 \left( u_{u_{i,j,k}}^{Z+} - u_{u_{i,j,k}}^{Z-} \right) \\ & + C_6 \left( \frac{u|_{w_{i,j,k}}^{p+} - u|_{w_{i,j,k}}^{m+}}{\Delta X_i^u} - \frac{u|_{w_{i,j,k}}^{p-} - u|_{w_{i,j,k}}^{m-}}{\Delta X_i^u} \right) \end{aligned} \right] \quad (C.33)$$

$$\begin{aligned}
G_v(u, v, w, p) = & \frac{1}{\Delta X_i^v} \left[ \begin{aligned} & C_7 \left( u_{v_{i+1,j,k}}^{X+} \cdot v_{v_{i,j,k}}^{X+} - u_{v_{i+1,j,k}}^{X-} \cdot v_{v_{i,j,k}}^{X-} \right) \\ & + C_8 \left( \tilde{w}_{v_{i,j,k}}^{X+} \cdot \check{v}_{v_{i,j,k}}^{X+} - \tilde{w}_{v_{i,j,k}}^{X-} \cdot \check{v}_{v_{i,j,k}}^{X-} \right) \\ & + C_1 \left( \frac{v_{i+1,j,k} - v_{i,j,k}}{\Delta x_i^u} - \frac{v_{i,j,k} - v_{i-1,j,k}}{\Delta x_{i-1}^u} \right) \\ & + C_9 \left( v_{v_{i,j,k}}^{X+} - v_{v_{i,j,k}}^{X-} \right) \end{aligned} \right] \\
& + \frac{1}{\Delta Y_j^v} \left[ \begin{aligned} & \left( \left( \check{v}_{v_{i,j,k}}^{Y+} \right)^2 - \left( \check{v}_{v_{i,j,k}}^{Y-} \right)^2 \right) \\ & + (p_{i,j+1,k} - p_{i,j,k}) \\ & + C_{10} \left( \frac{v_{i,j+1,k} - v_{i,j,k}}{\Delta Y_{j+1}^u} - \frac{v_{i,j,k} - v_{i,j-1,k}}{\Delta Y_j^u} \right) \end{aligned} \right] \\
& + \frac{1}{\Delta Z_k^u} \left[ \begin{aligned} & C_2 \left( u_{v_{i,j,k}}^{Z+} \cdot v_{v_{i,j,k}}^{Z+} - u_{v_{i,j,k}}^{Z-} \cdot v_{v_{i,j,k}}^{Z-} \right) \\ & + C_3 \left( \tilde{w}_{v_{i,j,k}}^{Z+} \cdot \check{v}_{v_{i,j,k}}^{Z+} - \tilde{w}_{v_{i,j,k}}^{Z-} \cdot \check{v}_{v_{i,j,k}}^{Z-} \right) \\ & + C_5 \left( \frac{v_{i,j,k+1} - v_{i,j,k}}{\Delta z_k^w} - \frac{v_{i,j,k} - v_{i,j,k-1}}{\Delta z_{k-1}^w} \right) \\ & + C_4 \left( v_{v_{i,j,k}}^{Z+} - v_{v_{i,j,k}}^{Z-} \right) \\ & + C_6 \left( \frac{v|_{c_{i,j,k}}^{p+} - v|_{c_{i,j,k}}^{m+}}{\Delta X_i^v} - \frac{v|_{c_{i,j,k}}^{p-} - v|_{c_{i,j,k}}^{m-}}{\Delta X_i^v} \right) \end{aligned} \right] \tag{C.34}
\end{aligned}$$

$$\begin{aligned}
G_w(u, v, w, p) = & \frac{1}{\Delta X_i^v} \left[ \begin{aligned} & C_7 \left( w_{w_{i,j,k}}^{X+} \cdot u_{w_{i,j,k}}^{X+} - w_{w_{i,j,k}}^{X-} \cdot u_{w_{i,j,k}}^{X-} \right) \\ & + C_8 \left( \left( \tilde{w}_{w_{i,j,k}}^{X+} \right)^2 - \left( \tilde{w}_{w_{i,j,k}}^{X-} \right)^2 \right) \\ & + C_8 \left( p_{w_{i,j,k}}^{X+} - p_{w_{i,j,k}}^{X-} \right) \\ & + C_1 \left( \frac{w_{i+1,j,k} - w_{i,j,k}}{\Delta x_i^u} - \frac{w_{i,j,k} - w_{i-1,j,k}}{\Delta x_{i-1}^u} \right) \\ & + C_9 \left( w_{w_{i,j,k}}^{X+} - w_{w_{i,j,k}}^{X-} \right) \end{aligned} \right] \\
& + \frac{1}{\Delta Y_j^u} \left[ \begin{aligned} & \left( \tilde{w}_{w_{i,j,k}}^{Y+} \cdot \check{v}_{w_{i,j,k}}^{Y+} - \tilde{w}_{w_{i,j,k}}^{Y-} \cdot \check{v}_{w_{i,j,k}}^{Y-} \right) \\ & + C_{10} \left( \frac{w_{i,j+1,k} - w_{i,j,k}}{\Delta Y_j^v} - \frac{w_{i,j,k} - w_{i,j-1,k}}{\Delta Y_{j-1}^v} \right) \end{aligned} \right] \\
& + \frac{1}{\Delta Z_k^w} \left[ \begin{aligned} & C_2 \left( w_{w_{i,j,k}}^{Z+} \cdot u_{w_{i,j,k}}^{Z+} - w_{w_{i,j,k}}^{Z-} \cdot u_{w_{i,j,k}}^{Z-} \right) \\ & + C_3 \left( \left( \tilde{w}_{w_{i,j,k}}^{Z+} \right)^2 - \left( \tilde{w}_{w_{i,j,k}}^{Z-} \right)^2 \right) \\ & + C_3 \left( p_{i,j,k+1} - p_{i,j,k} \right) \\ & + C_5 \left( \frac{w_{i,j,k+1} - w_{i,j,k}}{\Delta z_{k+1}^u} - \frac{w_{i,j,k} - w_{i,j,k-1}}{\Delta z_k^u} \right) \\ & + C_4 \left( w_{w_{i,j,k}}^{Z+} - w_{w_{i,j,k}}^{Z-} \right) \\ & + C_6 \left( \frac{w|_{u_{i,j,k}}^{p+} - w|_{u_{i,j,k}}^{m+}}{\Delta X_i^v} - \frac{w|_{u_{i,j,k}}^{p-} - w|_{u_{i,j,k}}^{m-}}{\Delta X_i^v} \right) \end{aligned} \right] \tag{C.35}
\end{aligned}$$

### Continuity equation

$$\begin{aligned}
\nabla \cdot V = & \frac{1}{\Delta X_i^v} \left[ \begin{aligned} & C_7 (u_{i,j,k} - u_{i-1,j,k}) \\ & + C_8 \left( w|_{u_{i,j,k}}^{m+} - w|_{u_{i,j,k}}^{m-} \right) \end{aligned} \right] + \frac{1}{\Delta Y_j^u} [( \check{v}_{i,j,k} - \check{v}_{i,j-1,k} )] \\
& + \frac{1}{\Delta Z_k^u} \left[ \begin{aligned} & C_2 \left( u|_{w_{i,j,k}}^{m+} - u|_{w_{i,j,k}}^{m-} \right) \\ & + C_3 (\tilde{w}_{i,j,k} - \tilde{w}_{i,j,k-1}) \end{aligned} \right] \tag{C.36}
\end{aligned}$$

## Spatial discretization of three successive sweeps:

### Z-sweep:

#### X-momentum

$$\begin{aligned}
& \overline{\Delta u}_{i,j,k-1} \cdot \left\{ \frac{\alpha \Delta \tau}{\Delta Z_k^u} \left[ \begin{array}{c} C_2 \left( -\check{u}_{u,i,j,k}^{Z-} \left( \frac{\nabla Z_k^u}{\Delta Z_{k-1}^w} \right) \right) \\ -C_3 \left( \check{w}_{u,i,j,k}^{Z-} \left( \frac{\nabla Z_k^u}{\Delta Z_{k-1}^w} \right) \right) \\ -C_4 \left( \frac{\nabla Z_k^u}{\Delta Z_{k-1}^w} \right) \\ +C_5 \left( \frac{1}{\Delta Z_{k-1}^w} \right) \end{array} \right] \right\} + \overline{\Delta u}_{i,j,k} \cdot \left\{ 1 + \right. \\
& \left. \frac{\alpha \Delta \tau}{\Delta Z_k^u} \left[ \begin{array}{c} C_2 \left( \check{u}_{u,i,j,k}^{Z+} \left( \frac{\nabla Z_{k+1}^u}{\Delta Z_k^w} \right) - \check{u}_{u,i,j,k}^{Z-} \left( \frac{\nabla Z_{k-1}^w}{\Delta Z_{k-1}^w} \right) \right) \\ +C_3 \left( \check{w}_{u,i,j,k}^{Z+} \left( \frac{\nabla Z_{k+1}^u}{\Delta Z_k^w} \right) - \check{w}_{u,i,j,k}^{Z-} \left( \frac{\nabla Z_{k-1}^w}{\Delta Z_{k-1}^w} \right) \right) \\ +C_4 \left( \left( \frac{\nabla Z_{k+1}^u}{\Delta Z_k^w} \right) - \left( \frac{\nabla Z_{k-1}^w}{\Delta Z_{k-1}^w} \right) \right) \\ +C_5 \left( \frac{-1}{\Delta Z_k^w} + \frac{-1}{\Delta Z_{k-1}^w} \right) \end{array} \right] \right\} + \overline{\Delta u}_{i,j,k+1} \cdot \left\{ \frac{\alpha \Delta \tau}{\Delta Z_k^u} \left[ \begin{array}{c} C_2 \left( \check{u}_{u,i,j,k}^{Z+} \left( \frac{\nabla Z_k^w}{\Delta Z_k^w} \right) \right) \\ +C_3 \left( \check{w}_{u,i,j,k}^{Z+} \left( \frac{\nabla Z_k^w}{\Delta Z_k^w} \right) \right) \\ +C_4 \left( \frac{\nabla Z_k^w}{\Delta Z_k^w} \right) \\ +C_5 \left( \frac{1}{\Delta Z_k^w} \right) \end{array} \right] \right\} \\
& = \Delta \tau R_u - \frac{c_6}{\Delta X_i^u} \frac{\alpha \Delta \tau}{\Delta Z_k^u} \left( \overline{\Delta u}_{w,i,j,k}^{p+} - \overline{\Delta u}_{w,i,j,k}^{m+} - \overline{\Delta u}_{w,i,j,k}^{p-} + \overline{\Delta u}_{w,i,j,k}^{m-} \right) - C_2 \frac{\alpha \Delta \tau}{\Delta Z_k^u} \left( \overline{\Delta p}_u^{Z+} - \overline{\Delta p}_u^{Z-} \right) \quad (\text{C.37})
\end{aligned}$$

## Y-momentum

$$\begin{aligned}
& \overline{\Delta v}_{i,j,k-1} \cdot \left\{ \frac{\alpha \Delta \tau}{\Delta Z_k^u} \left[ \begin{array}{l} C_2 \left( -u_{v_{i,j,k}}^{Z-} \cdot \left( \frac{\nabla Z_k^u}{\Delta Z_{k-1}^w} \right) \right) \\ -C_3 \left( w_{v_{i,j,k}}^{Z-} \cdot \left( \frac{\nabla Z_k^u}{\Delta Z_{k-1}^w} \right) \right) \\ -C_4 \left( \frac{\nabla Z_k^u}{\Delta Z_{k-1}^w} \right) \\ +C_5 \left( \frac{1}{\Delta Z_{k-1}^w} \right) \end{array} \right] \right\} + \overline{\Delta v}_{i,j,k} \cdot \left\{ 1 + \right. \\
& \left. \frac{\alpha \Delta \tau}{\Delta Z_k^u} \left[ \begin{array}{l} C_2 \left( u_{v_{i,j,k}}^{Z+} \cdot \left( \frac{\nabla Z_{k+1}^u}{\Delta Z_k^w} \right) - u_{v_{i,j,k}}^{Z-} \cdot \left( \frac{\nabla Z_{k-1}^w}{\Delta Z_{k-1}^w} \right) \right) \\ +C_3 \left( w_{v_{i,j,k}}^{Z+} \cdot \left( \frac{\nabla Z_{k+1}^u}{\Delta Z_k^w} \right) - w_{v_{i,j,k}}^{Z-} \cdot \left( \frac{\nabla Z_{k-1}^w}{\Delta Z_{k-1}^w} \right) \right) \\ +C_4 \left( \frac{\nabla Z_{k+1}^u}{\Delta Z_k^w} - \frac{\nabla Z_{k-1}^w}{\Delta Z_{k-1}^w} \right) \\ +C_5 \left( \frac{-1}{\Delta Z_k^w} + \frac{-1}{\Delta Z_{k-1}^w} \right) \end{array} \right] \right\} + \overline{\Delta v}_{i,j,k+1} \cdot \left\{ \frac{\alpha \Delta \tau}{\Delta Z_k^u} \left[ \begin{array}{l} C_2 \left( u_{v_{i,j,k}}^{Z+} \cdot \left( \frac{\nabla Z_k^w}{\Delta Z_k^w} \right) \right) \\ +C_3 \left( w_{v_{i,j,k}}^{Z+} \cdot \left( \frac{\nabla Z_k^w}{\Delta Z_k^w} \right) \right) \\ +C_4 \left( \frac{\nabla Z_k^w}{\Delta Z_k^w} \right) \\ +C_5 \left( \frac{1}{\Delta Z_k^w} \right) \end{array} \right] \right\} \\
& = \Delta \tau R_v - \frac{C_6}{\Delta X_i^v} \frac{\alpha \Delta \tau}{\Delta Z_k^u} \left( \overline{\Delta v} |_{c_{i,j,k}}^{p+} - \overline{\Delta v} |_{c_{i,j,k}}^{m+} - \overline{\Delta v} |_{c_{i,j,k}}^{p-} + \overline{\Delta v} |_{c_{i,j,k}}^{m-} \right) \tag{C.38}
\end{aligned}$$

## Z-momentum

$$\begin{aligned}
& \overline{\Delta w}_{i,j,k-1} \left\{ \frac{\alpha \Delta \tau}{\Delta Z_k^w} \left[ \begin{array}{l} C_2 \left( -u_{w,i,j,k}^{Z-} \left( \frac{\nabla Z_k^w}{\Delta Z_k^u} \right) \right) \\ -C_3 \left( w_{w,i,j,k}^{Z-} \left( \frac{\nabla Z_k^w}{\Delta Z_k^u} \right) \right) \\ -C_4 \left( \frac{\nabla Z_k^w}{\Delta Z_k^u} \right) \\ +C_5 \left( \frac{1}{\Delta Z_k^u} \right) \\ -C_{3w} C_{3p} \frac{\Delta \tau}{\delta} \left( \frac{1}{\Delta Z_k^u} \right) \end{array} \right] + \overline{\Delta w}_{i,j,k} \right\} 1 + \Delta \tau + \\
& \frac{\alpha \Delta \tau}{\Delta Z_k^w} \left[ \begin{array}{l} C_2 \left( u_{w,i,j,k}^{Z+} \frac{\nabla Z_{k+1}^w}{\Delta Z_{k+1}^u} - u_{w,i,j,k}^{Z-} \frac{\nabla Z_k^u}{\Delta Z_k^u} \right) \\ +C_3 \left( w_{w,i,j,k}^{Z+} \frac{\nabla Z_{k+1}^w}{\Delta Z_{k+1}^u} - w_{w,i,j,k}^{Z-} \frac{\nabla Z_k^u}{\Delta Z_k^u} \right) \\ +C_4 \left( \frac{\nabla Z_{k+1}^w}{\Delta Z_{k+1}^u} - \frac{\nabla Z_k^u}{\Delta Z_k^u} \right) \\ +C_5 \left( \frac{-1}{\Delta Z_{k+1}^u} + \frac{-1}{\Delta Z_k^u} \right) \\ -C_{3w} C_{3p} \frac{\Delta \tau}{\delta} \left( \frac{-1}{\Delta Z_{k+1}^u} + \frac{-1}{\Delta Z_k^u} \right) \end{array} \right] + \overline{\Delta w}_{i,j,k+1} \left\{ \frac{\alpha \Delta \tau}{\Delta Z_k^w} \left[ \begin{array}{l} C_2 \left( u_{w,i,j,k}^{Z+} \frac{\nabla Z_{k+1}^u}{\Delta Z_{k+1}^u} \right) \\ +C_3 \left( w_{w,i,j,k}^{Z+} \frac{\nabla Z_{k+1}^u}{\Delta Z_{k+1}^u} \right) \\ +C_4 \left( \frac{\nabla Z_{k+1}^u}{\Delta Z_{k+1}^u} \right) \\ +C_5 \left( \frac{1}{\Delta Z_{k+1}^u} \right) \\ -C_{3w} \cdot C_{3p} \frac{\Delta \tau}{\delta} \left( \frac{1}{\Delta Z_{k+1}^u} \right) \end{array} \right] \right\} \\
& = \Delta \tau R_w - C_6 \alpha \frac{\Delta \tau}{\Delta Z_k^w} \left( \frac{\overline{\Delta w}|_{u,i,j,k}^{p+} - \overline{\Delta w}|_{u,i,j,k}^{m+}}{\Delta X_i^p} - \frac{\overline{\Delta w}|_{u,i,j,k}^{p-} - \overline{\Delta w}|_{u,i,j,k}^{m-}}{\Delta X_i^p} \right) + C_{3w} \alpha \frac{\Delta \tau}{\Delta Z_k^w} \frac{\Delta \tau}{\delta} (\nabla \cdot V_{i,j,k+1} - \nabla \cdot V_{i,j,k}) + \\
& C_{3w} \cdot C_{2p} \alpha \frac{\Delta \tau}{\Delta Z_k^w} \frac{\Delta \tau}{\delta} \left[ \left( \frac{\overline{\Delta u}|_{w,i,j,k+1}^{m+} - \overline{\Delta u}|_{w,i,j,k+1}^{m-}}{\Delta Z_{k+1}^u} \right) - \left( \frac{\overline{\Delta u}|_{w,i,j,k}^{m+} - \overline{\Delta u}|_{w,i,j,k}^{m-}}{\Delta Z_k^u} \right) \right] \quad (C.39)
\end{aligned}$$

## Continuity equation

$$\overline{\Delta p}_{i,j,k} = -\frac{\Delta \tau}{\delta} \nabla \cdot V_{i,j,k} - \frac{\Delta \tau}{\delta} \left[ C_2 \left( \frac{\overline{\Delta u}|_{w,i,j,k}^{m+} - \overline{\Delta u}|_{w,i,j,k}^{m-}}{\Delta Z_k^u} \right) + C_3 \left( \frac{\overline{\Delta w}_{i,j,k} - \overline{\Delta w}_{i,j,k-1}}{\Delta Z_k^u} \right) \right] \quad (C.40)$$

## Y-Sweep:

### X-Momentum

$$\begin{aligned} \Delta u_{i,j-1,k} \cdot \left\{ \frac{\alpha \Delta \tau}{\Delta Y_j^u} \left[ -\check{v}_{u,i,j,k}^{Y-} \cdot \left( \frac{\nabla Y_j^u}{\Delta Y_{j-1}^p} \right) \right] + C_{10} \left( \frac{1}{\Delta Y_{j-1}^p} \right) \right\} + \Delta u_{i,j,k} \cdot \left\{ 1 + \frac{\alpha \Delta \tau}{\Delta Y_j^u} \left[ \check{v}_{u,i,j,k}^{Y+} \cdot \left( \frac{\nabla Y_{j+1}^u}{\Delta Y_j^p} \right) - \check{v}_{u,i,j,k}^{Y-} \cdot \left( \frac{\nabla Y_{j-1}^u}{\Delta Y_{j-1}^p} \right) \right] + C_{10} \left( \frac{-1}{\Delta Y_j^p} + \frac{-1}{\Delta Y_{j-1}^p} \right) \right\} + \\ \Delta u_{i,j+1,k} \cdot \left\{ \frac{\alpha \Delta \tau}{\Delta Y_j^u} \left[ \check{v}_{u,i,j,k}^{Y+} \cdot \left( \frac{\nabla Y_j^u}{\Delta Y_j^p} \right) \right] + C_{10} \left( \frac{1}{\Delta Y_j^p} \right) \right\} = \Delta u^* \end{aligned} \quad (\text{C. 41})$$

### Y-Momentum

$$\begin{aligned} \Delta v_{i,j-1,k} \cdot \left\{ \frac{\alpha \Delta \tau}{\Delta Y_j^p} \left[ -\check{v}_{v,i,j,k}^{Y-} \cdot \left( \frac{\nabla Y_j^p}{\Delta Y_j^u} \right) \right] + C_{10} \left( \frac{1}{\Delta Y_j^u} \right) - \frac{\Delta \tau}{\Delta Y_j^u} \right\} + \Delta v_{i,j,k} \cdot \left\{ 1 + \Delta \tau + \frac{\alpha \Delta \tau}{\Delta Y_j^p} \left[ \check{v}_{v,i,j,k}^{Y+} \cdot \left( \frac{\nabla Y_{j+1}^p}{\Delta Y_{j+1}^u} \right) - \check{v}_{v,i,j,k}^{Y-} \cdot \left( \frac{\nabla Y_j^p}{\Delta Y_j^u} \right) \right] + C_{10} \left( \frac{-1}{\Delta Y_{j+1}^u} + \frac{-1}{\Delta Y_j^u} \right) + \frac{\Delta \tau}{\Delta Y_{j+1}^u} + \frac{\Delta \tau}{\Delta Y_j^u} \right\} + \\ \Delta v_{i,j+1,k} \cdot \left\{ \frac{\alpha \Delta \tau}{\Delta Y_j^p} \left[ \check{v}_{v,i,j,k}^{Y+} \cdot \left( \frac{\nabla Y_{j+1}^p}{\Delta Y_{j+1}^u} \right) \right] + C_{10} \left( \frac{1}{\Delta Y_{j+1}^u} \right) - \frac{\Delta \tau}{\Delta Y_{j+1}^u} \right\} = \Delta v^*_{i,j,k} - \alpha \frac{\Delta \tau}{\Delta Y_j^p} (\Delta p^*_{i,j+1,k} - \Delta p^*_{i,j,k}) \end{aligned} \quad (\text{C. 42})$$

### Z-Momentum

$$\begin{aligned} \Delta w_{i,j-1,k} \cdot \left\{ \frac{\alpha \Delta \tau}{\Delta Y_j^u} \left[ -\check{v}_{w,i,j,k}^{Y-} \cdot \left( \frac{\nabla Y_j^u}{\Delta Y_{j-1}^p} \right) \right] + C_{10} \left( \frac{1}{\Delta Y_{j-1}^p} \right) \right\} + \Delta w_{i,j,k} \cdot \left\{ 1 + \frac{\alpha \Delta \tau}{\Delta Y_j^u} \left[ \check{v}_{w,i,j,k}^{Y+} \cdot \left( \frac{\nabla Y_{j+1}^u}{\Delta Y_j^p} \right) - \check{v}_{w,i,j,k}^{Y-} \cdot \left( \frac{\nabla Y_{j-1}^u}{\Delta Y_{j-1}^p} \right) \right] + C_{10} \left( \frac{-1}{\Delta Y_j^p} + \frac{-1}{\Delta Y_{j-1}^p} \right) \right\} + \\ \Delta w_{i,j+1,k} \cdot \left\{ \frac{\alpha \Delta \tau}{\Delta Y_j^u} \left[ \check{v}_{w,i,j,k}^{Y+} \cdot \left( \frac{\nabla Y_j^u}{\Delta Y_j^p} \right) \right] + C_{10} \left( \frac{1}{\Delta Y_j^p} \right) \right\} = \Delta w^*_{i,j,k} \end{aligned} \quad (\text{C. 43})$$

### Continuity Equation

$$\Delta p_{i,j,k} = \Delta p^*_{i,j,k} - \frac{\Delta \tau}{\Delta Y_j^u} (\Delta v_{i,j,k} - \Delta v_{i,j-1,k}) \quad (\text{C. 44})$$

**X-Sweep:**

**X-Momentum**

$$\begin{aligned}
& \Delta u^*_{i-1,j,k} \left\{ \frac{\alpha \Delta \tau}{\Delta X_i^u} \left[ \begin{array}{c} C_9 \left( -\frac{\nabla X_i^u}{\Delta X_i^v} \right) \\ -C_7 \left( \tilde{u}_{u_{i,j,k}}^{X-} \left( \frac{\nabla X_i^u}{\Delta X_i^v} \right) \right) \\ -C_8 \left( \tilde{w}_{u_{i,j,k}}^{X-} \left( \frac{\nabla X_i^u}{\Delta X_i^v} \right) \right) \\ +C_1 \left( \frac{1}{\Delta x_i^v} \right) \\ -\frac{\Delta \tau}{\delta} C_{7u} C_{7p} \left( \frac{1}{\Delta x_i^v} \right) \end{array} \right] \right\} + \Delta u^*_{i,j,k} \left\{ 1 + \Delta \tau + \right. \\
& \left. \frac{\alpha \Delta \tau}{\Delta X_i^u} \left[ \begin{array}{c} C_9 \left( \frac{\nabla X_{i+1}^u}{\Delta X_{i+1}^v} - \frac{\nabla X_i^v}{\Delta X_i^v} \right) \\ +C_7 \left( \tilde{u}_{u_{i,j,k}}^{X+} \left( \frac{\nabla X_{i+1}^u}{\Delta X_{i+1}^v} \right) - \tilde{u}_{u_{i,j,k}}^{X-} \left( \frac{\nabla X_i^v}{\Delta X_i^v} \right) \right) \\ +C_8 \left( \tilde{w}_{u_{i,j,k}}^{X+} \left( \frac{\nabla X_{i+1}^u}{\Delta X_{i+1}^v} \right) - \tilde{w}_{u_{i,j,k}}^{X-} \left( \frac{\nabla X_i^v}{\Delta X_i^v} \right) \right) \\ +C_1 \left( \frac{-1}{\Delta x_{i+1}^v} + \frac{-1}{\Delta x_i^v} \right) \\ -\frac{\Delta \tau}{\delta} C_{7u} C_{7p} \left( \frac{-1}{\Delta x_{i+1}^v} + \frac{-1}{\Delta x_i^v} \right) \end{array} \right] \right\} + \Delta u^*_{i+1,j,k} \left\{ \frac{\alpha \Delta \tau}{\Delta X_i^u} \left[ \begin{array}{c} C_9 \left( \frac{\nabla X_{i+1}^v}{\Delta X_{i+1}^v} \right) \\ +C_7 \left( \tilde{u}_{u_{i,j,k}}^{X+} \left( \frac{\nabla X_{i+1}^v}{\Delta X_{i+1}^v} \right) \right) \\ +C_8 \left( \tilde{w}_{u_{i,j,k}}^{X+} \left( \frac{\nabla X_{i+1}^v}{\Delta X_{i+1}^v} \right) \right) \\ +C_1 \left( \frac{1}{\Delta x_{i+1}^v} \right) \\ -\frac{\Delta \tau}{\delta} C_{7u} C_{7p} \left( \frac{1}{\Delta x_{i+1}^v} \right) \end{array} \right] \right\} \\
& = \bar{\Delta u} - C_{7u} \alpha \frac{\Delta \tau}{\Delta X_i^u} (\bar{\Delta p}_{i+1,j,k} - \bar{\Delta p}_{i,j,k}) \\
& \quad + \alpha \frac{\Delta \tau}{\Delta X_i^u} \frac{\Delta \tau}{\delta} C_{7u} C_{8p} \left( \frac{\Delta w^*|_{u_{i+1,j,k}}^{m+} - \Delta w^*|_{u_{i+1,j,k}}^{m-}}{\Delta X_{i+1}^v} - \frac{\Delta w^*|_{u_{i,j,k}}^{m+} - \Delta w^*|_{u_{i,j,k}}^{m-}}{\Delta X_i^v} \right) \quad (C.45)
\end{aligned}$$

## Y-Momentum

$$\begin{aligned}
& \Delta v^*_{i-1,j,k} \cdot \left\{ \frac{\alpha \Delta \tau}{\Delta X_i^p} \left[ \begin{array}{c} -C_9 \left( \frac{\nabla X_i^p}{\Delta X_{i-1}^u} \right) \\ -C_7 \left( u_{v_{i+1,j,k}}^{X-} \left( \frac{\nabla X_i^p}{\Delta X_{i-1}^u} \right) \right) \\ -C_8 \left( w_{v_{i+1,j,k}}^{X-} \left( \frac{\nabla X_i^p}{\Delta X_{i-1}^u} \right) \right) \\ +C_1 \left( \frac{1}{\Delta x_{i-1}^u} \right) \end{array} \right] \right\} + \Delta v^*_{i,j,k} \cdot \left\{ 1 + \right. \\
& \left. \frac{\alpha \Delta \tau}{\Delta X_i^p} \left[ \begin{array}{c} C_9 \left( \frac{\nabla X_{i+1}^p}{\Delta X_i^u} - \frac{\nabla X_{i-1}^u}{\Delta X_{i-1}^u} \right) \\ +C_7 \left( u_{v_{i+1,j,k}}^{X+} \left( \frac{\nabla X_{i+1}^p}{\Delta X_i^u} \right) - u_{v_{i+1,j,k}}^{X-} \left( \frac{\nabla X_{i-1}^u}{\Delta X_{i-1}^u} \right) \right) \\ +C_8 \left( w_{v_{i+1,j,k}}^{X+} \left( \frac{\nabla X_{i+1}^p}{\Delta X_i^u} \right) - w_{v_{i+1,j,k}}^{X-} \left( \frac{\nabla X_{i-1}^u}{\Delta X_{i-1}^u} \right) \right) \\ +C_1 \left( \frac{-1}{\Delta x_i^u} + \frac{-1}{\Delta x_{i-1}^u} \right) \end{array} \right] \right\} + \Delta v^*_{i+1,j,k} \cdot \left\{ \frac{\alpha \Delta \tau}{\Delta X_i^p} \left[ \begin{array}{c} C_9 \left( \frac{\nabla X_i^u}{\Delta X_i^u} \right) \\ +C_7 \left( u_{v_{i+1,j,k}}^{X+} \left( \frac{\nabla X_i^u}{\Delta X_i^u} \right) \right) \\ +C_8 \left( w_{v_{i+1,j,k}}^{X+} \left( \frac{\nabla X_i^u}{\Delta X_i^u} \right) \right) \\ +C_1 \left( \frac{1}{\Delta x_i^u} \right) \end{array} \right] \right\} = \\
& \overline{\Delta v} \tag{C.46}
\end{aligned}$$

## Z-Momentum

$$\begin{aligned}
& \Delta w^*_{i-1,j,k} \left\{ \frac{\alpha \Delta \tau}{\Delta X_i^v} \left[ \begin{array}{l} -C_9 \left( \frac{\nabla X_i^v}{\Delta X_{i-1}^u} \right) \\ -C_7 \left( u_{w_{i,j,k}}^{X-} \left( \frac{\nabla X_i^v}{\Delta X_{i-1}^u} \right) \right) \\ -C_8 \left( w_{w_{i,j,k}}^{X-} \left( \frac{\nabla X_i^v}{\Delta X_{i-1}^u} \right) \right) \\ +C_1 \left( \frac{1}{\Delta x_{i-1}^u} \right) \end{array} \right] \right\} + \\
& \Delta w^*_{i,j,k} \left\{ \frac{\alpha \Delta \tau}{\Delta X_i^v} \left[ \begin{array}{l} 1 + C_9 \left( \frac{\nabla X_{i+1}^v}{\Delta X_i^u} - \frac{\nabla X_{i-1}^u}{\Delta X_{i-1}^u} \right) \\ +C_7 \left( u_{w_{i,j,k}}^{X+} \left( \frac{\nabla X_{i+1}^v}{\Delta X_i^u} \right) - u_{w_{i,j,k}}^{X-} \left( \frac{\nabla X_{i-1}^u}{\Delta X_{i-1}^u} \right) \right) \\ +C_8 \left( w_{w_{i,j,k}}^{X+} \left( \frac{\nabla X_{i+1}^v}{\Delta X_i^u} \right) - w_{w_{i,j,k}}^{X-} \left( \frac{\nabla X_{i-1}^u}{\Delta X_{i-1}^u} \right) \right) \\ +C_1 \left( \frac{-1}{\Delta x_i^u} + \frac{-1}{\Delta x_{i-1}^u} \right) \end{array} \right] \right\} + \\
& \Delta w^*_{i+1,j,k} \left\{ \frac{\alpha \Delta \tau}{\Delta X_i^v} \left[ \begin{array}{l} C_9 \left( \frac{\nabla X_i^u}{\Delta X_i^u} \right) \\ +C_7 \left( u_{w_{i,j,k}}^{X+} \left( \frac{\nabla X_i^u}{\Delta X_i^u} \right) \right) \\ +C_8 \left( w_{w_{i,j,k}}^{X+} \left( \frac{\nabla X_i^u}{\Delta X_i^u} \right) \right) \\ +C_1 \left( \frac{1}{\Delta x_i^u} \right) \end{array} \right] \right\} = \overline{\Delta w}_{i,j,k} - C_8 \alpha \frac{\Delta \tau}{\Delta X_i^v} \left( \Delta p_{w_{i,j,k}}^{*X+} - \Delta p_{w_{i,j,k}}^{*X-} \right) \quad (C.47)
\end{aligned}$$

## Continuity Equation

$$\Delta p^*_{i,j,k} = \overline{\Delta p}_{i,j,k} - \frac{\Delta \tau}{\delta} \left( C_7 \frac{\Delta u^*_{i,j,k} - \Delta u^*_{i-1,j,k}}{\Delta X_i^v} + C_8 \frac{\Delta w^*_{u_{i,j,k}}^{m+} - \Delta w^*_{u_{i,j,k}}^{m-}}{\Delta X_i^v} \right) \quad (C.48)$$